Physics of the Solid State, Vol. 47, No. 12, 2005, pp. 2205–2206. Translated from Fizika Tverdogo Tela, Vol. 47, No. 12, 2005, pp. 2113–2115.

On the 75th Anniversary of Aleksandr Aleksandrovich Kaplyanskiĭ

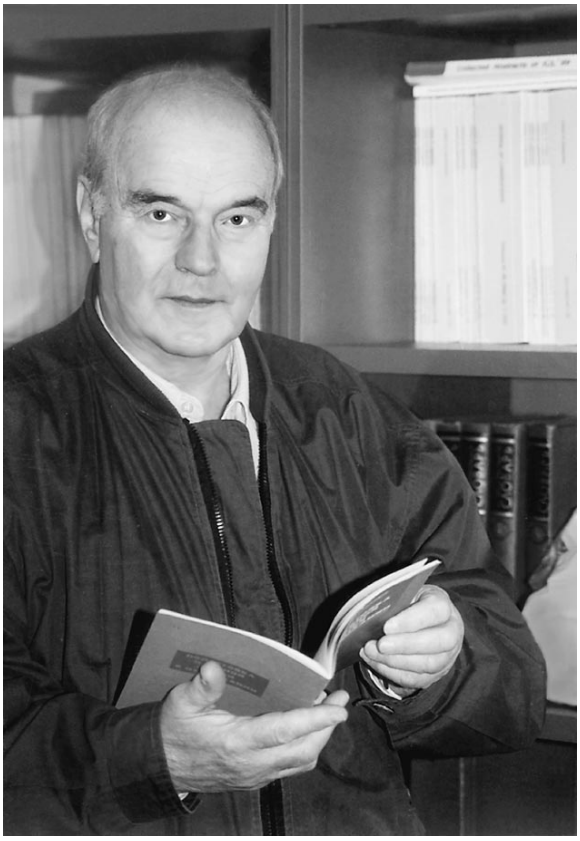

A.A. Kaplyanskiĭ was born in Leningrad into the family of an Elektrosila works engineer. After he graduated from secondary school, Kaplyanskiĭ entered the Faculty of Physics at Leningrad State University. Upon graduating from university, he was admitted to the Leningrad Physicotechnical Institute for post-graduate studies. Kaplyanskiĭ prepared his dissertation (1957) under the supervision of Corresponding Member of the USSR Academy of Sciences E.F. Gross, an outstanding scientist in the field of spectroscopy. His dissertation was devoted to the discovery and study of the line structure of the fundamental absorption edge of semiconductors associated with optical excitation of excitons.

In 1960, Aleksandr Aleksandrovich experimentally discovered optical anisotropy of cubic crystals; the anisotropy was observed in crystals of copper oxide (Cu_2O) in the region of excitonic resonance. This discovery has played an important role in the development of modern crystal optics with inclusion of spatial dispersion. Kaplyanskiĭ was the first to observe (in 1960) the reversible splitting of excitonic transition lines in the optical spectrum of Cu_2O crystals subjected to uniaxial elastic strains. Those observations initiated studies on the piezooptic effect in semiconductors. In 1966, a group of scientists, including Kaplyanskiĭ, was awarded the Lenin Prize for research on the physics of excitons in semiconductors.

In the late 1950s, Aleksandr Aleksandrovich started studying the optical spectra of dielectric crystals with impurity ions; these crystals attracted considerable interest after the invention of the ruby laser. In 1958, he discovered a new phenomenon in optical spectroscopy, namely, the reversible splitting of spectral lines of impurity centers in crystals subjected to directed elastic strains (Kaplyanskiĭ splitting). Based on this phenomenon, Kaplyanskiĭ developed an efficient piezooptic spectroscopic method for determining the local symmetry of impurity centers and point defects in crystals. This technique is of considerable current use. In 1975, Kaplyanskiĭ, P.P. Feofilov, and V.N. Medvedev (a colleague of Kaplyanskiĭ) were awarded the State Prize of the USSR for the development of new methods of studying impurity centers and defects in crystals.

In 1973, Kaplyanskiĭ, together with Yu.F. Markov, discovered a new class of ferroelastics (halides of univalent mercury) possessing highly anisotropic elastic and optical properties. Raman spectroscopy was used to establish the mechanism of the ferroelastic phase transition in these materials and to discover new spectroscopic manifestations of the dynamics of lattices with soft modes, which made it possible to employ mercury halides as model objects for spectroscopic studies of the general properties of structural phase transitions in crystals.

Aleksandr Aleksandrovich is recognized as having made a considerable contribution to the study of the fundamental properties of ultrahigh-frequency (terahertz) acoustic phonons to which traditional ultrasonic techniques are inapplicable. In 1975, Kaplyanskiĭ and coworkers (A.V. Akimov, S.A. Basun, S.P. Feofilov) began long-term studies in which they employed the technique of optical detection of nonequilibrium terahertz phonons injected into crystals at liquid-helium temperature to investigate the various modes of phonon propagation, phonon scattering from lattice defects and crystal surfaces, the interaction of phonons with electronic impurity levels and excitons, and anharmonic interactions. It has been found that terahertz phonons

1063-7834/05/4712-2205$26.00

exhibit specific behavior in noncrystalline solids, low-dimensional quantum-well semiconductor structures, and spatially inhomogeneous (ceramics) and spatially restricted (filaments) crystalline media. The collective monograph "Nonequilibrium Phonons in Nonmetallic Crystals," edited by W. Eisenmenger and Kaplyanskiĭ and published by the North-Holland Publishing Company in 1986, summarized the advances made in this important area of solid-state physics.

In 1983, Kaplyanskiĭ together with S.A. Basun and S.P. Feofilov discovered the following new photoelectric effect in dielectrics with impurities: stable domains of a strong electric field (10^5–10^6 V/cm) that were opposite in sign were observed to form spontaneously in crystals of concentrated ruby illuminated by light. It was shown experimentally that, in accordance with the phenomenological theory of this effect developed by D'yakonov, the crystals exhibited a negative absolute electrical conductivity, and the microscopic mechanism of this effect was established. The discovery of this phenomenon stimulated Kaplyanskiĭ and coworkers to perform comprehensive studies (in the 1990s) on various effects associated with impurity photoionization and with photoinduced charge transfer in dielectrics, ferroelectrics, and photorefractive crystals. In particular, Kaplyanskiĭ and coworkers, in cooperation with the University of Georgia (USA), determined the basic microscopic processes responsible for the photochemical (photoionization) burning of a narrow dip (hole) in the inhomogeneously broadened profile of a spectral line of impurity ions.

Since 1995, Aleksandr Aleksandrovich and his coworkers have carried out intensive studies concerned with a new area of research, spatially structured dielectric materials. In nanosized dielectrics doped with rare-earth or iron-group ions, the ions serve as a spectroscopic probe. This made it possible to use spectroscopic methods to observe important effects typical of nanoparticles, such as quantum confinement of acoustic phonons in nanocrystals (the Lamb modes). The study of dielectric media with a spatially modulated refractive index (photonic crystals) carried out by Kaplyanskiĭ and his coworkers in cooperation with a group headed by V.N. Bogomolov in 1995 was the first in which a synthetic opal was used as a photonic crystal in the visible spectral range. Synthetic opals are now basic materials for use in studying photonic crystals.

Kaplyanskiĭ is an expert in many fields of optical spectroscopy of solids. His studies, the results of which are universally recognized, were concerned with such fields as excitonic spectroscopy of semiconductors, optical and photoelectric spectroscopy of dielectrics doped with iron-group or rare-earth ions (laser crystals), terahertz microwave ultrasonics, photonic crystals, and spectroscopy of structural phase transitions.

Aleksandr Aleksandrovich places considerable emphasis on researcher training. He is a professor at the St. Petersburg State University and head of a branch of the department of solid-state physics of the Faculty of Physics at the Ioffe Physicotechnical Institute. In 1996, Aleksandr Aleksandrovich received a grant of head of a leading scientific school. He is a member of the editorial boards of the journals *Physics of the Solid State*, *Physics Uspekhi*, and *Journal of Luminescence*.

Kaplyanskiĭ enjoys high prestige in the international scientific community; he is a member of the permanent organizing committees of international conferences on phonon physics, luminescence, defects in dielectric materials, and dynamic processes in excited solids. He is a coordinator of the long-term Russian–German program "Defects in Dielectrics and Deep Centers in Semiconductors."

Kaplyanskiĭ has been awarded prizes from International Conferences on Luminescence (1990) and Phonon Scattering (2001) and the Humboldt Prize for research (1997). In 2005, Kaplyanskiĭ was awarded a prize of the St. Petersburg government and the St. Petersburg Center of the Russian Academy of Sciences for "Optical-Spectroscopy Studies into the Electronic and Vibrational States in Crystals."

In 1987, Kaplyanskiĭ was elected Corresponding Member of the USSR Academy of Sciences and then (in 2003) Member of the Russian Academy of Sciences. In 1999, he received the Order of Honor.

We congratulate Aleksandr Aleksandrovich on the occasion of his 75th birthday and wish him good health and every success for the progress of science in Russia.

Editorial Board of the Journal
Physics of the Solid State

Physics of the Solid State, Vol. 47, No. 12, 2005, pp. 2207–2212. Translated from Fizika Tverdogo Tela, Vol. 47, No. 12, 2005, pp. 2116–2120.

METALS AND SUPERCONDUCTORS

Stimulated Spin Echo upon Excitation with Pseudorandom Pulses

S. A. Baruzdin

St. Petersburg State University of Electrical Engineering, ul. Professora Popova 5, St. Petersburg, 197376 Russia
e-mail: bars@bars.etu.spb.ru

Received February 18, 2005

Abstract—Different regimes of excitation of a stimulated spin echo by pseudorandom pulses and short coherent delta-shaped pulses are considered. Radio pulses phase-shifted by a 127-element *M* sequence are used as pseudorandom signals. The shape of the complex envelope of the stimulated echo is simulated in linear and nonlinear regimes with respect to the phase-shifted pulses. It is demonstrated that the excitation pulses can be described by correlation functions. Appropriate conditions are determined under which the amplitude of the stimulated echo can be greater than the amplitude corresponding to the classical algorithm used for exciting a stimulated echo by three delta-shaped pulses. The results obtained can be used for analyzing the formation of a stimulated photon echo. © *2005 Pleiades Publishing, Inc.*

1. INTRODUCTION

In 1970, Ernst and Keiser used white Gaussian noise for the first time to excite nuclear spin systems [1–3]. In nuclear magnetic resonance (NMR) spectroscopy, this method is referred to as stochastic resonance. Unlike the traditional methods employed in NMR spectroscopy, the stochastic resonance method has an important advantage over the methods used in slow-scanning spectroscopy: it is characterized by a higher sensitivity owing to the broadband exciting process. The advantage of the stochastic resonance method over pulsed Fourier-transform spectroscopy is a lower excitation power; in the former case, the gain can be as large as 10^4–10^5. The use of this method makes it possible to obtain multidimensional spectra. Moreover, a decrease in the excitation power facilitates solution of the problem associated with the "dead time" of the receiver. Apart from NMR spectroscopy, the stochastic excitation method has been employed in electron paramagnetic resonance spectroscopy and optics.

At present, the stochastic resonance method is under development. In combination with the two-dimensional Fourier transform, this method has made it possible to obtain a large number of two-dimensional NMR spectra. It should be noted that the pseudorandom excitation has often been used instead of random noise [4]. In this case, after exciting a free-induction signal, its correlation with the initial pseudorandom signal is calculated [4, 5] and the spectrum is determined using either the Fourier transform or a Fourier transform modification.

In this paper, it will be demonstrated that, for inhomogeneously broadened systems, the correlation of the response with the initial pseudorandom signal can be calculated using the spin-echo technique. For this purpose, the excitation pulse sequence should involve two pseudorandom pulses that coincide in shape to within a constant.

2. THREE-PULSE EXCITATION MODE

The behavior of the magnetization vector in an external magnetic field is described by the Bloch equations [1, 6]. When the excitation pulse durations satisfy the relationship $\tau_n \ll T_1, T_2$ (where T_1 and T_2 are the longitudinal and transverse relaxation times, respectively), relaxation processes can be ignored. Then, the equation of motion of the magnetization vector of the isochromate in the coordinate system rotating at the frequency ω_0 can be represented in the form

$$\frac{d\mathbf{M}(t,\Omega)}{dt} = \mathbf{F}(t,\Omega)\cdot\mathbf{M}(t,\Omega),$$

$$\mathbf{M}(t,\Omega) = \begin{bmatrix} \tilde{M}(t,\Omega) \\ \tilde{M}^*(t,\Omega) \\ M_z(t,\Omega) \end{bmatrix}, \quad (1)$$

$$\mathbf{F}(t,\Omega) = \begin{bmatrix} i\Omega & 0 & -i\tilde{R}(t) \\ 0 & -i\Omega & i\tilde{R}^*(t) \\ -i\dfrac{\tilde{R}^*(t)}{2} & i\dfrac{\tilde{R}(t)}{2} & 0 \end{bmatrix},$$

where $\tilde{M}(t, \Omega)$ and $\tilde{M}^*(t, \Omega)$ are the complex transverse components of the magnetization vector; M_z is the longitudinal component of the magnetization vector; $\tilde{R}(t) = \gamma\tilde{B}(t)$ is the complex envelope of the excitation pulse in terms of the circular frequency (γ is the gyro-

magnetic ratio, $\tilde{B}$ is the complex transverse component of the magnetic vector); and $\Omega = \omega - \omega_0$ is the detuning of the frequency ω with respect to the carrier frequency ω_0 of the radio pulse, which coincides with the central frequency of the inhomogeneously broadened absorption line.

The formal solution to the system of equations (1) can be written in the matrix form

$$\mathbf{M}(t, \Omega) = \mathbf{A}(t, t_0, \Omega)\mathbf{M}(t_0, \Omega), \quad (2)$$

where $\mathbf{M}(t_0, \Omega)$ is the vector of the initial conditions at the instant of time t_0 and $\mathbf{A}(t, t_0, \Omega)$ is the transfer matrix of the state of the system.

In the intervals free of the excitation pulses, we have $\tilde{R}(t) = 0$ and the solution to the system of equations (1) takes the form

$$\mathbf{M}(t, \Omega) = \mathbf{B}(t, t_0, \Omega)\mathbf{M}(t_0, \Omega), \quad (3)$$

where the transfer matrix **B** can be written in the explicit form

$$\mathbf{B}(t, t_0, \Omega) = \begin{bmatrix} \exp[i\Omega(t-t_0)] & 0 & 0 \\ 0 & \exp[-i\Omega(t-t_0)] & 0 \\ 0 & 0 & 1 \end{bmatrix}. \quad (4)$$

By specifying the initial conditions for the vector $\mathbf{M}(-\tau_1/2, \Omega)$ in the form $\tilde{M} = \tilde{M}^* = 0$ and $M_z = M_0$ (where M_0 is the equilibrium magnitude of the magnetization vector), it is possible to determine the vector $\mathbf{M}(t, \Omega)$ after completing three excitation pulses formed at the instants of time $t_1 = 0$, t_2, and t_3. For this purpose, we sequentially use the formal solution (2) for excitation intervals and the explicit solutions (3) and (4) for free intervals. In the interval $t \geq t_3 + \tau_3$ (where τ_3 is the duration of the third pulse), the stimulated echo can be separated from the response of the spin system, which is formed by the transverse component $\tilde{M}(t, \Omega)$ of the magnetization vector and consists of nine terms. The complex envelope of the stimulated echo can be described by the relationship [6]

$$\begin{aligned} \tilde{m}_s(t) &= M_0 \int_{-\infty}^{\infty} S_s(\Omega)\exp[i\Omega(t-t_2-t_3)]d\Omega, \\ S_s(\Omega) &= g(\Omega)a_{13}^{(3)}(\Omega)a_{32}^{(2)}(\Omega)a_{23}^{(1)}(\Omega) \\ &\times \exp\left(i\Omega\frac{\tau_1+\tau_2-\tau_3}{2}\right), \end{aligned} \quad (5)$$

where $a_{kl}^{(n)}$ is the element of the transfer matrix for the nth excitation pulse and $g(\Omega)$ is the low-frequency equivalent of the inhomogeneously broadened absorption line.

In our case, the excitation of the stimulated echo is simulated by two types of pulses, namely, radio pulses phase-shifted by a 127-element M sequence and short coherent pulses referred to as delta-shaped pulses.

When forming the phase-shifted pulses, the coherent carrier is modulated in a phase that takes on two values, 0 and π. This is achieved with a binary M sequence generated at the output of the feedback shift register consisting of N stages [4, 7]. In particular, the seven-stage shift register has $2^7 = 128$ states, one of which (zero) is forbidden. Therefore, the binary pseudorandom sequence composed of 127 elementary (0, 1) pulses of duration τ is generated at the output of the shift register.

The transfer matrix for the elementary pulse has the form

$$\begin{aligned} a_{22}^* = a_{11} &= \frac{R^2 + (R^2 + 2\Omega^2)\cos\beta\tau}{2\beta^2} + i\frac{\Omega\sin\beta\tau}{\beta}, \\ a_{21}^* = a_{12} &= \frac{\tilde{R}^2}{\beta^2}\sin^2\left(\frac{\beta\tau}{2}\right), \\ a_{23}^* = a_{13} &= \frac{2\tilde{R}\Omega}{\beta^2}\sin^2\left(\frac{\beta\tau}{2}\right) - i\frac{\tilde{R}\sin\beta\tau}{\beta}, \\ a_{32}^* = a_{31} &= \frac{\tilde{R}^*\Omega}{\beta^2}\sin^2\left(\frac{\beta\tau}{2}\right) - i\frac{\tilde{R}^*\sin\beta\tau}{2\beta}, \\ a_{33} &= \frac{\Omega^2 + R^2\cos\beta\tau}{\beta^2}, \end{aligned} \quad (6)$$

where $\beta^2 = R^2 + \Omega^2$, $\tilde{R} = R\exp(i\varphi)$, R is the amplitude, and φ is the initial phase of the radio pulse. In this case, the symbols 1 and 0 indicate the carrier phases $\varphi = 0$ and π, respectively.

The transfer matrix for the entire phase-shifted pulse is obtained by multiplying matrices (6) for the elementary pulses with the inclusion of the algorithm for generating the M sequence in the shift register and its initial state, which is taken to be 0, 0, 0, 0, 0, 0, 1 from the input to the output. The total duration of the phase-shifted pulse is $\tau_M = 127\tau$.

Excitation pulses of the second type are delta-shaped pulses. These are rectangular radio pulses with an amplitude R_δ and initial phase φ_δ. The duration τ_δ of this pulse satisfies the condition $\tau_\delta \ll (\Delta F_L)^{-1}$, where ΔF_L is the width of the inhomogeneously broadened line. Excitation pulses of the second type exhibit properties similar to those of the Dirac delta function: these pulses are sufficiently short, and their spectrum remains almost unchanged in the band of frequencies that are inversely proportional to the pulse duration. For a delta-shaped pulse, the transfer matrix elements that are of

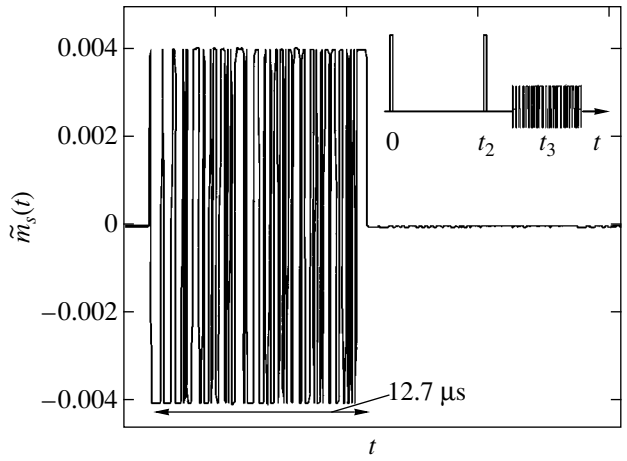

Fig. 1. Time diagram of the excitation pulses (inset) and the complex envelope of the stimulated echo in the linear regime.

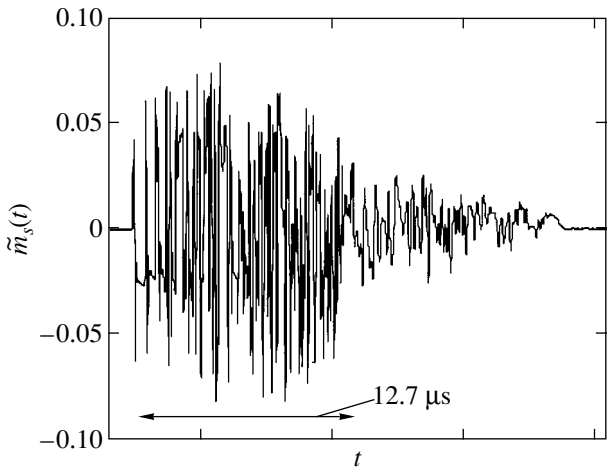

Fig. 2. Complex envelope of the stimulated echo in the nonlinear regime.

interest for the subsequent simulation of the excitation have the form

$$a_{13} = a_{23}^* = -i\sin\alpha\exp(i\varphi_\delta);$$
$$a_{32} = \frac{i}{2}\sin\alpha\exp(i\varphi_\delta), \qquad (7)$$
$$\alpha = R_\delta\tau_\delta, \quad \tilde{R}_\delta = R_\delta\exp(i\varphi_\delta).$$

As a rule, the stimulated echo with a maximum amplitude can be obtained using 90° pulses with $\alpha = \pi/2$.

Let us assume that the first and second excitation pulses are delta-shaped. In this case, we have $\alpha_1 = \alpha_2 = \pi/2$, $\varphi_{\delta 1} = 0$, and $\varphi_{\delta 2} = -\pi/2$. The third excitation pulse is assumed to be the phase-shifted pulse.

We will simulate thin polycrystalline ferromagnetic cobalt films with ^{59}Co nuclear resonance [8–12]. The central frequency of the absorption line of these films is equal to 217 MHz, and the linewidth is 10 MHz. The low-frequency equivalent $g(\Omega)$ of the inhomogeneously broadened absorption line is simulated by a Gaussian function with the parameter $\sigma_g = 2\pi \times 10^7$ rad/s.

The duration of the elementary pulse of the M sequence is taken to be $\tau = 0.1$ μs. Hence, the spectral width of the pulse $\Delta F = \tau^{-1}$ is equal to the width of the inhomogeneously broadened line of the cobalt films. The duration of the phase-shifted pulse is $\tau_3 = 12.7$ μs.

3. COMPLEX ENVELOPE OF THE STIMULATED ECHO

Figure 1 depicts the normalized (to the value of M_0) complex envelope of the stimulated echo for the amplitude of the phase-shifted pulse $R_3 = 10^5$ rad/s. The inset shows the time diagram of the excitation pulses. For the chosen parameters of the phases of the delta-shaped pulses, the complex envelope of the stimulated echo is a real alternating function. The change in the sign indicates a phase-shift keying of the stimulated echo. The shape of the stimulated echo in this regime follows the shape of the phase-shifted excitation pulse.

When the amplitudes of the excitation pulses are small, there arises a linear regime. In this case, the transfer matrix elements that are of considerable importance in analyzing the shape of the stimulated echo have the following form:

$$a_{13}(\Omega) = a_{23}^*(\Omega) \approx -iS(\Omega)\exp\left(i\frac{\Omega\tau_M}{2}\right);$$
$$a_{32}(\Omega) \approx \frac{i}{2}S(\Omega)\exp\left(-i\frac{\Omega\tau_M}{2}\right), \qquad (8)$$

where $S(\Omega)$ is the spectral density of the complex envelope of the excitation pulse.

In the case under consideration, the phase-shifted pulse is third and its effect is described by the coefficient $a_{13}^{(3)}(\Omega)$ proportional to the spectral density of the complex envelope of this pulse. Note that, if we interchange the first and third excitation pulses in the initial algorithm (Fig. 1), the shape of the stimulated echo appears to be specularly reflected; i.e., the echo is inverted in time. This can be explained by the fact that the effect of the phase-shifted pulse is described by the coefficient $a_{23}^{(1)}(\Omega)$ proportional to the spectral density $S^*(\Omega)$. It should also be noted that, upon interchanging the second and third excitation pulses, the coefficient $a_{32}^{(2)}(\Omega)$ describing the effect of the phase-shifted pulse will be again proportional to the spectral density $S(\Omega)$ and the echo will follow the shape of the phase-shifted pulse without inversion in time.

The initial algorithm of the excitation of the stimulated echo at $R_3 = 2 \times 10^6$ rad/s is illustrated in Fig. 2.

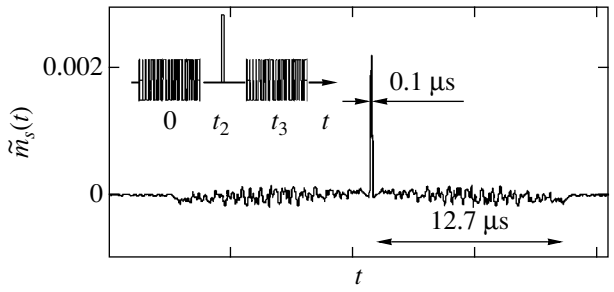

Fig. 3. Time diagram of the excitation pulses in algorithm Delta 2 (inset) and the complex envelope of the stimulated echo in the linear regime.

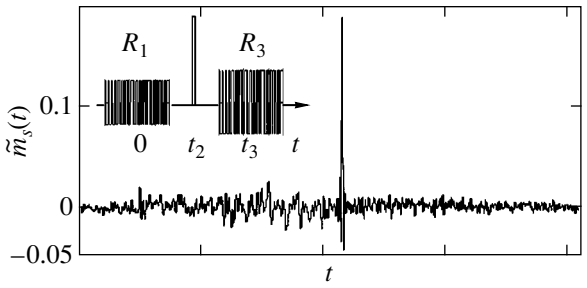

Fig. 4. Time diagram of the excitation pulses in algorithm Delta 2 (inset) and the complex envelope of the stimulated echo in the nonlinear regime.

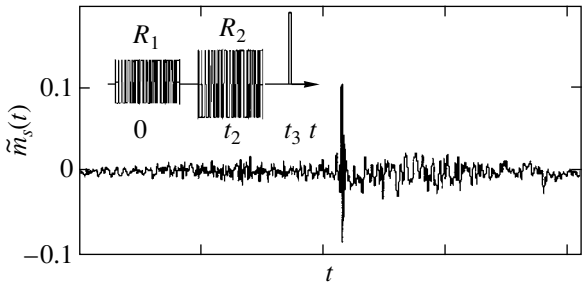

Fig. 5. Time diagram of the excitation pulses in algorithm Delta 3 (inset) and the complex envelope of the stimulated echo in the nonlinear regime.

This regime is nonlinear with respect to the phase-shifted pulse. Conditions (8) are not satisfied. The shape of the echo differs from that of the initial phase-shifted pulse. In particular, the echo duration is doubled. Note also that, when we interchange the first and third excitation pulses, the echo shown in Fig. 2 is inverted in time. However, unlike the linear regime, the interchange of the second and third excitation pulses leads to a change in the echo shape. This is associated with the fact that, in the nonlinear regime, unlike the linear regime, the coefficients $a_{13}^{(3)}(\Omega)$ and $a_{32}^{(2)}(\Omega)$ can differ significantly.

In the next excitation algorithm, the excitation of the stimulated echo is simulated by two identical phase-shifted pulses, *1* and *3* (the shift register is started from the same aforementioned initial state), and delta-shaped pulse *2*. This algorithm will be called Delta 2, because the delta-shaped pulse is second. The corresponding time diagram of the excitation pulses and the normalized (to the value of M_0) complex envelope of the stimulated echo are depicted in Fig. 3. The amplitudes of the phase-shifted pulses are equal to each other: $R_1 = R_3 = R = 10^5$ rad/s. The regime is linear with respect to these pulses, and they are reproduced in the form of the third pulse noninverted in time (as in Fig. 1) and the same (but inverted) first pulse. In this case, the stimulated echo in the form of the correlation function of the signal phase-shifted by the 127-element M sequence corresponds to the product of the spectral coefficients $a_{23}^{(1)}(\Omega)a_{13}^{(3)}(\Omega) \approx |S(\Omega)|^2$ in the time range. Thus, the response is symmetric, the total duration of the response is equal to 25.4 μs, and the width of the correlation peak is 0.1 μs, which corresponds to the duration τ of the elementary pulse. The maximum of the correlation peak is observed at the instant of time $t_2 + t_3$.

If the second and third excitation pulses are interchanged, we obtain algorithm Delta 3, in which the delta-shaped pulse is the third excitation pulse. For $R_1 = R_2 = R = 10^5$ rad/s, the regime is linear with respect to the phase-shifted pulses and the echo remains identical to that in algorithm Delta 2.

When the amplitudes of the phase-shifted pulses in algorithm Delta 2 increase to values lying outside the range of the linear regime, the complex envelope of the stimulated echo is represented by the autocorrelation function of the signal nonlinearly transformed by the system rather than of the initial phase-shifted signal. This is explained by the fact that the relationship $a_{13}^{(3)}(\Omega) = [a_{23}^{(1)}(\Omega)]^*$ holds for $R_1 = R_3$. For $R_1 = R_3 = R = 2 \times 10^6$ rad/s, the shape of the stimulated echo is determined by the correlation function of the pulse shown in Fig. 2.

For different amplitudes of the two phase-shifted pulses, the stimulated echo coincides in shape with the cross-correlation function of the signals reproduced by the spin system. For example, at $R_1 = 2 \times 10^6$ rad/s and $R_3 = 10^5$ rad/s, this is the cross-correlation function of the signals depicted in Figs. 2 and 1.

Figure 4 shows the complex envelope of the stimulated echo for algorithm Delta 2 at $R_1 = 2 \times 10^6$ rad/s and $R_3 = 3 \times 10^6$ rad/s. Upon interchanging the second and third excitation pulses, we obtain algorithm Delta 3 at $R_1 = 2 \times 10^6$ rad/s and $R_2 = 3 \times 10^6$ rad/s. The shape of the stimulated echo is shown in Fig. 5. It can be seen from Figs. 4 and 5 that the stimulated echoes obtained using these algorithms in the nonlinear regime can differ substantially. The echo shape corresponds to the

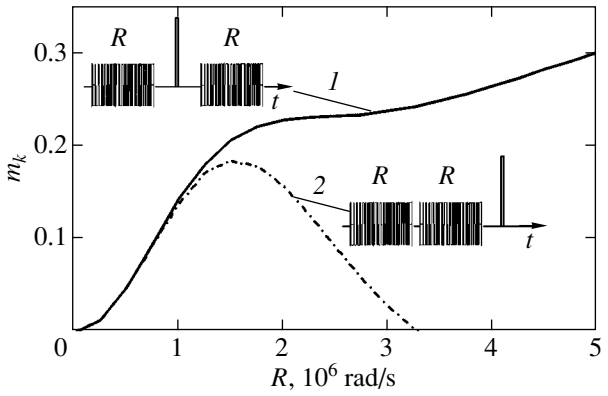

Fig. 6. Time diagrams of the excitation pulses in algorithms (*1*) Delta 2 and (*2*) Delta 3 and the corresponding dependences of the amplitude of the correlation peak in the complex envelope of the stimulated echo on the amplitude R of pseudorandom pulses.

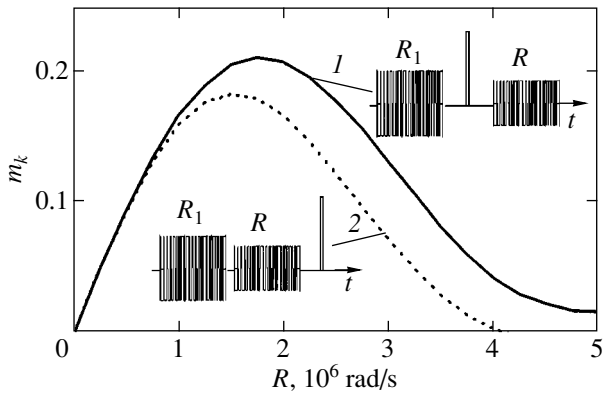

Fig. 7. Time diagrams of the excitation pulses in algorithms (*1*) Delta 2 and (*2*) Delta 3 and the corresponding dependences of the amplitude of the correlation peak in the complex envelope of the stimulated echo on the amplitude R of pseudorandom pulses at the amplitude $R_1 = 1.5 \times 10^6$ rad/s.

cross-correlation function of the phase-shifted signals that are nonlinearly transformed by the spin system.

The difference between these algorithms in the nonlinear regime also clearly manifests itself in the dependences of the amplitude of the correlation peak in the stimulated echo $m_k = \tilde{m}_s(t_2 + t_3)$ on the amplitude of the phase-shifted pulse. These amplitude dependences for algorithm Delta 3 at $R_1 = R_3 = R$ and algorithm Delta 2 at $R_1 = R_2 = R$ are shown in Fig. 6. Both dependences coincide with each other in the linear regime at $R < 10^6$ rad/s. For larger pulse amplitudes R, there is a fundamental difference between these dependences. For algorithm Delta 2, the echo amplitude increases with an increase in the pulse amplitude R, then flattens out, and reaches a value of 0.313. For algorithm Delta 3, the echo amplitude with an increase in the pulse amplitude R increases to a maximum value of 0.19 and then decreases.

Figure 7 shows the dependences of the amplitude of the correlation peak in the stimulated echo $m_k = \tilde{m}_s(t_2 + t_3)$ on the pulse amplitude $R_3 = R$ for algorithm Delta 2 and on the pulse amplitude $R_2 = R$ for algorithm Delta 3 at a fixed amplitude of the first pulse $R_1 = 1.5 \times 10^6$ rad/s. These dependences also coincide with each other in the linear regime at $R < 10^6$ rad/s. In the nonlinear regime, the dependences differ only quantitatively and exhibit a qualitatively identical behavior: in both cases, the echo amplitude increases with an increase in the pulse amplitude R, passes through a maximum, and then decreases.

4. CONCLUSIONS

The amplitude dependences obtained for algorithms Delta 2 and Delta 3 can be compared with those constructed upon excitation with white Gaussian noise [13, 14]. These dependences are qualitatively similar to each other. The somewhat smaller amplitudes of the echo in the case of pseudorandom excitation are explained by the fact that, unlike the spectrum of white Gaussian noise, phase-shifted pulses have an irregular spectrum.

The obtained amplitudes of the correlation peaks for algorithms Delta 2 and Delta 3 can be compared with the amplitude of the stimulated echo for the classical algorithm of excitation with three identical delta-shaped pulses. In this case, the amplitude of the stimulated echo is given by

$$A_\delta = (1/2)\sin^3\alpha M_0.$$

The maximum amplitude is $A_s = (1/2)M_0$ at $\alpha = \pi/2$, and the maximum amplitude normalized to M_0 is equal to 0.5. This echo amplitude is larger than those obtained for the proposed algorithms. However, the generation of coherent pulses whose parameters satisfy both conditions $\tau_\delta \ll (\Delta F_L)^{-1}$ and $\alpha = \pi/2$ is by no means easy. For an arbitrary parameter α, the amplitude ratio of the stimulated echoes for these two algorithms is defined by the expression

$$\frac{m_k \sin\alpha}{0.5(\sin\alpha)^3}.$$

Specifically, at $\alpha = 0.1$ and $m_k \approx 0.2$–0.3, the amplitude gain can reach 50 (power gain, 2500). This is especially important when exciting broadband NMR spectra. For example, the width of lines in ^{59}Co NMR spectra of Fe–Ni–Co thin films can be as large as 80 MHz at a central frequency of approximately 200 MHz [12].

The results obtained can be applied to simulate the stimulated electron spin echo and the photon echo, because they are based on the same mathematical model [15].

REFERENCES

1. R. Ernst, G. Bodenhauzen, and A. Wokaun, *Principles of Nuclear Magnetic Resonance in One and Two Dimensions* (Clarendon, Oxford, 1987; Mir, Moscow, 1990).
2. E. Bartholdi, A. Wokaun, and R. R. Ernst, Chem. Phys. **18**, 57 (1976).
3. W. Knight and R. Keiser, J. Magn. Reson. **48**, 293 (1982).
4. R. Kaiser, J. Magn. Reson. **15**, 44 (1974).
5. J. Paff and B. Blumich, Phys. Rev. A: At., Mol., Opt. Phys. **43** (7), 3640 (1991).
6. S. A. Baruzdin, Yu. V. Egorov, B. A. Kalinikos, N. G. Kovshikov, N. V. Kozhus', V. V. Matyushev, K. P. Naumov, Yu. G. Smirnov, and V. N. Ushakov, *Functional Devices for Processing of Signals (Fundamentals of the Theory and Algorithms): A Manual for Institutes of Higher Education*, Ed. by Yu. V. Egorov (Radio i Svyaz', Moscow, 1997) [in Russian].
7. L. E. Varakin, *Communication Systems with Noise-Like Signals* (Radio i Svyaz', Moscow, 1985) [in Russian].
8. V. B. Ustinov, S. P. Repnikov, É. O. Saakov, and V. A. Teryaev, Fiz. Tverd. Tela (Leningrad) **10** (5), 1589 (1968) [Sov. Phys. Solid State **10** (5), 1264 (1968)].
9. E. A. Turov and M. P. Petrov, *Nuclear Magnetic Resonance in Ferromagnets and Antiferromagnets* (Nauka, Moscow, 1969; Halsted, New York, 1972).
10. V. O. Golub, V. V. Kotov, and A. N. Pogorelyĭ, Fiz. Tverd. Tela (St. Petersburg) **40** (6), 1056 (1998) [Phys. Solid State **40** (6), 964 (1998)].
11. E. G. Apushkinskiĭ and V. V. Moskalev, Vestn. Leningr. Univ., Ser. 4: Fiz., Khim., No. 1, 86 (1991).
12. V. A. Ignatchenko and V. I. Tsifrinovich, *Nuclear Signals in Magnetically Ordered Media* (Nauka, Novosibirsk, 1993), p. 125 [in Russian].
13. S. A. Baruzdin, Opt. Spektrosk. **91** (2), 276 (2001) [Opt. Spectrosc. **91**, 255 (2001)].
14. S. A. Baruzdin, Kvantovaya Elektron. (Moscow) **31** (8), 719 (2001).
15. P. Bachmann, K. Sauer, and G. Wallis, Fortschr. Phys. **20** (3), 148 (1972).

Translated by O. Borovik-Romanova

Physics of the Solid State, Vol. 47, No. 12, 2005, pp. 2213–2218. Translated from Fizika Tverdogo Tela, Vol. 47, No. 12, 2005, pp. 2121–2126.

SEMICONDUCTORS AND DIELECTRICS

Atomic Structure of MBE-Grown GaAs Nanowhiskers

I. P. Soshnikov[1, 2], G. É. Cirlin[1, 2, 3], A. A. Tonkikh[2, 3], Yu. B. Samsonenko[1, 2, 3], V. G. Dubovskiĭ[1, 2], V. M. Ustinov[1, 2], O. M. Gorbenko[3], D. Litvinov[4], and D. Gerthsen[4]

[1]*St. Petersburg Physicotechnical Science & Education Center, Russian Academy of Sciences, St. Petersburg, 195220 Russia*
[2]*Ioffe Physicotechnical Institute, Russian Academy of Sciences, Politekhnicheskaya ul. 26, St. Petersburg, 194021 Russia*
e-mail: ipsosh@beam.ioffe.rssi.ru
[3]*Institute of Analytical Instrument Making, Rizhskiĭ pr. 26, Russian Academy of Sciences, St. Petersburg, 198103 Russia*
[4]*Technical University of Karlsruhe, Karlsruhe, D-76128 Germany*

Received December 28, 2004

Abstract—The structural properties of MBE-grown GaAs and $Al_{0.3}Ga_{0.7}As$ nanowhiskers were studied. The formation of wurtzite and 4*H*-polytype hexagonal structures with characteristic sizes of 100 nm or larger in these materials was demonstrated. It is concluded that the Au–Ga activation alloy symmetry influences the formation of the hexagonal structure. © *2005 Pleiades Publishing, Inc.*

Nanowhiskers (NW) [1] have been recently attracting considerable research interest, which should be assigned both to the properties of NWs and to recent novel techniques of their preparation, in particular, molecular beam epitaxy (MBE) [2–9]. Among the most essential properties of these objects [10–17] one should mention the high strength, the large height-to-diameter ratio (aspect ratio), quasi-one-dimensional optoelectronic spectra, etc. The unique properties of NWs increase their application potential in such devices as electronic emitters, gas microanalyzers, etc. It is well known that the optoelectronic and mechanical properties of nanoobjects depend strongly on their structure [6, 10–17], which, in turn, can be determined in large measure by the method of preparation employed.

Sears [18] had developed a theory of formation of whiskers around screw dislocations. Later it was found, however, that whiskers do not contain screw dislocations at all [1, 19, 20]. This motivated the development [1, 19–21] of a diffusion mechanism and a vapor–liquid–solid (VLS) mechanism of whisker formation. These mechanisms, while not requiring the presence of dislocations in a whisker, do not exclude the formation of defects in the process.

The formation of whiskers on a GaAs surface has been studied primarily by the chemical vapor deposition (CVD) method [1, 10, 12–17, 20, 22–24] under suppression of growth of the major surface. It was shown that, in these conditions, whiskers grow via the VLS mechanism, which is characterized by a growth rate V that increases with the whisker transverse size D: $V \sim (A - B/D)^2$, where A and B are constants. Some publications [3–5, 25, 26] reported on the growing of whiskers by MBE, a method based predominantly on the diffusion mechanism [25, 26], in which atoms are supplied to the NW growth zone (the interface between the whisker and the drop of the activation alloy) by surface diffusion; this brings about inverse variation (decreasing) of the NW growth rate with increasing transverse size. Note that the diffusion mechanism of formation may become realized in other methods of whisker formation as well [27–29].

Transmission electron microscopy (TEM) studies of the structure of GaAs whiskers grown both by MOCVD and by MBE revealed the formation of twins, stacking faults, and the wurtzite phase [1, 2, 6, 24].

Note that, despite the closeness of the enthalpies [30] (the difference is less than 0.014 eV/atom), the appearance of the wurtzite phase in GaAs and AlGaAs solid solutions is a unique effect. As far as we are aware, the wurtzite phase was observed to form in GaAs in growth on nonactivated surfaces only once and under fairly specific growth conditions [31]. The images presented in [1, 2, 6, 24] do not, however, instill confidence that the observed structure is indeed an extended wurtzite phase rather than a result of multiple defect formation. Moreover, those publications do not explain the mechanism of formation of the wurtzite phase.

This has motivated the present study of the structure of MBE-grown GaAs and AlGaAs NWs intended to unravel the possible mechanisms of formation of the wurtzite phase.

$Al_{0.3}Ga_{0.7}As$ NWs were prepared by a three-stage growth technique proposed earlier [3–5]. The key point in this technique is combining MBE with our methods of producing finely dispersed metal films [3–5]. The substrates were AGChK-3 gallium arsenide plates with (111)*B*- and (100)-oriented surfaces. The preliminary check of the surface quality and *in situ* NW formation was realized by RHEED.

The NW structure was studied with a CM 200FEG electron microscope in the TEM mode. Samples were

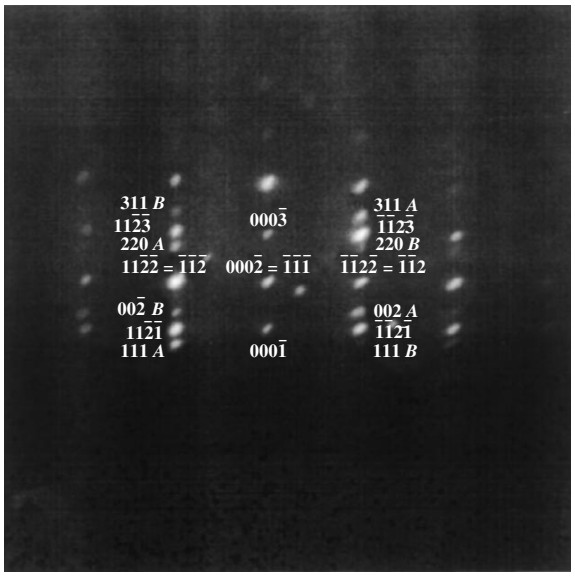

Fig. 1. RHEED image of the (111)*B* GaAs surface with a whisker array obtained in the [110] direction.

prepared by a traditional technique including mechanical treatment and, in the final stage, Ar^+ ion milling with an energy $E = 4$ keV. To preserve whiskers on the surface, samples were glued without clamping. The images were analyzed with a special code, DIAnaTEM [32].

Special studies revealed that whiskers grown on (100) and (111)*B* surfaces are identical in structure. Also, no dependence of the whisker structure on Al content was observed within the concentration range covered.

The morphology of the growing $Al_{0.3}Ga_{0.7}As$ and GaAs whisker ensembles is characterized by a transition to RHEED point patterns. Figure 1 illustrates such a pattern obtained in the (110) azimuthal direction. An analysis of the RHEED patterns showed them to be actually combinations of diffraction from bulk cubic (sphalerite) and hexagonal (wurtzite and/or 4*H*-polytype) crystals. Incidentally, the diffraction patterns reveal the presence of two cubic-phase orientations turned about the NW axis through 180° with respect to each other. The characteristic ratio of the distances between reflections identified as belonging to the hexagonal phase in the directions lateral and normal to the growth surface is 1.90 ± 0.05. This value corresponds to the $(001)/(11\bar{2}0)$ ratio of interplanar distances in $Al_{0.3}Ga_{0.7}As$ and GaAs crystals with wurtzite and/or 4*H*-polytype structure.

Figure 2 illustrates electron microscope cross-sectional images of $Al_{0.3}Ga_{0.7}As$ and GaAs whiskers grown on the (111)*B* GaAs surface. One clearly sees NWs grown in several shapes or in combinations of shapes, namely, prisms (Fig. 2a), bottleneck formations tapering off to the vertex (Fig. 2b), and truncated pyramids (Fig. 2c). The NW sizes of these three shape types or of their combinations may vary in overlapping ranges and were described in considerable detail in other papers [5].

Electron microscope images of NWs obtained in the structure-sensitive (220) reflections (Fig. 3) show that a NW contains regions with different crystallographic structures. In some cases, randomly periodic variations of the structure, apparently similar to that reported in [1, 2, 23, 24], were observed. The electron diffraction pattern obtained from several NWs and displayed in Fig. 3c is actually a combination of the diffraction pat-

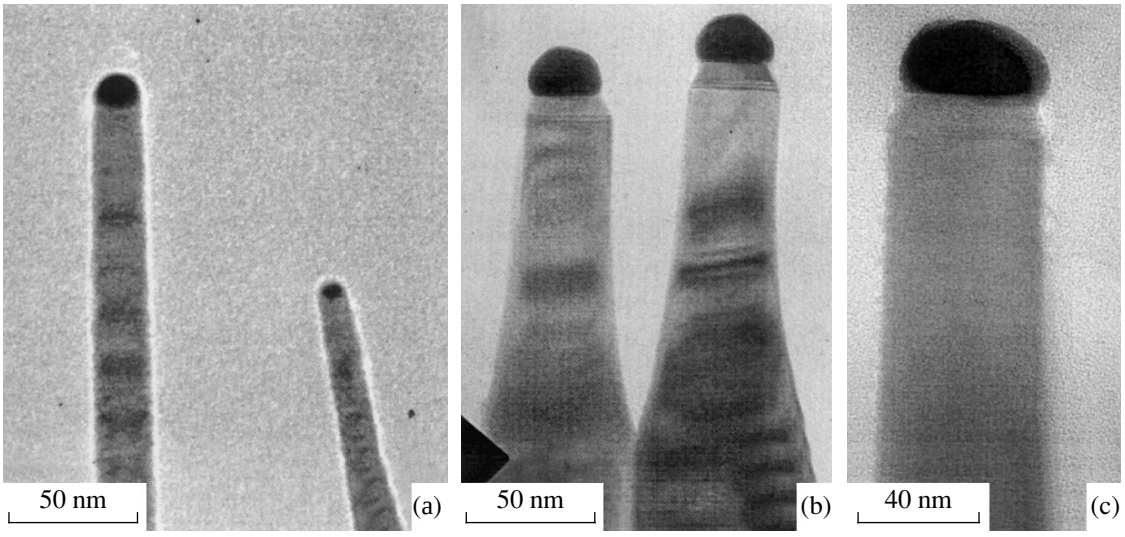

Fig. 2. Electron microscope images of the (110) cross sections of GaAs whiskers grown on the (111)*B* GaAs surface with morphologies of (a) a prism, (b) a bottleneck/truncated pyramid, and (c) a prism/truncated pyramid.

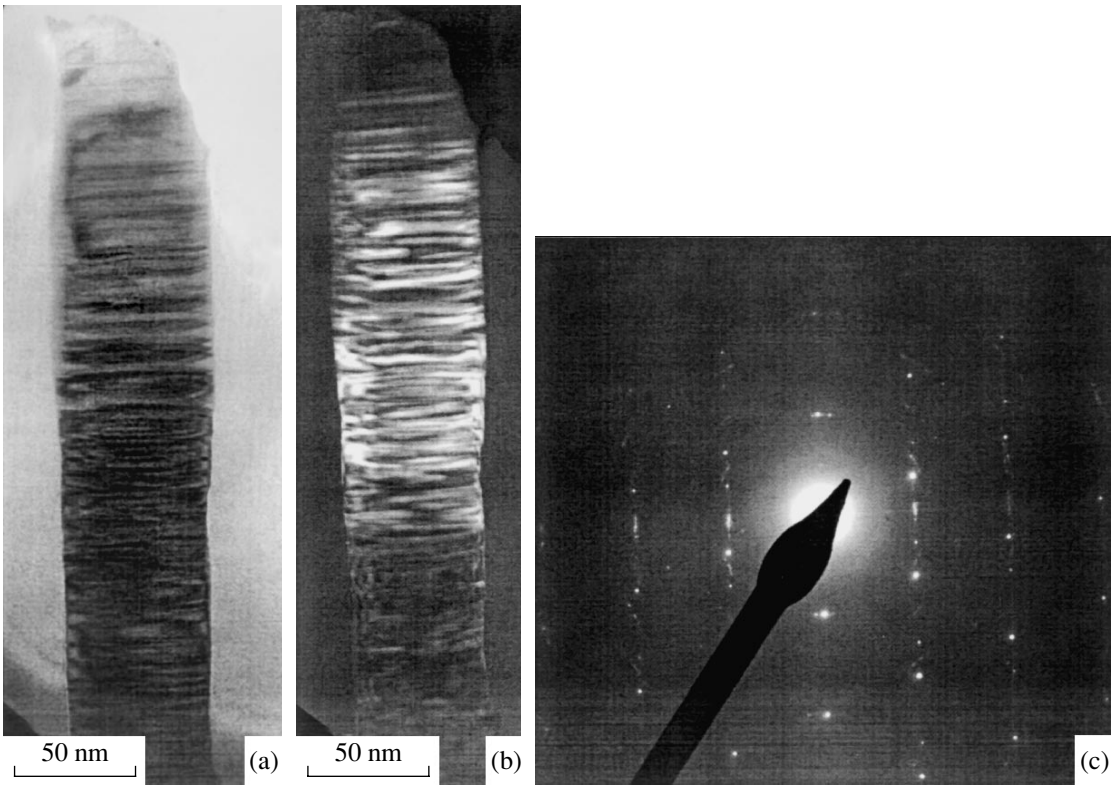

Fig. 3. (a) (220) bright-field and (b) (220) dark-field electron microscope images and (c) an electron microdiffraction pattern of a region in a GaAs NW with a variable structure.

terns from regions with different phases and orientations. One can, in particular, isolate reflections characteristic of the diffraction patterns from GaAs (and/or $Al_{0.3}Ga_{0.7}As$) in the (110) direction and turned through 180° about the NW axis with respect to one another. In addition, one observes reflections typical of twins. However, the electron diffraction patterns obtained contain a system of reflections which defy identification in terms of scattering from a sphalerite-type crystal. The electron diffraction pattern of the region presented in Fig. 3c was obtained in the direction coinciding with the [110] zone axis for the substrate and contains reflections arranged in the form of a rectangular grid. The ratio of the characteristic dimensions in the directions along and perpendicular to the NW axis is 1.92 ± 0.02. Estimating the characteristic distances yields 0.652 and 0.341 nm for the directions along and perpendicular to the NW axis, respectively. The observed diffraction pattern is characteristic of that for the $[1\bar{1}00]$ cross section of a hexagonal crystal. However, the appearance of reflections identified as [0001] and $[000\bar{1}]$ in the electron diffraction pattern argues for the formation of the 4*H*-polytype structure or for dynamical electron diffraction.

Figure 4 illustrates a high-resolution electron microscope image of a GaAs NW containing regions with different phases. The high-resolution electron microscope image of the region isolated in Fig. 4 likewise has a pattern typical of the $[1\bar{1}00]$ cross section of a hexagonal crystal (with a wurtzite and/or 4*H*-polytype structure). The Fourier transform of this image is of the same structure as the diffractogram and contains modes corresponding to the [0001] and $[000\bar{1}]$ reflections. This lends credence to the above conclusion regarding the formation of 4*H* polytypes or dynamical electron diffraction. Estimates of the interplanar distances drawn from the direct image yield 0.326 and 0.341 nm for the longitudinal and transverse directions, respectively, which agrees with the interplanar distances for the (0002) and $(1\bar{1}00)$ planes of the wurtzite GaAs, respectively. Similar results were also obtained for the $Al_{0.3}Ga_{0.7}As$ whisker.

A comparison of $Al_{0.3}Ga_{0.7}As$ and GaAs NWs in shape and structure (Fig. 2) suggests that bottleneck- and prism-shaped NWs may contain the cubic or hexagonal phase. By contrast, NWs shaped like truncated pyramids are signatures of the cubic phase.

Note that, sometimes in $Al_{0.3}Ga_{0.7}As$ and GaAs NWs, one observes a quasi-periodic transformation of phases. Moreover, the NW thickness may vary weakly (Fig. 5), which is a signal of structural stresses.

The observed quasi-periodic phase transformations find explanation in the framework of the kinetic theory

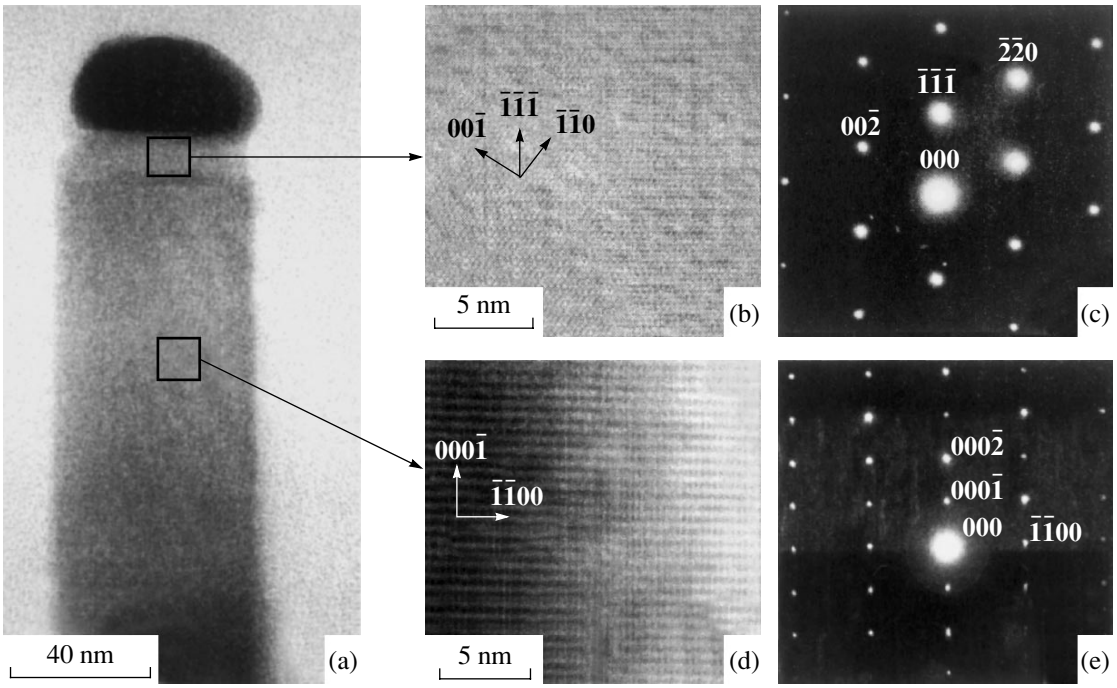

Fig. 4. (a, b, d) High-resolution electron microscope images of NW regions and (c, e) electron diffraction patterns taken from isolated regions with (b, c) cubic and (d, e) hexagonal crystal structures.

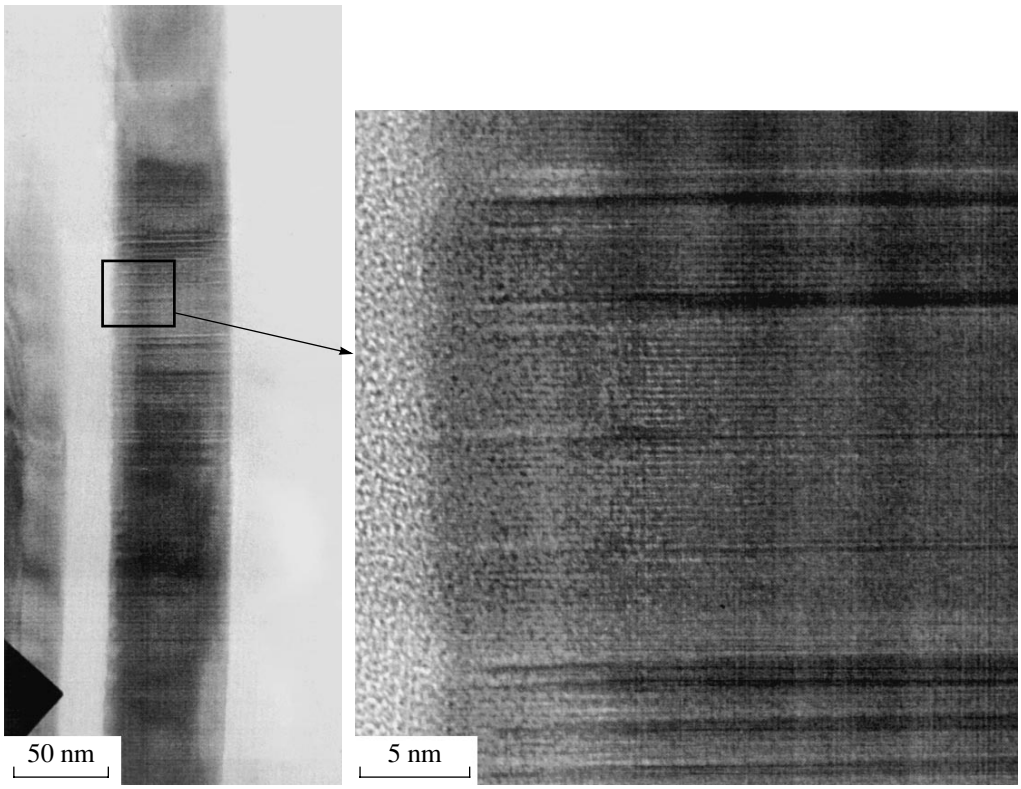

Fig. 5. Electron microscope image of a region of a GaAs NW with varying structure near the NW side face.

of crystal growth, because the lateral size of an NW is about 10–100 nm, which is substantially less than the effective size of a surface nucleus under our conditions (~1000 nm or greater). One may therefore assume that the layer-by-layer growth of the crystal phase at the NW tip from a supersaturated Au–GaAs solution proceeds via single-center nucleation [33]. This means that one nucleus has time to cover the entire face before the next nucleus forms. Hence, the NW structure should be laterally uniform within a layer.

It was shown in [2, 24] that a drop catalyst has a very low As content. The Ga/Au ratio was estimated to vary from 1 to 15% [2, 24]. An estimate of the alloy lattice parameter from electron microdiffraction patterns yields 4.07 ± 0.02 Å, which, recalling the dependence of the solution composition on the lattice parameter, gives ~0.1 for the Ga/Au ratio. In accordance with the phase diagram [34, 35], the temperatures used and the relevant Au–Ga alloy compositions allow observation of the *L*, α, and α' phases or of their combinations. Note that the α phase (substitutional solid solution) has cubic symmetry and that the peritectic phase α' possesses hexagonal-type symmetry $P6_3/mmc$. Fluctuations in the alloy composition and temperature may give rise to structural changes in the alloy. GaAs growing with a catalyst drop of Au–Ga alloy should apparently inherit the symmetry of the catalyst seed structure. This could possibly account for the formation of the 4*H*-polytype structure as resulting from inheritance of the α'-phase structure, which can be viewed as an ABAC... sequence of closely stacked atomic layers [34, 35]. This mechanism of phase transformation could explain the observed relation between the shape of a NW and its structure. Indeed, a decrease in Ga content in a catalyst drop gives rise to a proportional decrease of the drop in size and a possible transformation to the α phase (cubic alloy phase). Because the size of the upper part of an NW is dominated by that of the drop, a decrease of the drop in size should bring about a corresponding decrease of the NW in transverse size in the course of growth and a change in the alloy structure should cause a change in the crystal structure of the growing NW layers.

The observed quasi-periodic structural changes may ensue from changes in supersaturation at the surface. Indeed, it is known that supersaturation at the growth surface is related to effective filling of the growing adatom layer [36]. The effective filling varies quasi-periodically because of the formation of the next adatom layer. Hence, assuming NW growth to occur by the diffusion mechanism, the supply of Ga atoms (which depends on supersaturation on the nonactivated surface) and, as a consequence, the Ga content in the growth activator drop may vary in a quasi-periodic manner, which should produce the corresponding phase transformations in the drop and the NW.

Thus, we have shown that growth of GaAs and $Al_{0.3}Ga_{0.7}As$ NWs can be accompanied by the formation of regions with wurtzite and polytype phases measuring up to 100 nm or greater. The formation of a hexagonal wurtzite and/or polytype structure is accounted for by the effect of structural transformations in a catalyst drop.

ACKNOWLEDGMENTS

The authors are indebted to V.P. Ulin for helpful discussions of the work.

This study was supported in part by the Russian Foundation for Basic Research. G.É.C. expresses gratitude to Alexander von Humboldt Stiftung, and A.A.T., to Deutsche Forschungsgemeinschaft.

REFERENCES

1. K. Hiruma, M. Yazawa, K. Haraguchi, K. Ogawa, T. Katsuyama, M. Koguchi, and H. Kakibayashi, J. Appl. Phys. **74** (5), 3162 (1993).
2. B. J. Ohlsson, M. T. Bjork, M. H. Magnusson, K. Deppert, L. Samuelson, and L. R. Wallenberg, Appl. Phys. Lett. **79** (20), 3335 (2001).
3. V. G. Dubrovskii, I. P. Soshnikov, G. E. Cirlin, A. A. Tonkikh, Yu. B. Samsonenko, N. V. Sibirev, and V. M. Ustinov, Phys. Status Solidi B **241** (7), R30 (2004).
4. A. A. Tonkikh, G. E. Cirlin, Yu. B. Samsonenko, I. P. Soshnikov, and V. M. Ustinov, Fiz. Tekh. Poluprovodn. (St. Petersburg) **38** (10), 1239 (2004) [Semiconductors **38**, 1217 (2004)].
5. I. P. Soshnikov, A. A. Tonkikh, G. E. Cirlin, Yu. B. Samsonenko, and V. M. Ustinov, Pis'ma Zh. Tekh. Fiz. **30** (18), 28 (2004) [Tech. Phys. Lett. **30**, 765 (2004)].
6. X. Duan, J. Wang, and C. M. Lieber, Appl. Phys. Lett. **76** (9), 1116 (2000).
7. Z. H. Wu, X. Y. Mei, D. Kim, M. Blumin, and H. E. Ruda, Appl. Phys. Lett. **81** (27), 5177 (2002).
8. X. Mei, D. Kim, and H. E. Ruda, Appl. Phys. Lett. **81** (2), 361 (2002).
9. G. W. Pickrell, K. L. Chang, J. H. Epple, K. Y. Cheng, and K. C. Hsieh, J. Vac. Sci. Technol., B: Microelectron. Nanometer Struct.–Process., Meas., Phenom. **18** (6), 2611 (2000).
10. E. I. Givargizov, *The Growth of Whisker and Lamellar Crystals from Vapor* (Nauka, Moscow, 1977) [in Russian].
11. M. P. Persson and H. Q. Xu, Appl. Phys. Lett. **81** (7), 1309 (2002).
12. M. S. Gudiksen, L. J. Lauhon, J. Wang, D. C. Smith, and C. M. Lieber, Nature (London) **415** (6872), 617 (2002).
13. K. Hiruma, M. Yazawa, T. Katsuyama, K. Ogawa, K. Haraguchi, M. Koguchi, and H. Kakibayashi, J. Appl. Phys. **77** (2), 447 (1995).
14. K. Haraguchi, T. Katsuyama, and K. Hiruma, J. Appl. Phys. **75** (8), 4220 (1994).
15. Yu. P. Gaĭdukov, Usp. Fiz. Nauk **142** (4), 571 (1984) [Sov. Phys. Usp. **27**, 256 (1984)].
16. S. S. Varshava, P. P. Petrov, and A. D. Pyzh, Fiz. Tekh. Poluprovodn. (Leningrad) **15** (7), 1451 (1981) [Sov. Phys. Semicond. **15**, 841 (1981)].

17. S. S. Varshava, G. N. Mikhaĭlova, and K. S. Shcherba, Fiz. Tekh. Poluprovodn. (Leningrad) **14** (2), 413 (1980) [Sov. Phys. Semicond. **14**, 244 (1980)].
18. G. W. Sears, Acta Metall. **1**, 457 (1953).
19. R. S. Wagner and W. C. Ellis, Appl. Phys. Lett. **4** (7), 89 (1964).
20. E. I. Givargizov, Kristallografiya **20** (4), 812 (1975) [Sov. Phys. Crystallogr. **20**, 498 (1975)].
21. W. Dittmar and K. Neumann, Z. Elektrochem. **64**, 297 (1960).
22. S. M. Polyakov, E. N. Laverko, and V. M. Marakhonov, Kristallografiya **15** (3), 598 (1970) [Sov. Phys. Crystallogr. **15**, 519 (1970)].
23. M. Koguchi, H. Kakibyashi, M. Yazawa, K. Hiruma, and T. Katsuyama, Jpn. J. Appl. Phys., Part 1 **31** (7), 2061 (1992).
24. A. I. Person, M. W. Larsson, S. Stenstroem, B. J. Ohlson, L. Samuelson, and L. R. Wallenberg, Nat. Mater. **3** (10), 677 (2004).
25. V. G. Dubrovskii, G. E. Cirlin, I. P. Soshnikov, N. V. Sibirev, A. A. Tonkikh, Yu. B. Samsonenko, and V. M. Ustinov, Phys. Rev B: Condens. Matter **71**, 205 325 (2005).
26. L. Schubert, P. Werner, N. D. Zakharov, C. Gerth, F. M. Kolb, L. Long, U. Goesele, and T. Y. Tan, Appl. Phys. Lett. **84** (24), 4968 (2004).
27. I. P. Soshnikov, A. V. Lunev, M. E. Gaevskiĭ, L. G. Rotkina, S. I. Nesterov, M. M. Kulagina, V. T. Barchenko, I. P. Kalmykova, A. A. Efimov, and O. M. Gorbenko, Zh. Tekh. Fiz. **71** (7), 106 (2001) [Tech. Phys. **46**, 892 (2001)].
28. I. P. Soshnikov, A. V. Lunev, M. E. Gaevski, L. G. Rotkina, and N. A. Bert, Proc. SPIE—Int. Soc. Opt. Eng. **3048**, 404 (1997).
29. J. B. Malherbe, Crit. Rev. Solid State Mater. Sci. **19** (3), 127 (1994).
30. S. Froyen and M. Cohen, Phys. Rev. B: Condens. Matter **28** (6), 3258 (1983).
31. R. N. Kyutt, V. P. Ulin, A. A. Dyshekov, and Yu. P. Khapachev, Zh. Tekh. Fiz. **66** (12), 39 (1996) [Tech. Phys. **41**, 1220 (1996)].
32. I. P. Soshnikov, O. M. Gorbenko, A. O. Golubok, and N. N. Ledentsov, Fiz. Tekh. Poluprovodn. (St. Petersburg) **35** (4), 361 (2001) [Semiconductors **35**, 347 (2001)].
33. V. G. Dubrovskii and N. V. Sibirev, Phys. Rev. E: Stat., Nonlinear, Soft Matter Phys. **70**, 031 604 (2004).
34. *Phase Diagrams of Binary Gold Alloys: Monograph Series on Alloy Phase Diagrams*, Ed. by H. Okamoto and T. B. Massalski (ASM Int., Metals Park, Ohio, 1987).
35. C. J. Cooke and W. Hume-Rothery, J. Less-Common Met. **10** (1), 42 (1966).
36. V. G. Dubrovskii, Phys. Status Solidi B **171** (3), 345 (1992).

Translated by G. Skrebtsov

Physics of the Solid State, Vol. 47, No. 12, 2005, pp. 2219–2232. Translated from Fizika Tverdogo Tela, Vol. 47, No. 12, 2005, pp. 2127–2141.

SEMICONDUCTORS AND DIELECTRICS

Probing of the Shallow Donor and Acceptor Wave Functions in Silicon Carbide and Silicon through an EPR Study of Crystals with a Modified Isotopic Composition

P. G. Baranov*, B. Ya. Ber*, O. N. Godisov, I. V. Il'in*, A. N. Ionov*, E. N. Mokhov*, M. V. Muzafarova*, A. K. Kaliteevskiĭ**, M. A. Kaliteevskiĭ*, and P. S. Kop'ev***

**Ioffe Physicotechnical Institute, Russian Academy of Sciences, Politekhnicheskaya ul. 26, St. Petersburg, 194021 Russia*
e-mail: ivan.ilyin@mail.ioffe.ru
***CENTROTECH EHZ, pr. Stachek 47, St. Petersburg, 198096 Russia*
Received December 9, 2004

Abstract—The spatial distributions of the unpaired-electron wave functions of shallow N donors in SiC crystals and of shallow P and As donors in silicon crystals were determined by studying crystals with a modified content of the ^{29}Si and ^{13}C isotopes having a nonzero nuclear magnetic moment. As follows from the present EPR and available ENDOR data, the distribution of donor electrons in SiC depends substantially on the polytype and position in the lattice; indeed, in 4*H*-SiC, the unpaired electrons occupy primarily the Si *s* and *p* orbitals, whereas in 6*H*-SiC these electrons reside primarily in the *s* orbitals of C. The electron distributions for the N donor in the hexagonal position, which has a shallow level close to that obtained for this material in the effective-mass approximation, and for the donor occupying the quasi-cubic position differ substantially. The EPR spectrum of N in quasi-cubic positions was observed to have a hyperfine structure originating from a comparatively strong coupling with the first two coordination shells of Si and C, which were unambiguously identified. The effective-mass approximation breaks down close to the N donor occupying the quasi-cubic position, and the donor structure and the donor electron distribution become less symmetric. In silicon, reduction of the ^{29}Si content brought about a substantial narrowing of the EPR line of the shallow P and As donors and an increase in the EPR signal intensity, as well as a noticeable increase in the spin–lattice relaxation time T_1. This offers the possibility of selectively studying these spectra by optically exciting a region of the crystal in order to shorten T_1 and thereby precluding EPR signal saturation only in the illuminated part of the material. This method may be used to advantage in developing materials for quantum computers based on donors in silicon and SiC. © *2005 Pleiades Publishing, Inc.*

1. INTRODUCTION

Silicon carbide (SiC) occupies a prominent place among the promising materials for developing electronic devices designed for operation under high temperatures, with corrosive media, at high power levels, and in a hazardous radiation environment. The high binding energy between carbon and silicon (Si–C) makes SiC stable against extremal conditions. To develop instruments based on charge transfer, doping with donor and acceptor impurities is chosen; the most widely used among them are *n*-type nitrogen and phosphorus and *p*-type boron and aluminum. There is no doubt that it is necessary to gain a deeper insight into the electronic structure of donor and acceptor centers in order to further improve the electrical characteristics of the materials in question. As for SiC, study of this material, unlike other major semiconductors (silicon and the III–V compounds), encounters additional difficulties associated with the existence of several SiC polytypes and, accordingly, the presence of several crystallographic positions for donor and acceptors in these polytypes. The 4*H*-SiC and 6*H*-SiC polytypes hold the most promise as regards their considerable application potential. They are characterized by identical, hexagonal symmetry about the *c* axis. Each Si atom is coordinated by four C atoms, and vice versa. An analysis of the second coordination shells of 4*H*-SiC sites reveals two inequivalent lattice positions: quasi-cubic (*k*) and hexagonal (*h*) position. For the *k* position, the twelve atoms in the second coordination shell are arranged just as in the zinc blende cubic structure. For the *h* position, they are located as in the wurtzite hexagonal structure. These positions are distributed uniformly between the carbon and silicon sublattices. In 6*H*-SiC, there are three inequivalent positions: two quasi-cubic (k_1, k_2) and one hexagonal (*h*). An important model for theoretical calculations is the cubic 3*C*-SiC polytype, in which the symmetry and nearest neighbor environment of the C position are identical to those in the silicon crystal, whereas the symmetry and nearest neighbor environment of the Si position are the same as in diamond.

Donors and acceptors occupy different substitutional sites in SiC. It is believed that the nitrogen donors substitute for carbon and the phosphorus donors, for silicon, whereas the boron and aluminum acceptors substitute for silicon. Incidentally, different polytypes

differ markedly in terms of their band structure, which gives rise to a difference between the carrier effective masses and, hence, makes it necessary to properly select materials with optimum characteristics for device applications.

An essential characteristic of shallow impurities is the spatial distribution of their wave functions, which is directly connected with the possibility of employing effective-mass (EM) theory for description of such systems [1]. There are two main methods for probing the wave functions of shallow donors and acceptors, namely, EPR study of crystals with a modified isotope composition and ENDOR. Both methods have been successfully tested in the probing of wave functions of color centers in alkali halide crystals (F centers in the ground [2] and excited [3] states) and made it possible to establish the nature of these centers. These methods were also used to probe the wave functions of shallow donors in silicon [4]. EPR is one of the most informative methods of studying the electronic structure of impurity and native defects in semiconductors [5], including donor impurities of nitrogen, phosphorus, and arsenic in compounds of Group IV elements [4, 6] and shallow acceptors in silicon [7] and SiC [8, 9]. ENDOR is actually a refinement of the EPR method intended mainly for investigating systems in which the hyperfine (HF) structure is not resolved in EPR spectra [4, 10–12]. Combined use of both techniques is an optimum approach to obtaining reliable information on the spatial distribution of carrier wave functions, because these techniques are mutually complementary. ENDOR studies provide the most complete information possible, because they permit determination of both isotropic and anisotropic HF interactions, i.e., of the degree of unpaired-electron localization in the *s* and *p* orbitals. One cannot, however, rule out the possibility that even the strongest HF interactions may elude detection in ENDOR experiments, because such interactions occur with a small number of nuclei and, hence, ENDOR signals have a low intensity for nuclei of low-abundance isotopes.

Both carbon and silicon in SiC have isotopes with a nonzero nuclear spin. The natural abundance of the ^{29}Si isotope with nuclear spin $I = 1/2$ in silicon is 4.67%, and that of the ^{13}C isotope with the same nuclear spin, $I = 1/2$, is 1.11%. EPR studies yield an integrated characteristic of unresolved HF interactions and are most sensitive to the strongest interactions, which provide the major contribution to the linewidth. Because of the low abundance of ^{29}Si and ^{13}C in natural silicon and carbon, respectively, a resolved HF structure may remain unobserved in EPR spectra or its interpretation may be ambiguous. Therefore, investigating crystals enriched in isotopes can make it possible to tackle this problem as well.

Variations in the content of isotopes with nonzero nuclear magnetic moments (^{29}Si in silicon and ^{29}Si and ^{13}C in silicon carbide) should give rise to a change in the shallow-donor EPR linewidth, because this linewidth is dominated by the HF interaction of the unpaired electron with the neighboring ^{29}Si and ^{13}C nuclei. We consider the quantitative aspect of this issue. Let the EPR linewidth be determined by the unresolved HF structure, i.e., be inhomogeneously broadened, a condition mostly met for shallow donors in silicon, germanium, and silicon carbide. According to EM theory, the wave function of a defect extends over a large number of coordination shells; therefore, there are many ^{29}Si and ^{13}C isotope nuclei involved in hyperfine interactions.

The probability P_m of finding m specific atoms (in our case, atoms of a specific isotope) in a coordination shell around a defect consisting of n identical sites is given by

$$P_m = C_n^m f^m (1 - f)^{n-m}, \quad (1)$$

where C_n^m is the number of combinations of n elements taken m at a time and f is the relative concentration of the given isotope; $f(^{29}\text{Si}) = 0.0467$ and $f(^{13}\text{C}) = 0.0111$ are the natural abundances of the ^{29}Si and ^{13}C isotopes in silicon and carbon, respectively.

The FWHM of an unresolved EPR line ΔB for the case where this width is dominated by HF interactions is given by [4]

$$\Delta B = \frac{2}{g\mu_B}\left[\sum_i^R f(^N X) n_i(X) \frac{a_i^2(^N X) I(I+1)}{3}\right]^{1/2}, \quad (2)$$

where $^N X$ stands for ^{29}Si or ^{13}C, n_i is the number of equivalent sites for X atoms in the ith coordination shell, a_i is the HF interaction constant for $^N X$ atoms occupying equivalent sites in the ith coordination shell, g is the electronic g factor, μ_B is the Bohr magneton, and I is the nuclear angular momentum of the $^N X$ isotope ($I = 1/2$ for the ^{29}Si and ^{13}C isotopes). Note that the g factor for shallow donors may deviate substantially from $g = 2$ (for instance, in germanium), a point that should be taken into account in ΔB calculations. Isotropic HF interaction is proportional to the wave-function density at the nucleus site of the central or ligand (lth) atom, $a_l = (8\pi/3) g\mu_B g_I \mu_N |\psi(\mathbf{r}_l)|^2$, where g_I is the nuclear g factor, μ_N is the nuclear magneton, and $|\psi(\mathbf{r}_l)|^2$ is the wave-function density of a donor unpaired electron at site l.

As follows from Eq. (2), the concentration of isotopes with nonzero nuclear spins has a considerable effect on the linewidth if the isotropic HF interaction constant for these isotopes is large enough. The major contribution to the linewidth is due to several coordination shells closest to the impurity (here, we are certainly disregarding possible strong HF interactions that are resolvable in EPR spectra). Therefore, weak HF interactions for remote coordination shells can only be

found by ENDOR or estimated from EM theory. In practice, of course, an EPR linewidth can yield an estimate of only the isotropic HF interaction constants with the nearest coordination shells. More exact values of these quantities, as well as the anisotropic HF interaction constants, can be determined by ENDOR (for example, for shallow donors in silicon [4, 10], shallow nitrogen donors in SiC [12], and shallow boron acceptors in SiC [11]).

In [12], nitrogen donors in crystals of 4*H*-SiC (in the *k* position) and 6*H*-SiC (in positions *h*, k_1, k_2) were studied by pulsed microwave ENDOR. Preliminary EPR experiments were also performed with ^{13}C-enriched 4*H*- and 6*H*-SiC crystals. The general conclusion was that the spatial distributions of the wave functions of unpaired electrons in the 4*H*-SiC and 6*H*-SiC polytypes are essentially different. The main part of the spin density in 4*H*-SiC is localized in the *s* and *p* orbitals on the Si sublattice, with the fraction of the *p* orbitals being very significant. In 6*H*-SiC, the unpaired electrons for all three nitrogen donor positions are localized primarily in the *s* orbitals on the carbon sublattice. This conclusion found partial confirmation in a study of 4*H*-SiC and 6*H*-SiC crystals enriched in the ^{13}C isotope. This issue could be settled by studying crystals with a modified isotope composition in both carbon and silicon, and this is what motivated the present work. It seems appropriate to mention here an additional problem, namely, the appearance in some experiments of isotropic satellites in the EPR spectra of shallow nitrogen donors in the *k* positions of 4*H*-SiC, which have been assigned to strong HF interactions with four carbon atoms [13] or with one silicon atom [14]. We likewise observed satellites for nitrogen donors in some 6*H*-SiC and 4*H*-SiC crystals. An unambiguous answer to whether the observed satellites are actually a resolved HF structure originating from interaction with carbon and silicon atoms in the nearest coordination shells can be found only in experiments on crystals with a modified isotope composition.

For the sake of comparison, we also studied the EPR spectra of shallow phosphorus and arsenic donors in a silicon crystal with a modified isotopic composition grown from the same materials as SiC.

Studies of donors in crystals depleted in isotopes with nonzero nuclear magnetic moments benefit considerably from the substantial increase in the EPR signal intensity. The EPR linewidths of shallow donors in such crystals narrow markedly, which increases the EPR signal intensity (amplitude) in proportion to the ratio of the squares of the linewidths obtained on crystals with natural and modified isotope compositions. The enhanced EPR signal amplitude permits studies of thin samples of semiconductor materials, for instance, ion-implanted layers. Recently, such studies have been attracting considerable interest in connection with numerous proposals for employing such systems, namely, shallow donors in Si, Ge, SiGe, and SiC crystals, for the development of electronic devices for quantum computers. Reducing the concentration of nuclei with nonzero magnetic moments seems essential for slowing down spin relaxation processes in these systems. Earlier, we studied EPR signals due to shallow arsenic donors in germanium crystals with a low content of the ^{73}Ge isotope (having a nonzero nuclear magnetic moment) [15] and observed a substantial narrowing of the EPR lines.

2. EXPERIMENTAL TECHNIQUE

In this study, the EPR method was applied to 6*H*-SiC and 4*H*-SiC samples, primarily *n* type. In some samples, nitrogen was compensated to a considerable extent by boron and the EPR intensity ratio of nitrogen to shallow boron was varied by UV irradiation. Samples of four types were used: (i) with natural isotopic abundance; (ii) with a low ^{29}Si content, less than 0.5% ^{29}Si (the samples were grown using silicon enriched in the ^{28}Si isotope); (iii) with a low ^{29}Si content, less than 0.5% ^{29}Si (grown using ^{30}Si-enriched silicon); and (iv) ^{13}C-enriched 4*H*-SiC (with an enrichment of ~10% and ~15%) and 6*H*-SiC (with an enrichment of ~25%). Part of the 4*H*-SiC crystals enriched in the ^{13}C isotope (~15%) were grown on an *n*-type 6*H*-SiC substrate with natural isotopic abundances. The substrates were polished down to a thickness of less than 10 μm. In these crystals, superposition of the nitrogen donor EPR signals produced in the substrate and in the main crystal with a modified isotope composition was excluded, because the EPR signals from the 4*H*-SiC and 6*H*-SiC polytypes do not coincide.

In each case, the isotopic composition of only one element, Si or C, was varied.

SiC crystals of a chosen isotopic composition were grown by the sublimation sandwich technique [16]. The SiC vapor source was a SiC polycrystal grown from a mixture of silicon and carbon containing the isotope to be introduced. The source was placed in a sealed container together with a substrate (a SiC single crystal of the 6*H* or 4*H* polytype). The growth was carried out in vacuum at a temperature of 1900–2000°C in conditions providing reproducible growth of the substrate polytype. The thicknesses of the grown crystals ranged from 0.5 to 1.0 mm.

The crystals thus grown exhibited *n*- or *p*-type conduction with a carrier concentration of 10^{16}–10^{17} cm^{-3}, which should be attributed to the presence of nitrogen and boron impurities in background amounts. The type of conduction depended on the growth direction. Crystals grown in the [0001]C direction were predominantly *n* type, and those grown in the [0001]Si direction were *p* type.

The SiC crystals were cut or cleaved in the form of platelets with known orientations and could be rotated in the spectrometer cavity in certain planes.

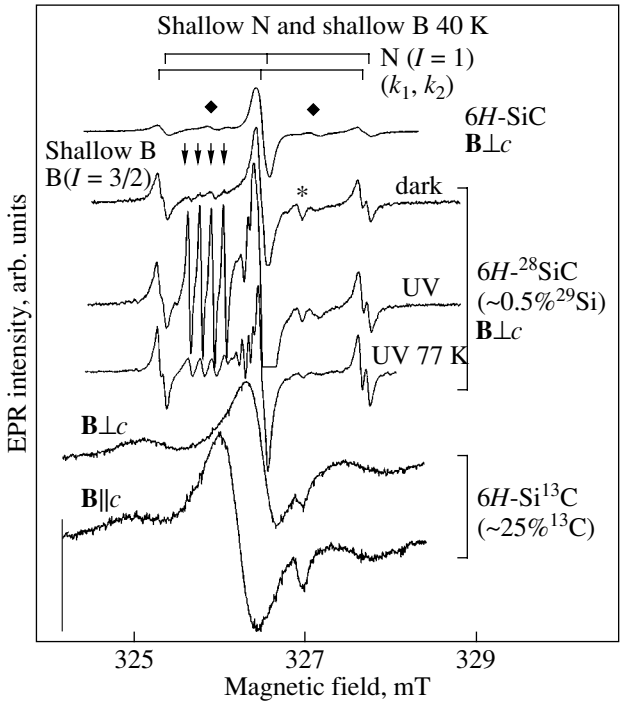

Fig. 1. EPR spectra of shallow nitrogen donors in three 6*H*-SiC crystals: with natural isotopic abundance, enriched in ^{28}Si (<0.5% ^{29}Si), and enriched in ^{13}C (~25%). The spectra were measured at 40 K with a magnetic field **B** ⊥ *c*. The spectra of 6*H*-Si^{13}C were obtained for magnetic field orientations **B** ⊥ *c* and **B** ∥ *c*. The ^{29}Si-depleted sample was used to obtain the EPR spectra before and after UV interband optical pumping and the EPR spectrum at 77 K. All spectra except the top one contain an asterisk-labeled reference signal of quartz.

We also studied a nominally undoped ^{30}Si crystal [17] with the ^{29}Si isotope present in a concentration of less than 0.5%. The starting material composition was as follows: 0.499% ^{28}Si, 0.496% ^{29}Si, and 99.005% ^{30}Si.

Experiments were conducted on a JEOL EPR spectrometer at a frequency of 9.3 GHz (*X* band) in a helium flow cryostat, which was manufactured in the laboratory and permitted temperature control within the range 4–300 K. All EPR spectra presented in the figures were obtained in one scan, without accumulation.

3. EXPERIMENTAL RESULTS

3.1. Nitrogen Donors in SiC

Figure 1 presents EPR spectra of shallow nitrogen donors in three 6*H*-SiC crystals: (i) with a natural isotopic abundance; (ii) enriched in the ^{28}Si isotope and, hence, depleted in ^{29}Si (less than 0.5%); and (iii) enriched in ^{13}C (~25%). The spectra were measured at 40 K for the magnetic field orientation **B** ⊥ *c*. For the crystal enriched in ^{13}C, the spectra are shown for two orientations, **B** ⊥ *c* and **B** ∥ *c*. Nitrogen donors occupying positions k_1 and k_2 produce three EPR lines each, because nitrogen has only one isotope (^{14}N, with an abundance of 99.63%) with a nonzero nuclear spin, $I = 1$ (the number of lines is $2I + 1$). Since the signals due to N donors in positions k_1 and k_2 differ in terms of their parameters, line splitting occurs. The vertical bars in Fig. 1 specify the nitrogen EPR signals for the k_1 and k_2 positions measured for the **B** ⊥ *c* orientation.

The EPR spectra of shallow nitrogen donors are described by the standard spin Hamiltonian

$$\hat{H} = \mu_B \mathbf{B} \cdot \mathbf{g} \cdot \mathbf{S} + \mathbf{S} \cdot \mathbf{A} \cdot \mathbf{I} + \sum_{i=1}^{N} \mathbf{S} \cdot \mathbf{a}_i \cdot \mathbf{I}_i, \qquad (3)$$

where the first term corresponds to the Zeeman interaction in a magnetic field B for a center with spin $S = 1/2$ and an anisotropic electronic g factor (tensor **g**); the second term relates to the HF interaction (characterized by tensor **A**) between the unpaired electron of the shallow donor and the ^{14}N nucleus with a nuclear spin $I = 1$; and the third term describes the HF interaction with ligands (characterized by tensor $\mathbf{a}_i$), more specifically, between the unpaired electron of the shallow donor and the nuclei of silicon ^{29}Si or of carbon ^{13}C that occupy equivalent sites in the *i*th coordination shell. The last interaction is frequently called superhyperfine (SHF). The unresolved HF structure in the EPR spectrum determines the EPR linewidth.

The HF interaction constant and the g factor are weakly anisotropic and symmetric about the c axis. Accounting for this axial symmetry, the HF interaction tensor components can be expressed in terms of the isotropic, A_S, and anisotropic, A_P, components as $A_\parallel = A_S + 2A_P$ and $A_\perp = A_S - A_P$. For the interaction with ligand atoms, whose symmetry axes, as a rule, do not coincide with the crystal axes, the isotropic and anisotropic constants of the HF interaction are denoted by a and b, respectively. Table 1 lists experimental characteristics for shallow N donors in 3*C*-SiC, 4*H*-SiC, and 6*H*-SiC crystals in different positions found by EPR and ENDOR [12, 18]. One can also find there the g factors, the isotropic (A_S) and anisotropic (A_P) HF interaction constants, and the corresponding spin densities for *s* and *p* electrons.

The spectrum in Fig. 1 for a natural-abundance 6*H*-SiC sample reveals additional lines, which are located between the main nitrogen HF components and denoted by rhombs. These lines are due to the interaction with two equivalent nitrogen atoms, which are possibly located in exchange-coupled pair centers [15, 19] or in centers of a more complex structure [15]. Because the transitions of single and pair centers in the central line coincide, this line is more intense. For the crystal depleted in ^{29}Si, Fig. 1 shows its spectra measured before and after UV interband optical pumping. A spectrum recorded at 77 K is also shown. We witness a certain increase in the nitrogen donor signal intensity and a substantial enhancement of the intensity of shallow

Table 1. Experimental characteristics of shallow N donors occupying different positions in 3*C*-SiC, 4*H*-SiC, and 6*H*-SiC crystals: ionization energies, valley-orbit splitting, *g* factors, isotropic (A_S) and anisotropic (A_P) HF interaction constants, and the corresponding *s*- and *p*-electron spin densities on N

SiC polytype	Position	Ionization energy E_g, meV (valley-orbit splitting)	$g_\parallel$	$g_\perp$	A_S, MHz	A_P, MHz	*s*, %	*p*, %	*s* + *p*, %
3*C*-SiC	*k*	54 (8.37)	2.0050	2.0050	3.5		0.19		0.19
4*H*-SiC	*h*	52.1 (7.6)	2.0055	2.0010	2.9	0.080	0.16	0.14	0.3
	k	91.8 (45.5)	2.0043	2.0013	50.97	0.004	2.8	0.007	2.81
6*H*-SiC	*h*	81 (12.6)	2.0048	2.0028	2.52	0.12	0.14	0.22	0.36
	k_1	137.6 (60.3)	2.0040	2.0026	33.221	0.004	1.83	0.007	1.84
	k_2	142.4 (62.6)	2.0037	2.0030	33.564	0.009	1.85	0.016	1.87
P		44 (11.7)	1.99850		117.53		0.9		0.9
As		49 (21.1)	1.99837		198.35		1.35		1.35

Note: Analogous parameters are also presented for shallow P and As donors in silicon for the sake of comparison.

acceptor signals induced by optical pumping. The arrows identify four HF transitions for shallow boron acceptors in the hexagonal position. Shown below are EPR spectra of nitrogen donors in ^{13}C-enriched crystals (~25%) obtained for the $\mathbf{B} \perp c$ and $\mathbf{B} \parallel c$ orientations. All spectra except for the top one are referenced to a quartz calibration signal labeled by an asterisk.

The high-field EPR components of shallow nitrogen donors in the k_1 and k_2 positions presented in Fig. 1 are displayed in Fig. 2 in an expanded scale. The slight narrowing of EPR lines resulting from a decrease of the ^{29}Si isotope concentration by an order of magnitude is seen to bring about a better resolution of the k_1 and k_2 signals. However, enrichment in the ^{13}C isotope causes a substantial broadening of the EPR lines. The EPR linewidths measured in crystals with a natural and modified isotope composition are listed in Table 2. The spectrum of the ^{29}Si-depleted crystal shown in Fig. 2 contains additional lines as satellites, which are arranged symmetrically about the central lines and identified by arrows. Such satellites are seen to be present for each component of the hyperfine structure of nitrogen in positions k_1 and k_2 (Fig. 1), with the line splitting, 0.5 mT (14 MHz), being practically independent of crystal orientation. Because these satellites are observed in crystals depleted in the ^{29}Si isotope, they can only be due to the HF interaction with carbon. In accordance with the natural ^{13}C abundance, the intensity ratio attests to interaction with four or five practically equivalent carbon atoms; this interaction is practically isotropic to within experimental error and is the same for positions k_1 and k_2.

Figures 3 and 4 illustrate the results of a study of shallow nitrogen donors in 4*H*-SiC crystals, which are similar to those shown in Figs. 1 and 2 for the 6*H*-SiC polytype. The EPR spectra in Fig. 3 relate to shallow nitrogen donors obtained on three 4*H*-SiC crystals: (i) with natural isotopic abundance; (ii) enriched in ^{28}Si and, thus, having a low content (less than 0.5%) of the ^{29}Si isotope; and (iii) enriched in ^{13}C (~15%). The spectra were obtained at 40 K in the $\mathbf{B} \perp c$ and $\mathbf{B} \parallel c$ geometries for the last two crystals and only in the $\mathbf{B} \parallel c$ geometry for the crystal with natural isotope abundance. The spectra of the ^{29}Si-depleted crystal were obtained under UV illumination, because this brought

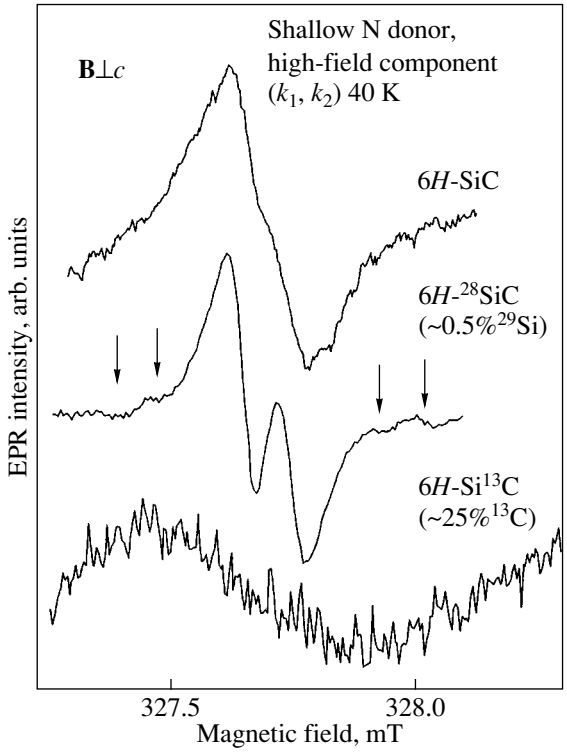

Fig. 2. High-field components of the EPR spectra of shallow nitrogen donors in positions *k* shown in Fig. 1 (in expanded scale) for the $\mathbf{B} \perp c$ orientation. The arrows indicate the satellites in the spectrum of the ^{29}Si-depleted sample.

Table 2. Experimental and calculated EPR linewidths (in mT) for shallow nitrogen donors in the *k* position in 4*H*-SiC and in the k_1 position in 6*H*-SiC with different ^{13}C and ^{29}Si isotope abundances: natural, enriched in ^{13}C (25% for 6*H*-SiC and 15% for 4*H*-SiC), and depleted in ^{29}Si (0.5%)

SiC polytype	Experiment			Calculation		
	ΔB_{pp} (natural)	ΔB_{pp} (^{13}C)	ΔB_{pp} (^{29}Si)	ΔB_{pp} (natural)	ΔB_{pp} (^{13}C)	ΔB_{pp} (^{29}Si)
6*H*-SiC	0.13	0.5	0.12	0.12	0.55	0.11
4*H*-SiC	0.21	0.35	0.07	0.21	0.29	0.08

Note: In each experiment, the content of only one isotope was varied.

about an enhancement of the nitrogen donor signal intensity by approximately one order of magnitude. All spectra are provided with the quartz signal labeled by an asterisk. The arrows in the spectra of 4*H*-Si^{13}C refer to signals of nitrogen donors in the remainder of the 6*H*-SiC substrate on which the 4*H*-SiC crystal was grown.

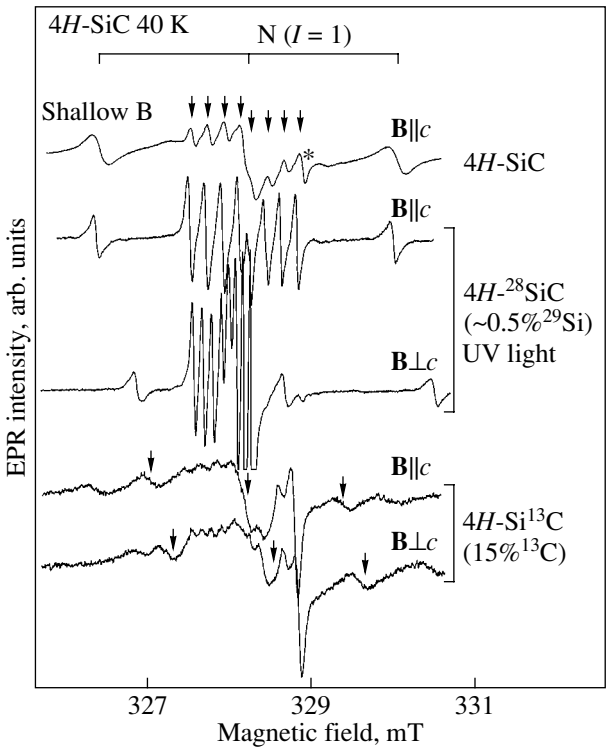

Fig. 3. EPR spectra of shallow nitrogen donors in various 4*H*-SiC samples: with natural isotopic composition, enriched in the ^{28}Si isotope (~0.5% ^{29}Si), and enriched in the ^{13}C isotope (~15%). The spectra were measured at 40 K for the **B** || *c* and **B** ⊥ *c* orientations; the spectrum of the natural-abundance crystal was obtained only for **B** || *c*. Vertical bars refer to the EPR lines of nitrogen in position *k* only for the **B** || *c* orientation. The EPR spectra of the ^{29}Si-depleted crystal were measured under UV illumination. All spectra contain a quartz reference signal labeled by an asterisk. The EPR spectrum of the ^{13}C-enriched crystal contains EPR lines (identified by arrows) belonging to nitrogen donors in the 6*H*-SiC substrate.

Figure 4a displays components of the nitrogen HF structure recorded for a 4*H*-SiC crystal with a low ^{29}Si content at 40 K (upper two spectra) and for a ^{13}C-rich crystal at 4.2 K (lower two spectra) in the **B** ⊥ *c* and **B** || *c* geometries. The satellite line pairs observed in crystals depleted in ^{29}Si are identified by vertical bars. The arrows related to the ^{13}C-enriched crystal specify the outer satellite-pair lines assigned to HF interaction with one ^{29}Si nucleus, estimated as 1.46 mT (41 MHz). The rhomb indicates one of the nitrogen pair lines, and the asterisk, the quartz signal. The central line of the nitrogen HF structure is presented in one spectrum only.

The high-field components of the EPR spectra that were recorded for shallow nitrogen donors occupying the *k* positions in 4*H*-SiC and shown in Figs. 3 and 4a are also displayed in Fig. 4b in an expanded scale. A decrease of the ^{29}Si isotope concentration by an order of magnitude is seen to result in a substantial narrowing of the EPR lines. However, enrichment by ^{13}C did not bring about noticeable EPR line broadening. This implies that the variation of the EPR linewidth in crystals with a modified isotopic composition in 4*H*-SiC differs markedly from what was observed in 6*H*-SiC. The ^{29}Si-depleted crystal reveals two additional lines located symmetrically about the central line. As is evident from Fig. 4a, similar satellites were observed with other *k*-nitrogen lines and there was practically no change in their relative intensity and line separation as the crystal orientation in the magnetic field was changed, although all lines change position because of the nitrogen donor *g* factor being slightly anisotropic. Because these lines were seen in crystals with a low ^{29}Si content, just as in the case with 6*H*-SiC, they certainly cannot originate from HF interaction with ^{29}Si nuclei. It stands to reason that these satellites are caused by HF interaction with ^{13}C; for crystals with a natural abundance of the ^{13}C isotope, the satellites are masked by the broader nitrogen donor lines. As in the case with the 4*H*-SiC crystal, the intensity ratio suggests that they derive from interaction with four or five carbon atoms, with the strength of this interaction being 0.6 mT (16.8 MHz). The method of isotope composition modification used in the present study provides compelling evidence for the HF interaction being with carbon alone. This conclusion fits the results of the study of ^{13}C-rich crystals. As seen from Fig. 4b, the EPR line shape for the crystal with natural isotopic abundance differs from that obtained on the ^{13}C-rich crystal. Indeed, the wings of the EPR line in the latter case fall off substantially slower. This is seen clearly from the bottom spectrum in Fig. 4b, where the dashed line shows a part of the EPR line of the crystal with natural isotopic abundance. The observed line shape reflects

the presence of satellites whose intensities are substantially higher in crystals enriched with the ^{13}C isotope. The 6*H*-SiC crystals with natural isotopic abundance exhibited satellites corresponding to a practically isotropic HF interaction with one Si atom, whose strength was 0.96 mT (26.9 MHz). No such satellites were observed in crystals with a low ^{29}Si content.

3.2. Boron Acceptors in SiC

All the crystals studied contained a residual boron impurity. Weak EPR signals of shallow boron acceptors, which were actually boron atoms substituted for silicon, were observed, as a rule, with no optical illumination, and their intensity grew noticeably under interband optical pumping. The energy levels of shallow boron referenced to the valence band edge (E_V) are 0.27, 0.31, and 0.38 eV for the *h* and two *k* positions in 6*H*-SiC, respectively. EPR signals of shallow boron acceptors provide valuable information. These spectra can be used to extract, besides the HF interaction with boron, a resolved HF structure due to anisotropic interaction with one carbon atom in the first coordination shell (which accounts for up to 30% of the spin density) and to practically isotropic interaction (~28 MHz) with three equivalent silicon atoms of the second coordination shell [8, 9, 11]. Thus, these spectra provided an estimate of the content of ^{29}Si in crystals enriched in the ^{28}Si or ^{30}Si isotopes and the concentration of ^{13}C in crystals enriched in this isotope. The EPR linewidths of shallow boron acceptors, as in the case of shallow nitrogen donors, offered the possibility of judging the spatial distribution of the shallow-acceptor wave function. Thus, the boron acceptor structure is characteristic of deep impurities. Note, however, that the boron level of about 0.30 eV, which is comparatively shallow for SiC, is customarily called shallow (shallow boron impurity). A pulsed microwave ENDOR study [11] suggests that the spin density is localized primarily on carbon atoms and that EM theory is applicable apparently only to comparatively remote coordination shells, the HF interaction with which accounts for the EPR linewidth. This conclusion is borne out by the present study; indeed, a decrease in the ^{29}Si content by more than one order of magnitude produced practically no effect on the EPR linewidth of shallow boron, whereas an increase in the ^{13}C content (by about 20 times) brought about a substantial broadening of the EPR lines.

3.3. Shallow Phosphorus and Arsenic Donors in ^{30}Si

Figure 5 shows an EPR spectrum of shallow phosphorus donors measured in a silicon crystal enriched in the ^{30}Si isotope (i.e., depleted in ^{29}Si) at 4.2 K under optical interband pumping. Also presented for comparison is an EPR spectrum of phosphorus in natural silicon. The inset displays in expanded scale the high-field phosphorus line in both crystals. We readily see that the

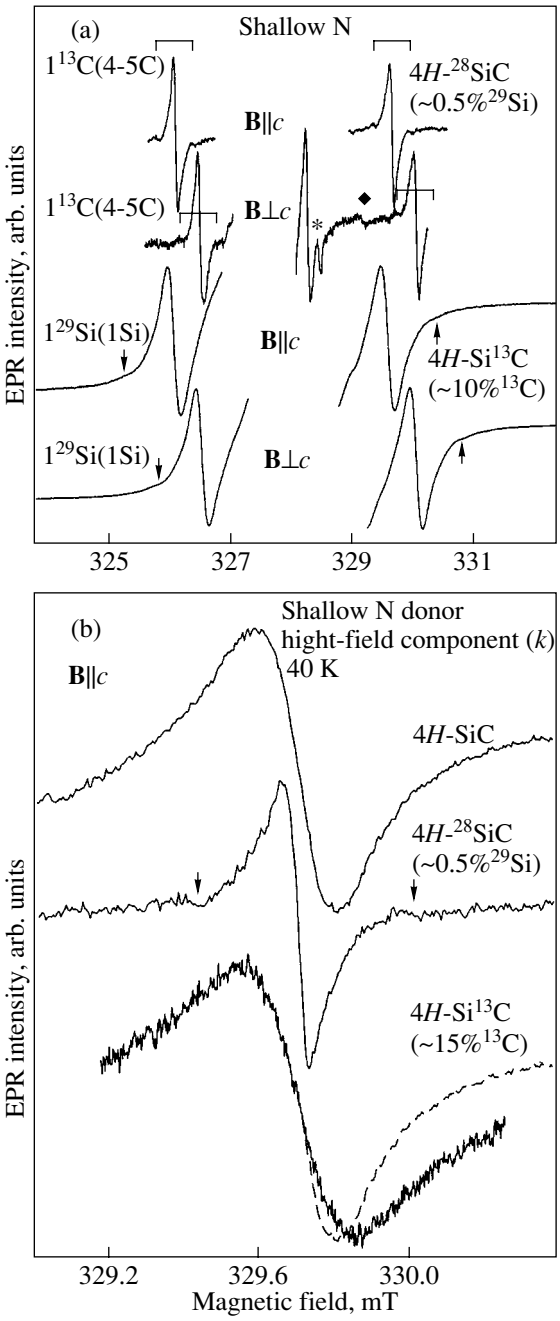

Fig. 4. EPR spectra of shallow nitrogen donors in 4*H*-SiC. (a) Individual nitrogen HF-structure components measured in 4*H*-SiC with a low ^{29}Si content at 40 K (upper two spectra) and in the ^{13}C-enriched crystal at 4.2 K (lower two spectra) for the **B** ∥ *c* and **B** ⊥ *c* orientations. The satellite line pairs deriving from the HF interaction with one ^{13}C nucleus are identified with vertical bars. Arrows refer to the outer lines of the satellite pairs assigned to the HF interaction with one ^{29}Si nucleus. The number of equivalent C or Si nuclei is indicated in parentheses. The rhomb relates to one of the nitrogen pair lines, and the asterisk, to the quartz signal. The central line of the carbon HF structure is given in one spectrum only. (b) The high-field components of the EPR spectra of shallow nitrogen donors in the *k* position presented in Fig. 3 for the **B** ∥ *c* orientation (in expanded scale). The arrows specify the satellites in the EPR spectrum of the ^{29}Si-depleted crystal. The dashed line shows a part of the EPR line for the crystal with natural isotopic abundance.

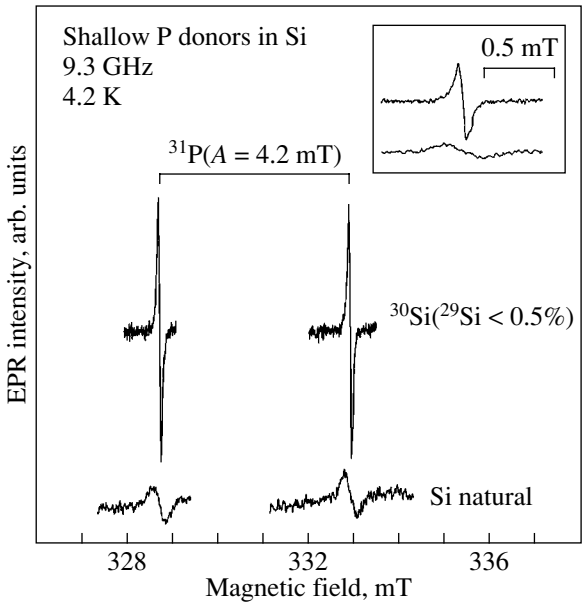

Fig. 5. EPR spectra of shallow phosphorus donors measured in a ^{30}Si crystal at 4.2 K under interband light pumping and in natural silicon. The inset shows in expanded scale the high-field EPR components of shallow phosphorus donors in ^{30}Si (top line) and in silicon with natural isotopic abundance (bottom line). The crystal orientation is not fixed, because the EPR spectrum of shallow donors is isotropic.

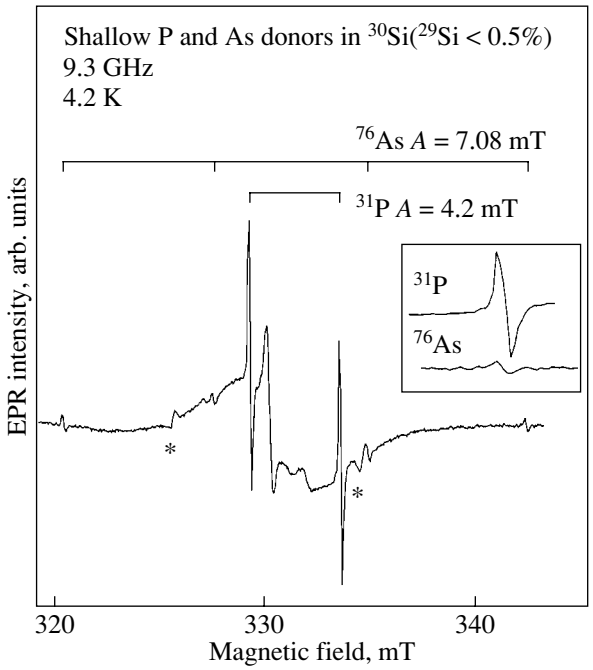

Fig. 6. EPR spectra of shallow P and As donors in ^{30}Si measured at 4.2 K at a frequency of 9.3 GHz under interband illumination. The asterisks identify two reference lines of manganese. The inset shows in expanded scale the high-field EPR components of shallow phosphorus and arsenic donors in ^{30}Si.

linewidth, which is 0.06 mT in the crystal with a reduced content (less than 0.5%) of ^{29}Si having a nonzero nuclear magnetic moment, narrows strongly as compared to that measured in the crystal with a natural abundance of silicon, 0.26 mT. As follows from Eq. (2), this narrowing corresponds to a ^{29}Si content of ~0.25%, i.e., to about one-half the figure specified in the certificate of the material [17].

Figure 6 displays EPR spectra of shallow phosphorus and arsenic donors obtained on a silicon crystal enriched in the ^{30}Si isotope at 4.2 K under optical interband pumping. The inset shows in expanded scale the high-field components of the EPR spectra of shallow phosphorus and arsenic donors measured in a silicon crystal enriched in ^{30}Si.

The EPR spectra of shallow phosphorus and arsenic donors could be recorded only under illumination, because with no illumination the EPR signals were saturated as a result of the very long spin–lattice relaxation time T_1. Illumination brings about a sharp decrease in T_1 caused by interaction with carriers [20] and, accordingly, the possibility of observing EPR. This effect is very useful, because it permits local study of the EPR signal, i.e., only in regions of optical excitation. This also opens up possibilities for investigating surface effects with high-energy photons capable of penetrating only into a thin surface silicon layer. The effect of light-induced shortening of T_1 may turn out to be promising in the case where ^{29}Si-depleted silicon with shallow donors is employed as a material for electronic devices intended for use in quantum computers, because this effect would provide an easy means to reset the system.

4. DISCUSSION OF THE RESULTS

The EPR spectra of shallow nitrogen donors occupying positions k in the 4H-SiC and 6H-SiC polytypes and having the deepest levels (Table 1) exhibit, in addition to the unresolved HF structure determining the EPR linewidths, HF interactions with nearest neighbor coordination shells. These interactions can be resolved as satellites in the EPR spectra. Satellites due to the HF interaction with silicon were observed in [13, 14] and in the present study, and satellites deriving from interaction with carbon were observed in this work. These additional EPR lines were unambiguously identified by studying crystals with a modified isotopic composition (indeed, this permitted observation of interaction with carbon due to EPR line narrowing) and by ENDOR [14].

Being an element of Group V, a donor atom has five valence electrons, with four of them forming valence bonds with the nearest lattice atoms and the fifth being acted upon by the Coulomb field of the remaining positive charge. In the EM approximation [1], a weakly bound electron is treated as a hydrogen-like atom in which the Coulomb attraction of the donor nucleus is

reduced by the semiconductor dielectric permittivity ε. It is also assumed that the electron moving in its orbit has an effective mass of a conduction electron. Under these assumptions, the wave function of a localized donor electron can be written as a product of the solution to the Schrödinger equation for a hydrogen-like atom formed by the donor and a weakly coupled electron and a Bloch function for an electron in the conduction band. Said otherwise, the Bloch function describing conduction band electrons is modulated by an envelope function which is a solution to the corresponding hydrogen-like Schrödinger equation. The result is the formation of a bound donor state with an ionization energy on the order of tens of millielectronvolts.

Si and SiC belong to Group IV of the periodic table and, therefore, besides some substantial differences, possess qualitatively similar energy level structures. These crystals are indirect-gap semiconductors, because the conduction band has several minima shifted relative to the center of the Brillouin zone. The pattern of this shift depends on the nature of the semiconductor material. Indeed, silicon has six minima displaced in the $\langle 100 \rangle$ directions and in SiC the character of the conduction band depends on the polytype. Because the conduction band has a many-valley character, shallow donor levels (which may be considered to be split off from the conduction band) are degenerate according to the number of minima; in silicon, for instance, there are six minima and they correspond to the A_1, E, or T_2 states. The EM approximation fails near the donor impurity, and the degeneracy is lifted. The level splitting, which is called valley–orbit splitting, is caused by the differences in electron distribution among the A_1, E, and T_2 states near the donor impurity. This difference is strongest in the energy of the A_1 singlet state, because in this case the wave function reaches its maximum amplitude on the donor atom.

The donor electron wave function (for instance, for silicon or the 3*C*-SiC cubic polytype) can be written as

$$\psi(\mathbf{r}) = \sum_{j=1}^{6} \alpha_j F_j(\mathbf{r}) \varphi_j(\mathbf{r}), \qquad (4)$$

where $\varphi_j(\mathbf{r}) = u_j(\mathbf{r}) e^{i\mathbf{k}_j \cdot \mathbf{r}}$ is the Bloch function at the jth minimum, which is located at point $\mathbf{k}_j$, and $u_j(\mathbf{r})$ is a periodic function. The coefficients α_j characterize the relative contribution of each valley and, thus, specify different combinations of the wave functions describing the regions near each minimum in the conduction band. The function $F_j(\mathbf{r})$ is the hydrogen-like solution to the Schrödinger equation for the donor electron. Because the actual type of ground state is *a priori* unknown, the existence of HF interaction in the donor atom strongly suggests that the ground state is the A_1 singlet; indeed, only in this state has the wave function a finite density at the donor nucleus site. In this case, the wave function is completely symmetric and the electron is spread uniformly over all the valleys; i.e., for Si or 3*C*-SiC, the wave function can be cast as

$$\psi(\mathbf{r}) = \frac{1}{\sqrt{6}} \sum_{j=1}^{6} F_j(\mathbf{r}) u_j(\mathbf{r}) r^{i\mathbf{k}_j \cdot \mathbf{r}}. \qquad (5)$$

In SiC, the degeneracy and further splitting depend on the polytype. In the cubic polytype 3*C*-SiC, we have a situation similar to that in silicon; i.e., the conduction band minima lie along the $\langle 100 \rangle$ axes, with the constant-energy surfaces in the proximity of the minima being shaped like ellipsoids extended along the $\langle 100 \rangle$ directions. The effective masses along and perpendicular to the ellipsoid axis are $m_l = 0.677m_0$ and $m_t = 0.247m_0$, respectively. The hexagonal polytypes feature a more complex pattern. The conduction band minima in the 4*H*-SiC and 6*H*-SiC polytypes are in essentially different positions, and this is what gives rise in the final count to differences between their electronic properties. The conduction band minimum in the 4*H*-SiC polytype is at point *M*, whereas that in 6*H*-SiC is located between points *M* and *L*, at a relative distance of approximately 60% from point *M*. The band structures are such that the effective masses in the plane perpendicular to the *c* axis are approximately the same for both polytypes ($m_\perp = 0.445m_0$ for 4*H*-SiC and $m_\perp = 0.43m_0$ for 6*H*-SiC, where m_0 is the free electron mass), while differing noticeably along the *c* axis. Indeed, for 4*H*-SiC, the effective mass along the *c* axis is $m_\parallel = 0.32m_0$, whereas for 6*H*-SiC we have $m_\parallel = 1.7m_0$. Thus, for the 4*H*-SiC polytype (and 3*C*-SiC), the electron wave function is very nearly spherically symmetric, while for 6*H*-SiC the electron wave function is contracted noticeably along the *c* axis, i.e., is pancake-shaped. It appears reasonable to use averaged effective masses m^* for electrons in the conduction bands. For 3*C*-SiC, $m^* = (m_l m_t m_t)^{1/3} = 0.345m_0$; for 4*H*-SiC, $m^* = (m_x m_y m_z)^{1/3} = 0.4m_0$; and for 6*H*-SiC, $m^* = 0.74m_0$. The effective Bohr radius of the shallow donor wave function is $a^* = [\varepsilon/(m^*/m_0)]a_0$, where $a_0 = 0.529$ Å is the Bohr radius. The shallow donor ionization energy is $E_{\text{eff}} = [(m^*/m_0)/\varepsilon^2]E_0$, where E_0 is the Rydberg energy. Thus, the effective Bohr radius of the electron wave function is $a^* = 15$ Å for 3*C*-SiC, $a^* = 13$ Å for 4*H*-SiC, and $a^* = 7.2$ Å for 6*H*-SiC and the corresponding shallow-donor ionization energies E_{eff} are 47 meV for 3*C*-SiC, 54 meV for 4*H*-SiC, and 101 meV for 6*H*-SiC.

Note that we are dealing here with the wave function of a donor electron which is not localized in any specific position, *k* or *h*, of the polytype under study; it appears, however, only natural that the properties of donor electrons should contain information on the free-electron wave function. Thus, the pronounced difference between the wave function properties of nitrogen donors in the *k* or *h* positions (which does not depend on the polytype) apparently derives only from the local symmetry of these positions and does not have direct

bearing on the general wave function of a band electron. These properties should be reflected in HF interactions with C and Si atoms in various coordination shells, which are proportional to the density of the donor wave function (5) $|\psi(\mathbf{r}_l)|^2$ at nucleus site l. Estimates of the wave function density on a nucleus are usually performed with a dimensionless quantity called the gain, which characterizes the degree of localization of the wave function near the nucleus; i.e., the gain is the density ratio of the actual wave function on the nucleus to the wave function envelope at the same site. The gain for the regions where the envelope wave function varies slowly (in accordance with EM theory and disregarding interference effects) can be expressed through a dimensionless quantity $\eta \equiv |u_j(\mathbf{r}_l)|^2/\langle u_j(\mathbf{r})\rangle_{\text{av}}^2$, where the denominator contains the cell-averaged Bloch function. This quantity is independent of the lattice site occupied by an atom but is dependent on the type of atom involved, Si or C.

As seen from Table 1, the donor level energies for 3*C*-SiC and for the hexagonal positions are comparable to the energies calculated in the EM approximation, whereas the levels for the *k* positions are substantially in excess of these values. The level depth should correlate with the spatial distribution of the wave functions of donor (or acceptor) electrons, which is evident, for instance, for the nitrogen donors in silicon or shallow boron acceptors in SiC. Introducing the dimensionless ratio of the level depth to the band width, we see that the electron localization within the first coordination shell correlates fairly well with this ratio. The degree of localization of the nitrogen donor electron in silicon within the first shell is ~80%, and the relative level depth is ~0.25, while for the shallow boron acceptor in SiC the degree of localization of the unpaired electron within the first shell is about ~40% and the relative level depth is ~0.12. Thus, judging from the level depths for the *k* positions, the degree of electron localization within the first coordination shell may be significant, about 5%, and this manifests itself in the resolved HF structure in EPR spectra. The fact that this structure has not thus far been observed in SiC for shallow donor levels in 3*C*-SiC and for hexagonal positions may suggest that the wave function distribution of donor electrons in these cases differs substantially from that of donors in quasi-cubic positions and, therefore, the EPR HF structure in this case is not resolved.

There are three major factors determining HF interactions for shallow donors in Group IV crystals, which are indirect-gap semiconductors: (i) smoothly decreasing modulation of HF interactions with increasing distance from the donor [in the effective mass approximation, this modulation is described by the envelope function $F(r)$]; (ii) the spin density localization on atoms, which is characterized by dimensionless gain coefficients and depends on the actual kind of atom and crystal involved; and (iii) interference effects [1, 4, 12] originating from the existence of several valleys in these semiconductors [the interference destroys the smooth falloff of HF interactions on atoms or groups of atoms with distance, which is described by the function $F(r)$]. Incidentally, this interference effect considerably complicates the interpretation of EPR and ENDOR spectra in indirect-gap semiconductors, unlike in direct-gap semiconductors (ZnO, AgCl, AgBr), in which HF and SHF interactions have been assigned with a high degree of confidence [21–23].

The isotropic structure for nitrogen donors in positions *k* due to the HF interaction with one Si atom, which is directly observed in EPR spectra, is 1.46 mT (41 MHz) and 0.96 mT (26.9 MHz) in 4*H*-SiC and 6*H*-SiC crystals, respectively. The isotropic HF splitting caused by interaction with four or five carbon atoms, which is also observed directly in the EPR spectra of these donors (incidentally, this splitting becomes clearly pronounced only in ^{29}Si-depleted crystals, where the EPR line narrows), is 0.6 mT (16.8 MHz) and 0.5 mT (14 MHz) in 4*H*-SiC and 6*H*-SiC, respectively. The observed isotropic HF interactions make it possible to estimate the unpaired-electron density in the *s* orbitals of Si and C and, thus, calculate the degree of electron localization in these orbitals. The corresponding degrees of localization of the unpaired electron (spin density) on one Si atom in 4*H*-SiC and 6*H*-SiC are 0.89 and 0.6%, respectively, and those on each of the four or five C atoms in 4*H*-SiC and 6*H*-SiC are 0.44 and 0.37%, respectively. Significantly, the spin density ratio on one Si atom for the 4*H*-SiC and 6*H*-SiC polytypes, which is 1.5, coincides, to within experimental error, with that on the nitrogen atom (Table 1). This suggests that N centers in positions *k* in 4*H*-SiC and 6*H*-SiC have identical structure and that one Si atom occupies the position closest to the N atom; the wave function density decreases smoothly to about one-third its value as we go from N to Si. The spin density ratio on each of the C atoms of the 4*H*-SiC and 6*H*-SiC polytypes, which is 1.2, is noticeably smaller than that on the N atom, which implies that these atoms are located farther away from the nitrogen atom. Thus, the results of our study support the conclusion that nitrogen in positions *k* substitutes for C. It stands to reason that the degree of localization on the remaining three nearest Si atoms is of the same order of magnitude as that on one Si atom, for which isotropic HF splitting in the EPR spectrum was observed. Quite possibly, localization will take place in the *s* and *p* orbitals, thus implying that the HF interaction with the three Si atoms of the first coordination shell may be anisotropic, which would account for its being not resolved in EPR spectra, because the isotropic HF interaction constant should decrease strongly if even a small part of the unpaired electron distribution extends to the *p* orbital. Thus, in 4*H*-SiC, the total degree of localization of the unpaired electron on the central N atom and in the first coordination shell (containing four Si atoms) should be 6.4%. We should add to this 2.2% for the assumed five C atoms of the second shell. Thus, the total spin density within the first two

coordination shells is approximately 8.5%. For 6*H*-SiC, the respective quantities should be 4.24 and 1.85%, adding up to 6.1%. These values should be added to those obtained in an ENDOR study [12], which, according to the new data, correspond to the HF interactions for the nitrogen *k* positions located beyond the first or second coordination shell.

Because the EPR linewidths reflect the density distribution of the unpaired electron of the shallow donor over more remote coordination shells in the case of positions *k* in SiC (probably starting with the third shell), to which the EM approximation applies, we consider the HF interactions with these coordination shells in more detail. According to Eq. (2), the ratio of the shallow-donor EPR linewidth in a silicon crystal depleted in the ^{29}Si isotope to that in a natural isotope abundance crystal is equal to the square root of the ratio of the percentage contents of this isotope. Thus, the phosphorus EPR line narrowing in ^{30}Si by a factor of 4.3 observed in our experiments corresponds to a nearly 20-fold decrease in ^{29}Si content. A similar effect of EPR line narrowing was revealed for As donors in ^{30}Si silicon.

In the case of SiC, the EPR linewidth ratio for shallow donors has a more complex pattern because of the presence of two types of atoms, Si and C. The actual value of this ratio depends on the contribution of the HF interaction with the ^{29}Si and ^{13}C nuclei to the linewidth. Assuming the linewidth to be completely determined by the HF interaction with ^{13}C, the linewidth ratio for 6*H*-SiC enriched in ^{13}C to 25% to that of a crystal with natural isotopic abundance is calculated to be $(0.25/0.011)^{1/2} = 4.8$ and the EPR linewidth should be (based on the experimental linewidth in a natural-abundance crystal (Table 2)) 0.62 mT. The analogous ratio for 4*H*-SiC enriched in ^{13}C to 15% is $(0.15/0.011)^{1/2} = 3.7$, and the EPR linewidth should be 0.78 mT. Assuming now that the linewidth derives fully from the HF interaction with ^{29}Si, calculating the linewidth ratio for 6*H*-SiC with 0.5% ^{29}Si (the crystal is enriched in ^{28}Si) to a natural-abundance crystal yields $(0.005/0.047)^{1/2} = 0.33$; so the EPR linewidth should be 0.04 mT. Similarly, the EPR linewidth for 4*H*-SiC can be found to be 0.07 mT.

A comparison of these figures with experiment (Table 2) shows that the first case (where the linewidth is fully determined by the HF interaction with ^{13}C) very nearly corresponds to the 6*H*-SiC polytype, whereas the second case should be identified with 4*H*-SiC, where the linewidth is primarily determined by the HF interaction with ^{29}Si. An increase in the ^{13}C content in the 6*H*-SiC polytype by approximately 20 times broadens the EPR linewidth nearly fourfold, while a decrease in the ^{29}Si content by approximately 10 times has practically no effect on the linewidth. By contrast, in 4*H*-SiC, a similar decrease in ^{29}Si content resulted in EPR line narrowing to one-third its previous width, with no noticeable broadening produced by a substantial increase in the ^{13}C content. Thus, our EPR study suggests the conclusion that the nitrogen-donor unpaired electron wave function distributions in the 4*H*-SiC and 6*H*-SiC polytypes are substantially different. In 4*H*-SiC, the wave function is primarily localized on silicon atoms, while in the 6*H*-SiC polytype it is localized mainly on carbon. This conclusion is in agreement with ENDOR studies [12], which also revealed a marked difference in the spatial distribution of the shallow N donor wave function between the 4*H*-SiC and 6*H*-SiC polytypes. It was demonstrated that, within the coordination shells the interactions with which account for the EPR linewidth, the unpaired electron is predominantly localized on silicon atoms in 4*H*-SiC and on carbon atoms in 6*H*-SiC. Also, the unpaired electron localized on silicon is distributed approximately evenly between the *s* and *p* orbitals, whereas on carbon the unpaired electron occupies predominantly the *s* orbitals. In other words, the gain coefficients for Si and C in these polytypes are essentially different. Indeed, judging from the maximum isotropic constants of HF interaction with ^{13}C, which in 4*H*-SiC and 6*H*-SiC are 5.02 and 10.75 MHz (k_2), respectively [12], the gain coefficient for carbon in 6*H*-SiC is approximately twofold that for 4*H*-SiC. However, the distribution of the unpaired electron on silicon *s* orbitals reveals the reverse; namely, the HF interaction constants are 6.54 and 3.86 MHz for 4*H*-SiC and 6*H*-SiC, respectively. This means that the gain coefficient for the isotropic spin density distribution on silicon in 4*H*-SiC is about 1.7 times that in 6*H*-SiC. Note that a similar gain coefficient for the unpaired electron distribution over the *p* orbitals cannot be introduced, because one can speak here only about the density of the envelope wave function on the Si or C nuclei. Nevertheless, one has to bear in mind that, while in the 4*H*-SiC and 6*H*-SiC polytypes the unpaired electron density in the *p* orbitals of C is small and about the same, the maximum constant of anisotropic SHF interaction *b* in the *p* orbitals of Si in 4*H*-SiC (1.26 MHz [12]) exceeds that for 6*H*-SiC by about 30 times.

It should be stressed that we do not compare the HF interaction constants for the first two coordination shells, for which EPR spectra revealed a split structure. These quantities have practically no bearing on the properties of the donor electron that are described by EM theory and are characteristic of a band electron. These constants determine the depth of a state, and, for comparatively deep states, the difference between the polytypes, as a rule, disappears. Indeed, the properties of shallow boron acceptors, whose depth is only twice that of nitrogen donors in the *k* positions, are practically independent of polytype.

It appeared of interest to calculate the EPR linewidth of shallow nitrogen donors with Eq. (2) using ENDOR data from [12]. Like the shallow donors in silicon, where about 80% of the linewidth is governed by the interaction with the lattice nuclei residing within a few coordination shells (in silicon, the first four coordi-

nation shells [4]), the linewidth is determined by the maximum unresolved HF interactions. Therefore, in our calculations, we included only the coordination shells for which the isotropic HF interactions exceeded 1 MHz. The number of atoms in each shell was assumed to be equal to six for both carbon and silicon. In EPR linewidth calculations for positions *k*, the HF interactions with the first two coordination shells (for which the HF structure in the EPR spectra was resolved) were disregarded. The results of calculations for positions *k* (position k_1 in 6*H*-SiC) are presented in Table 2. The experimentally observed EPR linewidths are seen to compare well to the calculations.

Table 1 lists the ionization energies of shallow N donors in the three SiC polytypes. Analogous parameters for shallow P and As donors in Si are also given for the sake of comparison. Examining the table reveals that the ionization energies for shallow N donors do not correlate directly with the constants of HF interaction with the nitrogen nucleus. The main feature that can be discerned for both 4*H*-SiC and 6*H*-SiC is that the isotropic HF interaction for the *h* positions, $A_S(h)$, is weaker than that for positions *k*, $A_S(k)$. The ratio $A_S(k)/A_S(h)$ is 17.6 and ~13 for 4*H*-SiC and 6*H*-SiC, respectively (the value of A_S for 6*H*-SiC is taken as the average over two *k* positions). For the anisotropic HF interaction constants A_P, the opposite situation occurs: the ratio $A_P(h)/A_P(k)$ is about ~20 for both polytypes. Thus, the wave function on the N atom for quasi-cubic positions is primarily *s*-type, whereas for the hexagonal positions this function has a 50% admixture of the *p* orbital. As seen from Table 1, the isotropic HF interaction constant for N donors in 3*C*-SiC is approximately as small as that for the *h* positions in the hexagonal polytypes. The only feature that is common for all these cases is a small valley–orbit splitting, which constitutes in the three cases only 15% of the level depth, whereas this quantity is in excess of 50% for the *k* positions in the 4*H*-SiC and 6*H*-SiC polytypes. Thus, it is quite probable that the admixture of the excited state in which the isotropic HF interaction is zero brings about a strong decrease of this interaction in the lowest ground state. Nevertheless, in all cases, the degree of donor electron localization on nitrogen is within 0.19–2.81%, which is comparable to that in silicon. To the best of our knowledge, only shallow lithium donors in silicon, which are interstitials, have an inverted energy level structure [24]; so the constant of HF interaction with the lithium atom approaches zero at low temperatures and increases with temperature. Because SiC did not reveal an increase in the isotropic constants of HF interaction with nitrogen in any of the above cases of weak isotropic HF interaction [25], one may safely conclude that the ground state here is the A_1 singlet. The closely lying excited states, however, give rise to a substantial decrease in the HF interaction constants. A pronounced part is quite probably played here by interference effects caused by the complex nature of the conduction band, which can manifest themselves particularly strongly if the donor atom is displaced from its equilibrium position along the *c* axis for the hexagonal positions in the 4*H*- and 6*H*-SiC polytypes.

As indicated above, the EPR spectra obtained for nitrogen *k* positions in the 4*H*-SiC and 6*H*-SiC polytypes revealed satellites with different but very nearly isotropic splittings, which can be identified, judging from their relative intensities with respect to the central EPR line, with the HF interactions with one silicon atom and four or five carbon atoms. All these interaction constants are substantially larger than the EPR lines and, thus, do not contribute to the EPR linewidth, except for ^{13}C-enriched crystals, where they significantly change the line shape by enhancing the wing intensity. Nevertheless, the EPR linewidth is determined primarily by the weaker HF interactions. One may thus suggest that the HF interactions with the first two Si and C shells are resolved for the *k* positions in 4*H*-SiC and 6*H*-SiC and that the EPR linewidth derives from the HF interactions with more remote shells, starting from the third. This situation is similar in some respect to the case of shallow boron acceptors, where the HF structure is resolved for the interactions with one C atom and three Si atoms. This problem, however, can probably be solved by studying ^{29}Si-enriched SiC crystals.

It appears only natural to compare now the properties of nitrogen donors in SiC with those in carbon (diamond) and silicon crystals. Nitrogen donors were first studied by EPR in diamond [26] and silicon [27, 28]. In both cases, the nitrogen donors had deep levels and their structure differed strongly from that of other donors in silicon belonging to Group V of the periodic table (P, As, Sb), which have shallow levels and whose electronic properties can be described in terms of the effective-mass approximation. EPR measurements show that nitrogen centers in diamond and silicon undergo strong trigonal distortions along one of the four ⟨111⟩ axes, which is caused by the nitrogen being in an off-center position. The donor electron occupies an antibonding orbital and is localized partially on the nitrogen atom in a substitutional position and partially on one of the four nearest neighbor carbon (in diamond) or Si (in silicon) atoms. In diamond, the unpaired donor electron is localized to 54.9% on one carbon atom (6% in the *s* orbital and 94% in the *p* orbital) and to 34% on the nitrogen atom (19% in the *s* orbital and 81% in the *p* orbital) and the donor level is ~2-eV deep. In silicon, the unpaired donor electron is localized to 72% on one Si atom (12% in the *s* orbital and 88% in the *p* orbital) and only to 9% on the nitrogen atom (28% in the *s* orbital and 72% in the *p* orbital) and the donor level depth is ~0.3 eV. A theoretical analysis of the formation of deep donor levels of nitrogen in silicon and diamond was performed in [29–32] and included the Jahn–Teller effect, pseudo-Jahn–Teller effect, and chemical rebonding. Because the issue of the formation of deep

nitrogen donor levels in silicon and diamond still remains unsolved, there has not been, as far as we know, any comparative consideration of the differences in the nitrogen behavior between silicon and diamond, on the one hand, and SiC, on the other.

A radically different situation is observed for nitrogen donors in SiC, which does not compare, even qualitatively, to the behavior of deep donors in Si and C. In SiC, nitrogen produces donors with relatively shallow levels and, most remarkably, no bonds are formed with the nearest lattice atoms and no noticeable lowering of the symmetry occurs, unlike in Si and C crystals. While, in the case of the hexagonal polytypes of SiC, the axial symmetry of the crystal may be suggested to play a certain role (the *g* factor and the hyperfine structure constant exhibit approximately axial symmetry with respect to the crystal *c* axis) and the off-center nitrogen atom in positions *k* may manifest itself, the cubic modification of SiC (3*C*-SiC) has the same symmetry as diamond or silicon. Thus, there are firm grounds for developing a general theory which would account for the radical difference in the behavior of nitrogen donor impurities between silicon and diamond, on the one hand, and SiC, on the other.

5. CONCLUSIONS

We have carried out an EPR study of shallow N donors and shallow B acceptors in SiC and of shallow P and As donors in silicon with a modified isotopic composition of Si and C. A change in the content of the ^{29}Si and ^{13}C isotopes having nonzero nuclear magnetic moments brings about substantial changes in the EPR spectra of shallow N donors and shallow B acceptors in SiC, as well as of shallow P and As donors in silicon. Information has been obtained on the spatial distribution of the shallow-donor and acceptor wave functions in these materials. The present study and published ENDOR measurements revealed that the spatial distribution of the donor electron in SiC depends substantially on the polytype and crystallographic position. Indeed, the unpaired electron in the 4*H*-SiC polytype occupies primarily the Si *s* and *p* orbitals, whereas in 6*H*-SiC it is localized mostly in the C *s* orbitals. The electron distribution of the N donor in the hexagonal position, which has a shallow level close to that calculated for this material in the EM approximation, differs strongly from that of the donor in the *k* position. In the latter case, the donor level is substantially deeper than that predicted from EM theory and the EPR spectrum reveals an HF structure deriving from a comparatively strong interaction with the first two coordination spheres of Si and C, which were identified reliably in measurements on crystals with a modified isotopic composition. Thus, the EM approximation fails near the N atom in the *k* position. Moreover, it can be suggested that the symmetry of the donor structure and of the donor electron distribution become lower, thus giving rise to a comparatively high isotropic spin density on one Si atom that lies on the *c* axis near the N atom in the neighboring carbon position.

The isotropic structure for N donors in the *k* positions caused by the HF interaction with one Si atom, which is observed directly in EPR spectra, is 41 MHz (a spin density of 0.89%) and 26.9 MHz (0.6%) in the 4*H*-SiC and 6*H*-SiC crystals, respectively. The isotropic HF splitting induced by the interaction with four or five C atoms, which is likewise seen directly in the EPR spectra of these donors and manifests itself as an EPR line narrowing in ^{29}Si-depleted crystals, is 16.8 MHz (0.44%) and 14 MHz (0.37%) in 4*H*-SiC and 6*H*-SiC, respectively. The ratio of the spin densities on one Si atom in the 4*H*-SiC and 6*H*-SiC polytypes (which is 1.5) coincides with that on the N atom, thus implying that the structure of N centers in positions *k* of 4*H*-SiC and 6*H*-SiC is qualitatively the same and that the Si atom involved occupies the position nearest to the N atom; the wave function density decreases by a factor of about 3 as one goes from N to Si. The ratio of the spin densities on each of the nearest C atoms in the 4*H*-SiC and 6*H*-SiC polytypes (which is 1.2) is considerably smaller than that on the N atom; i.e., these C atoms occupy more remote positions with respect to the N atom. Thus, the results of our measurements bear out the widespread opinion that N substitutes for C in the *k* position.

The total degree of localization of the unpaired electron on the central N atom and in the first shell of four Si atoms (assuming that the degree of localization on the other three nearest Si atoms is the same as that for one Si atom whose HF structure is resolved in the EPR spectra) is 6.4%, to which we should add 2.2%, the figure corresponding to electron localization on the assumed five C atoms of the second coordination shell. Said otherwise, the spin density within the first two coordination shells adds up to about 8.5%. For 6*H*-SiC, these quantities constitute 4.24 and 1.85%, respectively, adding up to 6.1%. These values should be added to those obtained by ENDOR for N atoms in positions *k* [12], which, according to the new data, should be identified with the HF interactions beyond the first or second shell.

The low-symmetry structure forms for the shallow B acceptor near the impurity [11], with the unpaired electron in the SiC polytypes studied being distributed primarily on the C atoms. Decreasing the ^{29}Si content had practically no effect on the EPR linewidth of the shallow B acceptor, which observation supports the above conclusion.

A decrease in the ^{29}Si content brings about a substantial narrowing of the EPR lines of the shallow P and As donors in silicon and, as a consequence, an increase in the EPR signal intensity, as well as a strong lengthening of the spin–lattice relaxation time T_1. In silicon enriched in ^{30}Si and depleted in ^{29}Si, the time T_1 for the shallow P and As donors is quite long. This offered the possibility of selectively studying these spectra by opti-

cally exciting the desired region of the crystal and thereby shortening T_1 through interaction with carriers and preventing EPR signal saturation, which permits one to observe EPR spectra from this region only. This observation may prove valuable for developing materials for use in quantum computers.

ACKNOWLEDGMENTS

The support of the Russian Foundation for Basic Research (project nos. 02-02-17605, 03-02-17645, 04-02-17632), the program under the Presidium of the Russian Academy of Sciences "Spin-Dependent Effects in Solids and Spintronics," and ISTC (project no. 2630) is gratefully acknowledged.

REFERENCES

1. W. Kohn and J. M. Luttinger, Phys. Rev. **97**, 1721 (1955); Phys. Rev. **98**, 915 (1955).
2. A. F. Kip, C. Kittel, R. A. Levy, and A. M. Portis, Phys. Rev. **91**, 1066 (1953).
3. P. G. Baranov, Yu. P. Veshchunov, and N. G. Romanov, Pis'ma Zh. Éksp. Teor. Fiz. **32** (1), 3 (1980) [JETP Lett. **32** (1), 1 (1980)].
4. G. Feher, Phys. Rev. **114**, 1219 (1959).
5. G. D. Watkins, in *Point Defects in Solids*, Ed. by J. H. Crowford and L. M. Slifkin (Plenum, New York, 1975), Vol. 2, p. 333; G. D. Watkins, in *Deep Centers in Semiconductors*, Ed. by S. T. Pantelides (Gordon and Breach, New York, 1986), p. 147.
6. D. K. Wilson, Phys. Rev. A **134**, 265 (1964).
7. G. Feher, J. C. Hensel, and E. A. Gere, Phys. Rev. Lett. **5**, 309 (1960).
8. H. H. Woodbury and G. W. Ludwig, Phys. Rev. **124**, 1083 (1961).
9. A. G. Zubatov, I. M. Zaritskiĭ, S. N. Lukin, E. N. Mokhov, and V. G. Stepanov, Fiz. Tverd. Tela (Leningrad) **27**, 322 (1985) [Sov. Phys. Solid State **27**, 197 (1985)].
10. J. L. Ivey and R. L. Mieher, Phys. Rev. B: Solid State **11**, 849 (1975).
11. A. van Duijn-Arnold, J. Mol, R. Verberk, J. Schmidt, E. N. Mokhov, and P. G. Baranov, Phys. Rev. B: Condens. Matter **60**, 15 829 (1999).
12. A. van Duijn-Arnold, R. Zondervan, J. Schmidt, P. G. Baranov, and E. N. Mokhov, Phys. Rev. B: Condens. Matter **64**, 085 206 (2001).
13. E. N. Kalabukhova, S. N. Lukin, and W. C. Mitchel, Mater. Sci. Forum **433–436**, 499 (2003).
14. N. T. Son, J. Isoya, S. Yamasaki, and E. Janzen, in *Book of Abstracts of the 5th European Conference on Silicon Carbide and Related Materials, Bologna, Italy, 2004* (CNR–IMM, Area Della Ricerca, Bologna, 2004).
15. P. G. Baranov, A. N. Ionov, I. V. Il'in, P. S. Kop'ev, E. N. Mokhov, and V. A. Khramtsov, Fiz. Tverd. Tela (St. Petersburg) **45**, 984 (2003) [Phys. Solid State **45**, 1030 (2003)].
16. Yu. A. Vodakov, E. N. Mokhov, G. Ramm, and A. D. Roenkov, Krist. Tech. **14**, 729 (1979).
17. O. N. Godison, A. K. Kaliteevskiĭ, V. I. Korolev, B. Y. Ber, V. Y. Davydov, M. A. Kaliteevskii, and P. S. Kop'ev, Fiz. Tekh. Poluprovodn. (St. Petersburg) **35**, 913 (2001) [Semiconductors **35**, 877 (2001)].
18. S. Greulich-Weber, Phys. Status Solidi A **162**, 95 (1997).
19. C. F. Young, K. Xie, E. H. Poindexter, G. J. Gerardi, and D. J. Keeble, Appl. Phys. Lett. **70**, 1858 (1997).
20. G. Feher and E. A. Gere, Phys. Rev. **114**, 1245 (1959).
21. M. T. Bennenbroek, A. Arnold, O. G. Poluektov, P. G. Baranov, and J. Schmidt, Phys. Rev. B: Condens. Matter **54**, 11 276 (1996).
22. D. M. Hofmann, A. Hofstaetter, F. Leiter, H. Zhou, F. Henecker, B. K. Meyer, S. B. Orlinskii, J. Schmidt, and P. G. Baranov, Phys. Rev. Lett. **88**, 045504 (2002).
23. H. Overhof and U. Gerstmann, Phys. Rev. B: Condens. Matter **62**, 12 585 (2000).
24. G. D. Watkins and Frank S. Ham, Phys. Rev. B: Solid State **1**, 4071 (1970).
25. E. N. Kalabukhova, in *Radiospectroscopy of Condensed Media*, Ed. by M. D. Glinchuk (Institute of Semiconductor Physics, National Academy of Sciences of Ukraine, Kiev, 2000), Chap. II, p. 157 [in Russian].
26. W. V. Smith, P. P. Sorokin, I. L. Gelles, and G. J. Lasher, Phys. Rev. **115**, 1546 (1959).
27. Keith L. Brower, Phys. Rev. Lett. **44**, 1627 (1980).
28. K. Murakami, H. Kuribayashi, and K. Masuda, Phys. Rev. B: Condens. Matter **38**, 1589 (1988).
29. R. P. Messmer and G. D. Watkins, Phys. Rev. B: Solid State **7**, 2568 (1973).
30. G. G. DeLeo, W. B. Fowler, and G. D. Watkins, Phys. Rev. B: Condens. Matter **29**, 3193 (1984).
31. S. T. Pantelides, W. A. Harrison, and F. Yndurain, Phys. Rev. B: Condens. Matter **34**, 6038 (1986).
32. F. G. Anderson, Phys. Rev. B: Condens. Matter **39**, 5392 (1989).

Translated by G. Skrebtsov

Physics of the Solid State, Vol. 47, No. 12, 2005, pp. 2233–2236. Translated from Fizika Tverdogo Tela, Vol. 47, No. 12, 2005, pp. 2142–2145.

SEMICONDUCTORS AND DIELECTRICS

The Poole–Frenkel Effect with Allowance for Multiphonon Deep-Center Ionization in Amorphous Silicon Nitride

Yu. N. Novikov

Institute for Semiconductor Physics, Siberian Division, Russian Academy of Sciences, pr. Akademika Lavrent'eva 13, Novosibirsk, 630090 Russia

e-mail: nov@isp.nsc.ru

Received January 25, 2005

Abstract—The Poole–Frenkel mechanism, both with and without allowance for multiphonon ionization of deep centers, was used to describe the conductivity of amorphous silicon nitride. The dependence of the frequency factor on electron–phonon coupling strength was considered. Taking into account the weak electron–phonon coupling in deep centers, the value of the frequency factor was found to be $\nu \approx 10^{15}$ s^{-1}, which is consistent with the estimates made by Frenkel. © *2005 Pleiades Publishing, Inc.*

Amorphous silicon nitride Si_3N_4 exhibits a memory effect, i.e., the ability to localize injected carriers for ~10 years at 300 K. This property of Si_3N_4 underlies the operation of electrically reprogrammable ROM devices. However, the charge state of the trap responsible for the memory effect in Si_3N_4 remains an open problem. Two types of traps are currently being discussed in the literature, namely, Coulomb (attractive, repulsive) and neutral (centers with a zero-radius potential) traps. The mechanism of ionization of attractive centers at high temperatures in weak electric fields is governed by the Poole–Frenkel effect and multiphonon phenomena [1, 2]. The mechanism of neutral-center ionization under the same conditions is determined by multiphonon phenomena [2]. The Poole–Frenkel effect consists essentially in a lowering of the thermal ionization energy of Coulomb attractive centers induced by an external electric field.

The fact that the traps are indeed of the Coulomb type and that the Poole–Frenkel effect can occur in Si_3N_4 is argued for by the following evidence: (i) some researchers have observed current–voltage characteristics in Si_3N_4 [3–6] that become linear when plotted in the log$J$ vs $\bar{E}^{1/2}$ coordinates (J is the current through the sample, $\bar{E}$ is the average electric field strength), and (ii) the trapping cross section is $\sim 5 \times 10^{-13}$ cm^2, which suggests Coulomb interaction of electrons and holes with deep centers in Si_3N_4 [7–9].

However, some attempts at describing experimental data in terms of the Poole–Frenkel mechanism have yielded an anomalously small frequency factor, $\nu \sim 10^5$–10^8 s^{-1}, and a low trap ionization energy, $W \sim 1.2$ eV [10–15]. Frenkel [1] estimated the magnitude of the frequency factor to be $\nu \approx W/\hbar \approx 10^{15}$ s^{-1}, where $\hbar$ is the Planck constant. In addition, a shallow trap with $W \sim 1.2$ eV, with no allowance made for electron–phonon coupling, is not capable of accounting for the long (~10 years) charge retention times in a localized state. This motivated our attempt to study, both experimentally and theoretically, the conductivity in silicon nitride drawing on the Poole–Frenkel effect and invoking the theory of multiphonon ionization.

According to Frenkel [1], the probability of ionization per unit time can be written as

$$P_{PF}(E, T) = \nu \exp\left(-\frac{W - \beta\sqrt{E}}{kT}\right), \qquad (1)$$

where E is the electric field strength, $\beta = \sqrt{e^3/\pi\varepsilon_\infty\varepsilon_0}$ is the Frenkel constant, k is the Boltzmann constant, $\varepsilon_\infty = 4.0$ is the high-frequency dielectric permittivity of Si_3N_4, ε_0 is the electric constant, and e is the electronic charge.

The Frenkel effect occurs in relatively weak electric fields, where the barrier is lowered by an amount less than the Coulomb energy scale in silicon nitride. The value of $\beta\sqrt{E}$ should not exceed the effective electron energy in the trap Coulomb potential [2] (the Rydberg energy), i.e., $\beta\sqrt{E} < e^4m/2\varepsilon_\infty\hbar^2$, where m is the electron mass. Estimates show that these conditions are satisfied if $E < 4 \times 10^6$ V/cm. Our studies were performed in this electric field range.

We studied charge transfer in a metal–nitride–oxide–semiconductor (MNOS) structure. Samples of MNOS structures were prepared on a Czochralski-grown *n*-type silicon substrate with an electrical resistivity of 7.5 Ω cm. A thin, 1.8-nm-thick tunneling-transparent oxide was grown at 750°C. A 53-nm-thick silicon nitride layer was deposited at 760°C in a low-pressure reactor. The SiH_2Cl_2/NH_3 ratio was 0.1. Alu-

1063-7834/05/4712-2233$26.00

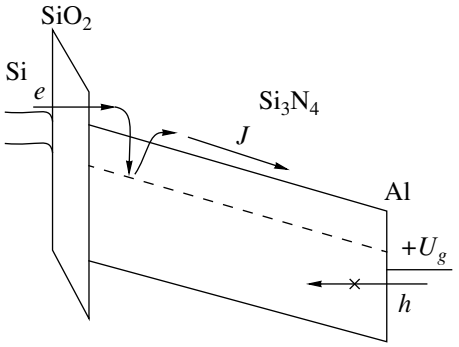

Fig. 1. Energy diagram for the monopolar conductivity model of an MNOS structure with a positive potential applied to the aluminum electrode.

minum electrodes 5×10^{-3} cm^2 in area were deposited through a mask.

We considered only the stationary conductivity that involves electrons ejected from the silicon substrate, with aluminum maintained at a positive potential (Fig. 1). Consideration of monopolar conductivity (due to electrons) appears appropriate in this case, because the tunneling oxide enhances electron injection from the silicon substrate; the injection of holes from aluminum is small [6] because of a high barrier (2.5 eV) for holes existing at the Al/Si_3N_4 interface [16]. Charge transfer is described with the one-dimensional one-band Shockley–Read–Hall equation

$$\frac{\partial n_t(x,t)}{\partial t} = \frac{\sigma J}{e}(N_t - n_t(x,t)) - n_t(x,t)P_{\mathrm{PF}}(x,t) \quad (2)$$

and the Poisson equation [10–13, 17] taking into account the nonuniform electric field distribution in the silicon nitride

$$\frac{\partial E(x,t)}{\partial x} = -\frac{e n_t(x,t)}{\varepsilon_N \varepsilon_0}, \quad (3)$$

where σ is the trapping cross section ($\sigma = 5 \times 10^{-13}$ cm^2 [7–14]), N_t is the trap concentration ($N_t = 3 \times 10^{19}$ cm^{-3} [8–10]), n_t is the concentration of filled traps, $\varepsilon_N = 7.5$ is the low-frequency dielectric permittivity of Si_3N_4, and J is the current density.

To describe the conductivity of silicon nitride, some authors solve Eqs. (2) and (3) self-consistently [10–14]. The injection current at the interface is calculated, as a rule, assuming the Fowler–Nordheim mechanism. This requires knowledge of parameters such as the tunneling mass and barrier height.

We invoked here another approach proposed in [17]. In a steady state, the time derivative in Eq. (2) vanishes

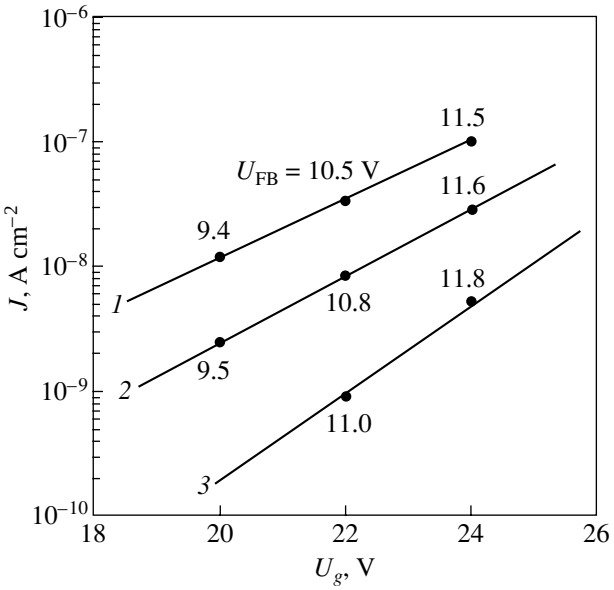

Fig. 2. Experimental steady-state current–voltage characteristics measured at (*1*) 423, (*2*) 380, and (*3*) 327 K. Adjoining the points are flat-band voltages U_{FB}.

and $n_t(E,T) = N_t\left(1 + \frac{e}{J\sigma}P_{\mathrm{PF}}(E,T)\right)^{-1}$. From the Poisson equation (3), one can obtain [17]

$$\int_{E(0)}^{E(D_N)} \frac{dE}{n_t(E,T)} = \frac{D_N e}{\varepsilon_N \varepsilon_0}, \quad (4)$$

$$\int_{E(0)}^{E(D_N)} \frac{E\,dE}{n_t(E,T)} = \frac{U_g^* e}{\varepsilon_N \varepsilon_0}, \quad (5)$$

where D_N is the thickness of Si_3N_4, $U_g^* = U_g - E_{\mathrm{ox}}D_{\mathrm{ox}}$ is the voltage drop across Si_3N_4, U_g is the voltage across the MNOS structure, E_{ox} is the electric field in the tunneling thin SiO_2 layer of thickness D_{ox}, and $E(D_N)$ is the field at the Si_3N_4/Al interface. The electric field at the SiO_2/Si_3N_4 interface in silicon nitride is given by $E(0) = E_{\mathrm{ox}}\varepsilon_{\mathrm{ox}}/\varepsilon_N = \varepsilon_{\mathrm{ox}}(U_g - U_{\mathrm{FB}})/L_{\mathrm{ox}}\varepsilon_N$ [12, 13], where $L_{\mathrm{ox}} = D_{\mathrm{ox}} + \varepsilon_{\mathrm{ox}}D_N/\varepsilon_N$ and U_{FB} is the flat-band voltage. The voltage drop across the semiconductor was neglected, because electrons are injected from the *n* semiconductor in an enriched state (Fig. 1).

The quantities measured experimentally on the MNOS structure at a given voltage U_g and temperature T were the current density J and the flat-band voltage U_{FB} (Fig. 2). Thus, experiment yielded U_g^*, J, and $E(0)$. Equations (4) and (5) are left with the unknowns W, ν, and $E(D_N)$. By setting W, one can find $E(D_N)$ and ν [17], and this was done here. We integrated Eqs. (4) and (5) numerically (using the trapezium rule) for the points in

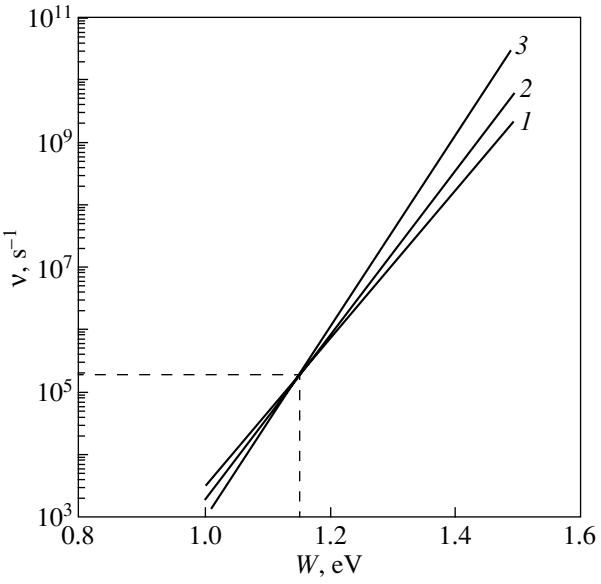

Fig. 3. Frequency factor vs trap ionization energy relations calculated for the experimental points from Fig. 2 at various values of T: (*1*) 423, (*2*) 380, and (*3*) 327 K.

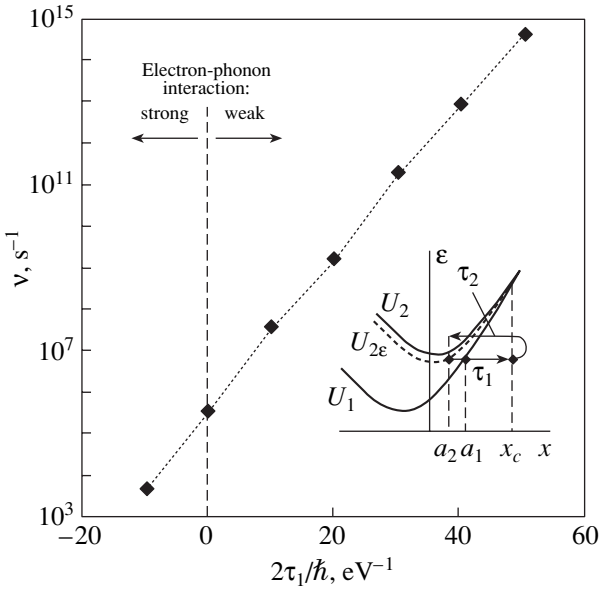

Fig. 4. Frequency factor characterizing the Poole–Frenkel effect as a function of the electron–phonon coupling strength. The inset shows a configuration diagram for the case of weak electron–phonon coupling (U_1, U_2, and $U_{2\varepsilon}$ are the adiabatic potentials for a defect with a trapped electron, without an electron, and without an electron in an electric field, respectively; a_1, a_2 are turning points; x_c is the term crossing point).

Fig. 2. The calculated ν(W) dependence is shown in Fig. 3.

This dependence can be qualitatively expressed as $\ln(\nu(W)) = \ln(P(E, T) - \beta\sqrt{E}/kT) + W/kT$, which follows from Eq. (1). The ν(W) lines plotted for different temperatures have different slopes. The ratio of $\nu_1(W_k)$ to $\nu_2(W_k)$ was found to be ≈1.04 (W_k is a fixed point in Fig. 3), which is close to unity. Therefore, the ν(W) graphs in Fig. 3 plotted for different electric fields at T = const practically coincided. Note that substitution of the found values of W, ν, and $E(D_N)$ and of the values of J, U_g^*, and $E(0)$ derived from experiment for each point in Fig. 2 into the nonlinear equations given in [17] yields an identity (with a relative error of <0.1%).

Inspection of Fig. 3 shows that all the ν(W) relations drawn in the scale chosen cross at the same point. Assuming that the trap ionization energy and the frequency factor do not change with temperature and local electric field strength in Si_3N_4, we see that this cross point corresponds to W = 1.15 eV and $\nu = 2 \times 10^5$ s^{-1}. The values of W and ν thus found are close to those quoted in [10–15].

It was shown in [2, 18] that taking into account multiphonon ionization for Coulomb centers should result in $1/kT$ in Eq. (1) being replaced by

$$\frac{1}{kT^*} = \frac{1}{kT} \pm \frac{2\tau_1}{\hbar} = \frac{2\tau_2}{\hbar}, \qquad (6)$$

where T^* is an effective temperature and τ_1 and τ_2 [2, 18] define, in configuration space, the defect tunneling times under the corresponding adiabatic potentials (see inset to Fig. 4). The plus sign corresponds to weak electron–phonon coupling, and the minus sign, to strong coupling.

Calculations carried out using the effective temperature T^* in place of T revealed that strengthening of the electron–phonon coupling leads to a decrease in the frequency factor and its weakening, to an increase in this factor (Fig. 4). The trap energy remains constant, $W \approx$ 1.15 eV. The same conclusion can be drawn qualitatively from a study of the slope of ln(ν(W)) relations described by Eq. (1). For $2\tau_1/\hbar \sim 50$ eV^{-1}, we obtain $\tau_1 = 1.6 \times 10^{-14}$ s and the corresponding frequency factor $\nu \sim 10^{15}$ s^{-1}. Note that the tunneling time τ_1 obtained in this way is comparable in order of magnitude to τ_1 found for deep impurities with a weak electron–phonon coupling in germanium, Ge : Au and Ge : Hg, where $\tau_1 = 4.1 \times 10^{-14}$ s [2].

Let us estimate the charge retention time t_{ret} in an MNOS structure with weak electron–phonon coupling using the relation $t_{ret} = \nu^{-1}\exp((W - \beta\sqrt{E})/kT^*)$ from [11]. For $E = 2 \times 10^6$ V/cm, T = 300 K, $2\tau_1/\hbar \sim 50$ eV^{-1}, $\nu \sim 10^{15}$ s^{-1}, and W = 1.15 eV, we obtain $t_{ret} \sim 4 \times 10^8$ s ~ 10 years.

Thus, we come to the conclusion that a trap with a captured electron in Si_3N_4 should be only weakly coupled with lattice vibrations. It is possible that a fairly shallow trap with $W \sim 1$ eV is responsible for the mem-

ory effect in Si_3N_4 (charge retention in a localized state for ~10 years at 300 K).

To sum up, the conductivity of amorphous silicon nitride at high temperatures in weak electric fields is described by the Poole–Frenkel effect. Allowing for multiphonon ionization and weak electron–phonon coupling, we have found that the deep-center ionization energy in Si_3N_4 is 1.15 eV and the frequency factor $\nu \sim 10^{15}$ s^{-1}.

ACKNOWLEDGMENTS

The author is indebted to V.A. Gritsenko and S.S. Shaĭmeev for providing experimental data and for helpful discussions of the work.

Support from the program of the Siberian Division of the Russian Academy of Sciences "Integration" (project no. 116) is gratefully acknowledged.

REFERENCES

1. Ya. I. Frenkel', Zh. Éksp. Teor. Fiz. **8** (12), 1292 (1938).
2. V. N. Abakumov, V. I. Perel', and I. N. Yassievich, *Nonradiative Recombination in Semiconductors* (North-Holland, Amsterdam, 1991; PIYAF Ross. Akad. Nauk, St. Petersburg, 1997).
3. S. M. Sze, J. Appl. Phys. **38** (7), 2951 (1967).
4. B. M. Tao, D. Park, S. N. Mohammad, D. Li, A. E. Botchkerav, and H. Morkoc, Philos. Mag. B **73** (4), 723 (1996).
5. A. S. Ginovker, V. A. Gritsenko, and S. P. Sinitsa, Mikroelektronika **2** (4), 283 (1973).
6. V. A. Gritsenko and E. E. Meerson, Mikroelektronika **17** (6), 532 (1988).
7. P. C. Arnett and B. H. Yun, Appl. Phys. Lett. **26** (3), 94 (1974).
8. C. M. Svensson, J. Appl. Phys. **48** (1), 329 (1977).
9. V. M. Maslovskiĭ, A. P. Nagin, and Yu. R. Chernyshev, Mikroelektronika **14** (3), 239 (1985).
10. K. A. Nasyrov, V. A. Gritsenko, M. K. Kim, H. S. Chae, S. D. Chae, W. I. Ryu, J. H. Sok, J.-W. Lee, and B. M. Kim, IEEE Electron. Device Lett. **23**, 336 (2002).
11. V. A. Gritsenko, E. E. Meerson, I. V. Travkov, and Yu. V. Goltvyanskiĭ, Mikroelektronika **16** (1), 42 (1987).
12. H. Bachhofer, H. Reisinger, E. Bertagnolli, and H. von Philipsborn, J. Appl. Phys. **89** (5), 2791 (2001).
13. S. Manzini, J. Appl. Phys. **62**, 3278 (1987).
14. Ross A. Williams and Moiz M. E. Beguwala, IEEE Trans. Electron. Devices **ED-25**, 1019 (1978).
15. V. A. Gurtov, A. I. Nazarov, and P. A. Raĭkerus, Mikroelektronika **16** (3), 269 (1987).
16. V. A. Gritsenko, E. E. Meerson, and Yu. N. Morokov, Phys. Rev. B: Condens. Matter **57**, R2 081 (1998).
17. P. C. Arnett, J. Appl. Phys. **46** (12), 5236 (1975).
18. V. N. Abakumov, V. Karpus, V. I. Perel', and I. N. Yassievich, Fiz. Tekh. Poluprovodn. (Leningrad) **22** (2), 262 (1988) [Sov. Phys. Semicond. **22**, 159 (1988)].

Translated by G. Skrebtsov

Physics of the Solid State, Vol. 47, No. 12, 2005, pp. 2237–2242. Translated from Fizika Tverdogo Tela, Vol. 47, No. 12, 2005, pp. 2146–2151.

SEMICONDUCTORS AND DIELECTRICS

Optical Properties of a Semiconductor in the Exciton Spectral Region under Exposure to a High-Power Pump Pulse in the *M*-Band Region

P. I. Khadzhi and L. Yu. Nad'kin

Dniester State University, ul. Dvadtsat' Pyatogo Oktyabrya 128, Tiraspol, MD 3300 Moldova
Institute of Applied Physics, Academy of Sciences of Moldova, Academiei str. 5, Chisinau, MD 2800 Moldova
e-mail: tdsu4@idknet.com
Received February 9, 2005

Abstract—The behavior of the dielectric susceptibility of a semiconductor is studied in the case where the exciton state is probed by weak-pulse photons in the presence of a high-power laser pulse in the region of the *M* band of CuCl luminescence. A pronounced Autler–Townes effect for the exciton transition is shown to occur. The absorption peak position is determined by the amplitude and frequency of the pump field. © *2005 Pleiades Publishing, Inc.*

1. INTRODUCTION

The pump–probe technique gained particular significance in experimental studies of the optical properties of semiconductors in the exciton spectral region at high excitation levels. This technique is based on the use of two laser beams: an intense pump beam and a weak probe beam. The weak beam probes the changes in the optical properties of a crystal caused by the intense pump beam.

The pump–probe technique has been applied to study the kinetics of radiative recombination of biexcitons, the nonlinear response of a high-density system of excitons and biexcitons [1–3], and the red and blue shifts of the exciton band under picosecond pump conditions [4–6]. The Autler–Townes effect on biexcitons in CuCl has been studied both experimentally and theoretically [7–9]. In [7], splitting of the biexciton absorption band in CuCl into two lines was observed experimentally at high excitation levels. In this case, biexciton states were probed via two-photon absorption, which causes the excitation of biexcitons from the crystal ground state in the presence of intense pumping in the absorption *M*-band region. From the splitting value, the authors of [7] determined the corresponding transition dipole moment in the *M*-band region. The idea behind this experiment was first proposed in [10].

Various aspects of the pump–probe technique for a high-density system of excitons and biexcitons were considered theoretically in [8–14]. In [14], it was shown that the susceptibilities of the semiconductor in the exciton spectral range exhibit a bistable behavior with variations in the frequency and intensity of a pump pulse if the elastic exciton–exciton interaction is taken into account. This behavior suggests that a weak signal can be amplified. In [8, 9], the dielectric susceptibilities of a CuCl-type crystal were studied in the case where an intense pump pulse corresponds to the *M*-band region and where probing is carried out via two-photon absorption of light with the formation of biexcitons. This raises the question of whether it is possible to probe CuCl-type crystals in the exciton spectral range using single-photon exciton excitation from the crystal ground state while retaining the pump in the *M*-band region. In this case, the model energy spectrum of the semiconductor consists of substantially nonequidistant excitonic and biexcitonic energy levels (Fig. 1). Pump pulse photons can provide only optical exciton–biexciton conversion but cannot be involved in probing due to the large resonance detuning with respect to the exciton transition frequency.

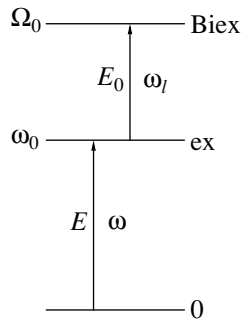

Fig. 1. Excitonic and biexcitonic energy levels in a CuCl-type crystal and quantum transitions under exposure to a pump field E_0 and a probe-pulse field E (schematic).

1063-7834/05/4712-2237$26.00

2. STATEMENT OF THE PROBLEM AND BASIC EQUATIONS

We consider the case where intense monochromatic coherent pulsed laser radiation (pump) with a field amplitude E_0 and a frequency $\omega_l \approx \Omega_0 - \omega_0$ (where Ω_0 and ω_0 are the eigenfrequencies of a biexciton and an exciton state, respectively) and a weak wave (probe pulse) with an amplitude E and a frequency $\omega \approx \omega_0$ are incident onto a CuCl-type semiconductor (Fig. 1). Photons of the former pulse mix the excitonic and biexcitonic states, significantly changing the semiconductor energy spectrum; photons of the latter pulse probe these changes in the exciton transition region. The interaction Hamiltonian of excitons and biexcitons with light in the resonance approximation can be written as

$$\begin{aligned} H &= -\hbar g[E^+ a^+ \exp(-i\omega t) + E^- a \exp(i\omega t)] \\ &- \hbar\sigma[E_0^- a^+ b \exp(i\omega_l t) + E_0^+ a b^+ \exp(-i\omega_l t)], \end{aligned} \quad (1)$$

where a and b are the amplitudes of excitonic and biexcitonic medium polarization waves, respectively; g is the exciton–photon coupling constant; σ is the optical exciton–biexciton conversion constant [15]; and $E_0^+(E^+)$ and $E_0^-(E^-)$ are the positive- and negative-frequency field components, respectively. From Eq. (1), one can easily derive the Heisenberg (material) equations for the amplitudes a and b:

$$\begin{aligned} i\dot{a} &= (\omega_0 - i\gamma_1)a - gE^+ \exp(i\omega t) \\ &- \sigma E_0^- b \exp(i\omega_l t), \end{aligned} \quad (2)$$

$$i\dot{b} = (\Omega_0 - i\gamma_2)b - \sigma E_0^+ a \exp(-i\omega_l t), \quad (3)$$

where γ_1 and γ_2 are phenomenological constants accounting for the damping of excitonic and biexcitonic levels due to scattering processes associated with excitons and biexcitons transferring from the coherent to incoherent modes.

Let us study the system response in all orders of perturbation theory in amplitude E_0 of the pump pulse and in the first order of perturbation theory in amplitude E_0 of the probe pulse field under steady-state conditions. From Eqs. (2) and (3), it is easy to find the steady-state amplitudes a and b and the polarization P and determine the susceptibility χ of the medium:

$$\chi = -\frac{\hbar g^2}{\Delta + i\gamma_1 - \dfrac{\sigma^2 E_0^2}{\Delta + \Delta_l + i\gamma_2}}, \quad (4)$$

where $\Delta = \omega - \omega_0$ and $\Delta_l = \omega_l - \Omega_0 + \omega_0$ are resonance detunings.

In the limit of vanishingly small damping constants, the susceptibility χ is a real function,

$$\chi = -\frac{\hbar g^2(\Delta + \Delta_l)}{\Delta(\Delta + \Delta_l) - \sigma^2 E_0^2}. \quad (5)$$

This susceptibility diverges at two values of the resonance detuning Δ for the weak pulse field, which are given by

$$\Delta_\pm = (-\Delta_l \pm \sqrt{\Delta_l^2 + 4\sigma^2 E_0^2})/2. \quad (6)$$

The detunings $\Delta_\pm$ define new, renormalized eigenfrequencies $\omega_\pm = \omega_0 + \Delta_\pm$ of excitonic states (quasilevels), which arise under exposure to the pump field. The difference between the quasilevel frequencies $\Omega = \omega_+ - \omega_- = \sqrt{\Delta_l^2 + 4\sigma^2 E_0^2}$ (Autler–Townes splitting) determines the optical nutation frequency in the system of excitons and biexcitons in the M-band region [15]. From Eq. (6) and Fig. 2, it is evident that the Autler–Townes splitting increases with the pump field amplitude E_0 and with the magnitude of detuning Δ_l. In the limit where the Rabi frequency σE_0 is much larger than the resonance detuning $|\Delta_l|$, the splitting increases linearly with E_0. In the inverse limit, where $|\Delta_l| \gg \sigma E_0$, we have $\Delta_+ \longrightarrow \sigma^2 E_0^2/\Delta_l$ and $\Delta_- \longrightarrow -\Delta_l$ at $\Delta_l > 0$ and $\Delta_+ \longrightarrow -\Delta_l$ and $\Delta_- \longrightarrow \sigma^2 E_0^2/\Delta_l$ at $\Delta_l < 0$.

We note that, at $\gamma_1, \gamma_2 \longrightarrow 0$, the absorption band of the weak pulse consists of two δ-function peaks at frequencies $\omega = \omega_+$ and $\omega = \omega_-$. Therefore, the curves in Fig. 2 describe the spectral position of absorption band peaks of weak light as functions of the resonance detuning Δ_l and pump-pulse field amplitude E_0.

Using Eq. (5), the dispersion relation $\omega(k)$ of probe-pulse photons in the presence of the pump field can be found to be

$$\frac{c^2 k^2}{\omega^2} = \varepsilon_\infty\left(1 - \omega_{LT}\left(\Delta - \frac{\sigma^2 E_0^2}{\Delta + \Delta_l}\right)^{-1}\right), \quad (7)$$

where ε_∞ is the background permittivity and ω_{LT} is the longitudinal–transverse splitting in the exciton spectral range. All the essential features of the dispersion relation that arise during variation of the pump field amplitude are located in the vicinity of the exciton transition frequency (Fig. 3). The dispersion dependence for photons contains three branches. The middle branch covers the spectral range that is bounded by frequencies ω_+ and ω_- and expands as E_0 increases. The lower and upper dispersion branches tend to the resonance detunings $\Delta_\pm = \omega_+ - \omega_-$ at large values of the wave vector k. As $|\Delta_l|$ increases, the dispersion branches shift to long (short) wavelengths at $\Delta_l > 0$ ($\Delta_l < 0$) (Fig. 3).

Let us introduce the normalized quantities $\delta = \Delta/\gamma_1$, $\delta_l = \Delta_l/\gamma_1$, $s = \gamma_2/\gamma_1$, $f_0 = \sigma E_0/\gamma_1$, and $\chi_0 = \hbar g^2/\gamma_1$. From Eq. (4), we find the real part (dispersion component, χ') and imaginary part (absorption component, χ'') of the susceptibility to be

$$\frac{\chi'}{\chi_0} = -\frac{\left(\delta - (\delta + \delta_l)\dfrac{f_0^2}{(\delta + \delta_l)^2 + s^2}\right)}{\left(\delta - (\delta + \delta_l)\dfrac{f_0^2}{(\delta + \delta_l)^2 + s^2}\right)^2 + \left(1 + s\dfrac{f_0^2}{(\delta + \delta_l)^2 + s^2}\right)^2}, \tag{8}$$

$$\frac{\chi''}{\chi_0} = \frac{\left(1 + s\dfrac{f_0^2}{(\delta + \delta_l)^2 + s^2}\right)}{\left(\delta - (\delta + \delta_l)\dfrac{f_0^2}{(\delta + \delta_l)^2 + s^2}\right)^2 + \left(1 + s\dfrac{f_0^2}{(\delta + \delta_l)^2 + s^2}\right)^2}. \tag{9}$$

3. DISCUSSION

It is evident from Eq. (9) that the absorption component χ'' is positively defined at any value of f_0, δ, and δ_l. This means that a weak signal can only be absorbed. The amplification effect is impossible.

It follows from Eqs. (8) and (9) that the susceptibilities χ' and χ'' are nonlinear functions of the field amplitude f_0 of the intense pump pulse and depend on the frequencies of both pulses, ω and ω_l. At exact resonance between the frequencies of both pulses and the frequencies of the respective transitions ($\omega = \omega_0$, $\omega_l = \Omega_0 - \omega_0$), we have $\chi' = 0$ and

$$\chi''/\chi_0 = (1 + f_0^2/s)^{-1}. \tag{10}$$

We can see that the absorption susceptibility component χ'' at exact resonance saturates rapidly as the pump intensity increases; i.e., the absorption of the weak pulse at the exciton transition frequency is suppressed at high excitation levels by the pump pulse in the *M*-band region.

Let us discuss the behavior of the absorption susceptibility component χ'' (the absorption band of the weak pulse in the exciton spectral range) with variations in the resonance detuning δ in the case where pump pulse photons are in exact resonance with the transition frequency in the *M*-band region ($\delta_l = 0$, $\omega_l = \Omega_0 - \omega_0$). At low excitation levels, the absorption band shape is Lorentzian, $\chi''/\chi_0 = (1 + \delta^2)^{-1}$, with a maximum at $\delta = 0$ (Fig. 4a). As the excitation level f_0 increases, the absorption peak amplitude decreases rapidly according to Eq. (10) and its half-width gradually increases. When the pump field intensity reaches $f_0^2 = s^3/(1 + 2s)$, the spectral shape of the absorption band changes drastically (Fig. 4a): the central peak at $\delta = 0$ transforms into a minimum and there appear two absorption band maxima symmetric with respect to $\delta = 0$ at resonance detunings,

$$\delta_\pm = \pm[(1 + s) f_0\sqrt{f_0^2 + s} - s(f_0^2 + s)]^{1/2}. \tag{11}$$

The spacing between the new absorption peaks increases with the pump field f_0, and their amplitudes

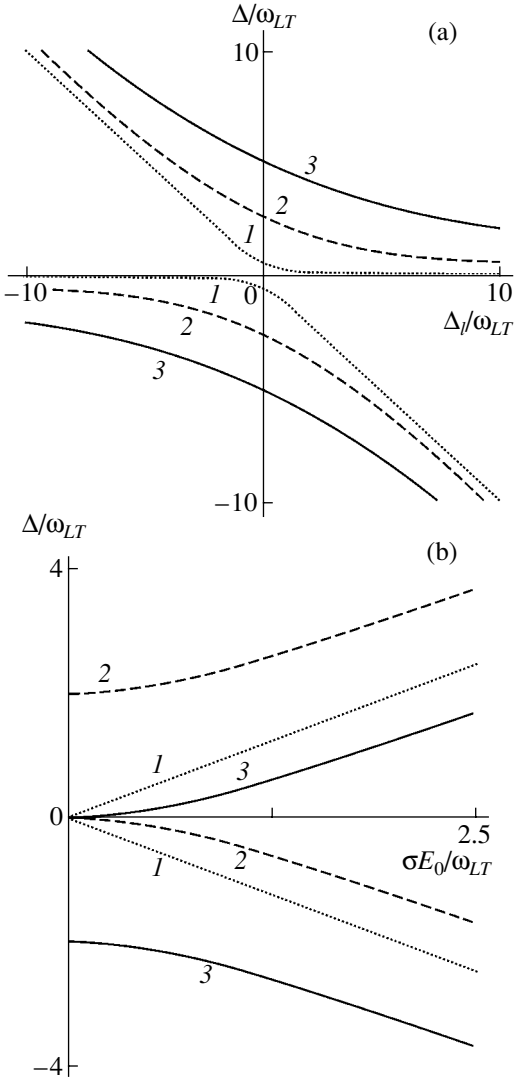

Fig. 2. Dependences of the renormalized frequencies $\omega_\pm - \omega_0 = \Delta_\pm$ of excitonic states (quasilevels) (a) on resonance detunings Δ_l of the pump field at fixed values of the pump field amplitude $\sigma E_0/\omega_{LT}$ equal to (*1*) 0.5, (*2*) 2.5, and (*3*) 5 and (b) on the field amplitude E_0 at various values of resonance detuning Δ_l/ω_{LT} of the pump pulse: (*1*) 0, (*2*) –2, and (*3*) 2.

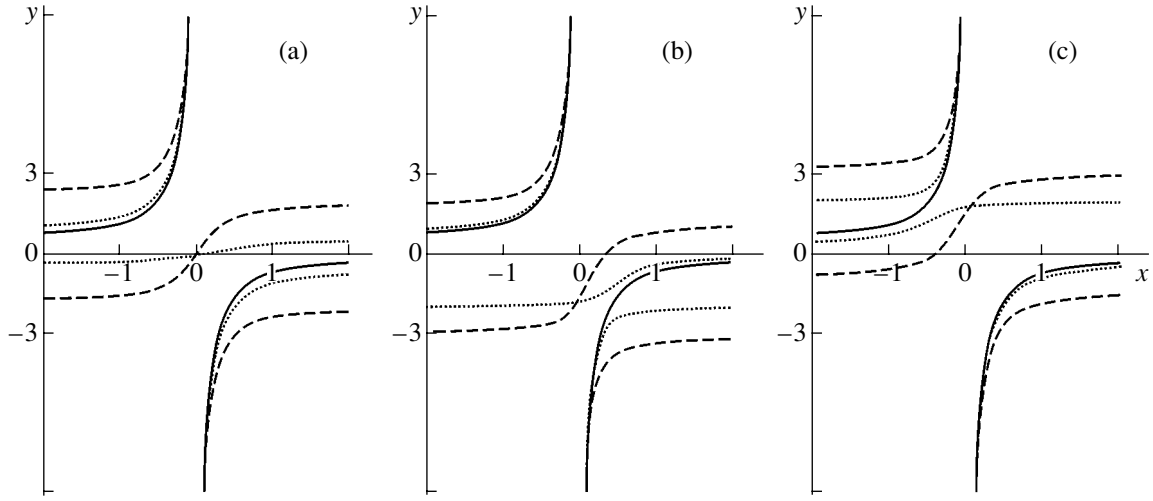

Fig. 3. Polariton-like dispersion relations for weak-pulse photons near the excitonic state with the pump field resonance detuning Δ_l/ω_{LT} equal to (a) 0, (b) –2, and (c) 2 for the pump field $\sigma E_0/\omega_{LT}$ equal to 0.5 (dotted curves) and 5 (dashed curves). The dispersion law of linear exciton polaritons in the absence of a pump field is shown by solid curves. Notation: $x = ck/\sqrt{\varepsilon_\infty}\omega_{LT}$ and $y = \Delta/\omega_{LT}$.

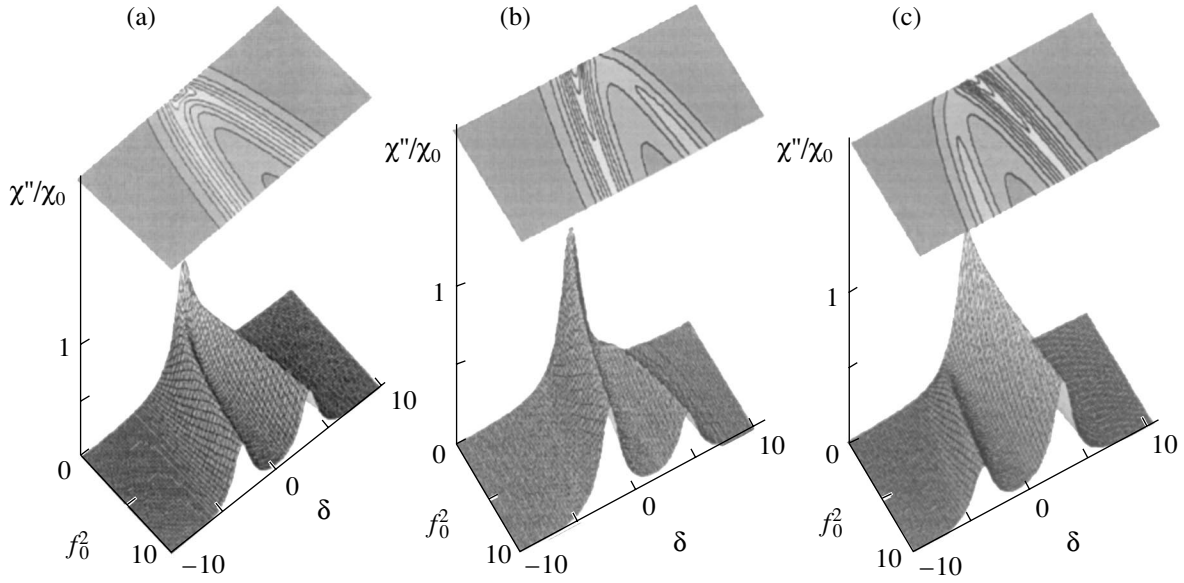

Fig. 4. Absorption component of susceptibility χ" as a function of the resonance detuning δ and of the pump field intensity f_0 at various values of the resonance detuning δ_l of pump pulse photons: (a) 0, (b) –2, and (c) 2.

decrease monotonically (Fig. 4a). The formation of the symmetric maxima and of the minimum is caused by renormalization of the energy spectrum of the semiconductor under exposure to an intense pump pulse. The excitonic level splits into two quasilevels, and their distance from the exciton level position increases monotonically with f_0. At $f_0^2 \gg s$, Eq. (11) yields $\delta_\pm = \pm f_0$, which coincides with Eq. (6) at $\Delta_l = 0$. We can see in Fig. 3 that, at $\delta_l = 0$, the upper and lower polariton branches of the dispersion relation shift symmetrically with respect to the frequency ω_0 of the exciton transition as the pump field amplitude f_0 increases.

If the resonance detuning of pump pulse photons is nonzero ($\delta_l \neq 0$), an appreciably asymmetric (with respect to $\delta = 0$) transformation of the absorption susceptibility component χ" occurs (Figs. 4b, 4c), which is caused by a change in the dispersion relation. In the absence of a pump field ($f_0 = 0$), the absorption band shape remains a symmetric Lorentzian. As the pump field amplitude f_0 increases at $\sigma_l = 0$, the spectral shape of the absorption band deforms: its maximum

decreases rapidly and shifts to long wavelengths; simultaneously, the half-width of the $\chi''(\delta)$ peak increases (Fig. 4b). At a certain value of the pump field amplitude, a weak short-wavelength peak splits off from the short-wavelength tail of the intense absorption band. The amplitude of this peak increases slowly with the excitation level, and the peak itself shifts monotonically to short wavelengths. As the excitation level f_0 increases further, the long-wavelength peak of the absorption band continues to shift to long wavelengths and its amplitude decreases monotonically, whereas the weak short-wavelength peak increases slowly and shifts to short wavelengths. At high excitation levels, the absorption component of the susceptibility consists of a pronounced long-wavelength peak and a weak short-wavelength peak, with both peaks having an almost Lorentzian shape (Fig. 4b). Similar effects occur in the case of $\delta_l > 0$ (Fig. 4c).

The dependence of the absorption susceptibility component χ'' on the pump field amplitude f_0 at fixed values of resonance detunings δ and δ_l is also of interest. It follows from Eq. (9) that, at $\delta_- < \delta < \delta_+$, the function $\chi''(f_0)$ decreases monotonically as f_0 increases. At $\delta \geq \delta_+$ and $\delta \leq \delta_-$, the function $\chi''(f_0)$ initially increases with f_0 and then, after reaching a maximum at

$$f_0^2 = \sqrt{s^2 + (\delta + \delta_l)^2}$$
$$\times [|(s+1)\delta + \delta_l| - \sqrt{s^2 + (\delta + \delta_l)^2}]/s,$$

decreases monotonically (Fig. 4). Here,

$$\delta_+ = (\sqrt{\delta_l^2 + s(2+s)} - \delta_l)/(2+s),$$

$$\delta_- = -(\sqrt{\delta_l^2 + s(2+s)} + \delta_l)/(2+s).$$

This behavior is due to the fact that the function χ'' is resonant not only in the resonance detuning δ of the weak pulse but also in the pump field amplitude f_0 at a fixed value of δ. Hence, the weak signal absorption can also be saturated in this case. However, at small pump amplitudes, absorption can increase with the excitation level (Fig. 4).

Figure 5 shows the dependence of absorption on δ and δ_l at a fixed excitation level. We can see that the peak of the long-wavelength (short-wavelength) absorption band shifts gradually to long wavelengths and decreases (increases) in amplitude as the resonance detuning δ_l of the pump pulse increases. At a large magnitude of negative (positive) detuning δ_l, only the long-wavelength (short-wavelength) peak remains in the absorption band.

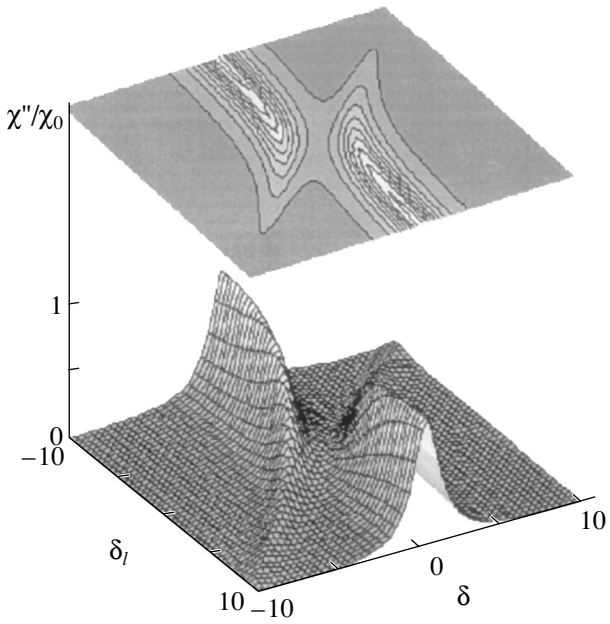

Fig. 5. Absorption component of susceptibility χ'' as a function of resonance detunings δ and δ_l of the probe and pump pulses at a pump field intensity f_0^2 equal to 5.

4. CONCLUSIONS

We note that the expressions obtained for the susceptibility in this study and in [8, 9] are qualitatively similar. These expressions were derived within the same model of the semiconductor energy spectrum and for the same method of pumping but for different methods of probing with weak pulses. In [8, 9], it was proposed to observe optical properties via two-photon excitation of biexcitons from the crystal ground state, whereas in this study we have considered the case of single-photon excitation of excitons. The Autler–Townes splitting for excitons and biexcitons is caused by pumping and, hence, arises in both cases. As for the spectral shapes of absorption bands, they are qualitatively similar in both cases but their details differ. Moreover, unlike in this study, the susceptibility $\chi^{(3)}$ was calculated in [8, 9]. In those two studies, it was assumed that the probe pulse is so weak that it does not change the semiconductor energy spectrum but only detects changes in the crystal optical properties that arise under exposure to an intense pump pulse in the *M*-band region.

Let us compare the results obtained in this study with the results of experimental studies on the optical properties of semiconductors in the exciton spectral range under exposure to an intense pump. As mentioned above, the results of this study agree qualitatively with the experimental data on absorption spectra reported in [7]. We also note that the results of this study are qualitatively similar to the results of studying the luminescence spectra in InGaAs quantum dots [16];

namely, the following effects were observed: (i) Autler–Townes splitting and doublet formation, (ii) a change in the splitting with a change in the pump wave intensity and in the resonance detuning, (iii) coincidence of the absorption (luminescence) band peaks, and (iv) a linear dependence of the Rabi frequency on the pump field amplitude. Changes in absorption bands with variations in the resonance detunings δ and δ_l at a fixed pump amplitude f_0 (Fig. 5) were observed both in [7] and [16]. Rabi oscillations in semiconductor quantum wells were observed in [17]. It was also confirmed experimentally that the frequency of these oscillations is proportional to the pump field amplitude.

Let us estimate the exciton transition dipole moment $\mu = \hbar\sigma$ using Eq. (6) and experimental data from [16], according to which the Autler–Townes splitting $\hbar\Omega$ is 93 μeV at an excitation intensity $J_0 = 18$ kW/cm^2. Since $J_0 = cE_0^2/4\pi$, we have $\mu = (1/4)\hbar\Omega\sqrt{c/\pi J_0} \approx 3 \times 10^{-17}$ CGSE = 30 D. In this case, the nutation frequency is 1.5×10^{11} s^{-1}.

Thus, the theoretical results obtained make it possible to perform more detailed studies not only of the optical absorption properties of semiconductors in the exciton spectral region but also of the dispersion properties using the pump–probe technique.

REFERENCES

1. R. Leonelli, A. Manar, J. B. Grun, and B. Hönerlage, Phys. Rev. B: Condens. Matter **45**, 4141 (1992).
2. G. O. Smith, E. J. Mayer, J. Kuhl, and K. Ploog, Solid State Commun. **92**, 325 (1994).
3. G. Finkelstein, S. Bar-Ad, O. Carmel, I. Bar-Joseph, and Y. Levinson, Phys. Rev. B: Condens. Matter **47**, 12 964 (1993).
4. D. Hulin and M. Joffre, Phys. Rev. Lett. **65**, 3425 (1990).
5. N. Peyghambarian, H. M. Gibbs, J. L. Jewell, A. Antonetti, A. Migus, D. Hulin, and A. Mysyrowicz, Phys. Rev. Lett. **53**, 2433 (1984).
6. A. von Lehmen, D. S. Chemla, J. E. Zucker, and J. P. Heritage, Opt. Lett. **11**, 609 (1985).
7. R. Shimano and M. Kuwata-Gonokami, Phys. Rev. Lett. **72**, 530 (1994).
8. P. I. Khadzhi, A. V. Korovaĭ, and D. V. Tkachenko, Fiz. Tverd. Tela (St. Petersburg) **44**, 774 (2002) [Phys. Solid State **44**, 804 (2002)].
9. P. I. Khadzhi, A. V. Corovai, O. V. Korovai, and D. V. Tkachenko, Moldavian J. Phys. Sci. **1**, 152 (2002).
10. E. Hanamura, Phys. Rev. B: Condens. Matter **44**, 8514 (1991).
11. S. A. Moskalenko, V. G. Pavlov, and V. R. Mis'ko, Fiz. Tverd. Tela (St. Petersburg) **40**, 924 (1998) [Phys. Solid State **40**, 850 (1998)].
12. S. A. Moskalenko and D. W. Snoke, *Bose–Einstein Condensation of Excitons and Biexcitons and Coherent Nonlinear Optics with Excitons* (Cambridge University Press, Cambridge, 2000).
13. G. S. Agarwal, Phys. Rev. A: At., Mol., Opt. Phys. **51**, R2711 (1995).
14. P. I. Khadzhi and D. V. Tkachenko, Fiz. Tverd. Tela (St. Petersburg) **40**, 934 (1998) [Phys. Solid State **40**, 860 (1998)].
15. P. I. Khadzhi, *Nonlinear Optical Processes in the System of Excitons and Biexcitons in Semiconductors* (Shtiintsa, Kishinev, 1985) [in Russian].
16. H. Kamada, H. Gotoh, J. Temmyo, T. Takagahara, and H. Ando, Phys. Rev. Lett. **87**, 246 401 (2001).
17. A. Schülzgen, R. Binder, M. E. Donovan, M. Lindberg, K. Wandke, H. M. Gibbs, G. Khitrova, and N. Peyghambarian, Phys. Rev. Lett. **82**, 2346 (1999).

Translated by A. Kazantsev

Physics of the Solid State, Vol. 47, No. 12, 2005, pp. 2243–2247. Translated from Fizika Tverdogo Tela, Vol. 47, No. 12, 2005, pp. 2152–2156.

SEMICONDUCTORS AND DIELECTRICS

Possibility of Inducing Superparaelectricity in Strontium Bismuth Titanate Ceramics $SrTiO_3$: Bi

V. A. Isupov

Ioffe Physicotechnical Institute, Russian Academy of Sciences, Politekhnicheskaya ul. 26, St. Petersburg, 194021 Russia

Received January 14, 2005

Abstract—Dielectric strontium bismuth titanate ceramics $SrTiO_3$: Bi is a complex solid solution consisting of the $Sr_{1-u}Bi_{2u/3}\square_{u/3}TiO_3$ perovskite matrix and small planar inclusions related to Aurivillius-type layered ferroelectric compounds with a high Curie temperature T_C (700–950 K). The matrix is characterized by a smeared ferroelectric phase transition in the temperature range 150–200 K and exhibits relaxation dielectric polarization. At temperatures below but close to the Curie temperature T_C, the state of the ceramics can be treated as superparaelectric. The concentration dependence of the temperature corresponding to the maximum of the permittivity is explained. © *2005 Pleiades Publishing, Inc.*

1. INTRODUCTION

Dielectric strontium bismuth titanate (SBT) ceramic materials $SrTiO_3$: Bi possess a number of unique properties revealed in 1956 by Skanavi and Matveeva [1]. These are the relaxation behavior of the dielectric polarization and the high permittivity ε_{20} (at 20°C), which, upon cooling, gradually increases, passes through a maximum at approximately –100°C, and then gradually decreases with a maximum in the dielectric loss tangent $\tan\delta$ (Fig. 1a). As a rule, the SBT ceramics is considered a solid solution based on the quantum ferroelectric $SrTiO_3$ with a perovskite structure, whose permittivity reaches large values at $T = 0$ K but does not pass through a maximum. Owing to the nonclassical behavior of the ferroelectric properties of strontium titanate, the SBT ceramics is assigned to nonferroelectric materials with thermal ion polarization, in which vacancies are formed in the strontium sublattice because of the different valences of Sr^{2+} and Bi^{3+} ions. These vacancies distort oxygen octahedra in adjacent crystal regions, so that Ti^{4+} ions can hop inside these octahedra from one potential well to another potential well due to thermal motion [1–3]. It was experimentally found that, as the bismuth content increases, the temperature T_m of the maximum in the dependence $\varepsilon(T)$ increases nonlinearly (Fig. 1b) [4].

Smolenskiĭ *et al.* [5] demonstrated that dielectric hysteresis loops are observed for strontium bismuth titanate in strong ac electric fields. These dielectric hysteresis loops share a number of traits with the dielectric hyster-

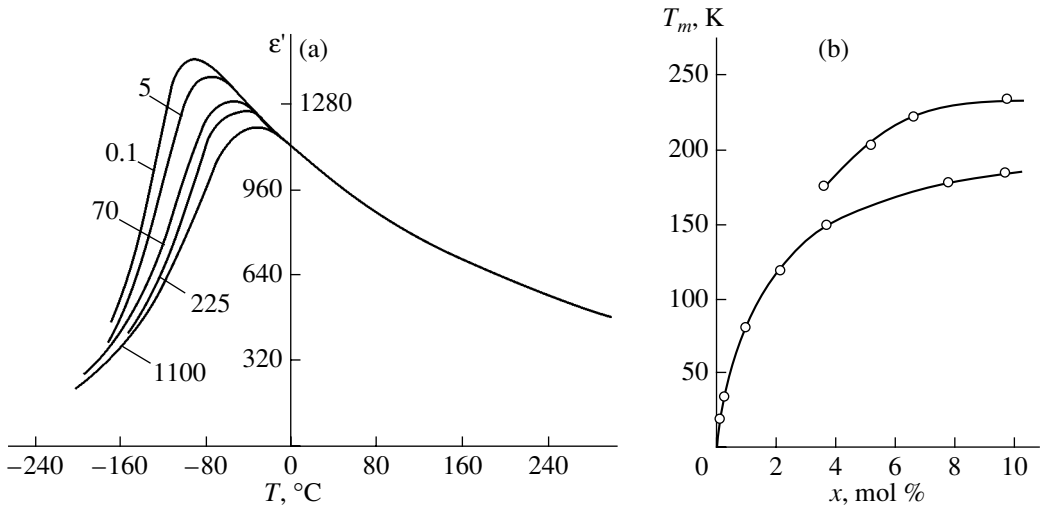

Fig. 1. Dielectric behavior of the $(1 - x)SrTiO_3 + xBi_2O_3 \cdot 3TiO_2$ ceramics: (a) temperature dependences of the permittivity for the ceramics with $x = 0.096$ at different frequencies (indicated by numbers in kHz near the curves) [3] and (b) concentration dependences of the temperature of the maximum in the dependence $\varepsilon(T)$ at frequencies of (*1*) 1.0 kHz and (*2*) 1.1 MHz [4].

1063-7834/05/4712-2243$26.00 © 2005 Pleiades Publishing, Inc.

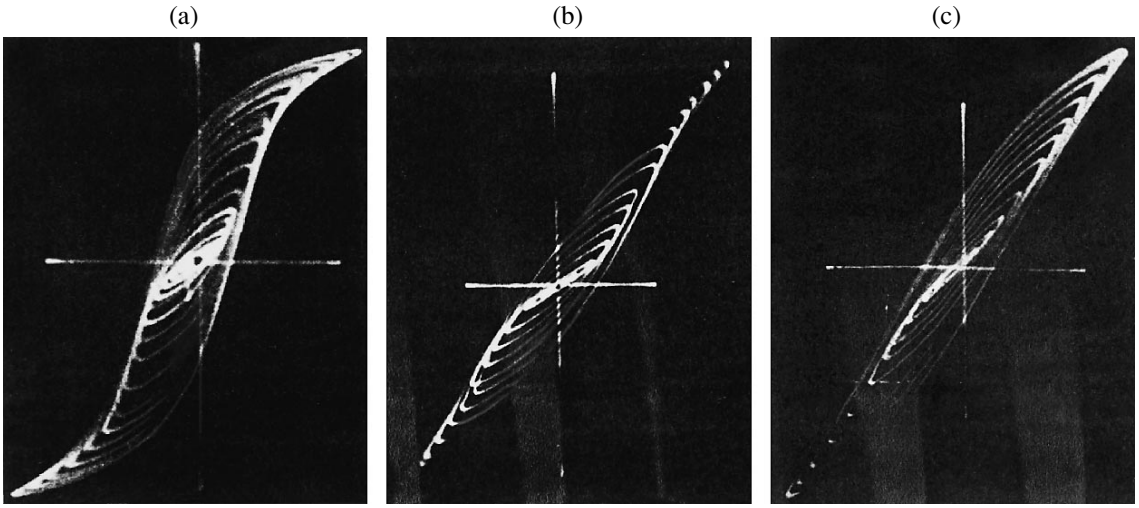

Fig. 2. Dielectric hysteresis loops for (a) the PMN ceramics at $T = 183$ K and $E_{max} = 20$ kV/cm, (b) the PNN ceramics at $T = 77$ K and $E_{max} = 60$ kV/cm, and (c) the $Sr_{0.85}Bi_{0.10}TiO_3$ ceramics at $T = 90$ K and $E_{max} = 67$ kV/cm [5].

esis loops characteristic of the well-known perovskites $PbMg_{1/3}Nb_{2/3}O_3$ (PMN) and $PbNi_{1/3}Nb_{2/3}O_3$(PNN) with smeared ferroelectric phase transitions (Fig. 2). It should be noted that the temperature dependences of the permittivity and the dielectric loss tangent for the SBT and PNN ceramics are also similar to each other (this gave impetus to investigations into the hysteresis loops of the SBT ceramics). As a result, the inference was made that the SBT ceramics also undergoes a smeared ferroelectric phase transition and that bismuth embedded in the strontium sublattice of the perovskite phase increases the mean temperature of the smeared ferroelectric phase transition and enhances its smearing.

The above concepts of the smeared ferroelectric phase transition in the SBT ceramics were criticized by Bogdanov (see, for example, [4]), because x-ray diffraction investigations of this ceramics over a wide range of temperatures [6, 7] did not reveal any phase transitions. Moreover, although an increase in the bismuth content x leads to a decrease in the quantity dT_m/dx, the smearing of the phase transition is enhanced (whereas this should result in a weakening of the smearing in accordance with the concept that composition fluctuations are responsible for the smearing of phase transitions [8]). The first argument is of little significance. This is associated with the fact that, upon the smeared ferroelectric phase transition, pseudocubic distortions of the lattice of samples not subjected to a strong electric field, as a rule, are not observed because of the very small sizes of the polar regions. The second argument is quite true and will be discussed in the present paper.

In this paper, we will analyze the specific features revealed in the formation of solid solutions, discuss the possibility of the superparaelectric state occurring in SBT ceramic materials, and explain a number of their physical properties.

2. CONCENTRATION AND THE CONCENTRATION RANGES

The problems associated with the bismuth titanate concentration in the SBT ceramics are rather complicated, if for no other reason than the possible non-single phase composition of the ceramics. It is often unclear which phase should be used as the basis for writing the composition. In the most general form reflecting only the chemical composition of the material, the composition of the SBT ceramics can be represented as

$$(1-x)SrTiO_3 + xBi_2O_3 \cdot 3TiO_2. \quad (1)$$

The advantage of this form is that it does not mislead with respect to the phase composition. Moreover, the composition can be written either in the form

$$(Sr_{1-y}Bi_{2y/3})TiO_3 \quad (2)$$

or in the form

$$(Sr_{1-1.5z}Bi_z)TiO_3. \quad (3)$$

These representations refer to the perovskite phase even in the case where the ceramics has a non-single-phase composition. It is common practice to use form (2), which is quite true when describing the total chemical composition of the ceramics. In order to change over from one form to another, we can use the relationships

$$y = 3x/(1+x); \quad x = y/(3-2y); \quad y = 1.5z. \quad (4)$$

Hereinafter, we will use the more traditional form (2), which describes only the chemical composition of the ceramics.

According to Kashtanova *et al.* [3], the x-ray diffraction patterns of the ceramics at concentrations $y = 0.098$ and 0.170 exhibit indications of one phase with a perovskite-type structure. At the concentration $y =$

0.242, traces of a new (anisotropic) phase manifest themselves in microsections of the ceramics, even though this phase has not been revealed by x-ray diffraction analysis. In the x-ray diffraction patterns, the anisotropic phase is identified beginning only from the concentration $y = 0.424$ and becomes the sole revealed phase at the concentration $y = 0.522$.

The results presented in [3] differ from those obtained by Chen and Zhi [9]. According to [9], samples with the concentration y varying in the range from 0 to 0.11 are sintered at a temperature of ~1400°C, easily lose oxygen, take on a gray color, and possess high permittivities ε and large dielectric loss tangents $\tan\delta$ at 20°C, as well as a high electrical conductivity that passes through a maximum at the concentration $y = 0.05$. It was assumed that vacancies in the strontium sublattice are absent and that excess charges of Bi^{3+} ions are compensated for in part by the transformation of Ti^{4+} ions into Ti^{3+} ions. At the concentration $y = 0.11$, the sintering temperature decreases, the gray color of the samples disappears, and the electrical conductivity decreases drastically. The assumption was made that the composition of the perovskite solid solutions formed in this case is described by formula (2). The temperature dependence of the permittivity turned out to be consistent with those shown in Fig. 1a. According to the x-ray diffraction data, a non-perovskite-like phase is formed in the samples with concentrations $y \geq 0.36$. (The differences between the results obtained in [3] and [9] can be associated in part with the strong dependence of the properties of the SBT ceramics on the atmosphere used during sintering and annealing [10].)

3. THE CONCEPT OF SUPERPARAELECTRICITY

The notion of superparaelectricity was introduced by Cross [11] for compounds with smeared ferroelectric phase transitions (such as PMN, PNN, $(Ba,Sr)Nb_2O_6$, etc.) by analogy with the term "superparamagnetism." However, as was noted in [12], this analogy is not valid for the aforementioned crystals.

According to [13–15], superparamagnetism is observed in composite systems consisting of a great number of small (with linear sizes of 10–100 Å) single-domain ferromagnetic particles that are distributed in a nonmagnetic matrix and interact weakly with each other. The direction of magnetization in these particles varies as a result thermal motion in weak magnetic fields due to the thermal fluctuations (which are very large because of the small sizes of the particles). As a consequence, the system behaves like a paramagnetic gas and obeys the Curie law, whereas the magnetization in the saturation region is described by the Langevin formula. The phenomenon of superparamagnetism can be illustrated by a system of small-sized cobalt particles that precipitated upon decomposition of Cu–Co (2% Co) solid solutions and a system of small-sized iron particles that precipitated in the β brass (0.1% Fe).

In a ferroelectric material with a smeared ferroelectric phase transition, polar regions with linear sizes smaller than 100 Å at temperatures higher than the mean Curie temperature (T_m) are surrounded by the paraelectric phase or, more precisely, by crystal microregions that do not exhibit spontaneous polarization but, at these temperatures, are close to their local Curie temperature and, hence, are "ready" to undergo a local ferroelectric phase transition. Therefore, polar microregions and microregions that are ready to become polar fill the entire volume of the crystal. It is obvious that this system cannot be treated as a paraelectric gas and the term "superparaelectricity" is inapplicable to its description.

It is clear that the system can be referred to as superparaelectric only in the case when it consists of a nonferroelectric matrix with embedded small-sized ferroelectric particles, such that the matrix either never transforms into the ferroelectric state or, at least, is far from its mean Curie temperature, whereas the direction of the dipole moments of the particles can vary under thermal fluctuations and in response to external electric fields.

4. DUAL CHARACTER OF SBT CERAMICS

We will not dwell on $SrTiO_3$ solid solutions with a low Bi content, in which Ti^{4+} ions can be reduced to Ti^{3+} ions and the ferroelectric phase transition can retain a quantum nature inherent in strontium titanate [16]. Let us consider the concentration range corresponding to the dielectric ceramics. We begin with the solid solution at the concentration $y = 0.242$, for which precipitates of the new (anisotropic) phase (thin short bright segments against the dark background) become visible in microsections [3]. These segments can be indications that the anisotropic phase can also exist in the form of smaller precipitates invisible under a microscope. (The new (anisotropic) phase in larger amounts was revealed by x-ray diffraction analysis at the concentrations $y = 0.424$ in [3] and $y = 0.36$ in [9].)

A question arises as to the nature of the new phase. Here, it is appropriate to recall that there are so-called Aurivillius compounds, such as the layered ferroelectric compounds $A_{n-1}Bi_2B_nO_{3n+3}$ ($SrBi_2Nb_2O_9$ at $n = 2$, $Bi_4Ti_3O_{12}$ at $n = 3$, $SrBi_4Ti_4O_{15}$ at $n = 4$, etc.), in which perovskite-like layers of different thicknesses (determined by the index n) alternate with bismuth–oxygen layers (Fig. 3) [17].

For bismuth titanate concentrations at which trivalent titanium is already absent but the new phase does not appear, it is reasonable to assume that the $Sr_{1-y}Bi_{2y/3}\square_{y/3}TiO_3$ perovskite solid solution is formed. It is evident that this phase serves as a matrix with an increase in the concentration y when there appear small-sized planar precipitates of layered compounds. (It is clear that these planar precipitates, while related,

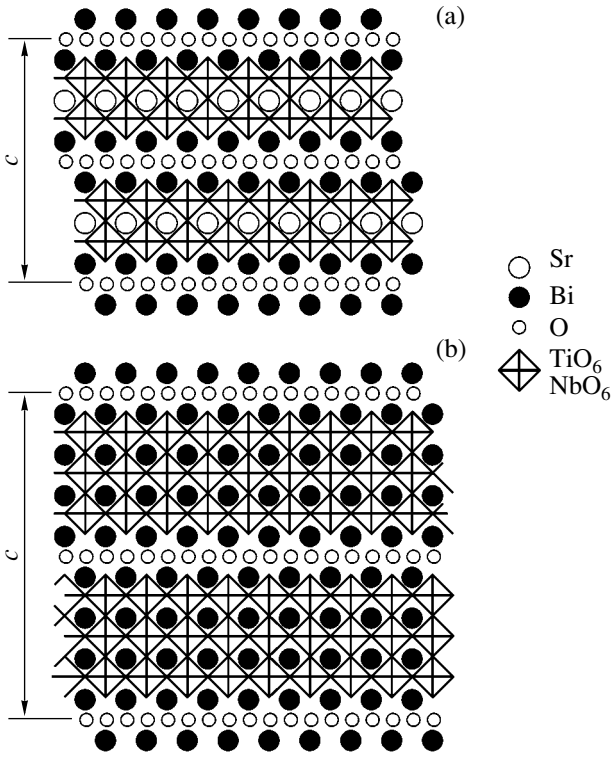

Fig. 3. Crystal structures of (a) $SrBi_2Nb_2O_9$ and (b) $Bi_4Ti_3O_{12}$ compounds in projections onto the (100) plane.

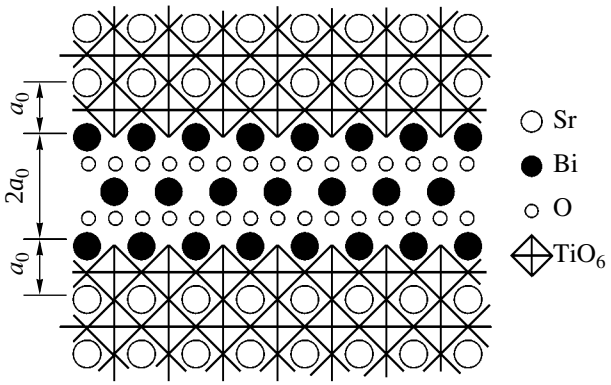

Fig. 4. A hypothetical bismuth–oxygen layer free of strontium titanate (without displacements of oxygen octahedra in the adjacent layers of strontium titanate).

are far from so-called intergrowth phases until they grow through macroscopic distances.)

In essence, until the precipitates of the new phase have nanosizes, the crystal lattice can be considered a defect solid solution (interstitial solid solution) in which planar defects in the form of "flakes" of layered compounds are dissolved in the perovskite matrix ($Sr_{1-u}Bi_{2u/3}\square_{u/3}TiO_3$ substitutional (omission) solid solutions). (Here, the index u in the formula differs from the index y due to a partial transfer of bismuth to flakes.) The crystal lattice can be treated as an interstitial solid solution, because the atomic planes of flakes are extensions of the atomic planes of the matrix and, hence, are coherent to them. As a result, these flakes are not only precipitates but are embedded in the crystal lattice of the matrix. We can assume that the planar defects under consideration are predominantly located in regions of line dislocations.

The strontium titanate–based matrix, which is assumed to be ferroelectric and has a low mean Curie temperature T_m (approximately 150–200 K), can be considered nonferroelectric at temperatures $T \geq T_m$. However, Aurivillius-type layered compounds have high Curie temperatures [for example, T_C = 700 K for $SrBi_2Nb_2O_9$ (Fig. 3a), T_C = 950 K for $Bi_4Ti_3O_{12}$ (Fig. 3b)]. When layered flakes undergo a ferroelectric phase transition and acquire spontaneous electric moments, the state of the crystal as a whole at temperatures considerably higher than the temperature T_m and close to the Curie point T_C but be treated as superparaelectric.

A question arises as to the composition of the aforementioned layered flakes. This question remains open. Layers of the $Bi_4Ti_3O_{12}$ (n = 3), $SrBi_4Ti_4O_{15}$ (n = 4), $Sr_2Bi_4Ti_5O_{18}$ (n = 5), and other compounds can be embedded in the perovskite lattice only with displacements of opposite layers formed by octahedra of the perovskite phase in the layer plane (Fig. 3). This induces mechanical stresses in adjacent regions of the perovskite lattice. Undeniably, these stresses do not exclude the possible formation of inclusions, because they do not exceed the mechanical stresses generated upon the formation of dislocations. However, it is possible to imagine a bismuth–oxygen layer embedded in the $SrTiO_3$ lattice without displacement of the octahedra (Fig. 4). These layers or groups of layers can form a flake. Of course, the layer depicted in Fig. 3 is hypothetical; however, we cannot rule out the possibility that such a layer exists.

5. DIELECTRIC BEHAVIOR

The smearing of the ferroelectric phase transition and the relaxation dielectric polarization in the SBT ceramics in the range 150–200 K are associated with the behavior of the $Sr_{1-u}Bi_{2u/3}\square_{u/3}TiO_3$ perovskite phase, whose mean Curie temperature T_m increases with an increase in the bismuth titanate concentration. In this case, composition fluctuations in nanoregions of the crystal result in the corresponding distribution of local Curie temperatures in these nanoregions. This leads to the formation of polar regions (in the presence of paraelectric regions), reorientation of the dipole moments of the polar regions, and motion of their boundaries due to thermal fluctuations and in response to electric fields. These factors are responsible for the relaxation polarization, as is the case with the PMN and PNN ceramics.

The behavior of the dependence $T_m(y)$ with an increase in the total bismuth titanate concentration y in the ceramics, i.e., a decrease in the rate of increase of the temperature of the permittivity at the maximum (Fig. 1b), is explained by the transformation of one type of solid solution into another type when layered flakes begin to precipitate from the $Sr_{1-y}Bi_{2y/3}\square_{y/3}TiO_3$ substitutional (omission) solid solution. (Most likely, the layered flakes precipitate during cooling of the ceramics from the sintering temperature.) Excess bismuth passes into the flakes, and the perovskite matrix is no longer enriched in bismuth. As a consequence, the temperature of the maximum in the dependence $\varepsilon(T)$ ceases to change with an increase in the bismuth titanate concentration y.

We can assume that, at temperatures below but close to the Curie temperature T_C of layered flakes, their dipole moments can vary under thermal fluctuations and in response to electric fields. Since the mean temperature T_m of the smeared ferroelectric phase transition of the perovskite matrix lies far beyond the aforementioned temperature range, an analogy can be drawn to superparamagnetism and this state of the material can be termed superparaelectric.

It should be noted that flakes induce random electric fields, which, as is known, can enhance the smearing of the ferroelectric phase transition in the matrix [18]. However, the polarization of flakes can provide an additional mechanism of dielectric relaxation in the SBT ceramics at high temperatures. Relaxation processes in the SBT ceramics at high temperatures were actually observed [19] but were attributed to the motion of oxygen atoms (oxygen vacancies). In this respect, it is necessary to elucidate the mechanism of the observed relaxation.

6. CONCLUSIONS

(1) Dielectric strontium bismuth titanate ceramics is a complex defect solid solution consisting of the perovskite matrix ($Sr_{1-u}Bi_{2u/3}\square_{u/3}TiO_3$ substitutional (omission) solid solution) and planar defects related to Aurivillius-type layered ferroelectric compounds.

(2) The relaxation dielectric polarization of the SBT ceramics is predominantly determined by the behavior of the matrix.

(3) The presence of planar defects (i.e., layered inclusions) in the matrix suggests a superparaelectric behavior of the system at high temperatures and can be responsible for the high-temperature relaxation processes.

(4) The formation of planar defects (flakes) explains well the concentration dependence of the temperature of the permittivity at the maximum.

REFERENCES

1. G. I. Skanavi and E. N. Matveeva, Zh. Éksp. Teor. Fiz. **30** (6), 1047 (1956) [Sov. Phys. JETP **3**, 905 (1956)].
2. G. I. Skanavi, Ya. M. Ksendzov, V. A. Trigubenko, and V. V. Prikhvatilov, Zh. Éksp. Teor. Fiz. **33**, 820 (1957) [Sov. Phys. JETP **6**, 250 (1957)].
3. A. M. Kashtanova, N. N. Kurtseva, and G. I. Skanavi, Izv. Akad. Nauk SSSR, Ser. Fiz. **24**, 114 (1960).
4. S. V. Bogdanov and K. V. Kiseleva, Izv. Akad. Nauk SSSR, Ser. Fiz. **28** (4), 636 (1964).
5. G. A. Smolenskiĭ, V. A. Isupov, A. I. Agranovskaya, and S. N. Popov, Fiz. Tverd. Tela (Leningrad) **2** (11), 2906 (1960) [Sov. Phys. Solid State **2** (11), 2584 (1960)].
6. K. V. Kiseleva, Kristallografiya **8**, 105 (1963) [Sov. Phys. Crystallogr. **8**, 78 (1963)].
7. A. N. Gubkin, A. M. Kashtanova, E. V. Potapov, and A. E. Solodukhin, Fiz. Tverd. Tela (Leningrad) **4** (11), 3293 (1962) [Sov. Phys. Solid State **4** (11), 2411 (1962)].
8. V. A. Isupov, Zh. Tekh. Fiz. **26** (9), 1912 (1956); Fiz. Tverd. Tela **5**, 187 (1963) [Sov. Phys. Solid State **5**, 136 (1963)]; Izv. Akad. Nauk SSSR, Ser. Fiz. **28** (4), 653 (1964).
9. A. Chen and Y. Zhi, J. Appl. Phys. **71** (9), 4451 (1992).
10. C. Ang, Z. Yu, and L. E. Cross, Phys. Rev. B: Condens. Matter **62** (1), 228 (2000).
11. L. E. Cross, Ferroelectrics **76**, 241 (1987); Ferroelectrics **151**, 305 (1994).
12. V. A. Isupov, Ferroelectrics **289**, 131 (2003).
13. S. V. Vonsovskiĭ, in *Physical Encyclopedia: Superparamagnetism* (Nauka, Moscow, 1966), Vol. 5 [in Russian].
14. S. V. Vonsovskii, *Magnetism of Elementary Particles* (Nauka, Moscow, 1973; Mir, Moscow, 1975).
15. A. S. Borovik-Romanov, in *Great Soviet Encyclopedia: Superparamagnetism*, Ed. by A. M. Prokhorov (Sovetskaya Éntsiklopediya, Moscow, 1976; Macmillan, New York, 1974–1983), Vol. 25.
16. C. Ang, Z. Yu, P. Vilarinha, and J. L. Baptista, Phys. Rev. B: Condens. Matter **57** (13), 7403 (1998); C. Ang, Z. Yu, J. Hemberger, P. Lunkenheimer, and A. Loidl, Phys. Rev. B: Condens. Matter **59** (10), 6665 (1999); C. Ang, Z. Yu, P. Lunkenheimer, J. Hemberger, and A. Loidl, Phys. Rev. B: Condens. Matter **59** (10), 6670 (1999).
17. G. A. Smolenskiĭ, V. A. Bokov, V. A. Isupov, N. N. Kraĭnik, R. E. Pasynkov, A. I. Sokolov, and N. K. Yushin, *Physics of Ferroelectric Phenomena* (Nauka, Leningrad, 1985) [in Russian].
18. B. E. Vugmeister and M. D. Glinchuk, Rev. Mod. Phys. **62** (4), 993 (1990).
19. Z. Yu, C. Ang, P. M. Vilanrinho, P. O. Mantas, and J. L. Baptista, J. Appl. Phys. **83** (9), 4874 (1998).

Translated by O. Borovik-Romanova

Physics of the Solid State, Vol. 47, No. 12, 2005, pp. 2248–2256. Translated from Fizika Tverdogo Tela, Vol. 47, No. 12, 2005, pp. 2157–2165.

SEMICONDUCTORS AND DIELECTRICS

Calculations of the Electronic Structure of Crystalline $SrZrO_3$ in the Framework of the Density-Functional Theory in the LCAO Approximation

R. A. Évarestov, A. V. Bandura, and V. E. Aleksandrov

St. Petersburg State University, Ul'yanovskaya ul. 1, Petrodvorets, St. Petersburg, 198904 Russia

e-mail: evarest@hm.csa.ru

Received March 25, 2005

Abstract—The electronic structures of four well-known modifications of crystalline $SrZrO_3$ with different symmetries, namely, the cubic (*Pm*3*m*), tetragonal (*I*4/*mcm*), and two orthorhombic (*Cmcm*, *Pbnm*) modifications, are calculated in the framework of the density-functional theory in the basis set of the linear combination of atomic orbitals (LCAO). A comparative analysis of the electronic properties of the crystals under consideration is performed on the basis of the calculated band structures and densities of states (the total densities of states and the densities of states projected onto the atomic states). The calculated relative stabilities of the different modifications are in good agreement with the experimental data on the phase transitions in the $SrZrO_3$ crystal: the low-temperature modifications with lower symmetry are more stable. The ionicities of chemical bonding in different modifications of crystalline $SrZrO_3$ are compared by analyzing the Mulliken populations and constructing the localized Wannier functions for the occupied energy bands. © *2005 Pleiades Publishing, Inc.*

1. INTRODUCTION

In recent years, perovskite-like crystals of the general formula ABO_3 (A = Ga, Ba, Cd, Sr; B = Ti, Sn, Zr) have been intensively investigated experimentally in view of the possibility of employing these materials in practice in the fabrication of fuel cells, gas sensors, information storage systems, and devices based on their ferroelectric properties [1].

Theoretically, titanates $ATiO_3$ (A = Ca, Sr, Ba) are best known [2], whereas zirconates are as yet little understood. In particular, prior to our recent study [3], only one calculation of the electronic structure of crystalline $SrZrO_3$ in the cubic modification (space group *Pm*3*m*) had been carried out by Mete *et al.* [4] within the framework of the density-functional theory (DFT) in the plane wave basis set. In [3], we briefly described the results of the first calculations of the electronic properties for all four modifications of $SrZrO_3$ crystals in the framework of the density-functional theory in the plane wave basis set with geometry optimization (the lattice constants, the parameters determining the positions of atoms in the unit cell). In our present paper, the density-functional theory in the linear combination of atomic orbitals (LCAO) approximation with optimized parameters of the crystal structure is applied to investigate in greater detail the specific features of the electronic structure and the nature of chemical bonding in four different modifications of crystalline $SrZrO_3$, namely, the cubic (*Pm*3*m*), tetragonal (*I*4/*mcm*), and two orthorhombic (*Cmcm*, *Pbnm*) modifications.

This paper is organized as follows. In Section 2, we report the experimental [5] and calculated (in our recent work [3]) data on the geometric structure of the crystals under investigation. In Section 3, we briefly describe the computational scheme based on the density-functional theory in the LCAO approximation and its capabilities for estimating the relative energies of different phases of the ZrO_2 crystals. In Section 4, we compare the relative stabilities (in terms of the energy per formula unit), the band structures, and the densities of states (both total and projected onto the atomic states) for different crystalline modifications of strontium zirconate. Moreover, we examine the change in the ionicity of chemical bonding upon phase transitions in strontium zirconate. In Section 5, the change in the ionicity of chemical bond is analyzed by constructing the localized Wannier functions for the valence energy bands. Section 6 provides the main conclusions.

2. CRYSTALLOGRAPHIC MODIFICATIONS OF THE $SrZrO_3$ ZIRCONATE

Thermal structural investigations [5] demonstrated that the $SrZrO_3$ zirconate crystallizes in four modifications existing in different temperature ranges. An increase in the temperature leads to second-order phase transitions accompanied by an increase in the symmetry of the system. The sequence of phase transitions is as follows: the orthorhombic modification *Pbnm* at approximately 970 K transforms into the orthorhombic modification *Cmcm*, which then at 1100 K transforms into the tetragonal modification *I*4/*mcm*, which, in turn,

1063-7834/05/4712-2248$26.00 © 2005 Pleiades Publishing, Inc.

Table 1. Experimental and optimized translation vectors (Å) of the crystallographic unit cell in the $SrZrO_3$ crystal

Phase	*Pm*3*m*	*I*4/*mcm*		*Cmcm*			*Pbnm*		
Parameter	*a*	*a*	*b*	*a*	*b*	*c*	*a*	*b*	*c*
Experiment [5]	4.154	5.870	8.309	8.270	8.273	8.259	5.786	5.815	8.196
Theory [3]	4.196	5.935	8.393	8.266	8.368	8.318	5.847	5.911	8.295

at 1400 K transforms into the cubic modification *Pm*3*m*. The melting temperature of the cubic modification is approximately equal to 2400 K. As a consequence, it is this cubic phase that is of special interest from the standpoint of high-temperature applications of $SrZrO_3$ crystals.

The cubic modification has a simple cubic lattice with space group *Pm*3*m*. In this case, the crystallographic unit cell coincides with the primitive cell and contains one formula unit $SrZrO_3$. Atoms of the same type are crystal chemically equivalent and occupy parameter-free Wyckoff positions: *a*(0, 0, 0) for Zr; *b*(1/2, 1/2, 1/2) for Sr; and *d*(1/2, 0, 0) for O. The constant of the simple cubic lattice is the sole parameter that varies in the course of optimization of the crystal structure without reduction of the symmetry [2].

The crystallographic unit cell of the tetragonal phase (space group *I*4/*mcm*, body-centered Bravais lattice) coincides with the doubled primitive cell and contains four formula units $SrZrO_3$. The structure of this modification is described by three parameters, namely, two parameters of the tetragonal lattice and one free parameter for the Wyckoff position occupied by the oxygen atom.

The orthorhombic modifications *Cmcm* (base-centered lattice, crystallographic unit cell contains two primitive cells) and *Pbnm* (simple Bravais lattice, crystallographic unit cell coincides with the primitive cell) contain four formula units $SrZrO_3$ per primitive cell. Both structures are described by three parameters of the orthorhombic lattice and free parameters for the corresponding atoms.

The experimental translation vectors of the crystallographic unit cells in the four $SrZrO_3$ modifications [5] and the translation vectors calculated in [3] are presented in Table 1. For the tetragonal (*I*4/*mcm*) and orthorhombic (*Cmcm*) modifications with the centered lattices, the crystallographic unit cell is twice as large as the primitive cell and the translation vectors in all crystals are orthogonal to each other. It can be seen from Table 1 that the calculated lattice constants for all the modifications exceed the experimental lattice constants by 3–5%. This overestimation is characteristic of DFT calculations with the inclusion of the gradient correction in the exchange–correlation functional but is not very significant when comparing different crystalline modifications. Table 2 lists only the coordinates for symmetry-inequivalent atoms that occupy the Wyckoff positions with free parameters in the crystallographic unit cell. The other atomic coordinates are uniquely determined by specifying the space group and the coordinates of the Wyckoff position occupied by the atoms. A comparison of the calculated and experimental atomic coordinates is given in [3]. The difference between the experimental and calculated values does not exceed 3–5%.

3. CHOICE OF THE DFT COMPUTATIONAL SCHEME IN THE LCAO APPROXIMATION

The calculations were performed by the DFT method in the LCAO basis set with the CRYSTAL-2003 code [6] and the Perdew–Burke–Ernzerhof (PBE) exchange–correlation potential [7] used in [3] for the geometry optimization in the generalized gradient approximation (GGA). For the Sr and Zr atoms, we used the Hay–Wadt pseudopotentials [8] in the small core approximation. In this case, the 4*s*, 4*p*, and 5*s* states of the Sr atom in the $4s^24p^65s^2$ configuration and the 4s, 4*p*, 4*d*, and 5*s* states of the Zr atom in the $4s^24p^64d^25s^2$ configuration were treated as valence states. The basis functions were taken as the atomic functions of the Sr atom from [9] and the 8–411*G** functions obtained for the Zr atom in [10] with optimization of the 5*sp*, 6*sp*, and 5*d* outer orbitals for the ZrO_2 crystal with experimental geometric parameters. For the oxygen atom, we used the full-electron basis set [9] describing the oxygen atom in the $1s^22s^22p^4$ configuration.

Table 2. Experimental [5] and optimized [3] (given in parentheses) fractional coordinates of the symmetry-inequivalent atoms in the crystallographic unit cell of the $SrZrO_3$ crystal

Phase	Atom	Coordinates		
		x	*y*	*z*
*I*4/*mcm*	O_2	0.265 (0.250)	0.765 (0.750)	0.000
Cmcm	Sr_1	0.000	0.993 (0.989)	0.250
	Sr_2	0.000	0.490 (0.495)	0.250
	O_1	0.269 (0.290)	0.000	0.000
	O_2	0.000	0.230 (0.214)	0.041 (0.048)
	O_3	0.286 (0.3000)	0.252 (0.255)	0.250
Pbnm	Sr_1	0.003 (0.007)	0.526 (0.533)	0.250
	O_2	0.927 (0.923)	0.982 (0.979)	0.250
	O_3	0.217 (0.213)	0.284 (0.287)	0.035 (0.041)

Table 3. Band gap ΔE_γ (eV) at the Γ point for the *Fm*3*m* cubic (*c*), $P4_2/nmc$ tetragonal (*t*), and $P12_1/c$ monoclinic (*m*) phases of the ZrO_2 crystal and their relative energies ΔE (eV/ZrO_2)

	HF	B3LYP	PBE	DFT–PW [12]
$\Delta E_{\gamma c}$ (4.5)	14.0	5.5	3.7	3.9
$\Delta E_{\gamma t}$ (5.0)	14.2	5.8	4.0	4.1
$\Delta E_{\gamma m}$ (5.3)	13.8	5.7	3.9	4.0
ΔE_t (−0.06)	+0.01	−0.04	−0.05	−0.05
ΔE_m (−0.12)	−0.04	−0.10	−0.09	−0.11

Note: The experimental values are given in parentheses. The energy per unit cell of the cubic phase is taken as the zero of the relative energy ΔE.

Table 4. Band gap ΔE_γ (eV) at the Γ point for the *Pm*3*m* cubic (*c*), $I4_2/mcm$ tetragonal (*t*), *Cmcm* orthorhombic (*o*1), and *Pbnm* orthorhombic (*o*2) phases of the $SrZrO_3$ crystal and their relative energies ΔE (eV/$SrZrO_3$)

	HF	B3LYP	PBE
$\Delta E^*_{\gamma c}$ (5.6)	13.0	5.0	3.3
$\Delta E_{\gamma t}$	13.0	5.0	3.3
$\Delta E_{\gamma o1}$	13.2	5.2	3.5
$\Delta E_{\gamma o2}$	13.5	5.4	3.6
ΔE_t	0.00	0.00	0.00
ΔE_{o1}	−0.16	−0.23	−0.24
ΔE_{o2}	−0.19	−0.28	−0.29

Note: The difference in the energies of the bottom of the conduction band at the Γ point and the top of the valence band at the *X* point is presented for the cubic phase. The experimental value is given in parentheses. The energy per unit cell of the cubic phase is taken as the zero of the relative energy ΔE.

In order to assess the capabilities of the LCAO approximation for calculating the relative stability of different crystal phases with the basis set chosen for the Zr and O atoms, the electronic structure of the ZrO_2 crystal in three modifications (cubic *Fm*3*m*, tetragonal $P4_2/nmc$, monoclinic $P12_1/c$) with experimental values of the lattice parameters and coordinates of atoms in the unit cell was calculated by the Hartree–Fock (HF) method, the DFT method with the PBE gradient correction (the exchange–correlation potential taken from [3]), and the B3LYP hybrid method [11]. The relative energies (the energy per unit cell of the cubic phase was taken as the zero of the relative energy) calculated per formula unit by the DFT method in the plane wave (PW) basis set [12], the HF method, the DFT method with the PBE gradient correction (the exchange–correlation potential used in [3]), and the B3LYP hybrid method [11] are compared with the experimental data in Table 3. The calculated and experimental band gaps ΔE_γ are also given in Table 3. It can be seen from this table that only the inclusion of the electron correlation makes it possible to reproduce correctly the relative energies of different phases. Note that the results obtained using the PBE and B3LYP schemes are close to each other. The band gap is closer to the experimental value in the case of the hybrid computational scheme and is considerably overestimated in the HF calculations.

For the cubic modification of the $SrZrO_3$ crystal, there are 46 electrons per unit cell (23 occupied energy bands, including three bands attributed to the O 1*s* core states). It is worth noting that the number of electrons and occupied energy bands is doubled for the tetragonal modification and increases fourfold for the orthorhombic modifications. The summation in the Brillouin zone was performed over the Monkhorst–Pack special points. For the isotropic cubic crystal (*Pm*3*m*), we used an $8 \times 8 \times 8$ set of special points. This corresponds to the simulation of an infinite crystal by a cyclic cluster consisting of 512 primitive cells [13]. In order to ensure an approximately identical density of the **k** points along each of the three vectors of the reciprocal lattice, the set of Monkhorst–Pack special points for the noncubic crystals was reduced in inverse proportion to the translation vector of the direct lattice in the corresponding direction. All the calculations were carried out for the geometry optimized in [3]. The accuracy of the summation in the direct lattice was chosen equal to 10^{-12} for the exchange integrals and 10^{-6} for the other integrals of the atomic functions. The procedure providing the self-consistency with respect to the density matrix was performed until the difference between the total energies per unit cell for two consecutive iterations reached 10^{-7} au.

The band gaps and relative energies calculated for each of the crystalline modifications of strontium zirconate by the same methods that were used in the calculations for the ZrO_2 crystals are given in Table 4. For the cubic crystal, the experimental band gap [14] is compared with the theoretical values obtained in the plane wave basis set [4] and in the LCAO basis set [3]. The values listed in Table 4 confirm the inferences made for the modifications of the ZrO_2 crystals.

The results of the calculations discussed below for the $SrZrO_3$ crystals were obtained (as in [3]) by the DFT method (the PBE variant).

4. ELECTRONIC STRUCTURES OF DIFFERENT MODIFICATIONS OF STRONTIUM ZIRCONATE

The calculated band structures and densities of states for four modifications of the $SrZrO_3$ crystals are presented in Figs. 1a–4a and 1b–4b, respectively. A comparison of the results obtained shows that, in general, the electronic structures of the cubic and tetragonal phases are similar to each other. The same is also true for two orthorhombic structures. A substantial change in the electronic structure is observed upon

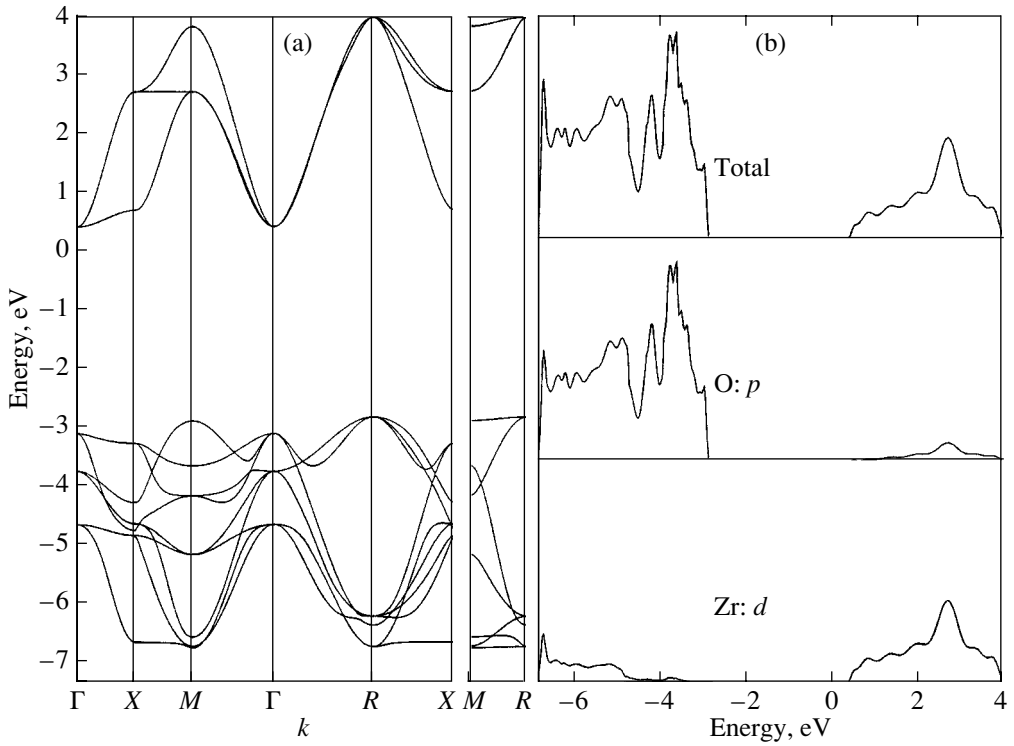

Fig. 1. (a) Band structure and (b) densities of states for the cubic modification (space group *Pm*3*m*) of the $SrZrO_3$ crystal.

changing over from the tetragonal modification to the orthorhombic modification.

Analysis of the total and partial densities of states for the cubic and tetragonal crystals (Figs. 1, 2) demonstrates that the total density of states in the upper valence band is predominantly formed by the O 2*p* states. It can also be seen that the Zr 4*d* states make the dominant contribution to the bottom of the conduction band. Similar features of the electronic structure are observed for the orthorhombic phases.

The atomic charges determined for all four modifications from the Mulliken population analysis are compared in Table 5. The charges are given for all crystal chemically inequivalent atoms in the crystallographic unit cell. It can be seen from Table 5 that, upon changing over from the cubic modification to the tetragonal modification, the atomic charges remain virtually unchanged. For the two orthorhombic phases, the atomic charges are also close to each other. However, upon changing over from the tetragonal phase to the orthorhombic phases, the atomic charges change significantly. This distribution of the atomic charges indicates that the electronic structure of the cubic and tetragonal modifications differs substantially from the electronic structure of the two orthorhombic modifications of the $SrZrO_3$ crystals.

A comparative analysis of the specific features of the chemical bonding in different modifications of crystalline $SrZrO_3$ was also performed using the localized Wannier functions. The results obtained are considered in the next section.

5. LOCALIZED WANNIER FUNCTIONS AND CHEMICAL BONDING IN THE $SrZrO_3$ CRYSTAL

The localized Wannier functions $W_n(\mathbf{r} - \mathbf{g})$ (where $n = 1, \ldots, N$ is the number of localized Wannier functions per primitive cell and $\mathbf{g}$ is the translation vector of the direct lattice) are determined in terms of the Bloch functions $\psi_t(\mathbf{k}_j)$ for N energy bands according to the relationship

$$W_n(\mathbf{r}-\mathbf{g}) = L^{-1/2}\sum_{t=1}^{N}\sum_{j=1}^{L} U_{nt}(\mathbf{k}_j)\psi_{i\mathbf{k}_j}(\mathbf{r})e^{-i\mathbf{k}_j\mathbf{g}}. \quad (1)$$

Table 5. Mulliken charges (*e*) at the atoms in the $SrZrO_3$ crystal

Atom	Phase			
	*Pm*3*m*	*I*4/*mcm*	*Cmcm*	*Pbnm*
Sr_1	+1.855	+1.855	+1.828	+1.834
Sr_2			+1.845	
Zr	+2.035	+2.035	+2.085	+2.091
O_1	–1.297	–1.297	–1.308	–1.307
O_2		–1.297	–1.303	–1.309
O_3			–1.311	

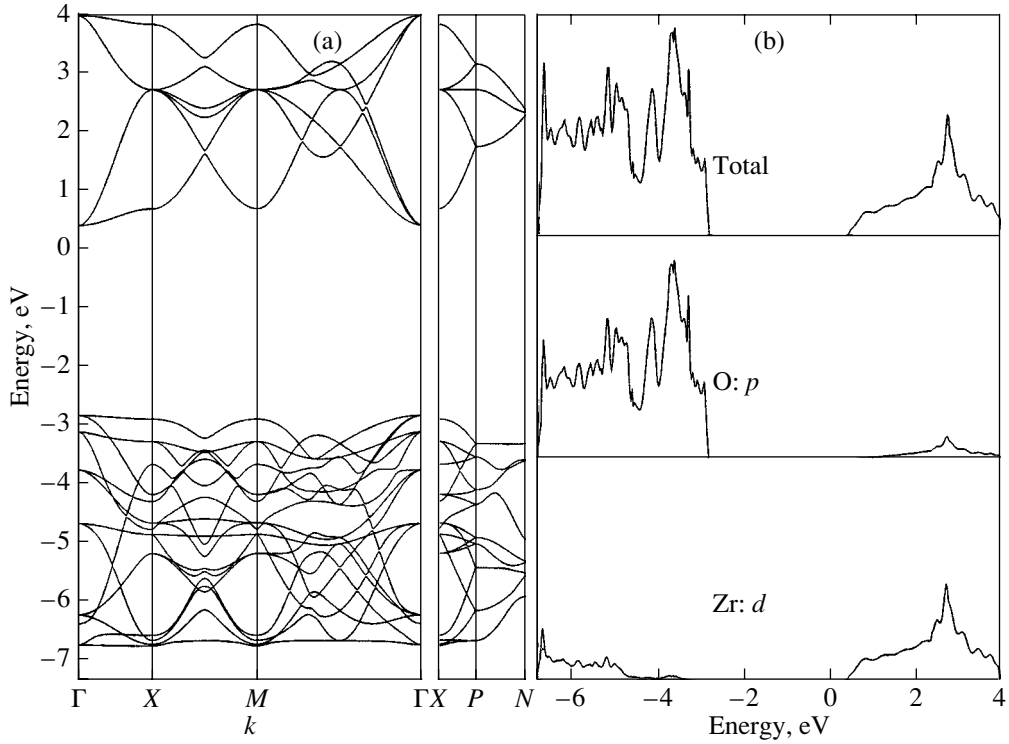

Fig. 2. (a) Band structure and (b) densities of states for the tetragonal modification (space group *I*4/*mcm*) of the $SrZrO_3$ crystal.

Here, L is the number of primitive cells in the cyclic system (the range of variation in vectors **g**) and the points $\mathbf{k}_j$ (j = 1, 2, 3, …) in the Brillouin zone satisfy the relationship $\exp(-i\mathbf{k}_j\mathbf{T}) = 1$ for the translation vectors **T** of the cyclic system as a whole [15].

The matrices $U(\mathbf{k}_j)$ of the unitary transformation (1) of the Bloch functions into the localized Wannier functions are determined in accordance with a specified criterion for localization of the Wannier functions. Marzari and Vanderbilt [16] and Zicovich-Wilson *et al.* [17] used the Boys criterion, according to which the spread of the localized Wannier functions with respect to the centroid **q** in the direct lattice must be minimum; that is,

$$\begin{aligned} \min I_n &= \min \int (\mathbf{r}-\mathbf{q})^2 |W_n(\mathbf{r})|^2 d\tau, \\ \mathbf{q} &= \int |W_n(\mathbf{r})|^2 \mathbf{r} d\tau. \end{aligned} \tag{2}$$

In order to analyze the chemical bonding in the crystal, the summation in expression (1) is performed over occupied energy bands [17] or groups of occupied bands [16]. This determines the symmetry of the constructed localized Wannier functions as basis sets of irreducible representations of the local symmetry group of the centroid **q** [18]. The constructed localized Wannier functions describe both the *A*–*B* diatomic bonds between atoms *A* and *B* in the crystal (the centroid **q** is located either on the line of the bond or in its vicinity) and the lone electron pairs at atoms or ions (the centroid **q** is located near the relevant atomic nucleus). The Bloch functions can be calculated in the plane wave basis set [16] and in the LCAO approximation [17]. In the latter case, the localized Wannier functions can be expressed in terms of the functions of the initial atomic basis set:

$$W_n(\mathbf{r}) = \sum_{\mu=1}^{M} \sum_{\mathbf{g}} C_{\mu n}^{\mathbf{g}} \varphi_\mu(\mathbf{r}-\mathbf{g}), \tag{3}$$

where the coefficients $C_{\mu n}^{\mathbf{g}}$ refer to the atomic function φ_μ in the cell **g** and are related to the coefficients $a_{\mu t}^{\mathbf{k}}$ of the Bloch function $\psi_{i\mathbf{k}_j}$ by the expression

$$C_{\mu n}^{\mathbf{g}} = L^{-1} \sum_{t=1}^{N} \sum_{j=1}^{L} U_{nt}(\mathbf{k}_j) e^{i\mathbf{k}_j\mathbf{g}} a_{\mu t}^{\mathbf{k}_j}. \tag{4}$$

The contribution from the *A*th atom of the cell **g** to the population of the *n*th localized Wannier function (the total population of the localized Wannier function is equal to 2) is defined by the relationship

$$q_{An}^{\mathbf{g}} = 2 \sum_{A} \sum_{\mu \in A} \sum_{\nu} \sum_{\mathbf{g}'} C_{\mu n}^{\mathbf{g}} C_{\nu n}^{\mathbf{g}+\mathbf{g}'} S_{\mu\nu}^{0\mathbf{g}'}. \tag{5}$$

Here, the sum $\sum_A \sum_{\mathbf{g}} q_{An}^{\mathbf{g}}$ is equal to 2 for any n = 1, 2, …, N (the summation is performed over all atoms

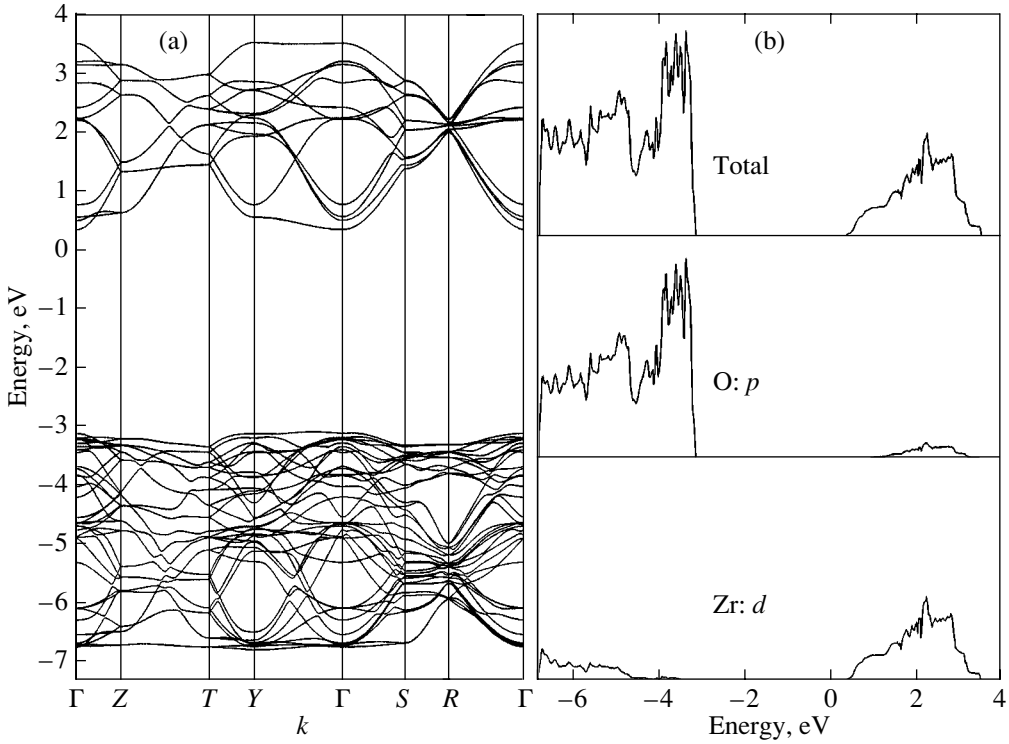

Fig. 3. (a) Band structure and (b) densities of states for the orthorhombic modification (space group *Cmcm*) of the $SrZrO_3$ crystal.

and cells of the chosen cyclic system) and $S_{\mu\nu}^{0\mathbf{g}'}$ are the overlap integrals of the atomic basis functions. It is obvious that the total number of electrons per primitive cell is $n_e = 2N$. Since transformation (1) is unitary, the Mulliken atomic populations satisfy the relationship

$$q_A = 2\sum_{A}\sum_{n\mathbf{g}} q_{An}^{\mathbf{g}} = 2\sum_{t=1}^{N}\sum_{\mu\in A}\sum_{\nu\mathbf{g}'}\sum_{\mathbf{k}\mathbf{k}'} a_{\mu t}^{\mathbf{k}} a_{\nu t}^{\mathbf{k}'} S_{\mu\nu}^{0\mathbf{g}'}; \quad (6)$$

i.e., they correspond to the results of the traditional population analysis in the initial atomic basis set.

It should be noted that the population analysis can also be performed in the basis set of the Wannier-type atomic functions (WTAF), which correspond to the minimal basis set and were introduced in [19]. However, in this case, the localized Wannier functions must be constructed using the Bloch functions not only of the occupied states but also of the vacant states determined from the symmetry requirements [18]. The results of the population analysis in the WTAF basis set differ from those obtained in the initial atomic basis set and, in the majority of cases, more correctly describe the chemical bonding in the crystal as compared to the traditional population analysis. Moreover, the atomic populations in the crystal can be analyzed using the projection technique [20], which is not related to the construction of the localized Wannier functions.

Zicovich-Wilson *et al.* [17] introduced an index characterizing the degree of localization of Wannier functions, that is,

$$\lambda_n = \left[\sum_{A}\sum_{\mathbf{g}} (q_{An}^{\mathbf{g}})^2\right]^{-1}, \quad (7)$$

which is equal to unity when the Wannier function is almost completely localized in the vicinity of an individual atom and is larger than unity in other cases (for the Wannier function localized at the center of the bond, this index is equal to two).

The ionicity of the chemical bond, which is formed between atoms A (with the coordinate $\mathbf{r}_A$) and B (with the coordinate $\mathbf{r}_B$) and is described by the nth Wannier function centered at the point $\mathbf{q}_n$, can be evaluated using the index

$$p_n = 2\frac{(\mathbf{q}_n - \mathbf{r}_B)(\mathbf{r}_A - \mathbf{r}_B)}{|\mathbf{r}_A - \mathbf{r}_B|^2} - 1. \quad (8)$$

It is assumed that atoms A and B make a maximum contribution to the population of this Wannier function as compared to other atoms. The index p_n given by expression (8) is equal to unity for a purely ionic bond and zero for a purely covalent bond. Intermediate values of the index p_n can be related to the ionicity of chemical bonds.

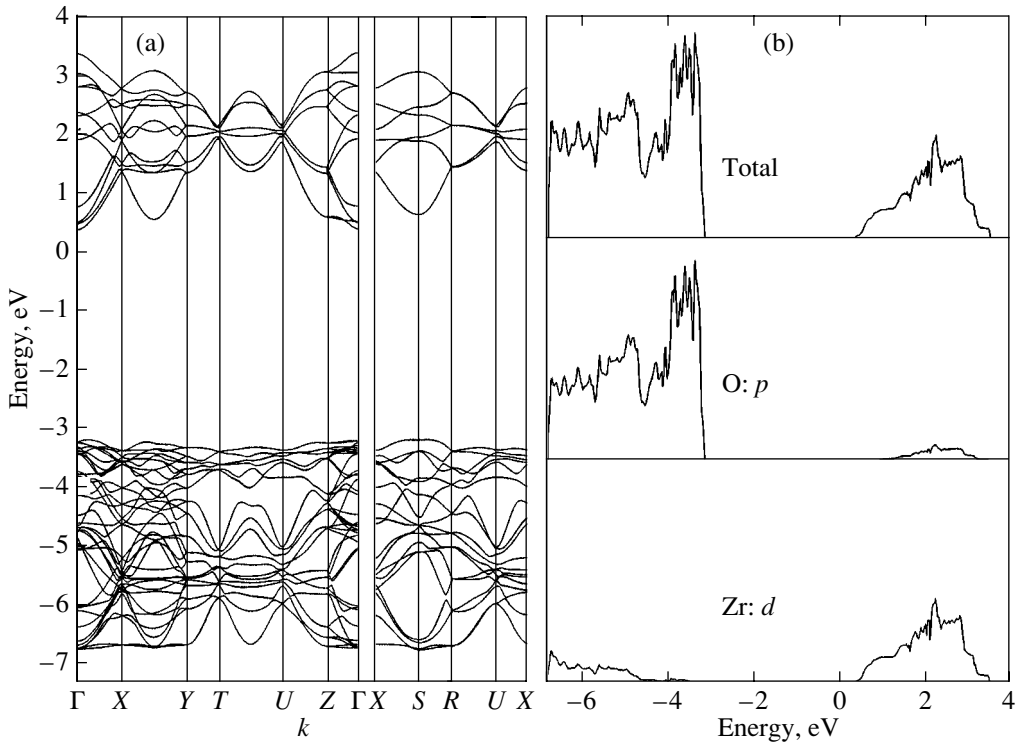

Fig. 4. (a) Band structure and (b) densities of states for the orthorhombic modification (space group *Pbnm*) of the $SrZrO_3$ crystal.

In order to investigate the chemical bonding in the $SrZrO_3$ crystal, we calculated the localized Wannier functions for the occupied energy bands with the CRYSTAL code [5]. The localization characteristics were determined for two upper valence bands (consisting of 15, 30, and 60 branches for the cubic, tetragonal, and orthorhombic modifications, respectively). The lower valence band is hybrid (formed by the O 2*s* states and Sr 4*p* states), whereas the upper valence band, as can be seen from Figs. 1–4, is formed by the O 2*p* states. The numerical values of the delocalization index, the ionicity of the Zr–O chemical bond, and the contribution of the oxygen atom (without regard for the spin) to the population of the symmetry-inequivalent Wannier functions of the upper valence band were determined from relationships (7), (8), and (5). The numerical data obtained for the cubic and orthorhombic modifications are given in Table 6. The last four columns of Table 6 list numerical values of the populations of the *s* and *p* functions for the oxygen atom near which the corresponding Wannier function is centered.

In the cubic modification, all three oxygen atoms in the primitive cell are symmetrically equivalent and four Wannier functions are centered in the vicinity of each oxygen atom. Let us assume that the oxygen atom and the two nearest zirconium atoms are arranged along the *z* axis. It can be seen from Table 6 that two of the four Wannier functions (Figs. 5a, 5b) are located perpendicular to the bond and aligned with the *x* and *y* axes (this is confirmed by the analysis of the corresponding contributions to the population). The ionicity of the Zr–O bond, which is described by these functions, is close to unity; i.e., they are actually the O p_x and O p_y orbitals in the crystal. The other two localized orbitals (Figs. 5c, 5d) are equivalent, lie almost exactly along the *z* axis, and, as follows from the populations, correspond approximately to the O sp_z hybrid orbitals. For these orbitals, the bond ionicity (0.61) is substantially different from unity. This indicates a significant covalency of the Zr–O bond, which also manifests itself in the atomic charges (Table 5). The distance from the centroid **q** to the oxygen atom is equal to 0.25 Å for the former two Wannier functions and 0.44 Å for the latter two Wannier functions. The corresponding distances from the centroid to the line of the Zr–O bond are equal to 0.24 and 0.16 Å. These data correlate with the above interpretation of the localized orbitals.

For the tetragonal modification, the indices (characterizing the chemical bonds) of the Wannier functions localized at the oxygen atoms are close for symmetry-inequivalent oxygen atoms and differ only slightly from those for the cubic modification. This correlates with nearly identical atomic charges in the cubic and tetragonal modifications (Table 5).

It can be seen from Table 6 that, for the orthorhombic modification, the Wannier functions localized at the symmetry-inequivalent oxygen atoms and directed along the Zr–O bonds (Figs. 5g, 5h) also differ only slightly from those for the cubic modification, even

Table 6. Characteristics of the localized Wannier functions for the $SrZrO_3$ crystal

Phase, atom	λ_s	p_n	q_{0_n}	q_s	q_{p_x}	q_{p_y}	q_{p_z}
*Pm*3*m*	1.183	0.999	0.918	0.136	0.005	0.778	0
	1.183	0.999	0.918	0.136	0.778	0.005	0
	1.302	0.610	0.870	0.343	0.064	0.064	0.403
	1.300	0.610	0.870	0.341	0.066	0.066	0.400
Pbnm, O_1	1.158	1.050	0.928	0.193	0.694	0.043	0
	1.175	1.011	0.921	0.147	0.001	0.775	0
	1.296	0.599	0.872	0.308	0.107	0.047	0.414
	1.296	0.599	0.872	0.308	0.107	0.047	0.414
Pbnm, O_2	1.182	0.994	0.919	0.138	0.179	0.164	0.439
	1.153	1.041	0.930	0.196	0.263	0.289	0.184
	1.293	0.605	0.873	0.308	0.267	0.146	0.155
	1.293	0.601	0.873	0.316	0.161	0.269	0.131

though they do not correspond to the pure sp_z hybridization ($\angle ZrOZr = 155°$, and the p_x and p_y orbitals make a noticeable contribution to the populations of the Wannier functions due to the symmetry reduction). As regards the two other pairs of localized orbitals (Figs. 5e, 5f), their orientation differs from the orientation of the corresponding pair in the cubic crystal and the total contribution of the *p* orbitals to these functions is somewhat smaller than the analogous contribution in the cubic phase. There is no significant difference between the orbitals localized at the O_1 and O_2 atoms.

If the constructed localized orbitals are considered only in the upper valence band, it is impossible to distinguish orbitals corresponding to the directional Zr–O bonds. Therefore, the O *s* band makes a substantial contribution to the density distribution of valence electrons. However, when analyzing the energy spectrum and the corresponding density of states, the O *p* and O *s* bands can be treated as relatively independent. For

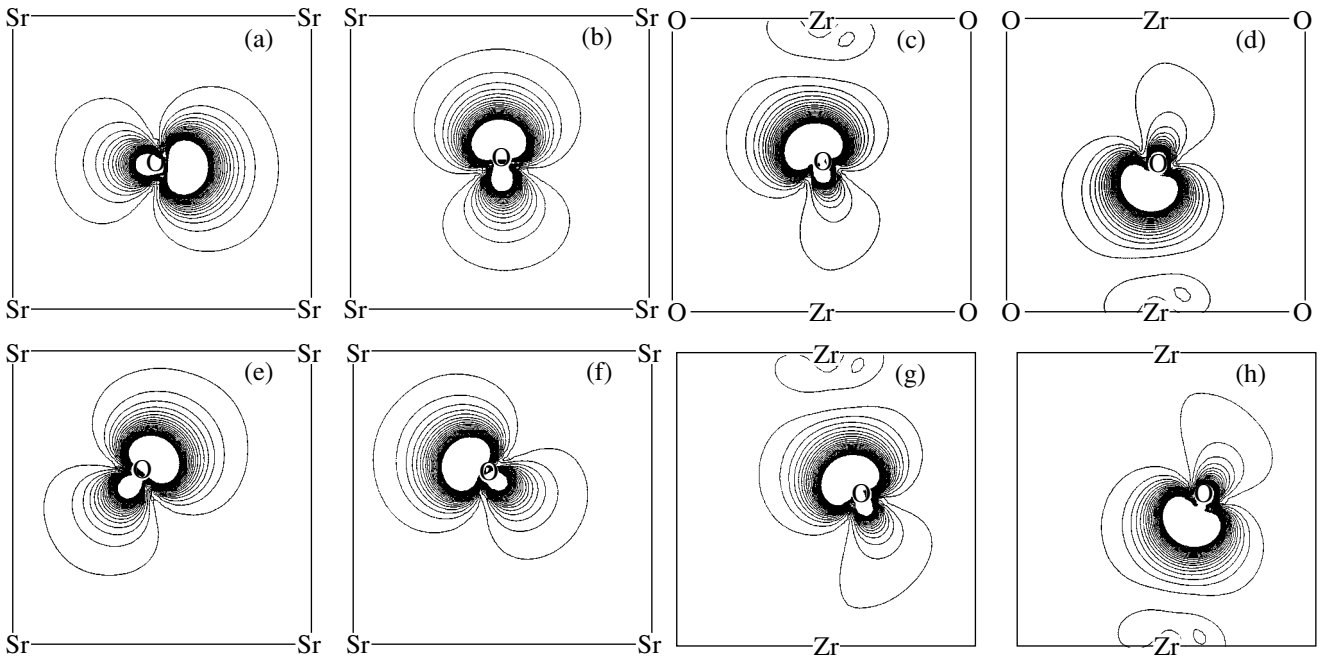

Fig. 5. Localized Wannier functions for the oxygen atoms in (a–d) cubic and (e–h) orthorhombic modifications of the $SrZrO_3$ crystal. The electron density distributions are represented in (a, b, e, f) the plane formed by the strontium atoms nearest to the oxygen atom, (c, d) the σ_x plane, and (g, h) the plane passing through the bound Zr–O–Zr atoms. Symbols of the elements indicate the positions of the atoms in the planes under consideration.

example, as was noted in Section 4, the total density of states in the energy range of the upper valence band nearly coincides with the partial density of O *p* states.

The above treatment demonstrates that the use of the localized Wannier functions in analyzing the chemical bonding in the crystal essentially complements and provides details for the information obtained in the population analysis.

6. CONCLUSIONS

The electronic structure (the energy band spectrum, densities of states, and Wannier functions) of four modifications of crystalline $SrZrO_3$ was calculated in the framework of the density-functional theory in the LCAO approximation with the parameters of the atomic structure previously optimized in the plane wave basis set. The main results obtained in this study can be summarized as follows.

(1) The energy stability of the high-temperature (tetragonal and cubic) modifications is less than that of the low-temperature orthorhombic modifications. This is in agreement with experimental data.

(2) The calculated band gap for the low-temperature modifications is greater than that for the high-temperature modifications. This is consistent with the fact that, according to the Mulliken population analysis, the chemical bonding in the low-temperature modifications is characterized by a higher ionicity.

(3) The localized Wannier functions for the two upper valence energy bands were calculated and analyzed. The obtained characteristics of the Wannier functions (the positions of the centroid, the ionicity indices, the atomic contributions to the populations of the localized orbitals) made it possible to describe quantitatively the covalent component of the chemical bonding in the $SrZrO_3$ crystals.

ACKNOWLEDGMENTS

This work was supported by the Russian Foundation for Basic Research, project no. 05-03-32002-a.

REFERENCES

1. T. Matsuda, S. Yamanaka, K. Kurosaki, and S. Kobayashi, J. Alloys Compd. **351**, 43 (2003).
2. E. Heifets, R. I. Eglitis, E. A. Kotomin, J. Maier, and G. Borstel, Phys. Rev. B: Condens. Matter **64**, 235 417 (2001).
3. R. A. Evarestov, A. V. Bandura, V. E. Alexandrov, and E. A. Kotomin, Phys. Status Solidi B **242** (2), R11 (2005).
4. E. Mete, R. Shaltaf, and S. Ellialtioglu, Phys. Rev. B: Condens. Matter **68**, 035 119 (2003).
5. B. J. Kennedy, C. J. Howard, and B. C. Chakoumakos, Phys. Rev. B: Condens. Matter **59**, 4023 (1999).
6. V. R. Saunders, R. Dovesi, C. Roetti, R. Orlando, C. M. Zicovich-Wilson, N. M. Harrison, K. Doll, B. Civalleri, T. Bush, Ph. D'Arco, and M. Llunell, *CRYSTAL-2003: User's Manual* (Torino University, Torino, 2003).
7. J. P. Perdew, K. Burke, and M. Ernzerhof, Phys. Rev. Lett. **77**, 3865 (1996).
8. P. J. Hay and W. R. Wadt, J. Chem. Phys. **82**, 270 (1985).
9. S. Piskunov, E. Heifets, R. I. Eglitis, and G. Borstel, Comput. Mater. Sci. **29**, 165 (2004).
10. S. Gennard, F. Cora, and C. R. A. Catlow, J. Phys. Chem. B **103**, 10 158 (1999).
11. A. D. Becke, J. Chem. Phys. **98**, 5648 (1993).
12. A. D. Dash, N. Vast, P. Baranek, M. Cleynet, and L. Reining, Phys. Rev. B: Condens. Matter **70**, 245 116 (2004).
13. R. A. Evarestov and V. P. Smirnov, Phys. Rev. B: Condens. Matter **70**, 233 101 (2004).
14. Y. S. Lee, J. S. Lee, T. W. Noh, D. Y. Byum, K. S. Yoo, K. Yamaura, and E. Takayama-Muromachi, Phys. Rev. B: Condens. Matter **67**, 113 101 (2003).
15. R. A. Évarestov and I. I. Tupitsyn, Fiz. Tverd. Tela (St. Petersburg) **44**, 1582 (2002) [Phys. Solid State **44**, 1656 (2002)].
16. N. Marzari and D. Vanderbilt, Phys. Rev. B: Condens. Matter **56**, 12 847 (1997).
17. C. M. Zicovich-Wilson, R. Dovesi, and V. R. Saunders, J. Chem. Phys. **115**, 9708 (2001).
18. R. A. Évarestov, D. E. Usvyat, and V. P. Smirnov, Fiz. Tverd. Tela (St. Petersburg) **45**, 1972 (2003) [Phys. Solid State **45**, 2072 (2003)].
19. V. P. Smirnov, R. A. Evarestov, and D. E. Usvyat, Int. J. Quantum Chem. **88**, 642 (2002).
20. I. I. Tupitsyn, R. A. Évarestov, and V. P. Smirnov, Fiz. Tverd. Tela (St. Petersburg) **47** (10), 1768 (2005) [Phys. Solid State **47** (10), 1837 (2005)].

Translated by O. Borovik-Romanova

Physics of the Solid State, Vol. 47, No. 12, 2005, pp. 2257–2261. Translated from Fizika Tverdogo Tela, Vol. 47, No. 12, 2005, pp. 2166–2169.

DEFECTS, DISLOCATIONS, AND PHYSICS OF STRENGTH

Diffusion in Dislocation Germanium and the Model of a Liquid Dislocation Core

É. V. Dobrokhotov

Lobachevskiĭ Nizhni Novgorod State University, pr. Gagarina 23, Nizhni Novgorod, 603950 Russia

e-mail: doev4@uic.nnov.ru

Received December 9, 2004; in final form, May 2, 2005

Abstract—Experimental data on the diffusion of ^{71}Ge, ^{113}Sn, ^{114}In, and ^{124}Sb isotopes in dislocation germanium are discussed within the model of a liquid dislocation core and the filament model of diffusion along dislocations. The temperature dependences of the diffusion permeability along the dislocations are matched to the corresponding temperature dependences of the coefficient of diffusion in the melt in order to determine the absolute values of the coefficient of diffusion along dislocations and the effective diffusion radius of the dislocation core. The experimental results are discussed in terms of thermodynamic parameters of the liquid state and the parameters of diffusion in the melt. The results obtained are consistent with the cooperative diffusion mechanism and the mechanism of diffusion through relaxed vacancies. © *2005 Pleiades Publishing, Inc.*

1. INTRODUCTION

Numerous experimental and theoretical investigations into the diffusion along dislocations and low-angle grain boundaries have revealed that enhanced transfer occurs in these objects. Enhanced diffusion along a dislocation has often been explained as resulting from the motion of vacancies whose concentration and mobility are significantly higher than those of vacancies in the bulk of the material [1, 2]. An increase in the concentration and mobility of the vacancies is directly attributed to the disturbance of the crystal structure in the region around the dislocation [1–4].

The existing mathematical models of diffusion along dislocations enable one to determine only the diffusion permeability $D'S$ [4], where D' is the coefficient of diffusion along a dislocation and $S = \pi r_d^2$ is the cross-sectional area of the dislocation (r_d is the effective diffusion radius of the dislocation). Consequently, a great deal of the reasoning about mechanisms of diffusion along dislocations lacks rigorous justification. In this respect, it is obviously important to choose a physical model that would enable one to unambiguously determine the coefficient of diffusion along a dislocation and the effective cross section of the dislocation.

Earlier [2], it was noted that, as the melting point is approached, regions of dislocation outcrop on the germanium surface undergo melting in the temperature range 920–935°C. It can be assumed that, in the vicinity of the melting temperature, the structure of the dislocation core is similar to the structure of the melt; therefore, the dislocation core can be simulated by a liquid state.

2. MODEL OF A LIQUID DISLOCATION CORE

The model of a liquid dislocation core has been successfully used to describe the configuration of the dislocation core, the energy of the interface between the core and the matrix, and the elastic stresses arising in the core and in the matrix [5].

Lange [6] demonstrated that, upon extrapolation to the melting point, the coefficients of diffusion along the dislocations and in the melt coincide to within the limits of experimental error. At the same time, there is a difference of several orders of magnitude between the experimental data on the diffusion along the dislocations and in the melt, on the one hand, and the results obtained for the diffusion in the bulk of the material, on the other hand. The degree of coincidence between the temperature dependences of the coefficient of diffusion along the dislocations and in the liquid state depends on the change in the coordination number upon passing through the melting point [2].

From the aforesaid, it can be concluded that the structure of the dislocation core is similar to the structure of the melt in the vicinity of the melting temperature. This does not mean that the dislocation core is universally analogous to the liquid state. The model of a liquid dislocation core is only an approximation to the real structure of the dislocation core.

Nonetheless, the physical model of a liquid dislocation core enables one to analyze the processes occurring in dislocation crystals with the use of the thermodynamic potentials and parameters (including diffusion parameters) characteristic of the liquid state.

In simulating the dislocation core by a liquid state, we assume that the coefficients of diffusion along the dislocations are equal to those in the melt at the melting point: $D' = D_L$ at $T = T_{melt}$ (where T_{melt} is the melting

temperature and D_L is the coefficient of diffusion in the melt). By assuming that the effective diffusion radius of the dislocation r_d is constant and independent of temperature, it is possible to determine the "absolute" values of the coefficients of diffusion along the dislocations, which cannot be done within the known mathematical models.

In order to use the model of a liquid dislocation core for analyzing the experimental data on the diffusion in dislocation crystals, it is necessary to obtain comprehensive information on the diffusion in the liquid phase. For this purpose, we studied the diffusion of ^{71}Ge, ^{113}Sn, ^{114}In, and ^{124}Sb isotopes in germanium in the temperature range 950–1250°C [7, 8].

Then, we proposed a filament model accounting for the influence of the dislocation on the diffusion in the bulk over a wide range of temperatures up to the melting point [9].

The problem is reduced to solving the system of differential equations

$$\frac{\partial C}{\partial t} = D\Delta^2 C + Kf(z, t), \tag{1}$$

$$\frac{\partial C'}{\partial t} = D'\frac{\partial^2 C'}{\partial z^2} - \frac{1}{S}f(x, t), \tag{2}$$

where K is a constant; S is the cross section of the dislocation; D and D' are the coefficients of diffusion in the bulk and along the dislocation, respectively; and C' is the concentration of impurities along the dislocation.

In the above system, Eqs. (1) and (2) describe the diffusion outside the dislocation region and along the dislocations, respectively.

The problem is solved at first-order boundary conditions (a steady source at the surface), which are of most frequent occurrence in practice:

in the bulk,

$$C(x, y, z, t) = C_0 \quad \text{for} \quad z = 0, \quad t > 0;$$

along the dislocation,

$$\delta(x, y)C(x, y, z, t) = C'(z, t) \quad \text{for} \quad z > 0, \quad t = 0. \tag{3}$$

Under the condition

$$S < \frac{(Dt)^{3/2}}{\sqrt{D't}}, \tag{4}$$

the solution to the system of equations (1) and (2) has the form

$$\bar{C} = C_0 \operatorname{erfc}\frac{z}{2\sqrt{Dt}} + C_0 NS\frac{D'}{D}\frac{K\pi}{4}\frac{z}{2\sqrt{Dt}}\exp\left(-\frac{z^2}{4Dt}\right). \tag{5}$$

Let us introduce the following notation:

$$\Phi^*(z, t) = \operatorname{erfc}\frac{z}{2\sqrt{Dt}},$$

$$\Phi_2^*(z, t) = \frac{4}{\sqrt{\pi}}\frac{z}{2\sqrt{Dt}}\exp\left(-\frac{z^2}{4Dt}\right), \tag{6}$$

$$P = N\frac{D'}{D}S\frac{K\pi}{4}.$$

Then, relationship (5) takes the form

$$C/C_0 = \Phi^*(z, t) + P\Phi_2^*(z, t). \tag{7}$$

Relationship (7) was used to construct a set of standard dependences of $\log C/C_0$ on $\log\frac{Z}{2\sqrt{Dt}}$ for different parameters P.

The curves obtained were used for analyzing the experimental data on the diffusion in plastically deformed germanium specimens.

3. DISCUSSION OF THE EXPERIMENTAL DATA ON THE DIFFUSION IN DISLOCATION GERMANIUM WITHIN THE MODEL OF A LIQUID DISLOCATION CORE AND THE FILAMENT MODEL

Specimens of GES-10 germanium were subjected to bending about the [112] direction according to the technique described in our earlier work [9]. The density of dislocations, which was determined visually with an MIM-7 microscope, ranged from 5×10^{-3} to 10^7 cm^{-3}.

The diffusion of ^{71}Ge, ^{113}Sn, ^{114}In, and ^{124}Sb isotopes in germanium was studied over a wide range of temperatures from 600 to 900°C. The annealing time was varied from ten to several hours. Homogenizing annealing was performed in sealed quartz ampules with weighed portions, whose temperature approximately corresponded to the annealing temperature (i.e., it was 20–30°C lower). The distribution of impurities was determined using layer-by-layer etching in standard etchants and was controlled by measuring the length on an IZV-2 length meter and by weighing on a microanalytical balance.

The experimental curves were compared with the theoretical standard curves according to the technique described in [9, 10].

Figure 1 shows the temperature dependences of the coefficient of ^{71}Ge self-diffusion and the coefficient of diffusion of ^{113}Sn, ^{114}In, and ^{124}Sb isotopes along dislocations in germanium. These dependences are matched to the corresponding temperature dependences of the coefficient of diffusion in the germanium melt at $T = T_{\text{melt}}$. The curves were constructed under the above assumption that the structure of the dislocation core is similar to the structure of the melt in the vicinity of the melting point and that the coefficients of diffusion in

the melt are equal to those along the dislocations. These coefficients can be represented in analytical form:

$$D' = 5 \times 10^4 \exp\left(-\frac{2.3}{RT}\right) \quad (\text{Ge} \longrightarrow \text{Ge}),$$

$$D' = 4 \times 10^2 \exp\left(-\frac{1.28}{RT}\right) \quad (\text{Sb} \longrightarrow \text{Ge}),$$

$$D' = 3.1 \times 10^5 \exp\left(-\frac{2.35}{RT}\right) \quad (\text{Sn} \longrightarrow \text{Ge}),$$

$$D' = 1.2 \times 10^5 \exp\left(-\frac{2.3}{RT}\right) \quad (\text{In} \longrightarrow \text{Ge}).$$

The effective diffusion radii of dislocations are presented in the table.

For the vacancy mechanism of diffusion along a dislocation, the preexponential factor D_0' in the diffusion equation can be written in the form

$$D_0' = \varepsilon g a^2 \nu_{\text{jump}} \exp\frac{\Delta S}{kT}, \tag{8}$$

where ε and g are the correlation and geometric factors, respectively; a is the lattice parameter; ν_{jump} is the frequency of jumps, which approximately corresponds to the Debye frequency; and ΔS is the entropy term. According to [11, 12], the change in the entropy can be estimated from the relationship

$$\Delta S = \lambda Q_d \frac{1}{\mu}\frac{\partial \mu}{\partial t}, \tag{9}$$

where λ is a constant close to unity, Q_d is the activation energy of diffusion along the dislocation, and μ is the shear modulus. For the vacancy mechanism of diffusion, the activation energy of diffusion along the dislocation can be represented in the following form [1]:

$$Q_d = E_b + E_d^m + E_d^v, \tag{10}$$

where the first term characterizes the energy of bonding between the diffusing impurity atom (vacancy in the case of self-diffusion) and the dislocation, the second term stands for the energy of migration, and the third term describes the energy of formation of a vacancy.

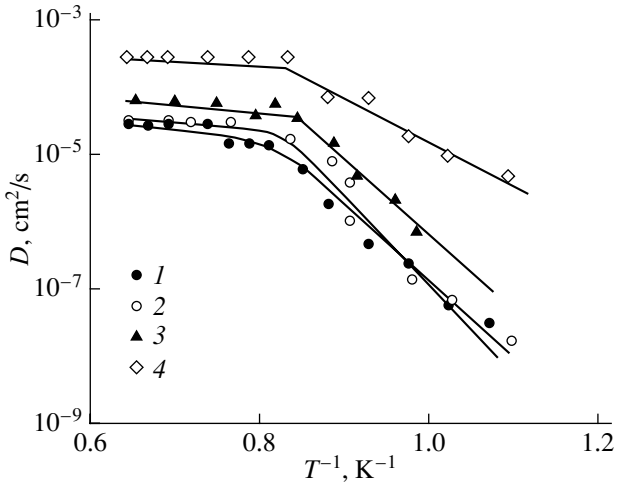

Fig. 1. Temperature dependences of the diffusion coefficient of ^{71}Ge, ^{113}Sn, ^{114}In, and ^{124}Sb isotopes in the germanium melt and the temperature dependences of the coefficient of diffusion of the same elements along the dislocations in germanium according to the calculation within the model of a liquid dislocation core: (*1*) self-diffusion of ^{71}Ge and diffusion of (*2*) ^{113}Sn, (*3*) ^{114}In, and (*4*) ^{124}Sb in germanium.

According to the model of a liquid dislocation core, we can assume that the following relationship holds:

$$E_d^m + E_d' = (Q_L)_{T_{\text{melt}}}. \tag{11}$$

The bonding energy was calculated under the assumption that the impurity atom (or vacancy) and the dislocation are involved in an elastic interaction with the inclusion of the dimensional E_1 and modular E_2 effects (other effects were disregarded). In the case of an edge dislocation [4, 13], we have

$$E_1 = -\frac{1}{3\pi}\frac{1+\nu}{1-\nu}\mu b \Delta V \frac{1}{r_d}, \tag{12}$$

$$E_2 = -\frac{15\mu b^2}{8\pi(1-\nu)(\nu-5\nu)}\frac{V}{r_d}, \tag{13}$$

where ν is the Poisson ratio, b is the strength of the dislocation, V is the atomic volume of the diffusing element, and ΔV is the change in the atomic volume in an elementary diffusion event. In the case of self-diffu-

Calculated and experimental parameters of the diffusion along the dislocations in germanium

Diffusing element	$(Q_L)_{T_{\text{melt}}}$, eV	r_d, Å	ΔV, cm/g-at	E_b, eV	D_0'		$E_b + (Q_L)_{T_{\text{melt}}}$, eV	Q_d, eV
					calculation	experiment		
^{71}Ge	2.1	5	1.53	0.24	0.15	5.0×10^4	2.34	2.3
^{113}Sn	2.1	25	2.6	0.042	0.15	3.1×10^5	2.14	2.35
^{114}In	1.75	12	2.0	0.09	0.16	1.2×10^5	1.8	2.1
^{124}Sb	1.1	40	4.6	0.05	0.09	4.0×10^2	1.15	1.28

sion, the parameter ΔV is the change in the volume due to the formation of a vacancy, which can be estimated from the following considerations [14, 15].

Taking into account the empirical relationship between the activation energy of self-diffusion and the heat of melting, as well as the geometric features of the crystal structure, the change in the volume due to the formation of vacancies in a number of materials was calculated from the expression

$$\left(\frac{\Delta V}{V}\right)_D = \frac{Q}{L}\left(\frac{\Delta V}{V}\right)_{T_{\text{melt}}}. \quad (14)$$

Here, Q and L are the energy of self-diffusion and the heat of melting, respectively; $\left(\frac{\Delta V}{V}\right)_D$ is the relative change in the volume in an elementary diffusion event; and $\left(\frac{\Delta V}{V}\right)_{T_{\text{melt}}}$ is the relative change in the volume due to the melting of the crystal.

Kuz'menko [14, 15] disproved the validity of relationship (14) for diffusion in germanium and silicon semiconductors, because the relative change in the volume due to melting is negative for semiconductors, i.e., $\left(\frac{\Delta V}{V}\right)_{T_{\text{melt}}} < 0$, and is positive for metals, i.e., $\left(\frac{\Delta V}{V}\right)_{T_{\text{melt}}} > 0$.

Indeed, the transfer in metals implies that an elementary diffusion event is a displacement of a single atom into a single vacancy, which corresponds to the inequality $\left(\frac{\Delta V}{V}\right)_{T_{\text{melt}}} > 0$ for close-packed structures. If an elementary event of diffusion in loose structures of germanium and silicon is considered a cooperative process involving a large number of atoms (for example, local melting or the Seeger mechanism of relaxation vacancies and interstices [16]), the idea developed in [14, 15], together with expression (14), can be used to describe the diffusion in silicon and germanium semiconductors satisfying the inequalities $\left(\frac{\Delta V}{V}\right)_D < 0$ and $\left(\frac{\Delta V}{V}\right)_{T_{\text{melt}}} < 0$.

The energy of bonding between the impurity atom (vacancy) and the dislocation can be written as the sum

$$E \approx E_1 + E_2. \quad (15)$$

We demonstrated that the experimental data on the diffusion along dislocations in metals, which were obtained using the model of a liquid dislocation core, are consistent with the vacancy mechanism of diffusion [2].

A comparison of the experimental data on the diffusion in germanium with the results calculated within the model of a liquid dislocation core is given in the table. The activation energy of diffusion can be represented as $Q_d \approx (Q_L)_{T_{\text{melt}}} + E_b$. It turned out that the experimental coefficients D_0' are three to five orders of magnitude greater than the calculated values. This is explained by the fact that the diffusion can occur through the mechanism of relaxed vacancies [16] along dislocations in germanium [2, 4] (as opposed to the pure vacancy mechanism of diffusion along dislocations in metals). In dislocation regions of close-packed metals, the elementary diffusion event is determined by a displacement of a single atom into a single vacancy. In dislocations of crystals with loose packing, such as germanium and silicon, this process should probably involve cooperative motion of a large number of atoms during the formation and migration of such an extended vacancy [16].

When an atom leaves the loose lattice with a diamond-type structure, four directional bonds are broken and the equilibrium between the surrounding atoms is disturbed. This leads to a local disturbance of the short-range order (melting) in the region around the vacant site. It is this mechanism of diffusion through relaxed vacancies that provides an explanation for the decrease in the volume during the formation of a vacancy and which allows the use of the model proposed in [14, 15] for calculating the quantity ΔV from expression (14). A relaxed vacancy has a much greater number of configurations than a conventional monovacancy, and every elementary diffusion event involves a large number of atoms. This brings about an increase in the entropy term in expression (8) and an increase in the quantity D_0'. Since the dislocation core has an even looser structure than that in the bulk of the material, the probability of formation of extended vacancies at dislocations is still higher than that in the bulk of the material and the coefficient of diffusion along the dislocations (D_0'), as a rule, is greater than that in the bulk (D_0).

Pavlov *et al.* [17] explained the large values of D_0' in terms of another cooperative mechanism of diffusion along a dislocation. This mechanism is based on the assumption that, within short time intervals, an atom travels large (as compared to the volume) distances through a series of intermediate equilibrium states in the immediate vicinity of the dislocation core. In other words, the diffusing atom executes relay-race jumps. However, this mechanism also involves cooperative processes.

In close-packed metallic structures, the probability of formation of relaxed vacancies is apparently not very high.

Figure 2 shows the dependence of the effective diffusion radius of dislocations r_d on the change in the volume ΔV in an elementary diffusion event. As can be seen, the effective diffusion radius of the dislocation r_d increases in proportion to the change in the volume ΔV. It seems likely that an increase in the change in the vol-

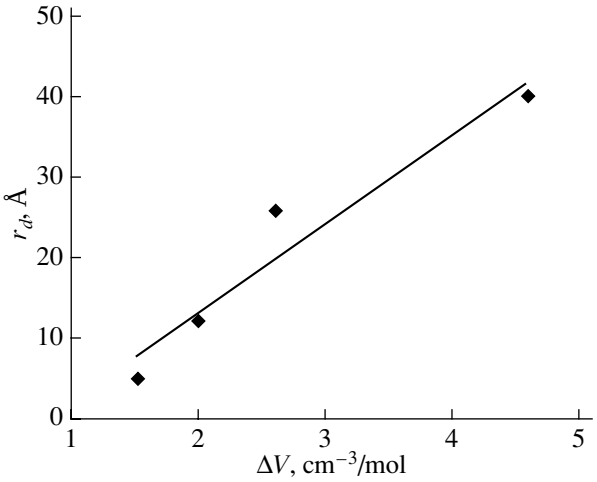

Fig. 2. Dependence of the effective diffusion radius of dislocations on the change in the volume in an elementary diffusion event.

ume ΔV favors expansion of the distorted region around the dislocation.

4. CONCLUSIONS

The experimental data on the diffusion along dislocations in germanium, which were analyzed within the model of a liquid dislocation core and the filament model of diffusion along dislocations, are consistent with the mechanism of diffusion through relaxed vacancies. A tendency exists toward an increase in the distorted region around the dislocation, and this increase is proportional to the change in the volume in an elementary diffusion event.

REFERENCES

1. R. Balluffy, in *Thermally Activated Processes in Crystals* (Mir, Moscow, 1973), pp. 42–46 [in Russian].
2. P. V. Pavlov and É. V. Dobrokhotov, in *Problems of Solid State Physics*, Uch. Zap. Gor'k. Gos. Univ. im. N. I. Lobachevskogo **167**, 84 (1973).
3. R. Ballou and R. Newmen, in *Thermally Activated Processes in Crystals* (Mir, Moscow, 1973), p. 75 [in Russian].
4. I. Kaur and W. Gust, *Fundamentals of Grain and Interphase Boundary Diffusion* (Ziegler, Stuttgart, 1989; Mashinostroenie, Moscow, 1991).
5. N. E. Glickeman and C. L. Vold, Surf. Sci. **31** (6), 50 (1972).
6. W. Lange, Z. Metallkd. **57** (8), 653 (1966).
7. P. V. Pavlov and É. V. Dobrokhotov, Fiz. Tverd. Tela (Leningrad) **12** (1), 281 (1970) [Sov. Phys. Solid State **12** (1), 225 (1970)].
8. P. V. Pavlov and É. V. Dobrokhotov, Fiz. Tverd. Tela (Leningrad) **15** (9), 3112 (1973) [Sov. Phys. Solid State **15** (9), 2080 (1973)].
9. P. V. Pavlov and É. V. Dobrokhotov, Fiz. Tverd. Tela (Leningrad) **16** (1), 3 (1974) [Sov. Phys. Solid State **16** (1), 1 (1974)].
10. É. V. Dobrokhotov and P. V. Pavlov, Fiz. Tverd. Tela (Leningrad) **18** (7), 2807 (1976) [Sov. Phys. Solid State **18** (7), 1640 (1976)].
11. B. I. Boltaks, *Diffusion and Point Defects in Semiconductors* (Nauka, Moscow, 1972) [in Russian].
12. B. Z. Bokshteĭn, S. Z. Bokshteĭn, and L. A. Zhukhovitskiĭ, *Thermodynamics and Kinetics of Diffusion in Solids* (Metallurgiya, Moscow, 1974), p. 26 [in Russian].
13. J. Fridel, *Dislocations* (Pergamon, Oxford, 1964; Mir, Moscow, 1967).
14. P. P. Kuz'menko, Ukr. Fiz. Zh. (Russ. Ed.) **17** (4), 569 (1972).
15. P. P. Kuz'menko, in *Metallophysics* (Naukova Dumka, Kiev, 1972), Vol. 42, p. 37 [in Russian].
16. A. Seeger and J. P. Chick, Phys. Status Solidi **29** (1), 445 (1968).
17. P. V. Pavlov *et al.*, Fiz. Tverd. Tela (Leningrad) **8** (3), 725 (1966) [Sov. Phys. Solid State **8** (3), 580 (1966)].

Translated by V. Artyukhov

Physics of the Solid State, Vol. 47, No. 12, 2005, pp. 2262–2267. Translated from Fizika Tverdogo Tela, Vol. 47, No. 12, 2005, pp. 2170–2175.

DEFECTS, DISLOCATIONS, AND PHYSICS OF STRENGTH

Mechanical Behavior of Ti–Zr–Ni Quasicrystals during Nanoindentation

V. M. Azhazha*, S. S. Borisova, S. N. Dub***, S. V. Malykhin**, A. T. Pugachov**, B. A. Merisov****, and G. Ya. Khadzhay ******

**Institute of Solid-State Physics, Materials Science, and Technologies, National Scientific Center "Kharkov Physicotechnical Institute," ul. Akademicheskaya 1, Kharkov, 61108 Ukraine*

***National Technical University "Kharkov Polytechnic Institute," ul. Frunze 21, Kharkov, 61002 Ukraine*

e-mail: Malykhin@kpi.kharkov.ua

****Bakul' Institute for Superhard Materials, National Academy of Sciences of Ukraine, Avtozavodskaya ul. 2, Kiev, 04074 Ukraine*

*****Kharkov National University, pl. Svobody 4, Kharkov, 61077 Ukraine*

Received October 29, 2004; in final form, April 18, 2005

Abstract—The parameters and mechanisms of deformation of a $Ti_{41.5}Zr_{41.5}Ni_{17}$ quasicrystal and a W + 12 at. % Ta single crystal under nanoindentation conditions were studied and compared. It was found that, initially, the deformation of the quasicrystal is elastoplastic; however, beginning from a certain critical load, the deformation acquires a steplike character with alternating segments of slow elastoplastic deformation and rapid plastic deformation. A qualitative model is proposed for the plastic deformation of quasicrystals during nanoindentation. © *2005 Pleiades Publishing, Inc.*

1. INTRODUCTION

Since the discovery of a quasicrystalline structure by Shechtman *et al.* [1], significant progress has been achieved in understanding the mechanisms of plastic deformation of quasicrystalline (QC) materials [2, 3]. In most studies on the mechanical properties of quasicrystals, experimental tension–compression curves at elevated temperatures have been analyzed [4–8]. The plastic deformation of quasicrystals at high temperatures was shown to occur via dislocation nucleation and motion [1, 4–7]. At room temperature, quasicrystals are brittle materials, which is explained by the absence of translational order and the presence of strong bonds between the atoms forming clusters. Numerous incommensurate length scales in quasicrystals and the absence of small repeating periodic cells make dislocation motion rather difficult [1, 4, 9–11]. The ductility–brittleness transition temperature is ~70–80% of the liquidus temperature (600–750°C) [1, 2].

One fruitful method of mechanical testing is nanoindentation. Apart from the determination of the nanohardness and the Young modulus, this method allows one to study the nature and mechanisms of deformation in the real-time mode in a local microvolume [13]. In particular, nanoindentation has made it possible to reveal the discrete formation of isolated shear bands in metallic glasses [14, 15]. In crystalline materials, displacement "bursts" have been detected in nanoindentation curves and related to the nucleation of single dislocations [16–18]. Moreover, fine effects, such as the strain-induced crystallization of an amorphous alloy in the vicinity of an indentation [9] and the semiconductor–metal phase transformation in a silicon single crystal under an indenter tip at a load of 12 mN [20], have been revealed.

The load–indenter-displacement curve for the elastoplastic region of Al–Cu–Fe quasicrystals was found to be steplike [21, 22]. In our recent work [23], we showed that such discreteness of the load–displacement curve for nanoindentation is characteristic of *i*-Ti–Zr–Ni quasicrystals.

The purpose of this work is to continue study of the plastic behavior of Ti–Zr–Ni quasicrystals during nanoindentation and to develop a qualitative (phenomenological) physical model for the deformation of a quasicrystal as compared to a single crystal.

2. EXPERIMENTAL

We examined $Ti_{41.5}Zr_{41.5}Ni_{17}$, $Ti_{45}Zr_{38}Ni_{17}$, and $Ti_{53}Zr_{27}Ni_{20}$ ribbons melt-quenched according to the process described in [23, 24]. To reveal the specific features of the mechanical behavior of quasicrystals as compared to ordinary crystals, we studied a W + 12 at. % Ta (111) single crystal, whose hardness was estimated to be close to the hardness of the quasicrystalline samples.

The elemental composition of the samples was controlled by x-ray fluorescence and energy-dispersive x-ray spectroscopy to an accuracy of better than 0.5%. The sample structure was examined by x-ray diffraction, and the x-ray diffraction patterns were compared with the JCPDS file to reveal crystalline phases [25].

The quasicrystalline phase was identified according to the procedure described in [26–28]. The structure of the quasicrystalline phase was characterized by a lattice parameter a_{6D} in six-dimensional (hypercubic) space, which is connected with the modulus of the diffraction vector Q by the relation

$$Q = \frac{2\sin\vartheta}{\lambda} = \frac{1}{a_{6D}}\sqrt{\frac{N + M\tau}{2(2 + \tau)}} = \frac{1}{a_q}\sqrt{\frac{N + M\tau}{2 + \tau}}, \quad (1)$$

where $\tau = 1.618\ldots$ is the irrational golden section, a_q is a quasi-crystallinity parameter in three-dimensional space, and (N, M) are the Cahn indices [26]. The coherent-domain size L was estimated from the diffraction-line width by an approximation method. For studies, we also used scanning electron microscopy (SEM, REMMA-101A microscope).

The mechanical properties of the samples were investigated by nanoindentation [29–31] on a Nano Indenter-II device (MTS Systems Corporation, Oak Ridge, TN, USA) using a Berkovich trihedral pyramid. The accuracy of indentation-depth measurements was ±0.04 nm, and the accuracy of measurement of the load applied to the indenter was ±75 nN. Indentations were spaced 30 μm apart, and five measurements were carried out on each sample. Each test consisted of two cycles. In the first cycle, we determined the elastic modulus and hardness using the Oliver–Pharr technique [30]. Samples were loaded up to 15 mN at a rate of 1 mN/s, then held for 10 s at this load, unloaded by 95%, and held for 30 s at a small load to measure the thermal drift. In the second nanoindentation cycle, we recorded an elastoplastic loading curve, which characterizes the mechanical behavior of a sample during contact loading. When an indentation was formed, the samples were repeatedly loaded to 25 mN at a rate of 0.5 mN/s, held for 10 s at this load, and then completely unloaded. As the load increased, the average contact pressure (ACP) exerted on an indentation was determined by the procedure described in [22] with allowance for the elastic flexure of the sample surface at the edge of the contact area. The strain rate $\dot{\varepsilon}$ was calculated as $\dot{\varepsilon} = \frac{1}{h}\frac{dh}{dt}$. To analyze the transition from elastic to plastic deformation, we plotted the load dependences of the strain rate.

3. RESULTS

X-ray fluorescence analysis shows that the elemental composition of the samples is close to that described by the chemical formulas given above. To an accuracy of 0.5 at. %, the deviation from the nominal composition at the surface and in the depth of a ribbon is less than 1.5 at. %. The grain size as determined from SEM micrographs is 1–20 μm (Fig. 1). It is seen in Fig. 1 that many grains are shaped like irregular pentagons with relatively smooth boundaries.

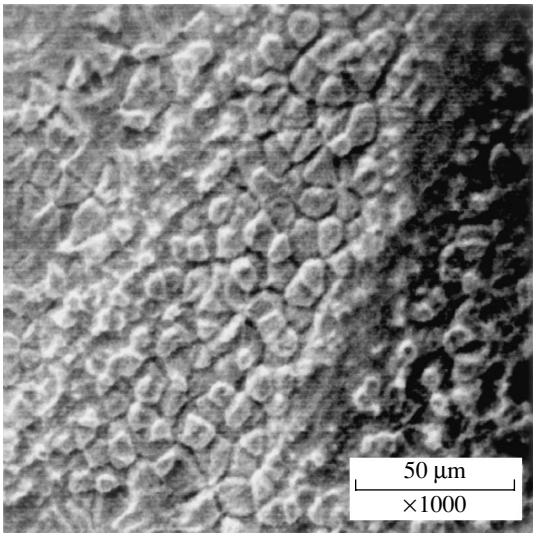

Fig. 1. SEM micrograph of the $Ti_{41.5}Zr_{41.5}Ni_{17}$ quasicrystal surface.

According to x-ray diffraction analysis, the quasicrystalline icosahedral phase (*i*-QC) is predominant in all the ribbons. Typical x-ray diffraction patterns were presented in our previous papers [23, 24], and the results agree well with the phase diagram from [32–36] and with the data from [37–39]. The single-phase quasicrystalline samples have the composition of $Ti_{41.5}Zr_{41.5}Ni_{17}$. In these samples, the quasi-crystallinity parameter a_q, the lattice parameter a_{6D}, and the coherent-domain size are maximum.

Figure 2 shows typical load–indenter-displacement curves (P–h curves) for a single-phase quasicrystalline $Ti_{41.5}Zr_{41.5}Ni_{17}$ sample and a W + 12% Ta (111) crystal. In the first nanoindentation cycle, the curves are qualitatively similar. However, in the stage of unloading, the quasicrystal exhibits a higher degree of elastic recovery as compared to that of the crystal. The stiffness (dP/dh) of the quasicrystalline sample as determined in the initial unloading segment is almost half the stiffness of the crystal. The calculated values of the Young modulus of the samples range from 60 to 100 GPa (depending on the composition and perfection of the QC phase) and agree well with the data from [40].

The maximum differences between the quasicrystal and crystal are observed in the second nanoindentation cycle. The P–h curve of the quasicrystal contains clear steps (plateaus on which the indenter displacement changes by Δh in a jump) corresponding to an increase in the indentation depth with almost no increase in load. In quasicrystals, analogous jumps have been detected earlier in the Al–Cu–Fe system [21, 22]. This effect of steplike deformation is most pronounced in the single-phase $Ti_{41.5}Zr_{41.5}Ni_{17}$ sample (Fig. 2b), where the steps are of almost equal length (about 6 nm). For the single-crystal W + 12 at. % Ta sample tested under the same conditions, steps are not observed. Depending on the

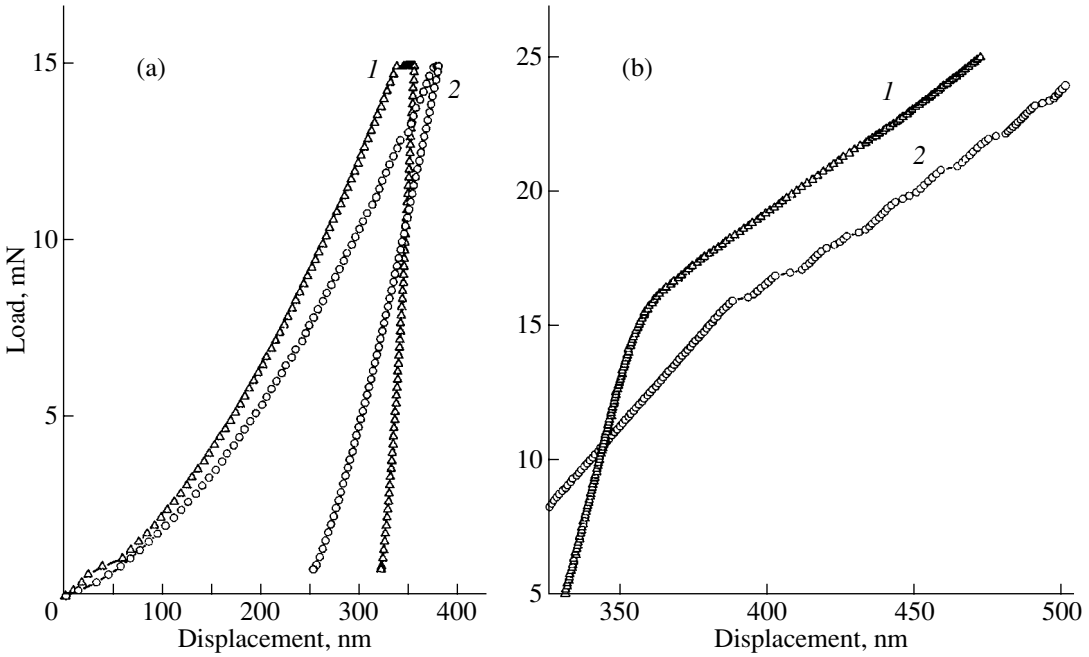

Fig. 2. Loading curves for (*1*) a single crystal and (*2*) a quasicrystal as recorded with a Berkovich indenter in (a) the first cycle and (b) the second cycle.

relative indentation depth $(h - h_0)/h_0$ (where h_0 is the indentation depth after the first cycle), the ACP in a quasicrystalline sample increases nonlinearly to ≈30% and then decreases stepwise by 1–1.5 GPa, with the increase and decrease segments alternating. In the crystal, the ACP increases almost linearly to 6.2 GPa as the indentation depth increases to 7.5–8% and then deformation occurs at a constant ACP (experimental curves can be found in [23]).

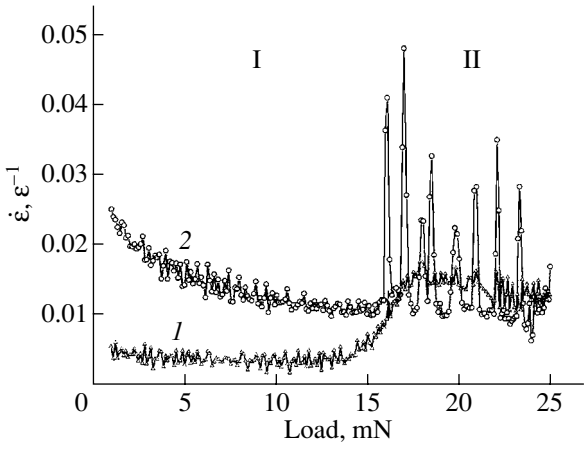

Fig. 3. Strain rate $\dot{\varepsilon}$ as a function of load P for (*1*) the W + 12 at. % Ta single crystal and (*2*) the $Ti_{41.5}Zr_{41.5}Ni_{17}$ quasicrystal. The vertical dashed line conventionally separates region I of elastic strain and region II of plastic strain of the crystal.

The specific features of the quasicrystal deformation as compared to the crystal deformation are clearly visible in the dependence of the strain rate $\dot{\varepsilon}$ on the load P (Fig. 3). In the quasicrystal, the initial strain rate is high (four to six times greater than that for the crystal). However, as the load increases, the strain rate decreases nonlinearly. As the load reaches $P \approx 16$ mN (which corresponds to an indentation depth of greater than 350 nm; see Fig. 2), the $\dot{\varepsilon}(P)$ curve exhibits bursts corresponding to very rapid motion of the indenter to a depth of ~4–6 nm. These bursts alternate with drops, whose lowest points fall on the continuation of the initial dependence (Fig. 3, curve *2*). For the crystal, the curve contains a region of elastic strain, where the strain rate is constant (~0.004 s^{-1}). A transition to plastic deformation occurs in a certain load range (13–17 mN, which corresponds approximately to the onset of bursts in the curve for the quasicrystal) and is accompanied by an almost threefold increase in the strain rate (Fig. 3, curve *1*). In [23], we showed that the lower the volume fraction of the quasicrystalline phase in a sample, the less intense and less pronounced the teeth and the smaller their number. Hence, steplike deformation is characteristic of the quasicrystal. As noted above, the lower the volume fraction of the crystalline phases and the higher the homogeneity of the quasicrystalline phase, the greater a_q. Figure 4 shows the effect of the quasi-crystallinity parameter a_q on the rapid-deformation step length Δh, the calculated values of the Young modulus E, the nanohardness H, and the coherent-domain size L. Note that, apart from the $E(a_q)$ curve, the other dependences demonstrate a linear increase. According to existing con-

cepts [1, 41], the perfection of a quasicrystalline structure increases with the coherent-domain size and with the quasi-crystallinity parameter a_q. The characteristic grain size of the quasicrystalline phase (10–20 μm, as measured by SEM) are well above the indentation size (~2.5 μm). This means that nanoindentation is performed within one grain and that rapid plastic deformation takes place in even a smaller volume of the QC phase. Thus, it is reasonable to assume that steplike deformation occurs in a single quasicrystal.

4. DISCUSSION OF THE RESULTS

A substantial difference in the character of deformation between the quasicrystal and the W + 12 at. % Ta single crystal with a similar hardness manifests itself in the elastoplastic loading stage. The $\dot{\varepsilon}(P)$ dependences can be divided into two characteristic sections (I and II in Fig. 3). For the crystal, these sections correspond to elastic and plastic strains, respectively. In the first section, the strain rate is constant. The boundary between the regions of elastic and plastic strains for the crystal can be taken to be the inflection point in the $\dot{\varepsilon}(P)$ curve (shown by the vertical dashed line in Fig. 3). The quasicrystal begins to deform at a rate that is almost five times that of the crystal, and this rate decreases exponentially with increasing load by the end of the first section. The initial ratio between the strain rates of the quasicrystal and the crystal significantly exceeds the ratio of their elastic moduli. At about $P \approx 13$ mN, the strain-rate ratio is approximately equal to the ratio of the elastic-moduli of these two materials. This behavior suggests that plastic deformation in the quasicrystal occurs even in the initial segment of the second deformation cycle. The exponential character of the $\dot{\varepsilon}(P)$ dependence implies the activated diffusion absorption of point defects by dislocations during dislocation climb. The decrease in the strain rate mentioned above is well known as strain hardening. Many researchers relate this effect to the accumulation of phason strains and to an increase in the phason component of the Burgers vector ($b_\perp$) of perfect dislocations [1, 3–8, 12, 42].

The first strain-rate burst in the quasicrystal is observed at $P \approx 16$ mN. The ACP before the burst is $P \sim 7.4$ GPa. Each subsequent burst requires a lower value of ACP. This phenomenon was earlier detected for quasicrystals subjected to tension–compression tests and is called strain-induced disordering [1, 6, 7, 12]. The formation of a step in the $P(h)$ curve (Fig. 2b) or a strain-rate burst may indicate a change in the deformation mechanism (Fig. 3). The work done by an indenter in overcoming the material resistance to penetrate into it can be estimated as the product of the load P multiplied by the displacement h. During rapid plastic deformation, the work is consumed in changing the quasicrystal substructure. The effective work of rapid deformation can be written as

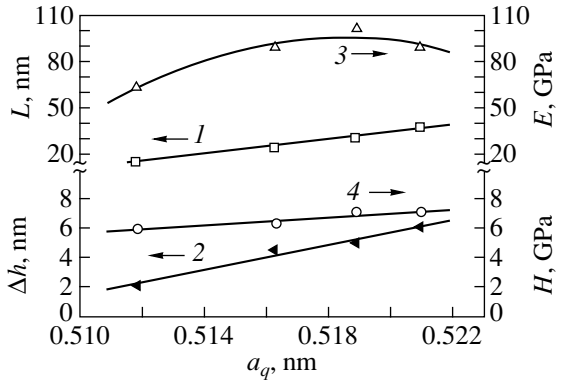

Fig. 4. Dependences of various structural and mechanical characteristics on the quasi-crystallinity parameter a_q: (*1*) coherent-domain size L, (*2*) rapid-deformation step length Δh, (*3*) Young modulus E, and (*4*) nanohardness H.

$$\Delta W = \Delta h_c \Delta P, \tag{2}$$

$$\Delta P = \frac{dP}{dh} h - P, \tag{3}$$

where ΔP is the change in the load per step length Δh_c (minus the flexure) and dP/dh determines the slope of the $P(h)$ curve before the burst. The characteristic work is done on the volume $\Delta V = \Delta h_c S$, where S is the projection of the indentation area. To estimate the number of atoms in this volume N_V, we use the crystal approximant structure model [43, 44]. The quantity $E_c = \Delta W/N_V$ is the change in the enthalpy per atom for rapid plastic deformation. As the load and, hence, $(h - h_0)/h_0$ increase, E_c decreases exponentially. Extrapolation to $h - h_0 = 0$ gives a value of about 0.71 eV/atom. This value virtually coincides with the thermal activation energy for dislocation motion (~0.75 eV/atom) in Al-based quasicrystals [1].

Nanoindentation experiments reveal the discrete nature of plasticity due to the nucleation and motion of single dislocations in crystals [16–18] and quasicrystals [45] or to the formation of shear bands in metallic glasses [14, 15, 46]. However, the curves in Fig. 3 indicate that the deformation mechanisms operating in crystals and quasicrystals are different. Plastic deformation of crystals is described by several mechanisms, namely, dislocation slip, diffusion-controlled dislocation climb, and mechanical twinning [47]. The hypothetic mechanisms of plastic deformation of quasicrystals discussed in the literature are as follows: (i) nucleation of perfect dislocations [1, 4, 10, 11]; (ii) dislocation motion via pure diffusion climb [48]; (iii) deformation via a martensite-like transformation [1]; and (iv) deformation as a result of the accumulation of specific phason strains, the formation of phason walls, and the recession of partial dislocations [3, 12, 42].

These mechanisms are similar in many respects to those known for crystals. Nevertheless, there are signif-

icant differences. In quasicrystals, the motion of perfect dislocations is hindered at low temperatures; at elevated temperatures, a wall of phason defects forms behind a moving dislocation and distorts the perfect quasi-lattice [1]. The nature of phason strains and their effect on plastic deformation were studied comprehensively in [3] and were defined as matching faults. Physically, these defects consist of discrete but collective atomic displacements, which introduce a structural and chemical disorder. According to modern concepts, phason strains play a key role in the plastic deformation of quasicrystals. The Burgers vector of a dislocation in a quasicrystal has two components, $b_\parallel$ and $b_\perp$, where $b_\parallel$ is responsible for the phonon part of deformation and $b_\perp$ is related to phason strain. According to a model developed by Feuerbacher *et al*. [4–9], plastic deformation in quasicrystals is related to the evolution of two substructure parameters, namely, the dislocation density and the deformation accommodation parameter $\xi = |b_\perp|/|b_\parallel|$, which is responsible for strain-induced disordering and thermally activated reordering. The accommodation parameter increases with plastic strain, whereas the dislocation density can decrease. The plastic strain of a quasicrystal is thought to be sensitive to the loading rate and temperature [1, 4–9]. The Feuerbacher model was developed for high deformation temperatures; however, according to recent data, the dislocation mechanism can be operative at low temperatures and low strain rates [10, 49]. During nanoindentation, the martensite-like mechanism is unlikely to operate, since the strain rate is insufficiently high. We believe that the observed effects can be accounted for by the following dislocation mechanisms.

Plastic flow in the initial segment ($\leq P \approx 15.5$ mN) of the second loading cycle is caused by the diffusion climb of dislocations, which effectively absorb point defects in the stress field created under the indenter (stress-induced predominant adsorption [49]). The diffusion nature of this process is indicated by the exponential load dependence of the strain rate. A decrease in the strain rate to the level corresponding to the elastic limit of the crystal is likely related to a total decrease in the concentration of quenching-induced point defects and to the simultaneous accumulation of phason strains and dislocations. These dislocations cannot move via slip, which causes hardening.

At $P > 15.5$ mN, an event of rapid plastic deformation occurs. We assume that each such event is accompanied by the limiting saturation of the phason component ($b_\perp$) of the Burgers vector of a perfect dislocation. The strain accommodation parameter ξ reaches a certain limiting value after which the splitting of a perfect dislocation into two partial dislocations and their recession with the formation of a microtwin ("phason step") become energetically favorable. Every strain-rate burst is related to the introduction of new dislocations (as was the case in crystals subjected to very slow deformation [16–18]), and every drop is related to the formation of a phason wall, which can only be overcome by increasing the load. In the course of deformation, phason strains accumulate continuously in the quasicrystal, which favors strain-induced disordering, and each subsequent rapid deformation occurs at a lower contact pressure. Thus, the deformation curve of a quasicrystal consists of alternating segments of elastoplastic (as in the initial stage) and rapid plastic strains.

5. CONCLUSIONS

Nanoindentation has been used to perform a comparative study into the deformation mechanisms operating within one grain of a *i*-$Ti_{41.5}Zr_{41.5}Ni_{17}$ quasicrystal and in a W + 12 at. % Ta single crystal. It has been found that the elastic modulus of the *i*-$Ti_{41.5}Zr_{41.5}Ni_{17}$ quasicrystal is 90 ± 1 GPa and its microhardness is 7.1 ± 0.2 GPa. Under contact-loading conditions, above a certain critical load, the deformation curve for a quasicrystal acquires a steplike character with alternating segments of elastoplastic deformation and rapid plastic deformation. Under nanoindentation at room temperature, the plastic-strain activation energy of the quasicrystal has been found to be 0.71 eV/atom, which virtually coincides with the thermal activation energy for plastic strain.

The mechanical behavior of the quasicrystal during nanoindentation is described well by the quasicrystal deformation mechanisms derived from experiments on high-temperature deformation. The initial stage of quasicrystal plastic deformation is related to the processes of diffusion dislocation climb and the accumulation of phason strains. An increase in the phason-defect density favors deformation-induced disordering; so each subsequent rapid deformation occurs at a lower contact pressure. A strain-rate burst can be caused by the "slip" of extended dislocations with the formation of a single slip band, and a drop in the strain rate can be related to the introduction of new phason defects and the formation of a phason wall.

ACKNOWLEDGMENTS

This work was supported by the Swiss National Science Foundation (project no. 7UKPJ062171) and the Science and Technology Center in Ukraine (project no. 1997).

REFERENCES

1. Z. M. Stadnik, *Physical Properties of Quasicrystals* (Springer, Berlin, 1999).
2. M. Ricker, J. Bachteler, and H.-R. Trebin, Eur. Phys. J. B **23**, 351 (2001).
3. M. Kleman, cond-mat/0211687 (2002).
4. M. Feuerbacher, C. Metzmacher, M. Wollgarten, K. Urban, B. Baufeld, M. Bartsch, and U. Messerschmidt, Mater. Sci. Eng., A **226–228**, 943 (1997).

5. P. Schall, M. Feuerbacher, M. Bartsch, U. Messerschmidt, and K. Urban, Philos. Mag. Lett. **79** (10), 785 (1999).
6. M. Heggen, M. Feuerbacher, P. Schall, H. Klein, I. R. Fisher, P. C. Canfield, and K. Urban, Mater. Sci. Eng., A **294–296**, 781 (2000).
7. M. Feuerbacher, P. Schall, Y. Estrin, and Y. Brechet, Philos. Mag. Lett. **81** (7), 473 (2001).
8. M. Heggen, M. Feuerbacher, T. Lange, and K. Urban, J. Alloys Compd. **342**, 330 (2002).
9. W. Yang, M. Feuerbacher, and K. Urban, J. Alloys Compd. **342**, 164 (2002).
10. J. Bonneville, M. Texier, and A. Proult, in *Proceedings of the 13th International Conference on the Strength of Metals and Alloys, Budapest, Hungary, 2003* (Eötvös Loränd University, Budapest, 2003), p. 364.
11. M. Texier, A. Proult, J. Raier, and J. Bonneville, in *Proceedings of the 13th International Conference on the Strength of Metals and Alloys, Budapest, Hungary, 2003* (Eötvös Loränd University, Budapest, 2003), p. 412.
12. M. Feuerbacher, C. Metzmacher, M. Wollgarten, K. Urban, B. Baufeld, M. Bartsch, and U. Messerschmidt, Mater. Sci. Eng., A **233**, 103 (1997).
13. Yu. V. Mil'man, *Modern Materials Science in the XXI Century* (Naukova Dumka, Kiev, 1998), p. 637 [in Ukrainian].
14. C. A. Schuh and T. G. Nieh, Acta Mater. **51**, 87 (2003).
15. R. Vaidyanathan, M. Dao, G. Ravichadran, and S. Suresh, Acta Mater. **49**, 3781 (2001).
16. A. Goldstone, H.-J. Koh, K.-Y. Zeng, A. E. Giannakopoulos, and S. Suresh, Acta Mater. **48**, 2277 (2000).
17. S. G. Corcoran, R. J. Colton, E. T. Lilleodden, and W. W. Gerberich, Phys. Rev. B: Condens. Matter **55** (24), R16 057 (1997).
18. S. Suresh, T.-G. Nieh, and B. W. Choi, Scr. Mater. **41** (9), 951 (1999).
19. J. J. Kim, Y. Choi, S. Suresh, and A. S. Argon, Science (Washington) **295**, 654 (2002).
20. V. Domnich and Yu. Gogotsi, Rev. Adv. Mater. Sci. **3**, 1 (2002).
21. S. N. Dub, Yu. V. Milman, D. N. Lotsko, and A. N. Belous, J. Mater. Sci. Lett. **20**, 1043 (2001).
22. S. Dub, N. Novikov, and Yu. Milman, Philos. Mag. A **82** (10), 2161 (2002).
23. V. Azhazha, S. Dub, G. Khadzhay, S. Malykhin, B. Merisov, and A. Pugachov, Philos. Mag. **84** (10), 983 (2004).
24. V. Azhazha, G. Khadzhay, S. Malykhin, B. Merisov, and A. Pugachov, Phys. Lett. A **319**, 539 (2003).
25. *Powder Diffraction File: Inorganic Sets 1–37* (ASTM–JCPDS, Swarthmore, Pennsylvania, 1977–1988).
26. J. W. Cahn, D. Shechtman, and D. Gratias, J. Mater. Res. **1** (1), 13 (1986).
27. S. Ebalard and F. Spaepen, J. Mater. Res. **4** (1), 39 (1989).
28. P. J. Lu, K. Deffeyes, P. J. Steinhardt, and N. Yao, Phys. Rev. Lett. **87**, 275 507 (2001).
29. S. I. Bulychev, V. P. Alekhin, M. Kh. Shorshorov, A. P. Ternovskiĭ, and G. D. Shnyrev, Zavod. Lab. **39**, 1242 (1973).
30. W. C. Oliver and G. M. Pharr, J. Mater. Res. **7** (6), 1564 (1992).
31. D. F. Bahr, D. E. Kramer, and W. W. Gerberich, Acta Mater. **46** (10), 3605 (1998).
32. V. P. Eremenko, E. L. Semenova, and L. A. Tkachenko, Metally **6**, 191 (1990).
33. S. A. Sibirtsev, V. N. Chebotnikov, V. V. Molokanov, and Yu. K. Kovneristyĭ, Pis'ma Zh. Éksp. Teor. Fiz **47** (25), 61 (1988) [JETP Lett. **47**, 744 (1988)].
34. S. Yi and W. J. Kim, J. Mater. Res. **15** (4), 892 (2000).
35. J. P. Davis, E. H. Majzoub, J. M. Simmons, and K. F. Kelton, Mater. Sci. Eng., A **294–296** (15), 104 (2000).
36. K. F. Kelton, A. K. Gangopadhyay, G. W. Lee, L. Hannet, R. W. Hyers, S. Krishnan, M. B. Robinson, J. Rogers, and T. J. Rathz, J. Non-Cryst. Solids **312–314**, 305 (2002).
37. R. M. Stroud, K. F. Kelton, and S. T. Misture, J. Mater. Res. **12** (2), 434 (1997).
38. R. Nicula, A. Jianu, A. R. Biris, D. Lupu, R. Manaila, A. Devenyi, C. Kumpf, and E. Burkel, Eur. Phys. J. B **3** (2), 1 (1998).
39. R. Nicula, A. Jianu, U. Ponkratz, and E. Burkel, Phys. Rev. B: Condens. Matter **62** (13), 8844 (2000).
40. K. Foster, R. G. Leisure, J. B. Shaklee, J. Y. Kim, and K. F. Kelton, Phys. Rev. B: Condens. Matter **59**, 11 132 (1999).
41. S. Roche, G. T. de Laissardiere, and D. Mayou, J. Math. Phys. **38** (4), 1794 (1997).
42. V. Franz, M. Feuerbacher, M. Wollgarten, and K. Urban, Philos. Mag. Lett. **79** (6), 333 (1999).
43. W. J. Kim, P. C. Gibbons, and K. F. Kelton, Philos. Mag. Lett. **76** (3), 199 (1997).
44. W. J. Kim, P. C. Gibbons, K. F. Kelton, and W. B. Yelon, Phys. Rev. B: Condens. Matter **58**, 2578 (1998).
45. H. Kreuzer and R. Pippan, in *Proceedings of the 13th International Conference on the Strength of Metals and Alloys, Budapest, Hungary, 2003* (Eötvös Loränd University, Budapest, 2003), p. 78.
46. Yu. I. Golovin, V. I. Ivolgin, V. A. Khonik, K. Katagava, and A. I. Tyurin, Scr. Mater. **45**, 947 (2001).
47. L. A. Shuvalov, A. A. Urusovskaya, I. S. Zheludev, A. V. Zalesskiĭ, S. A. Semiletov, B. N. Grechushnikov, I. G. Chistyakov, and S. A. Pikin, in *Modern Crystallography*, Vol. 4: *Physical Properties of Crystals*, Ed. by B. K. Vainshtein (Nauka, Moscow, 1979; Pergamon, Oxford, 1981).
48. R. W. Cahn and P. Haasen, *Physical Metallurgy*, Vol. 3: *Strength of Materials and Alloys* (Pergamon, Oxford, 1979; Metallurgiya, Moscow, 1987).
49. F. Mompiou, L. Bresson, D. Gratias, and D. Caillard, in *Proceedings of the 13th International Conference on the Strength of Metals and Alloys, Budapest, Hungary, 2003* (Eötvös Loränd University, Budapest, 2003), p. 19.

Translated by K. Shakhlevich

Physics of the Solid State, Vol. 47, No. 12, 2005, pp. 2268–2273. Translated from Fizika Tverdogo Tela, Vol. 47, No. 12, 2005, pp. 2176–2181.

MAGNETISM AND FERROELECTRICITY

Modulation Instability of Magnetostatic Waves in a Magnetically Coupled Two-Layer Structure

A. M. Shutyĭ and D. I. Sementsov

Ul'yanovsk State University, ul. L'va Tolstogo 42, Ul'yanovsk, 432970 Russia

e-mail: shuty@mail.ru

Received December 7, 2004

Abstract—Modulation instability of direct bulk magnetostatic waves in structures consisting of two magnetically coupled planar films separated by a nonmagnetic layer is studied. It is found that, depending on the type of excitation of the waveguide modes, mode coupling can either change the characteristics of the modulation wave instability or ensure their stability with respect to the corresponding perturbations by affecting the dispersion properties of the structure.

1. INTRODUCTION

The interest shown in magnetostatic waves (MSWs) in recent years is due, above all, to the fact that these waves are substantially nonlinear even at low intensities [1–3] and can be used for the creation of new devices using the nonlinear properties of MSWs in the microwave range important in engineering [4]. Due to its nonlinear character, MSW dynamics gives rise to a number of effects: self-modulation, self-focusing, instability with respect to disintegration into new waves [5, 6], and the formation of bright and dark wave envelope solitons [7–9]. Among these effects, modulation instability occupies a special place, since, for different system parameters and different initial conditions, it can result in the formation of various dynamic wave structures, including ones that are undesirable in terms of the practical application of MSWs. The theoretical analysis of MSW dynamics available in the literature is basically restricted to structures with one waveguide layer. However, using multilayer structures as a waveguide medium offers greater possibilities for the control of dynamic MSW characteristics, since in such structures, due to the coupling of the magnetic moments of neighboring layers, the dynamic properties of the spin subsystem are substantially modified and new types of spin-wave excitations occur [10–12]. The main types of interlayer magnetic coupling are dipole–dipole [13] and exchange [14] interactions or their combination [15]. The effect of the interlayer magnetic coupling is most important for the formation of unified MSW excitations in the case where waves in separate layers are phase matched. We study the features of the modulation instability of the envelope of direct bulk MSWs propagating in a normally magnetized two-layer ferrite-garnet structure with magnetic interlayer interaction of sufficient strength for a unified wave packet to form.

2. EQUATIONS FOR COUPLED MODES

We consider a three-layer planar structure oriented normal to the z axis and consisting of two (100)-oriented ferrite-garnet films separated by a nonmagnetic layer. Let a wave packet formed by interacting MSW modes belonging to each of the films be excited and propagate in this structure along the x axis. In this case, the magnetostatic potential of the wave packet can be represented as a sum of the eigenmodes of the isolated magnetic films forming the structure. The interlayer coupling is effective only between those two modes of the complete set of modes of each film for which the phase-matched conditions are most exactly satisfied, namely, for which the quantities $2\delta_\omega = \omega_1 - \omega_2$ and $2\delta_k = k_1 - k_2$ are minimum or zero (here, $\omega_{1,2}$ are the carrier frequencies of pulses formed by the MSW eigenmodes of the isolated films and $k_{1,2}$ are the propagation constants of these modes). In what follows, we assume that there are no other perturbations (for example, periodic inhomogeneity of the layer parameters) that might cause modes of different orders to become phase matched. Therefore, pulses are formed only by coupled modes of the same order (in particular, by first-order modes, since they are less attenuated) corresponding to the different waveguide layers. The magnetostatic potential can be written as

$$\Psi = \sum_{n=1,2} \Psi_n = \sum_n \frac{4\pi M_{0n}}{k_n\sqrt{\chi_n^2 + \chi_{an}^2}} U_n(z)\varphi_n(x, t)\exp[i(\omega_n t - k_n x)], \quad (1)$$

where M_{0n} is the magnetization of the corresponding film. We assume that the effective field $\mathbf{H}$ (including the bias magnetic field $\mathbf{H}_0$ and the cubic- and growth-anisotropy field $\mathbf{H}_a$) is directed along the z axis ($\mathbf{H} \parallel \mathbf{M}_{0n} \parallel \mathbf{z}$).

1063-7834/05/4712-2268$26.00

In this case, the diagonal and off-diagonal components of the magnetic susceptibility tensor (in the absence of damping) are determined by the expressions $\chi_n = \omega_{Mn}\omega_{Hn}/(\omega_{Hn}^2 - \omega_n^2)$ and $\chi_{an} = \chi_n\omega_n/\omega_{Hn}$, where we introduced the notation $\omega_{Mn} = 4\pi\gamma M_{0n}$ and $\omega_{Hn} = \gamma H - \omega_{Mn}$. The profile function $U_n(z)$ (describing the mode distribution in a cross section of each of the n layers) and its coefficient can be found from the relation between the magnetostatic potential and the variable magnetic field of an MSW and from the Walker equation

$$\operatorname{grad}\Psi_n = \mathbf{h}_n, \quad \operatorname{div}(\hat{\mu}_n\nabla\Psi_n) = 0, \tag{2}$$

where $\hat{\mu}_n$ is the magnetic permeability tensor for the nth film. The dimensionless complex amplitude of the magnetostatic potential is expressed in terms of normalized complex values of the variable components of the magnetic moments $\varphi_n = \sqrt{m_{xn}^2 + m_{yn}^2}/M_{0n}$ and, due to mode coupling, is a slowly varying function of coordinate and time. The dispersion equation for direct bulk MSWs has the form

$$\tan k_{zn}l_n = -\frac{2\sqrt{-\chi_n - 1}}{\chi_n + 2}, \tag{3}$$

where l_n is the thickness of the corresponding film and the transverse wavenumber of an MSW is related to the propagation constant by the expression $k_{zn} = k_n\sqrt{-\chi_n - 1}$. In the long-wavelength approximation, we have $k_n \ll k_{zn}$ and the dispersion equation assumes the form $k_n l_n = -2/\chi_n$. The two dispersion parameters obtained from this equation and the parameter describing the nonlinearity of the medium are determined by the following derivatives taken at $k_n \longrightarrow 0$ and $\varphi_n \longrightarrow 0$:

$$v_n = \frac{\partial\omega_n}{\partial k_n} = \frac{\omega_{Mn}l_n}{4},$$

$$d_n = \frac{\partial^2\omega_n}{\partial k_n^2} = -\frac{\omega_{Mn}^2 l_n^2}{16\omega_{Hn}}\left(1 + \frac{8}{3}\frac{\omega_{Hn}}{\omega_{Mn}}\right),$$

$$g_{cn} = \frac{\partial\omega_n}{\partial|\varphi_n|^2} = \frac{\omega_{Mn}}{2}.$$

The first dispersion parameter determines the group velocity of an MSW, the second dispersion parameter describes the dispersion of the group velocities, and the parameter g_{cn} characterizes the nonlinear self-action of the system.

In the presence of a phase mismatch between the interacting modes, we assume that the coupling of the propagating modes makes their wavenumbers equal ($\delta_k = 0$) and that a slight difference in the parameters of the films (e.g, in their thickness) produces a difference in the MSW eigenfrequencies according to dispersion equation (3), i.e., that $\delta = \delta_\omega \neq 0$.

The dynamics of the envelope of the coupled pulses, i.e., of the slowly varying amplitudes of each of the interacting MSWs, can be described by the equation

$$i\frac{\partial\varphi_n}{\partial t} + iv_n\frac{\partial\varphi_n}{\partial x} + \frac{d_n}{2}\frac{\partial^2\varphi_n}{\partial x^2} = q_n\exp(\pm 2i\delta t)\varphi_{3-n} + g_{cn}|\varphi_n|^2\varphi_n, \tag{4}$$

where the upper sign in the argument of the exponential function corresponds to the mode with $n = 1$, the lower sign corresponds to the mode with $n = 2$, and q_n is a mode-coupling coefficient determined by the overlap of the profile functions.

3. EQUATIONS FOR THE PARTIAL PULSES

Let us introduce the following characteristic times: the mode interaction time $T_{qn} = q_n^{-1}$, the dispersion time $T_{dn} = L_{0n}^2/|d_n|$, the group-mismatching time $T_{rn} = L_{0n}/v_n$, and the self-modulation time $T_{gn} = g_{cn}^{-1}|\varphi_{0n}|^{-2}$, where L_{0n} and φ_{0n} are the initial duration (at $t = 0$) and the initial amplitude of the input mode pulses. In the case of strong mode coupling, we have $T_{qn} \ll T_{dn}$, T_{rn}, T_{gn}. Therefore, in the absence of losses, the variation in the pulse power caused by spatial dispersion, group-velocity dispersion, and cubic nonlinearity in time T_{qn} is negligible. Hence, we may assume that, during the time interval T_{qn}, the condition $|\varphi_1|^2 + |\varphi_2|^2 = \text{const}$ is satisfied fairly accurately. From this condition, it follows that the mode-coupling coefficients satisfy the equation $q_1 = q_2^* = q$. The existence of an upper bound for the quantity q is related to the fact that, for the MSW envelope, the characteristic time of the amplitude variation must be much greater than the wave period. Taking into account this fact and the fact that, for pulses propagating in the waveguide, the group-mismatching time is shorter than the self-modulation and dispersion times, we find that, in the case of strong mode interaction, the mode-coupling coefficient must obey the condition $\tau_n^{-1} \ll q \ll \omega_n$, where τ_n are the durations of MSW pulses that form in each of the layers of the structure. This condition can be satisfied by varying the coupling between the magnetic moments of the layers through appropriate choice of the intermediate-layer thickness and the interface topology.

The approximation of strong mode coupling makes it possible to write the time envelopes of the pulses as the sum of two partial pulses that are not coupled in the linear approximation [16, 17]:

$$\begin{aligned}\varphi_1 &= a_1(x,t)\exp[i(\sigma+\delta)t] \\ &+ a_2(x,t)\exp[-i(\sigma-\delta)t], \\ \varphi_2 &= \rho_1 a_1(x,t)\exp[i(\sigma-\delta)t] \\ &+ \rho_2 a_2(x,t)\exp[-i(\sigma+\delta)t],\end{aligned} \tag{5}$$

where $a_j(x, t)$ are slowly varying amplitudes of the partial pulses. Here, we introduced the parameters $\sigma = \sqrt{\delta^2 + |q|^2}$ and $\rho_j = q^*[\delta + (-1)^j\sigma]^{-1}$. Substituting Eqs. (5) into Eq. (4) and passing to the running coordinate $\xi = x - 2V_1V_2(V_1 + V_2)^{-1}t$, we obtain equations for the amplitudes of the partial pulses

$$\begin{aligned}&i\frac{\partial a_j}{\partial t} - i\tilde{V}_j\frac{\partial a_j}{\partial \xi} + \frac{D_j}{2}\frac{\partial^2 a_j}{\partial \xi^2} \\ &= (G_{cj}|a_j|^2 + G_{kj}|a_{3-j}|^2)a_j,\end{aligned} \tag{6}$$

where $\tilde{V}_j = (-1)^j V_j(V_1 - V_2)/(V_1 + V_2)$ and the following effective parameters (describing the dynamics of the corresponding partial pulses) are introduced: the group velocity

$$V_j = \frac{v_1 + v_2}{2} - (-1)^j\frac{\delta}{2\sigma}(v_2 - v_1),$$

the group velocity dispersion

$$D_j = \frac{d_1 + d_2}{2} - (-1)^j\frac{1}{2\sigma}[\delta(d_2 - d_1) + 2v_1v_2],$$

the self-modulation factor

$$G_{cj} = g_{c1} + \frac{1}{2}g_{c2}|\rho_j|^2\left[1 - (-1)^j\frac{\delta}{\sigma}\right]$$

and the partial-pulse cross-modulation factor

$$G_{kj} = \frac{1}{2}g_{c2}|\rho_{3-j}|^2\left[1 - (-1)^j\frac{\delta}{\sigma}\right].$$

Under the phase-matched conditions ($\omega_1 = \omega_2 = \omega$, $\delta = 0$), the effective parameters are given by

$$V_j = V = \frac{v_1 + v_2}{2}, \quad D_j = \frac{d_1 + d_2}{2} - (-1)^j\frac{v_1v_2}{\sigma},$$

$$G_{cj} = G_c = \frac{3}{2}g_c, \quad G_{kj} = G_k = \frac{1}{2}g_c.$$

Equations (6) should be solved together with the initial conditions for the amplitudes of partial pulses. Starting from the expansion in terms of partial pulses (5), we can express the initial amplitudes of the partial pulses in terms of the initial amplitudes of the two coupled modes:

$$a_{j0} = \frac{1}{2}\varphi_{10} + (-1)^j\frac{1}{2\sigma}(\delta\varphi_{10} + q\varphi_{20}). \tag{7}$$

It follows from Eq. (7) that, under the phase-matched conditions in the case of symmetric or antisymmetric excitation of the film structure (where $\varphi_{10} = \pm\varphi_{20}$), the amplitude of one of the partial pulses is equal to zero ($a_1 = a_{10} = 0$ for symmetric excitation, $a_2 = a_{20} = 0$ for antisymmetric excitation) and the dynamics of the entire wave packet is determined by the dynamics of only one of the partial pulses.

If the input wave packet is sufficiently long and the dispersion terms can be disregarded (quasi-monochromatic approximation), the solutions to Eqs. (6) for the partial pulses with weak perturbations of their amplitudes can be written as

$$\begin{aligned}a_j(t,\xi) &= [a_{j0} + \zeta_j(t,\xi)] \\ &\times \exp[-i(G_{cj}a_{j0}^2 + G_{kj}a_{3-j0}^2)t],\end{aligned} \tag{8}$$

where ζ_j is the complex amplitude of the partial pulse perturbation and $a_{j0} \gg |\zeta_j|$. Substituting Eq. (8) into Eqs. (6) and linearizing them with respect to weak perturbations ζ_j, we obtain a system of equations for perturbations

$$\begin{aligned}&i\frac{\partial \zeta_j}{\partial t} - i\tilde{V}_j\frac{\partial \zeta_j}{\partial \xi} + \frac{D_j}{2}\frac{\partial^2 \zeta_j}{\partial \xi^2} \\ &= G_{cj}a_{j0}^2(\zeta_j + \zeta_j^*) + G_{kj}a_{10}a_{20}(\zeta_{3-j} + \zeta_{3-j}^*).\end{aligned} \tag{9}$$

In the case of phase matching, the equations for perturbations assume the form

$$i\frac{\partial \zeta_j}{\partial t} + \frac{D_j}{2}\frac{\partial^2 \zeta_j}{\partial \xi^2} = G_c\left(a_{j0}^2 + \frac{1}{3}a_{3-j0}^2\right)(\zeta_j + \zeta_j^*). \tag{10}$$

We describe the dynamics of perturbations by harmonic functions:

$$\zeta_j = b_{j1}\cos(\kappa_j\xi - \Omega_j t) + ib_{j2}\sin(\kappa_j\xi - \Omega_j t). \tag{11}$$

Here, κ_j and Ω_j are the wavenumber and frequency of perturbations ($\Omega_j = \omega - \omega_{ij}$, where ω_{ij} is the frequency of a signal perturbation wave or of spontaneous noise perturbation). Substituting Eq. (11) into Eq. (10) with $a_{3-j0} = 0$, we obtain a system of two homogeneous equations whose solution gives the dispersion relation,

$$\Omega_j = \pm\frac{1}{2}|D_j\kappa_j|\sqrt{\kappa_j^2 + \bar{\kappa}_j^2\,\mathrm{sgn}(D_j)}, \tag{12}$$

where $\mathrm{sgn}(\ldots)$ is the signum function and $\bar{\kappa}_j^2 = 4G_ca_{j0}^2/|D_j|$. It follows from Eq. (12) that, for a positive effective dispersion, the frequency Ω_j is real at any value of the wavenumber κ_j and the MSW steady state is stable with respect to weak perturbations. In the case where $D_j < 0$ and $|\kappa_j| < \bar{\kappa}_j$, the frequency becomes

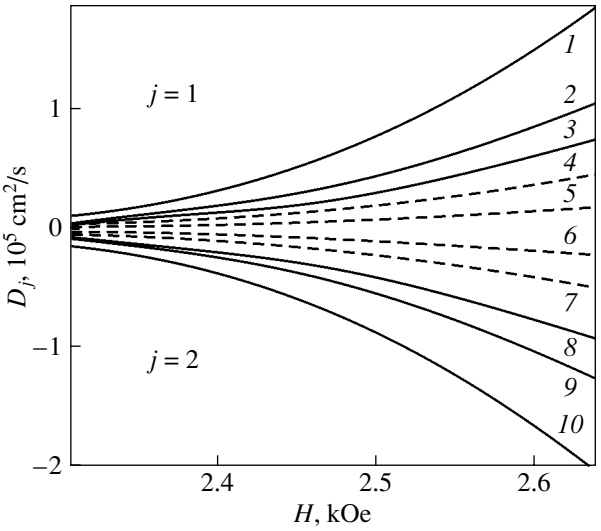

Fig. 1. Field dependence of the effective dispersion D_j for antisymmetric ($j = 1$) and symmetric ($j = 2$) excitation of the structure calculated for $l = 5$ (dashed curves) and 10 μm (solid curves); $q = 3 \times 10^8$ (curves *1, 4, 7, 10*), 5×10^8 (curves *2, 9*), and 7×10^8 s^{-1} (curves *3, 5, 6, 8*); $\omega/2\pi = 2.5$ GHz.

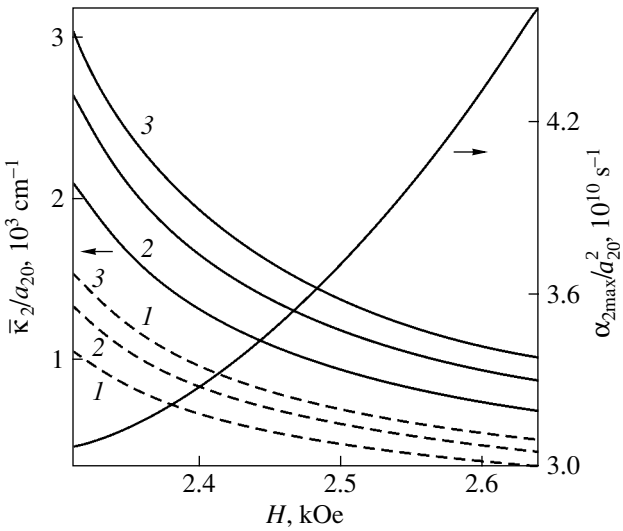

Fig. 2. Field dependence of the normalized limiting wavenumber $\bar{\kappa}_2$ and normalized maximum amplification factor $\alpha_{2\max}$ calculated for $l = 5$ (solid curves) and 10 μm (dashed curves); $q = (3, 5, 7) \times 10^8$ s^{-1} (curves *1–3*, respectively).

imaginary and the perturbation ζ_j increases exponentially in time. The amplification factor is given by

$$\alpha_j = 2\mathrm{Im}(\Omega_j) = |D_j\kappa_j|\sqrt{\bar{\kappa}_j^2 - \kappa_j^2}. \quad (13)$$

The maximum value of the amplification factor $\alpha_{j\max} = 2G_c a_{j0}^2$ is reached at $|\kappa_{jm}| = \bar{\kappa}_j/\sqrt{2}$. An important feature of the magnetically coupled structure under study is that the modulation instability can occur in the case of normal dispersion of MSW eigenmodes of each of the layers.

4. NUMERICAL ANALYSIS

Analyzing the above relations numerically makes it possible to obtain some important dependences characterizing the MSW modulation instability in two-layer structures. We choose the parameters of the magnetic layers corresponding to ferrite-garnet films: $4\pi M_{0n} = 4\pi M_0 = 1750$ G and $\gamma = 1.76 \times 10^7$ Oe^{-1} s^{-1}. In the case where the anisotropy of the magnetic layers is included and the coordinate axes are taken to be along the {100} crystallographic directions, we define the effective field to be $H = H_0 + H_a$. Here, H_0 is an external bias magnetic field and $H_a = 2(K_1 + K_u)/M_0$ is the magnetic anisotropy field, where K_1 and K_u are the crystallographic and growth anisotropy constants of the layers [18, 19]. To obtain the graphic dependences shown below, the initial dispersion equation (3) and its first and second derivatives with respect to frequency were solved numerically, since the $k_n \longrightarrow 0$ approximation used to derive the corresponding analytical expressions appears to be incorrect in many cases [19].

Figure 1 shows the dependence of the effective dispersion D_j on the effective field H obtained for single-partial modes in the cases of antisymmetric ($j = 1$) and symmetric ($j = 2$) excitation of the structure, provided that the phase-matched conditions are satisfied. The thicknesses of the magnetic layers are chosen to be identical and equal to $l = 5$ and 10 μm; the frequency $\omega/2\pi = 2.5$ GHz; and the mode-coupling coefficient $q = 3 \times 10^8$, 5×10^8, and 7×10^8 s^{-1}. From Fig. 1, it follows that, in the case of antisymmetric excitation of the structure, the effective dispersion is always positive; hence, MSWs in a magnetically coupled system are stable against modulation (in contrast to MSWs in isolated films). In the case of symmetric excitation, the effective dispersion is negative and the modulation instability must appear. An increase in the magnetic field and a decrease in the mode-coupling coefficient give rise to an increase in the magnitude of the effective dispersion of partial pulses, and the H dependence of D_j becomes more substantial as the thickness of the magnetic layers increases.

In Fig. 2, the quantity $\bar{\kappa}_2$ (which determines the width of the interval of wavenumbers for which perturbations of the MSWs increase in time) and the maximum amplification factor $\alpha_{2\max}$ normalized to the initial amplitude of the partial pulses and to its square, respectively, are plotted as a function of the effective magnetic field for symmetric excitation of the structure with the abovementioned parameter values: $q = (3, 5, 7) \times 10^8$ s^{-1}, and $l = 5$ and 10 μm. We see that the quantity $\bar{\kappa}_2$ increases as the field H decreases or the mode-coupling coefficient and the thickness of the magnetic layers increase. Moreover, the maximum amplification factor

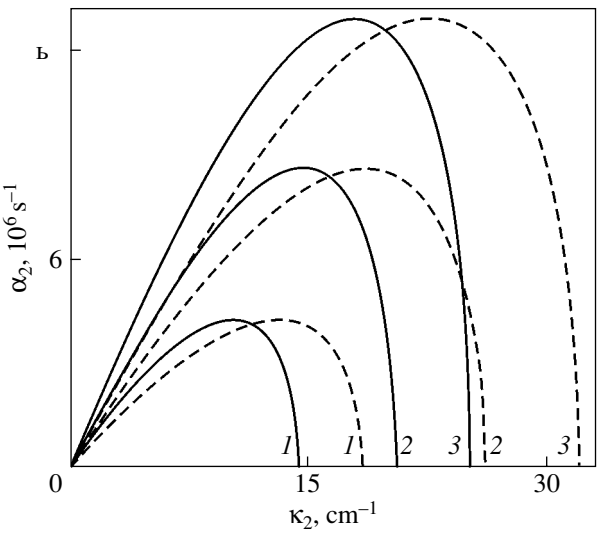

Fig. 3. Dependence of the amplification factor of an MSW perturbation on its wavenumber calculated for $q = 3 \times 10^8$ (solid lines) and 5×10^8 s^{-1} (dashed lines), $a_{20}^2 = (1, 2, 3) \times 10^{-4}$ (curves *1–3*, respectively), $l = 5$ μm, and $H = 2.6$ kOe.

does not depend on the layer thickness and the coupling coefficient and increases with the effective magnetic field. Thus, the narrower the interval of the wavenumbers corresponding to the MSW modulation instability, the smaller the minimum time of the increase in the amplitude of a modulating quasi-monochromatic signal wave. We note that, by properly choosing the growth anisotropy of ferrite-garnet films, one can substantially reduce the external bias magnetic field necessary to obtain the required effective magnetic field; this circumstance is important for practical control of the parameters of the modulation instability of coupled modes in the structure.

The amplification factor for a modulating MSW signal is plotted in Fig. 3 as a function of its wavenumber. The following parameter values were used in the calculations: $q = (3, 5) \times 10^8$ s^{-1}, $l = 5$ μm, and $H = 2.6$ kOe, and the dimensionless amplitude squared was $a_{20}^2 = (1, 2, 3) \times 10^{-4}$, which corresponds to an MSW power of 2.2–6.4 mW per centimeter of the width of the two-layer waveguide structure. We see that the width of the region of the modulation instability and the maximum value of the amplification factor increase as the intensity of the input radiation or the nonlinearity parameter increases. As noted above, the increase in the coupling coefficient causes an increase in the width of the modulation instability region only.

A numerical solution to Eq. (10) for the case of symmetric excitation ($\zeta_1 = 0$, $\zeta_2 \neq 0$) is shown in Fig. 4; the following parameter values were used: $l = 5$ μm, $H = 2.6$ kOe, $q = 5 \times 10^8$ s^{-1}, $a_{20}^2 = 3 \times 10^{-4}$, and the wavenumber of the modulating signal $\kappa_2 = 10$ and 22.83 cm^{-1} (the latter value corresponds to the maximum amplification of a perturbation at the chosen values of the system parameters and the effective field H). As the initial condition, we chose a sufficiently broad stepped MSW pulse modulated by the harmonic function $\zeta_2 = b_{21} \cos \kappa_2 \xi$, where $b_{21} = a_{20} \times 10^{-3}$. Curves *1* correspond to the initial modulation signal ($t = 0$), and curves *2* and *3* to the modulation amplitudes at $t \approx 292$ and 585 ns, respectively. The results of the numerical solution of Eq. (10) confirm the validity of the analytical expressions obtained above and show that a modulation signal

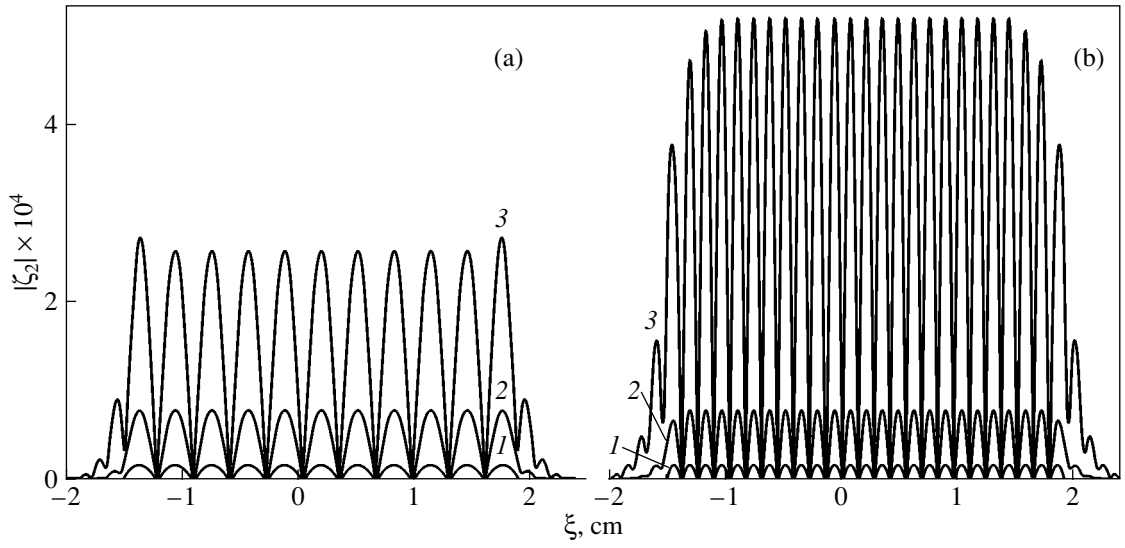

Fig. 4. Distributions of the MSW perturbation magnitude along the waveguide length at the instants of time (*1*) $t \approx 0$, (*2*) 292, and (*3*) 585 ns calculated for κ_2 equal to (a) 10 and (b) 22.83 cm^{-1}; $a_{20}^2 = 3 \times 10^{-4}$, $l = 5$ μm, $H = 2.6$ kOe, and $q = 5 \times 10^8$ s^{-1}.

remains almost harmonic over the time during which an MSW pulse travels a distance of ≈1 cm in the structure. The distortions arising at the edges are related to the spatial boundaries of the perturbation. We note that, in the absence of damping, the growth of the perturbation amplitude is unbounded. The damping limiting this growth can be taken into account by introducing either a relaxation frequency into the components of the magnetic permeability tensor [19] or a relaxation term directly into the original dynamic equations.

5. CONCLUSIONS

Our analysis has shown that, in two-layer magnetic structures, the modulation instability of direct bulk MSWs with respect to longitudinal (i.e., growing in the longitudinal direction) perturbations occurs in the case of symmetric initial excitation of both waveguide layers. In the case of antisymmetric excitation, MSWs in the structure considered appear to be stable against modulation. The coupling between the magnetostatic eigenmodes of each of the layers substantially affects the interval of wavenumbers of an amplified perturbation; namely, an increase in the coupling coefficient widens this interval and increases the wavelength that corresponds to the maximum amplification of the modulating MSW perturbation. However, the maximum amplification factor appears to be independent of mode coupling. The simulation has also shown that, as the effective magnetic field increases, the interval of wavenumbers of the amplified signal becomes narrower and the maximum amplification factor increases. Thus, using the structure under study as a waveguide for MSWs allows one to realize situations of both modulation stability and modulation instability (with the characteristic parameters preset in certain limits) by choosing the initial excitation only. From the above analysis it also follows that, in the case where MSWs (in particular, surface MSWs) in isolated waveguide layers are stable, a magnetically coupled two-layer structure can be used to realize (under symmetric excitation) the modulation instability of coupled MSW modes.

ACKNOWLEDGMENTS

This study was supported by the Ministry of Education of the Russian Federation, project no. PD02-1.2-72.

REFERENCES

1. A. K. Zvezdin and A. F. Popkov, Zh. Éksp. Teor. Fiz. **84** (2), 606 (1983) [Sov. Phys. JETP **57**, 350 (1983)].
2. P. de Gasperis, R. Morcelli, and G. Miccolli, Phys. Rev. Lett. **59** (4), 481 (1987).
3. B. A. Kalinikos, N. G. Kovshikov, and A. N. Slavin, J. Appl. Phys. **67** (9), 5633 (1990).
4. A. V. Vashkovskiĭ, V. S. Stal'makhov, and Yu. P. Sharaevskiĭ, *Magnetostatic Waves in Microwave Electronics* (Saratov Gos. Univ., Saratov, 1993) [in Russian].
5. Yu. V. Gulyaev, P. E. Zil'berman, S. A. Nikitov, and A. G. Temiryazev, Fiz. Tverd. Tela (Leningrad) **28** (9), 2774 (1986) [Sov. Phys. Solid State **28** (9), 1553 (1986)].
6. A. S. Kindyak and V. V. Kindyak, Fiz. Tverd. Tela (St. Petersburg) **41** (7), 1272 (1999) [Phys. Solid State **41** (7), 1162 (1999)].
7. J. M. Nash, C. E. Patton, and P. Kabos, Phys. Rev. B: Condens. Matter **51** (21), 15079 (1995).
8. A. V. Kokin and S. A. Nikitov, Fiz. Tverd. Tela (St. Petersburg) **43** (5), 851 (2001) [Phys. Solid State **43** (5), 884 (2001)].
9. Kh. Benner, B. A. Kalinikos, N. G. Kovshikov, and M. P. Kostylev, Pis'ma Zh. Éksp. Teor. Fiz. **72** (4), 306 (2000) [JETP Lett. **72**, 213 (2000)].
10. R. E. Camley, T. S. Rahman, and D. L. Mills, Phys. Rev. B: Condens. Matter **27** (1), 261 (1983).
11. S. L. Vysotskiĭ, G. T. Kazakov, and A. V. Maryakhin, Pis'ma Zh. Éksp. Teor. Fiz. **61** (8), 673 (1995) [JETP Lett. **61**, 693 (1995)].
12. A. M. Shutyĭ and D. I. Sementsov, Pis'ma Zh. Éksp. Teor. Fiz. **78** (8), 952 (2003) [JETP Lett. **78**, 480 (2003)].
13. S. V. Tarasenko, Fiz. Tverd. Tela (St. Petersburg) **36** (9), 2554 (1994) [Phys. Solid State **36** (9), 1390 (1994)].
14. H. Puszkarski, Surf. Sci. Rep. **20** (2), 45 (1994).
15. S. L. Vysotskiĭ, G. T. Kazakov, M. L. Kats, and Yu. A. Filimonov, Fiz. Tverd. Tela (St. Petersburg) **35** (5), 1191 (1993) [Phys. Solid State **35** (5), 606 (1993)].
16. G. Agrawal, *Nonlinear Fiber Optics* (Academic, San Diego, 1995; Mir, Moscow, 1996).
17. I. O. Zolotovskiĭ and D. I. Sementsov, Zh. Tekh. Fiz. **73** (9), 84 (2003) [Tech. Phys. **48**, 1165 (2003)].
18. V. V. Shagaev, Fiz. Tverd. Tela (St. Petersburg) **40** (11), 2089 (1998) [Phys. Solid State **40** (11), 1892 (1998)].
19. A. G. Gurevich and G. A. Melkov, *Magnetization Oscillations and Waves* (Nauka, Moscow, 1994; CRC, Boca Raton, FL, 1996).

Translated by I. Zvyagin

Physics of the Solid State, Vol. 47, No. 12, 2005, pp. 2274–2280. Translated from Fizika Tverdogo Tela, Vol. 47, No. 12, 2005, pp. 2182–2188.

MAGNETISM AND FERROELECTRICITY

The Spin-Glass State in $Y_2Co_{2/3}Mo_{4/3}O_7$ and $Y_2Fe_{2/3}Mo_{4/3}O_7$ Complex Oxides

G. V. Bazuev* and A. V. Korolev**

**Institute of Solid-State Chemistry, Ural Division, Russian Academy of Sciences, ul. Pervomaĭskaya 91, Yekaterinburg, 620219 Russia*

e-mail: bazuev@ihim.uran.ru

***Institute of Metal Physics, Ural Division, Russian Academy of Sciences, ul. S. Kovalevskoĭ 18, Yekaterinburg, 620219 Russia*

Received December 27, 2004

Abstract—The magnetic properties of $Y_2B_{2/3}Mo_{4/3}O_7$ complex oxides (B = Co, Fe) were studied in the temperature range 2–300 K. At low temperatures, these compounds exhibit spin-glass properties with freezing temperatures T_f = 26 and 33 K, respectively, and typical features in the magnetic hysteresis and in the dependences of the real part of the dynamic magnetic susceptibility on temperature and ac magnetic field frequency. Above T_f, the static magnetic susceptibility of the samples studied depends on the applied magnetic field, which is tentatively assigned to the presence of metallic cobalt and/or yttrium orthoferrite $YFeO_3$ introduced in the course of sample preparation. © *2005 Pleiades Publishing, Inc.*

1. INTRODUCTION

$A_2B_{2/3}B'_{4/3}O_7$ complex oxides [where A stands for rare-earth (RE) elements; Bi, B is a 3d transition metal; and B' is Nb^{5+}, Ta^{5+}, Mo^{5+}, or Re^{5+}] are attracting intense research interest due to the specific features in their structure and electrical and magnetic properties [1–9]. The crystal structure of these compounds was originally identified with that of rhombohedrally distorted pyrochlore $A_2B_2O_7$ with the following parameters (in the hexagonal basis): $a_h \sim 2^{1/2}a_c$ and $c_h \sim 3^{1/2}a_c$, where a_c is the lattice parameter of cubic pyrochlore. High-resolution electron spectroscopy and electron and x-ray diffraction studies performed in [5, 6] revealed two structural modifications characteristic of these compounds, namely, trigonal (space group $P3_121$, z = 6, zirkelite-type structure) and monoclinic (space group $C2/c$, z = 8, 2M $CaZrTi_2O_7$ zirconolite-type structure). In particular, $Er_2Mn_{2/3}Mo_{4/3}O_7$, which is similar in structure to the $Y_2Co_{2/3}Mo_{4/3}O_7$ and $Y_2Fe_{2/3}Mo_{4/3}O_7$ oxides studied in this work, was assigned to the monoclinic crystal system with space group $C2/c$ and lattice parameters a = 12.781 Å, b = 7.378 Å, c = 11.643 Å, and β = 100.53°. In the unit cell of this oxide, two kinds of Er^{3+} cations are in the 8f positions, a Mo^{5+} ion is in the 8f position, Mn^{2+} cations of the first type are in the 4e positions, and Mn^{2+} of the second type and the Mo^{5+} ion are in position 4e in the proportion 0.33Mn + 0.67Mo.

We studied the magnetic properties of the pyrochlore-like oxides $Ln_2Mn_{2/3}Mo_{4/3}O_7$ (Ln = Y, Sm, Gd, Tb [10]) in the temperature range 2–300 K. It was found that, at low temperatures (T < 10–12 K), these compounds possess spin-glass properties with characteristic features of magnetic and thermal hysteresis and with typical dependences of the imaginary and real parts of the dynamic magnetic susceptibility on temperature and ac magnetic field frequency. In the paramagnetic region, the temperature dependence of static magnetic susceptibility χ is described by a generalized Curie–Weiss law with a temperature-independent component of ~10^{-6} cm^3/g and a negative Weiss constant $\theta < 0$ ($|\theta| < 16$ K).

It appeared of interest to study the magnetic properties of analogous oxides, in particular, of compounds formed by substituting other 3d elements for Mn. We present here the results of an investigation of $Y_2Co_{2/3}Mo_{4/3}O_7$ and $Y_2Fe_{2/3}Mo_{4/3}O_7$.

2. EXPERIMENTAL

The compounds to be studied were prepared in solid-phase reactions [3] from the oxides Y_2O_3 (99.95%), Co_3O_4, Fe_2O_3, MoO_3 (99.9%), and metallic molybdenum (99.9%). The synthesis was conducted in vacuum at a pressure of 10^{-3} Pa at 1423 K in a furnace with a W heater. The chemical reactions were monitored using a DRON-2 x-ray diffractometer (CuK_α radiation). The lattice parameters were deduced from measurements of interplane lattice distances. The data were processed with the Fullprof 2004 code.

Magnetic measurements were carried out at the Magnetometry Center of the Institute of Metal Physics (UD, RAS) with an MPMS-5-XL SQUID magnetometer (QUANTUM DESIGN). Samples of

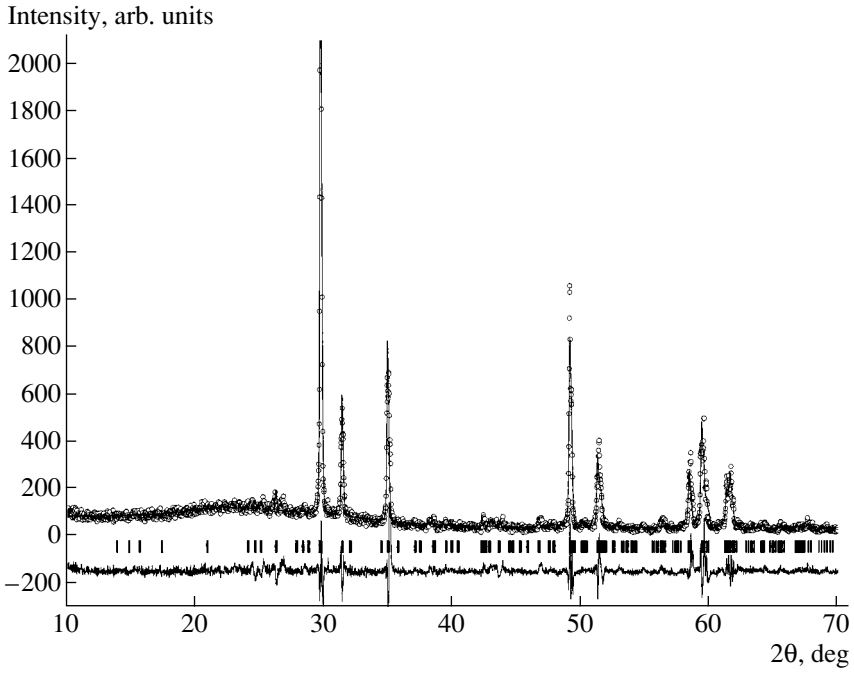

Fig. 1. Experimental (circles), calculated (solid line), and difference (bottom curve) diffractograms of $Y_2Fe_{2/3}Mo_{4/3}O_7$. Vertical bars specify theoretical positions of the reflections.

$Y_2Co_{2/3}Mo_{4/3}O_7$ (in powder form) and $Y_2Fe_{2/3}Mo_{4/3}O_7$ (sintered) were placed in a gelatin capsule. The temperature interval covered was 2–300 K. The magnetic field H could be varied up to 50 kOe. Measurements of the static magnetic moment of a sample were used to calculate the magnetization M and static magnetic susceptibility $\chi = M/H$. The real part χ' of the dynamic magnetic susceptibility was measured in an ac magnetic field with an amplitude of up to 4 Oe at frequencies f ranging from 1 to 10000 Hz.

3. RESULTS AND DISCUSSION

The products of sintering of the original reagents performed in the conditions specified above were shown to produce x-ray diffraction patterns similar to those of the complex oxides $Ln_2A_{2/3}B_{4/3}O_7$ [2–4]. Figure 1 compares an experimental diffractogram of $Y_2Fe_{2/3}Mo_{4/3}O_7$ with the calculated pattern and difference curve obtained by Rietveld refinement (space group $P3_121$). Both diffraction patterns were indexed using the trigonal unit cell with parameters a = 7.425(2) Å and c = 17.028(4) Å for $Y_2Co_{2/3}Mo_{4/3}O_7$ and a = 7.4172(4) Å and c = 17.115(1) Å for $Y_2Fe_{2/3}Mo_{4/3}O_7$. The positions of atoms in the unit cell were not refined. Inspection of the x-ray data permits the conclusion that there is almost a complete absence of any other phases in the samples.

3.1. Magnetic Properties of $Y_2Co_{2/3}Mo_{4/3}O_7$

The temperature dependences of the magnetization M and susceptibility χ were measured in two experimental regimes referred to subsequently as ZFC and FC. In the ZFC regime, a sample is cooled to T = 2 K, after which a dc magnetic field of a given strength H is applied and the magnetization is measured in the course of heating. In the FC regime, the sample is cooled from the high temperature reached and magnetic measurements are performed in the course of cooling in the same field. The $\chi(T)$ dependence measured for $Y_2Co_{2/3}Mo_{4/3}O_7$ in a field H = 0.5 kOe is displayed in Fig. 2. The inset to Fig. 2 shows the reciprocal susceptibility $1/\chi$ plotted versus temperature. The $\chi(T)$ graph in Fig. 2 suggests that the $Y_2Co_{2/3}Mo_{4/3}O_7$ oxide undergoes a magnetic phase transition at about 25 K. It is at this temperature and below it that the $\chi(T)$ function is strongly dependent on the magnetic prehistory of the sample. The $\chi(T)$ curves obtained for the sample under cooling at H = 0 (ZFC regime) and under cooling in a field H = 0.5 kOe (FC regime) diverge at $T \le 26$ K. The $\chi(T)$ curve obtained in the ZFC mode passes through a maximum at 23.5 K. These results suggest that the spin-glass state forms in the oxide under study, as has been observed by us in $Ln_2Mn_{2/3}Mo_{4/3}O_7$ [9]. The pronounced divergence of the $\chi(T)$ curves at low temperatures (Fig. 2) apparently indicates a cluster character of the spin-glass state in $Y_2Co_{2/3}Mo_{4/3}O_7$.

The formation of the spin-glass state in $Y_2Co_{2/3}Mo_{4/3}O_7$ is corroborated by a study of the temperature and frequency dependence of the real part χ' of

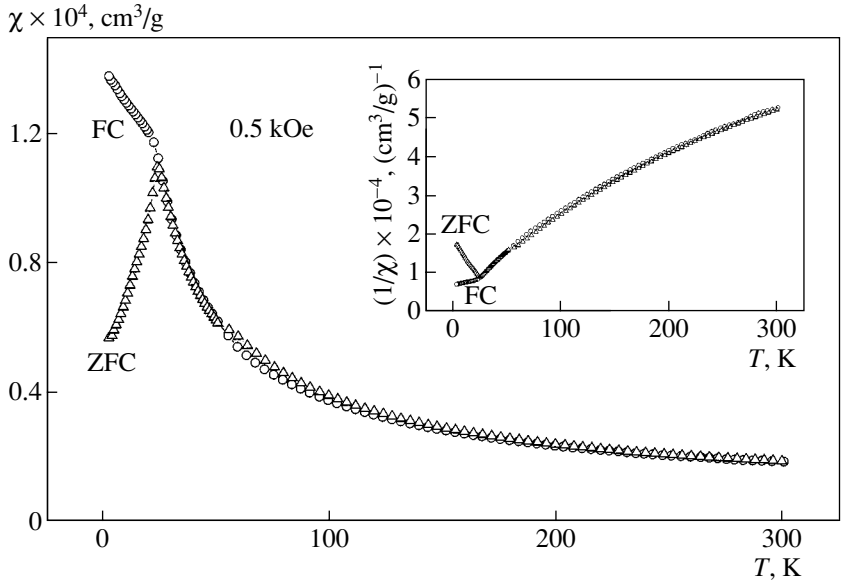

Fig. 2. Temperature dependence of the magnetic susceptibility χ of $Y_2Co_{2/3}Mo_{4/3}O_7$ measured in a magnetic field of 0.5 kOe. The inset shows the reciprocal magnetic susceptibility $1/\chi = f(T)$ measured in a field of 5 kOe.

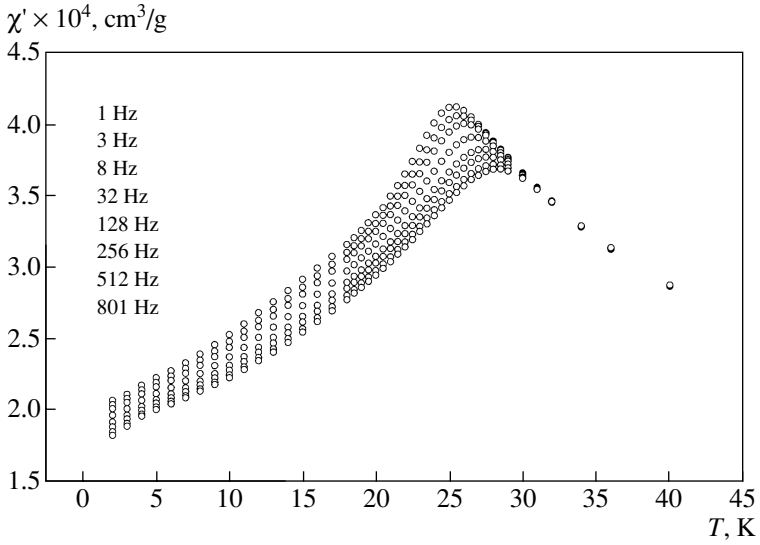

Fig. 3. Temperature dependence of the real part χ' of the dynamic magnetic susceptibility of $Y_2Co_{2/3}Mo_{4/3}O_7$ measured with an ac magnetic field with an amplitude of 4 Oe at frequencies from 1 to 801 Hz.

the dynamic magnetic susceptibility. These experiments were conducted at an ac magnetic field amplitude $H_{\sim} = 4$ Oe. The frequency dependence of $\chi'(f)$ is shown graphically in Fig. 3 for the low-temperature region $T \le 40$ K. We readily see that the magnetic transition temperature depends substantially on the frequency f, with the maximum in the $\chi'(T)$ relation shifting to higher temperatures as the frequency increases. This behavior of the ac susceptibility is characteristic of the spin-glass state.

The dependences of the magnetization M on magnetic field measured at different temperatures are displayed in Figs. 4 and 5. Note that the $M(H)$ functions are nonlinear at 2 and 20 K; in addition, experiment reveals magnetic hysteresis (Fig. 4). The coercive force is 2.5 kOe at 2 K. These findings can likewise be accounted for within the concept of the cluster character of the spin-glass state.

Magnetization measurements suggest (Fig. 5) that the dependence of the magnetic susceptibility on magnetic field persists in a region above the freezing tem-

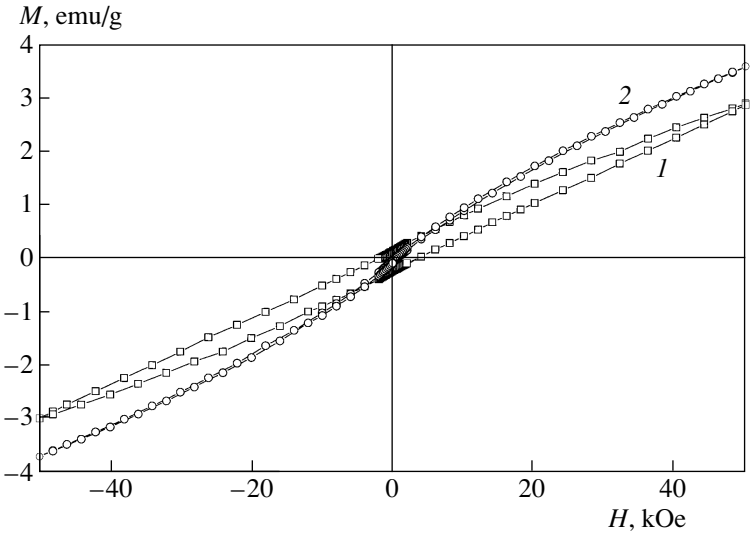

Fig. 4. Magnetization vs field isotherms of $Y_2Co_{2/3}Mo_{4/3}O_7$ measured in the cyclic mode at temperatures of (*1*) 2 and (*2*) 20 K.

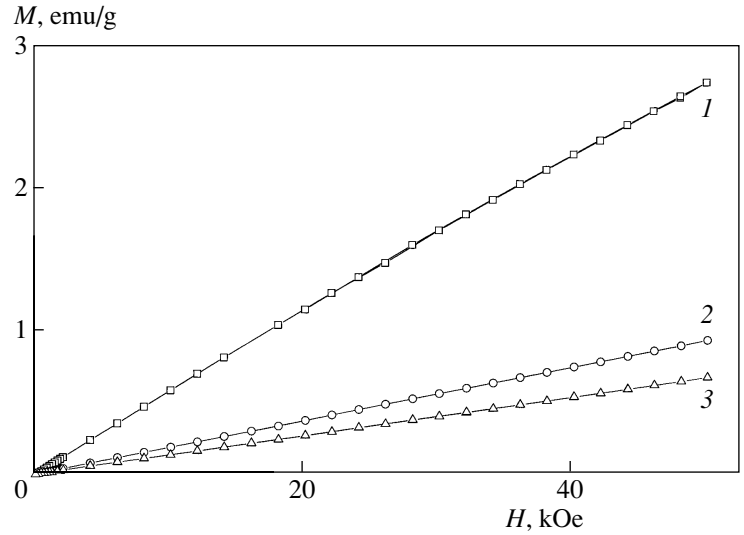

Fig. 5. Magnetization vs magnetic field relation measured on a $Y_2Co_{2/3}Mo_{4/3}O_7$ sample at temperatures of (*1*) 50, (*2*) 200, and (*3*) 300 K.

perature T_f, including 300 K. The spontaneous magnetic moment calculated for 300 K is ~0.001 μ_B. We believe that the existence of a ferromagnetic component above the magnetic transformation point indicates the presence of a small amount of metallic cobalt in the sample. The origin of this metal can be understood from the analysis of the products of synthesis of $Y_2Ni_{2/3}Mo_{4/3}O_7$ [8]. We made an attempt to obtain not only $Y_2Co_{2/3}Mo_{4/3}O_7$ but also a complex nickel-containing oxide of a similar composition in the same conditions (in vacuum at a pressure of 10^{-3} Pa). X-ray diffraction analysis of the product of $Y_2Ni_{2/3}Mo_{4/3}O_7$ synthesis showed as the main phase, however, a MoO_3-based complex oxide and metallic nickel. This may be obviously accounted for by the redox reaction

$$Ni^{2+} + Mo^{5+} \longrightarrow Ni + Mo^{6+}$$

occurring in the course of the synthesis.

One cannot rule out the possibility that the formation of $Y_2Co_{2/3}Mo_{4/3}O_7$ is accompanied by a chemical reaction in which Co^{2+} is reduced to the metallic state in amounts not detectable by x-ray diffraction measurements. The possible occurrence of this reaction is suggested by the electrode potential of Co/Co^{2+} (–0.277 eV), which is close to that of Ni/Ni^{2+} (–0.250 eV) [11].

The $\chi(T)$ and $M(H)$ functions (Figs. 3, 4) are similar in character to those observed with the pyrochlore-like

Curie constant C, Weiss constant θ, and the quantity χ_0 involved in the Curie–Weiss law for the $Y_2Co_{2/3}Mo_{4/3}O_7$ and $Y_2Fe_{2/3}Mo_{4/3}O_7$ compounds

Compound	C_{exp}, cm^3 K/mol	θ, K	$\chi_0 \times 10^6$, cm^3/mol	C_{calc}, cm^3 K/mol
$Y_2Co_{2/3}Mo_{4/3}O_7$	1.60	–9.69	3.95	1.75 (Co^{2+}–Mo^{5+})
$Y_2Fe_{2/3}Mo_{4/3}O_7$	2.95	–82.3	–	2.50 (Fe^{2+}–Mo^{5+})
				3.84 (Fe^{3+}–Mo^{5+}–Mo^{4+})

oxides $Ln_2Mn_{2/3}Mo_{4/3}O_7$ (Ln = Y, Sm, Gd, Tb), in which a spin glass was identified as the ground magnetic state.

The totality of the data obtained permits the conclusion that below ~30 K the $Y_2Co_{2/3}Mo_{4/3}O_7$ oxide resides in the spin-glass state.

A specific feature of the magnetic susceptibility for $T > 30$ K is the deviation of the $1/\chi(T)$ relation from the Curie–Weiss law. This is indicated by the temperature dependence of $1/\chi$ measured in a field of 5 kOe (see inset to Fig. 2). The nonlinear character of this dependence $1/\chi(T)$ at 5 kOe is expressed by the generalized Curie–Weiss law

$$\chi = \chi_0 + C/(T - \theta),$$

where χ_0 is a temperature-independent component, C is the Curie constant, and θ is the Weiss constant. Table 1 lists experimental values of χ_0, θ, and C_{exp} and the values of C_{calc} derived from the corresponding theoretical values for the Co^{2+} and Mo^{5+} cations (1.875 and 0.375 cm^3 K/mol, respectively) with due allowance for their content in the $Y_2Co_{2/3}Mo_{4/3}O_7$ molecule. C_{exp} is seen to be slightly smaller than C_{calc}, which may tentatively be assigned to the fact that the contribution of Mo^{5+} cations to the magnetic susceptibility in the temperature range covered is determined not only by the Curie–Weiss law but also by the temperature-independent component χ_0.

3.2. Magnetic Properties of $Y_2Fe_{2/3}Mo_{4/3}O_7$

The results of magnetization and magnetic susceptibility measurements performed on a $Y_2Fe_{2/3}Mo_{4/3}O_7$ sample are presented in Figs. 6–8. As can be seen from Fig. 6, the values of the magnetic susceptibility χ obtained in the ZFC and FC regimes at ~33 K differ noticeably. In addition, similar to the Co-containing oxide, χ was found to be magnetic-field-dependent above this temperature. The origin of the field dependence of susceptibility of $Y_2Fe_{2/3}Mo_{4/3}O_7$ is, however, not associated with the presence of metallic iron, because the electrode potential of Fe^{2+}/Fe is substantially lower (–0.440 eV [11]) than that of cobalt. It is very likely that the samples contain as a ferromagnetic impurity a very small amount of iron orthoferrite $YFeO_3$, which is a noncollinear antiferromagnet with T_N = 640 K. The presence of the $YFeO_3$ oxide as an

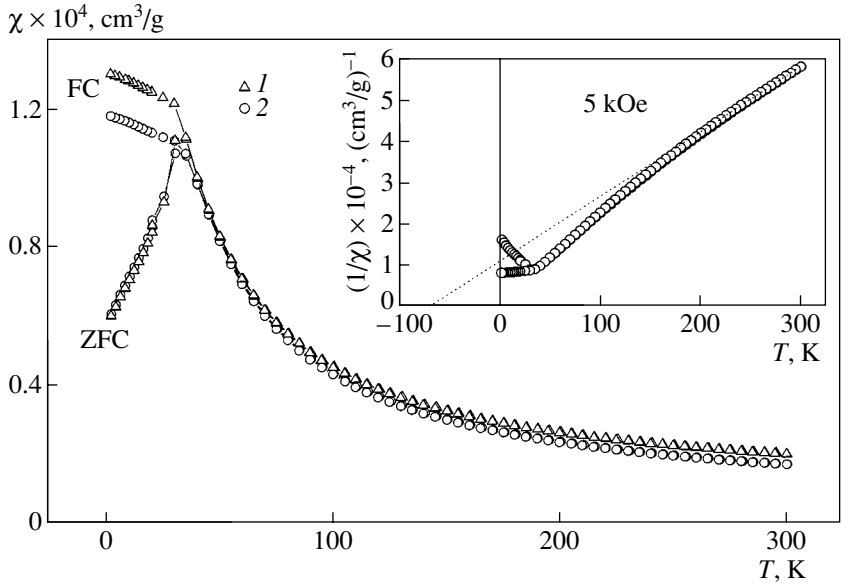

Fig. 6. Temperature dependence of the magnetic susceptibility χ of $Y_2Fe_{2/3}Mo_{4/3}O_7$ measured in the ZFC and FC modes in magnetic fields of (*1*) 0.5 and (*2*) 5 kOe. The inset shows the temperature dependence of the reciprocal magnetic susceptibility $1/\chi = f(T)$ obtained in a field of 5 kOe.

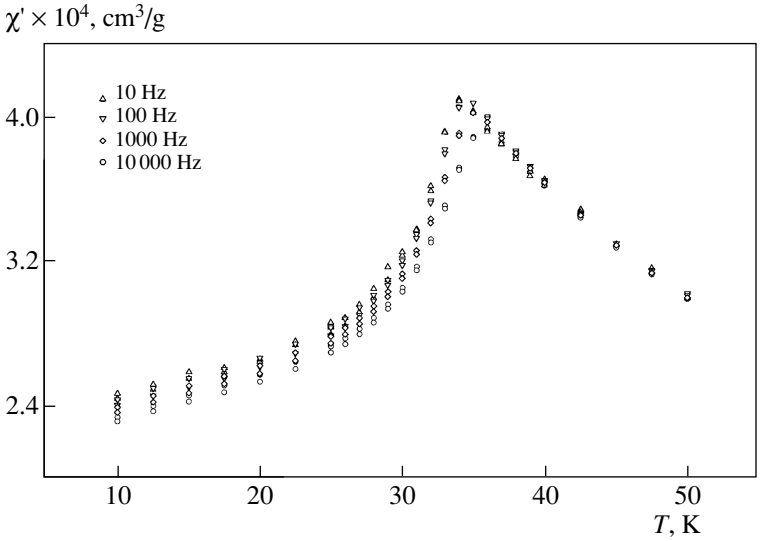

Fig. 7. Temperature dependence of the real part χ' of the dynamic magnetic susceptibility of $Y_2Fe_{2/3}Mo_{4/3}O_7$ measured with an ac magnetic field with an amplitude of 4 Oe at frequencies ranging from 10 to 10000 Hz.

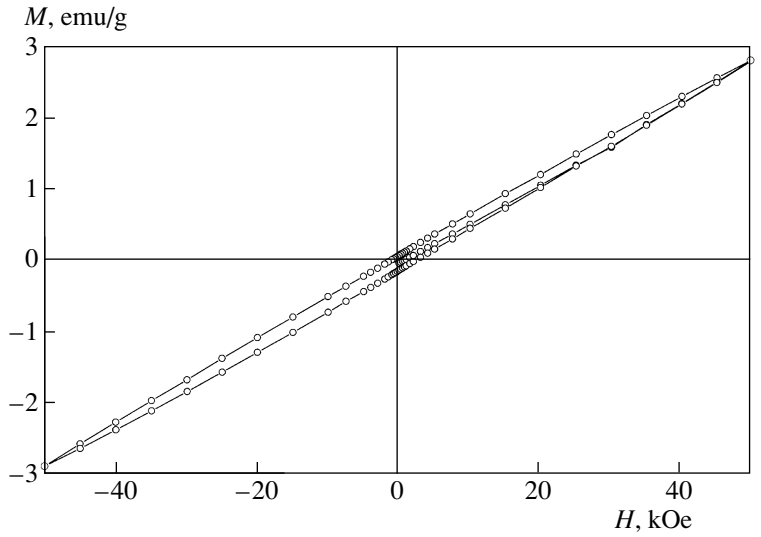

Fig. 8. Magnetization–field isotherm for $Y_2Fe_{2/3}Mo_{4/3}O_7$ measured in the cyclic mode at 2 K.

impurity phase was detected earlier [3] in attempts to synthesize Ln_2FeMoO_7 compounds, where *Ln* stands for RE elements (from Nd to Tm and Y).

As follows from measurements carried out in a magnetic field of 5 kOe, the reciprocal magnetic susceptibility $1/\chi$ at temperatures above the magnetic transition point obeys the Curie–Weiss law $\chi = C/(T - \theta)$ only in the range 220–300 K. The value of the constant *C* listed in the table slightly exceeds that calculated for the $(2/3)Fe^{2+}$–$(4/3)Mo^{5+}$ cation combination but is smaller than that obtained for another possible combination, $(2/3)Fe^{3+}$–$(2/3)Mo^{5+}$–$(2/3)Mo^{4+}$. It is appropriate to mention here the Mössbauer studies performed in [12], according to which the cation combination characteristic of the ALaFeMoO$_6$ perovskites (A = Ca, Ba) is Fe^{3+}–Mo^{4+}, in contrast to the manganese-containing compounds ALaMn^{2+}Mo^{5+}O$_6$.

We made an attempt to describe the observed temperature dependence of magnetic susceptibility above the magnetic transition point T_f in terms of a modified Curie–Weiss law,

$$\chi = \chi_0 + C/(T - \theta),$$

where $\chi_0 = 4.19 \times 10^{-6}$ cm^3/g and $\theta = 1.98$ K. The value of the Curie constant *C* obtained in this approximation (1.75 cm^3 K mol^{-1}) turned out, however, to be very

small as compared to those calculated for the above cation combinations.

According to the data displayed in Figs. 7 and 8, the temperature of the magnetic transition in $Y_2Fe_{2/3}Mo_{4/3}O_7$, exactly as in the case of $Y_2Co_{2/3}Mo_{4/3}O_7$, shifts to higher temperatures with increasing frequency and a magnetic hysteresis loop is observed at 2 K.

4. CONCLUSIONS

The results obtained in this study permit the conclusion that both oxides prepared here, $Y_2Fe_{2/3}Mo_{4/3}O_7$ and $Y_2Co_{2/3}Mo_{4/3}O_7$, are spin glasses with freezing temperatures of ~33 and 26 K, respectively. Just as in the case of $Ln_2Mn_{2/3}Mo_{4/3}O_7$, the spin-glass state in $Y_{2/3}B'_{2/3}Mo_{4/3}O_7$ (B' = Co, Fe) is a consequence of frustrated magnetic interactions among the disordered subsystems of the transition metals occupying the B and B' positions.

ACKNOWLEDGMENTS

This study was supported by the Russian Foundation for Basic Research, project no. 02-03-32972.

REFERENCES

1. F. Basile, P. Poix, and A. Michel, Ann. Chem. (Warsaw) **2** (6), 283 (1977).
2. G. V. Bazuev, O. V. Makarova, and G. P. Shveĭkin, Zh. Neorg. Khim. **29**, 875 (1984).
3. G. V. Bazuev, O. V. Makarova, and N. A. Kirsanov, Zh. Neorg. Khim. **34**, 23 (1989).
4. G. V. Bazuev, T. I. Chupakhina, and V. N. Krasil'nikov, Pis'ma Zh. Éksp. Teor. Fiz. **74** (7), 440 (2001) [JETP Lett. **74**, 401 (2001)].
5. H. Nakano and N. Kamegashira, J. Am. Ceram. Soc. **84** (6), 1374 (2001).
6. G. Chen, K. Takasaka, and N. Kamegashira, J. Alloys Compd. **233**, 206 (1996).
7. G. V. Bazuev, T. I. Chupakhina, and G. P. Shveĭkin, Zh. Neorg. Khim. **48** (5), 715 (2003).
8. T. Levin, T. G. Amos, J. C. Nino, T. A. Vanderch, I. M. Reany, C. A. Randall, and M. T. Lanagen, J. Mater. Res. **17** (6), 1406 (2002).
9. G. V. Bazuev, Zh. Neorg. Khim. **35** (12), 3063 (1990).
10. A. V. Korolev and G. V. Bazuev, Fiz. Tverd. Tela (St. Petersburg) **46** (2), 297 (2004) [Phys. Solid State **46** (2), 294 (2004)].
11. L. Pauling and P. Pauling, *Chemistry* (Freeman, San Francisco, 1975; Mir, Moscow, 1978).
12. T. Nakamura and J.-H. Choy, J. Solid State Chem. **20** (2), 233 (1977).

Translated by G. Skrebtsov

Physics of the Solid State, Vol. 47, No. 12, 2005, pp. 2281–2286. Translated from Fizika Tverdogo Tela, Vol. 47, No. 12, 2005, pp. 2189–2194.

MAGNETISM AND FERROELECTRICITY

Magnetoresistance of $La_{0.67}Sr_{0.33}MnO_3$ Epitaxial Films Grown on a Substrate with Low Lattice Mismatch

Yu. A. Boĭkov*, T. Claeson, and V. A. Danilov***

**Ioffe Physicotechnical Institute, Russian Academy of Sciences, Politekhnicheskaya ul. 26, St. Petersburg, 194021 Russia*

e-mail: yu.boikov@mail.ioffe.ru

***Chalmers Technical University, Göteborg, S-41296 Sweden*

Received January 28, 2005

Abstract—The structure, electrical resistivity, and magnetoresistance of $La_{0.67}Sr_{0.33}MnO_3$ heteroepitaxial films (120-nm thick) practically unstrained by lattice mismatch with the substrate were studied. A strong maximum of negative magnetoresistance of ≈27% (for $\mu_0 H = 4$ T) was observed at $T \approx 360$ K. While the magnetoresistance decreased monotonically in magnitude with decreasing temperature, it was still in excess of 2% at 150 K. For $T < 250$ K, the temperature dependence of the electrical resistivity ρ of $La_{0.67}Sr_{0.33}MnO_3$ films is fitted well by the relation $\rho = \rho_0 + \rho_1(H)T^{2.3}$, where $\rho_0 = 1.1 \times 10^{-4}$ Ω cm, $\rho_1(H = 0) = 1.8 \times 10^{-9}$ Ω cm/K$^{2.3}$, and $\rho_1(\mu_0 H = 4\text{ T})/\rho_1(H = 0) \approx 0.96$. The temperature dependence of a parameter γ characterizing the extent to which the electrical resistivity of the ferromagnetic phase of $La_{0.67}Sr_{0.33}MnO_3$ films is suppressed by a magnetic field ($\mu_0 H = 5$ T) was determined. © *2005 Pleiades Publishing, Inc.*

1. INTRODUCTION

Perovskite-like manganites $La_{1-x}(Sr,Ca)_xMnO_3$ have promising application potential for use in magnetoresistive sensors [1], memory cells [2], and active (or passive) elements of spintronics, on which considerable progress has been made in recent years [3, 4].

Manganites are characterized by a strong interrelation between the spin, charge, and orbital interactions. This feature makes it possible to optimize (tailoring) their electronic parameters by properly varying the doping level (the index x in the chemical formula), applying a magnetic field, or changing the structure, type, and magnitude of elastic strains in the unit cell.

To use the potential inherent in $La_{1-x}(Sr,Ca)_xMnO_3$ films to the full extent, as well as to unravel the fundamental mechanisms underlying their electric and magnetic transport properties, one needs to have thin epitaxial layers that are uniform in thickness, composition, and Curie temperature T_{Curie}. However, even at $T < T_{Curie}$ and even in compositionally uniform manganite films, there are not only ferromagnetic domains but also inclusions of various (paramagnetic, antiferromagnetic, etc.) phases. The difference between the values of T_{Curie} in the bulk of a $La_{1-x}(Sr,Ca)_xMnO_3$ film, at the free surface, and near the interface with the substrate can be as much as a few tens of kelvins [5]. The extent to which nonferromagnetic phase inclusions can affect electron transport in a manganite film depends on their concentration, size, and spatial orientation, which vary with temperature and magnetic field strength [6]. This considerably complicates the obtainment of reliable information on the electronic parameters of the ferromagnetic phase in a manganite film.

We report here on a study of the dependence of the electrical resistivity ρ of $La_{0.67}Sr_{0.33}MnO_3$ films (LSMO), $d = 120$ nm thick, on temperature and magnetic field strength. To reduce the effect of nonuniform strains on electron transport, manganite films were grown on substrates of a perovskite-like oxide with a very small lattice misfit.

2. EXPERIMENT

LSMO films (120-nm thick) were grown on $(LaAlO_3)_{0.3} + (Sr_2AlTaO_6)_{0.7}$ (LSATO) substrates by laser evaporation (KrF, $\lambda = 248$ nm, $\tau = 30$ ns). In the course of evaporation of a starting LSMO ceramic target, the substrate temperature was 790°C and the oxygen pressure in the growth chamber was maintained at a level of 0.3 mbar. The conditions of preparation of the manganite films are described in [7].

The structure of LSMO films was studied by x-ray diffraction (Philips X'pert MRD, $\omega/2\theta$ and θ scans, rocking curves). The $\omega/2\theta$ diffractograms were obtained with the incident and reflected x-ray beams lying in the plane normal to (001) or (101) LSATO. The manganite film surface morphology was visualized with atomic force microscopy (AFM, NanoScope-IIIa).

The resistance R of the films was measured in the van der Pauw configuration, both in a magnetic field and without it. The magnetic field ($\mu H = 0$–5 T) was parallel to the substrate plane but orthogonal to the measuring current direction. Four silver electrodes in

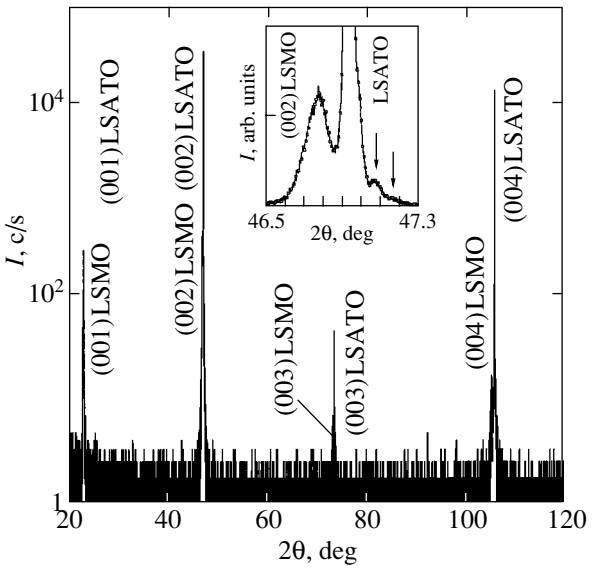

Fig. 1. Diffraction pattern (ω/2θ, Cu$K_{\alpha 1}$ radiation) of a (120-nm) LSMO(LSATO) film. The plane containing the incident and reflected x-ray beams is perpendicular to the substrate plane. The inset shows a fragment of the same pattern in proximity to the (002) LSMO peak. The (002) peak of the manganite film and the stronger substrate peak are clearly resolved. Arrows in the inset identify satellite Laue peaks of the manganite film.

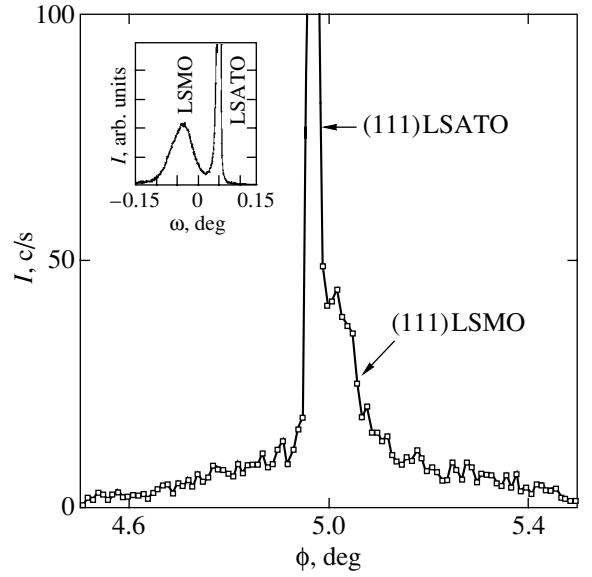

Fig. 2. Fragment of an x-ray ϕ scan of the (111) reflections from an LSATO substrate and a (120-nm) LSMO manganite film grown on its surface. The manganite film peak is distorted, with tails about 0.4° wide seen on both sides of the relatively narrow central part of the peak. The inset shows (ω–2θ) rocking curves for the (002) x-ray peaks due to the manganite film and the substrate.

the corners of a square were thermally deposited on the free surface of a manganite film through a metal template. The electrical resistivity ρ of the films was calculated from the relation $\rho = \pi dR/\ln 2$ [8].

3. RESULTS AND DISCUSSION

Mechanical strains exert a noticeable effect on the nucleation of films of multicomponent perovskite-like oxides, in particular, on the stoichiometry of stable nuclei of the condensing phase. It was shown in [6] that, as the lattice misfit between a substrate and a manganite film atop it increases, the composition of the latter deviates progressively more strongly from that of the starting target. The lattice parameter of pseudocubic LSATO films (a_1 = 3.868 Å [9]) closely approaches that of the rhombohedral cell of LSMO (a_2 = 3.876 Å, α = 90.46° [10]). The small lattice misfit and the similar values of the linear thermal expansion coefficients [9, 10] account for our selection of polished (001) LSATO plates (5 × 5 mm) as substrates for LSMO films.

3.1. The Structure of LSMO Films

X-ray studies of the grown LSMO films did not reveal any macroscopic inclusions of secondary phases in their volume. The ω/2θ diffractograms contained only peaks due to the substrate and the manganite film (Fig. 1). For 2θ > 40°, the x-ray peaks from the substrate and the LSMO film were clearly resolved (see inset to Fig. 1). The presence of Laue satellite peaks (identified by arrows in the inset) in the diffraction patterns indicates that the films are uniform in thickness *d*. The satellite width data were used to monitor the magnitude of *d*.

Measured ϕ scans for the {111} LSMO/LSATO reflections exhibited four equidistant (90°-spaced) peaks. Since the lattice misfit between the manganite film and the substrate was small, the peaks due to the latter in a ϕ scan overlapped the corresponding peaks from the LSMO layer (Fig. 2).

The width of the substrate peaks measured at half maximum (FWHM ≈ 0.01°) coincides with the instrumental resolution in angle ϕ. The peaks due to the manganite film show considerable distortions and are a few times wider than the substrate peaks. The relatively narrow (FWHM ≈ 0.08°) main part of the LSMO peak is joined on both sides by two tails with an angular width of about 0.4° each (Fig. 2). The manganite peak in an x-ray ϕ scan is shifted by approximately 0.06° with respect to the corresponding substrate peak. This may be partially accounted for by rhombohedral distortions of the LSMO unit cell.

The ω–2θ rocking curve for the (002) reflection from a (120-nm-thick) film of LSMO/LSATO is given in the inset to Fig. 2. The width of the rocking curve measured at half maximum, ~0.07°, is in good agreement with the data obtained for high-quality epitaxial manganite films thermally treated at a high temperature in an oxygen environment [11]. This value exceeds, however, the rocking curve width (~0.006°, shown in the same inset) of the (002) reflection from the substrate by about an order of magnitude. The fact that the rocking curve width of a manganite film is larger than that

of a single crystal substrate should be assigned to the comparatively high defect density in the bulk of the film.

The x-ray diffraction data suggest that the grown manganite films are predominantly oriented both relative to the normal to the substrate plane and azimuthally and that (001)[010]LSMO||(001)[010]LSATO. The values of 2θ for the (303) and (004) peaks in the measured ω/2θ x-ray scans were used to determine the lattice parameters of the LSMO film in the substrate plane ($a_\parallel$ = 3.873 ± 0.005 Å) and along the surface normal ($a_\perp$ = 3.884 ± 0.005 Å). The parameter $a_\perp$ of the manganite film is slightly in excess of the parameter $a_\parallel$, which practically coincides with the measured lattice parameter for the substrate, a = 3.869 ± 0.003 Å. Thus, the LSMO films were coherently grown on the substrate surface and experienced only very weak mechanical biaxial compressive stresses.

The grown (120-nm-thick) LSMO films consisted of grains with lateral dimensions of 30–80 nm (Fig. 3). The azimuthal grain misorientation in the LSMO film was, on the average, about 0.1°, but there were grains in the bulk of the film with misorientation two- to fourfold larger than this value. The main reason accounting for grain misorientation in a manganite film is the lattice misfit between LSATO and LSMO. Grain boundaries in the manganite film were distinctly decorated by depressions on the free surface (Fig. 3).

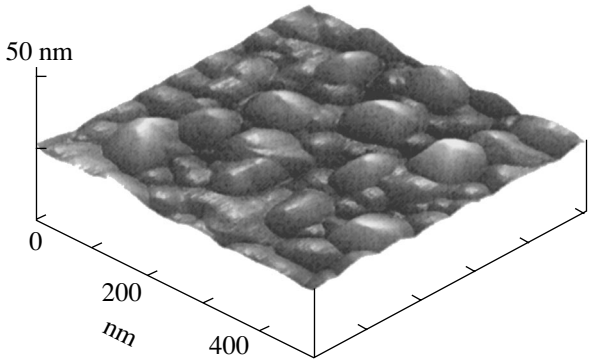

Fig. 3. AFM image of the free surface of a (120-nm) LSMO/LSATO film. The small-angle grain boundaries in the manganite film are decorated by characteristic depressions on its free surface.

3.2. Response of Electrical Resistivity to a Magnetic Field at Different Temperatures

Figure 4 shows the temperature dependences of electrical resistivity ρ of the (120-nm) LSMO/LSATO film measured under cooling at $\mu_0 H$ = 0 (curve *1*) and 4 T (curve *2*). The sharp drop in ρ(H = 0) with decreasing temperature started at $T \approx T_{Curie}$ (for LSMO crystals, T_{Curie} = 378 K [12]). For $T < T_{Curie}$, the decrease in the electrical resistivity of the film with a decrease in temperature is caused by the increased ferromagnetic domain concentration in its bulk. Growth of domains with distinct predominant spatial spin orientation gives rise to the formation of high-conductivity ferromagnetic percolation channels in the LSMO layer. A magnetic field favors an increase in the temperature of ferromagnetic spin ordering in a manganite film and suppresses spatial misorientation of spins on the manganese ions. This accounts for the observed decrease in ρ of films in a magnetic field and for the high-temperature shift of the maximum in the ρ(T, H) curve with respect to the corresponding maximum observed at H = 0.

Data on the temperature dependence of the magnetic susceptibility of epitaxial LSMO films [12] suggest that, at $T < 0.5\ T_{Curie}$, ferromagnetic domains occupy most of the manganite film volume. There are very few theoretical papers in the literature dealing with electron transport in manganites [13]. According to the

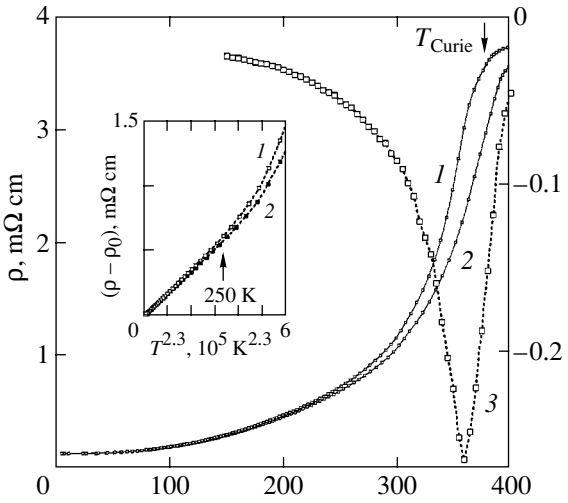

Fig. 4. Temperature dependences of (*1*, *2*) the electrical resistivity ρ and (*3*) magnetoresistance MR of a (120-nm) LSMO(LSATO) film measured for $\mu_0 H$ equal to (*1*) 0 and (*2*, *3*) 4 T. The Curie temperature for bulk LSMO crystals [12] is specified by an arrow. The inset shows a fragment of the (ρ – ρ_0) vs. $T^{2.3}$ dependence obtained on the same film at $\mu_0 H$ equal to (*1*) 0 and (*2*) 4 T; $\rho_0 \equiv \rho(H = 0, T = 4.2\ \text{K}) = 1.1 \times 10^{-4}\ \Omega\ \text{cm}$.

available theoretical models [14, 15], the relaxation of electrons in 3*d* ferromagnetic metals is due to their interaction with phonons and spin waves and electron–electron interaction. When electron–electron and electron–magnon scattering dominate, the electrical resistivity of ferromagnetic metals should depend quadratically on temperature. The electrical resistivity of manganite films for $T \ll T_{Curie}$ was found in [16, 17] to scale as $\rho \sim T^n$, where n = 2–2.5. The main mechanisms governing carrier relaxation were assumed in [16, 17] to be the electron–electron, electron–phonon, and electron–magnon interactions.

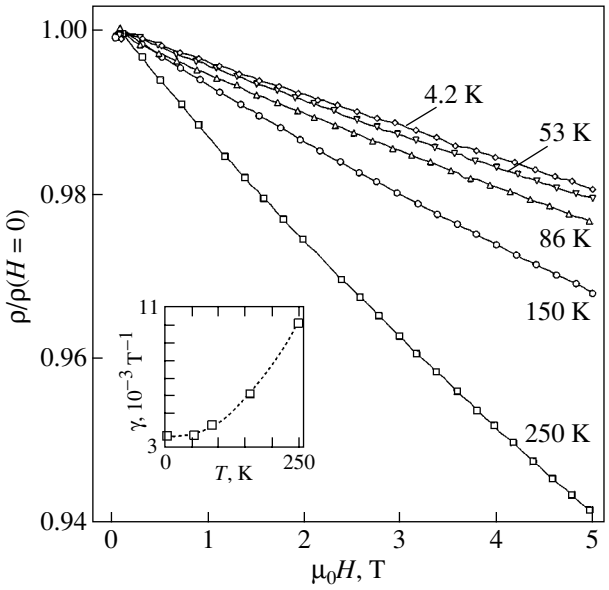

Fig. 5. Ratio $\rho/\rho(H = 0)$ for a (120-nm) LSMO/LSATO film plotted vs $\mu_0 H$ for various temperatures. The inset shows the temperature dependence of parameter γ; the dotted line is the $\gamma(T)$ dependence given by Eq. (3).

The inset to Fig. 4 shows the electrical resistivity of a (120-nm) LSMO/LSATO film plotted versus $T^{2.3}$. For $T < 250$ K, the temperature dependence of the electrical resistivity of our manganite films is fitted well by the relation

$$\rho = \rho_0 + \rho_1(H)T^{2.3}, \quad (1)$$

where

$$\rho_0 \equiv \rho(H = 0, T = 4.2\ \text{K}) = 1.1 \times 10^{-4}\ \Omega\ \text{cm},$$

$$\rho_1(H = 0) = 1.8 \times 10^{-9}\ \Omega\ \text{cm/K}^{2.3},$$

$$\rho_1(\mu_0 H = 4\ \text{T})/\rho_1(H = 0) \approx 0.96.$$

The coefficient ρ_1 was quoted in [16, 17] to decrease almost linearly with increasing H.

The $\rho(H)$ relations measured at $T \ll T_{\text{Curie}}$ offer information on the contribution of electron–magnon interaction to carrier relaxation in manganite films. The $\rho(H)$ curves obtained on (120-nm) LSMO/LSATO films at various temperatures in the range 4.2–250 K are shown in Fig. 5. For $T < 100$ K, the electrical resistivity of a manganite film obeys the relation

$$\rho(H) = \rho(H = 0)(1 - \gamma\mu_0 H), \quad (2)$$

where the coefficient γ is practically independent of H and of the measuring current passed through the sample. At $T > 100$ K, spacers of phases with a lower Curie temperature may contribute heavily to the electrical resistivity of LSMO films. Such spacers, as a rule, form at grain boundaries as a result of distortions in stoichiometry and nonuniform strains. As follows from the data from Fig. 5, the negative slope of the $\rho(H, 250\ \text{K})$ graph for $\mu_0 H < 2$ T is larger in magnitude than the slope of this curve for $\mu_0 H > 3$ T. A magnetic field favors the transformation of nonferromagnetic to ferromagnetic spacers and reduces the spin misorientation of manganese ions at grain boundaries. Therefore, the slope of the $\rho(H, 250\ \text{K})$ curve for $\mu_0 H > 3$ T is more strongly affected by the magnetic-field-induced change in the ferromagnetic phase parameters than the slope for $\mu_0 H < 2$ T. The values of the coefficient γ for (120-nm) LSMO/LSATO films at different temperatures were calculated using the relation $\gamma = \rho(H = 0)^{-1} d\rho/d(\mu_0 H)$, where $d\rho/d(\mu_0 H)$ was determined at $\mu_0 H = 4$–5 T. Incidentally, for $T < 250$ K, the values of $d\rho/d(\mu_0 H)$ for (120-nm) LSMO/LSATO films exceed manifold those for films of 3*d* ferromagnetic metals. At $T \approx 150$ K, the derivative $d\rho/d(\mu_0 H)$ for the manganite films under study was about 2 $\mu_0\Omega$ cm T^{-1}, which is about three orders of magnitude larger than that for iron [15]. As follows from the data displayed in the inset to Fig. 5, the coefficient γ for (120-nm) LSMO/LSATO films increases noticeably with temperature. The variation in γ with temperature fitted well to the relation

$$\gamma = \gamma_0 + \gamma_1 T + \gamma_2 T^2, \quad (3)$$

where $\gamma_0 = 3.8 \times 10^{-3}$, $\gamma_1 = -3.4 \times 10^{-6}$, and $\gamma_2 = 1.2 \times 10^{-7}$. The $\gamma(T)$ curve for Eq. (3) is drawn in the inset to Fig. 5 (dotted line). In the range 4.2–250 K, the contribution of the second term on the right-hand side of Eq. (3) does not exceed 10%.

In [18], the parameter γ was used to derive information on the contribution of electron–magnon scattering to the electrical resistivity of thin Fe, Co, and Ni films and on the effect of a magnetic field on spin-wave damping for $T/T_{\text{Curie}} < 0.6$. The pattern of the temperature dependence of the parameter γ for films of ferromagnetic metals compares well to the data displayed in the inset to Fig. 5. However, as the temperature decreases to $T < 0.1T_{\text{Curie}}$, the parameter γ of (120-nm) LSMO/LSATO films remains practically constant rather than tending to zero, as is the case with thin films of ferromagnetic metals [18]. This may be due to the fact that the magnetic fields employed in the studies of films of ferromagnetic metals were about an order of magnitude higher than those in our work. At temperatures close to $0.1T_{\text{Curie}}$, magnetic fields of a few tens of teslas efficiently freeze electron–magnon scattering in ferromagnetic metals [15].

Electron–magnon scattering in 3*d* ferromagnetic metals is accompanied by electron spin rotation through 180° [15, 18]. In perovskite-like manganites, this rotation of spins requires a substantially larger energy than in the above metals. The conduction band in manganites is split into two subbands, each corresponding to electrons with a certain spin orientation (up or down) [19]. Because the Hund energy in the manga-

nites $La_{1-x}(Sr,Ca)_xMnO_3$ is substantially higher than the subband width, the subbands are separated by a gap of about 1 eV [20]. The Fermi level lies in the lower subband; therefore, the electrons in the manganites, unlike those in 3*d* ferromagnetic metals, are almost completely polarized. The specific features of electron–magnon scattering in manganite films require further theoretical and experimental refinement.

$La_{1-x}(Sr,Ca)_xMnO_3$ heteroepitaxial films are characterized by a pronounced anisotropy in the magnetoresistance, magnetization, etc. The spontaneous magnetization vector in a $La_{1-x}(Sr,Ca)_xMnO_3$ film strained mechanically by a substrate is perpendicular to the substrate plane under biaxial compression and is parallel to this plane in the case of biaxial tension. The films dealt with in this paper were acted upon by weak in-plane compressive stresses. Due to the effect of a demagnetizing field [21], the spontaneous magnetization vector in the (120-nm) LSMO/LSATO films should be parallel to the substrate plane and to the [100] LSATO direction [22] (in [23], the predominant direction of spontaneous magnetization is indicated to be [110]). At temperatures below 100 K, the $\rho(H)$ relations reveal hysteresis and an additional relative minimum at small values of $\mu_0 H$ (see inset to Fig. 6). This is a manifestation of an anisotropy in the electronic and magnetic properties of our manganite films. The anisotropy in the magnetic parameters noticeably affects the magnetoresistance of strained magnetic films even in a comparatively weak magnetic field ($\mu_0 H < 0.5$ T) [24].

The maximum magnitude of the negative magnetoresistance, $MR = [\rho(\mu_0 H = 4\text{ T}) - \rho(\mu_0 H = 0)]/\rho(\mu_0 H = 0) = -0.27$, was observed in the (120-nm) LSMO/LSATO films at $T_M \approx 360$ K (Fig. 4).

In [12], the maximum magnitude of the MR(*T*) of LSMO films exposed to oxygen at a high temperature was observed at practically the same temperature. The sharp drop of MR in magnitude with increasing temperature for $T > T_M$ indicates that the dispersion in T_{Curie} of grains making up the LSMO film is slight. The decrease in the magnitude of MR with decreasing temperature observed to occur for 250 K $< T < T_M$ is caused primarily by the decreased concentration of nonferromagnetic phase inclusions in the bulk of a manganite film and the decreased relative spatial spin misorientation in ferromagnetic domains. Figure 6 displays the MR(*H*) dependence measured on a (120-nm) LSMO/LSATO film at a temperature 10 K below T_M. This dependence is reproduced practically without hysteresis under a repeated sweep of $\mu_0 H$ from –5 to +5 T and back. The absolute values of the derivative $d(MR)/dH$ decrease with increasing *H*, but the dependence of the magnetoresistance on the strength of the magnetic field does not become linear even at $\mu_0 H \approx 5$ T.

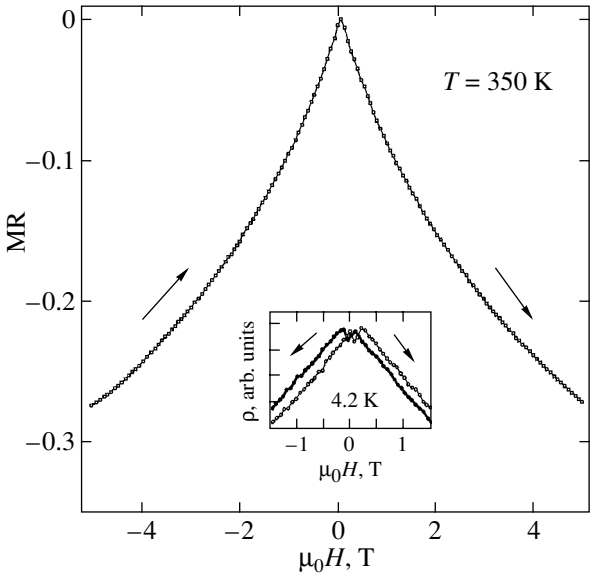

Fig. 6. Magnetic field dependences of the magnetoresistance MR obtained on (120-nm) LSMO/LSATO films at $T = 350$ K. The inset shows a fragment of the $\rho(H, T = 4.2\text{ K})$ relation measured with $\mu_0 H$ varied from +5 to –5 T and back.

4. CONCLUSIONS

To sum up, the temperature dependences of the electrical resistivity of (120-nm) LSMO films (which are only weakly strained by the substrate and are predominantly oriented both in azimuth and relative to the film normal) measured in a magnetic field (with $\mu_0 H$ up to 5 T) and without it agree well with the corresponding data available for bulk crystals. The negative magnetoresistance has been found to reach a maximum magnitude at temperatures about 15 K below T_{Curie} for stoichiometric bulk samples. At low temperatures ($T <$ 100 K), the decrease in ρ of manganite films observed to occur in a magnetic field originates to a considerable extent from the decreased intensity of electron–magnon interaction due to spin wave damping.

ACKNOWLEDGMENTS

This study was carried out in the framework of scientific cooperation between the Russian Academy of Sciences and the Swedish Royal Academy of Sciences. This work was supported in part by the Russian Foundation for Basic Research (project no. 04-02-16212-a) and the program under the Presidium of the Russian Academy of Sciences “Low-Dimensional Quantum Structures” (project no. 9B19).

REFERENCES

1. M. Pannetier, C. Fermon, G. de Goff, J. Simola, and E. Kerr, Science (Washington) **304** (5677), 1648 (2004).

2. S. S. P. Parkin, K. P. Roche, M. G. Samant, P. M. Rice, R. B. Beyers, R. E. Scheuerlein, E. J. O'Sullivan, S. L. Brown, J. Bucchigano, D. W. Abraham, Y. Lu, M. Rooks, P. L. Trouiloud, R. A. Wanner, and W. G. Gallagher, J. Appl. Phys. **85** (8), 5828 (1999).
3. Z. W. Dong, R. Ramesh, T. Venkatesan, M. Johnson, Z. Y. Chen, S. P. Pai, V. Talyansky, R. P. Sharma, R. Shreekala, C. J. Lobb, and R. L. Greene, Appl. Phys. Lett. **71** (12), 1718 (1997).
4. M. Bowen, M. Bibes, A. Barthelemy, J.-P. Contour, A. Anane, Y. Lemaitre, and A. Fert, Appl. Phys. Lett. **82** (2), 233 (2003).
5. V. Garcia, M. Bides, A. Barthelemy, M. Bowen, E. Jacquet, J.-P. Contour, and A. Fert, Phys. Rev. B: Condens. Matter **69** (5), 052 403 (2004).
6. Yu. A. Boikov, R. Gunnarsson, and T. Claeson, J. Appl. Phys. **96** (1), 435 (2004).
7. Yu. A. Boĭkov and T. Claeson, Fiz. Tverd. Tela (St. Petersburg) **47** (2), 274 (2005) [Phys. Solid State **47** (2), 287 (2005)].
8. T. I. Kamins, J. Appl. Phys. **42** (9), 4357 (1971).
9. Yu. A. Boikov and T. Claeson, Physica B (Amsterdam) **311** (3–4), 250 (2002).
10. M. C. Martin, G. Shirane, Y. Endoh, K. Hirota, Y. Moritomo, and Y. Tokura, Phys. Rev. B: Condens. Matter **53** (21), 14 285 (1996).
11. Yu. A. Boĭkov, T. Claeson, and A. Yu. Boĭkov, Zh. Tekh. Fiz. **71** (10), 54 (2001) [Tech. Phys. **46**, 1260 (2001)].
12. G. J. Snyder, R. Hiskes, S. DiCarolis, M. R. Beasly, and T. H. Geballe, Phys. Rev. B: Condens. Matter **53** (21), 14434 (1996).
13. K. Kubo and N. Ohata, J. Phys. Soc. Jpn. **33** (1), 21 (1972).
14. D. A. Goodings, Phys. Rev. **132** (2), 542 (1963).
15. B. Raquet, M. Virtet, J. M. Broto, E. Sondergard, O. Cespedes, and R. Mamy, J. Appl. Phys. **91** (10), 8129 (2002).
16. P. Schiffer, A. P. Ramirez, W. Bao, and S.-W. Cheong, Phys. Rev. Lett. **75** (18), 3336 (1995).
17. J. M. de Teresa, M. R. Ibarra, J. Blasco, J. Garcia, C. Marquina, P. A. Algarabel, Z. Arnold, K. Kamenev, C. Ritter, and R. von Helmolt, Phys. Rev. B: Condens. Matter **54** (2), 1187 (1996).
18. B. Raquet, M. Viret, E. Sondergard, O. Cespedes, and R. Mamy, Phys. Rev. B: Condens. Matter **66** (2), 024 433 (2002).
19. Y. Tokura, in *Colossal Magnetoresistive Oxides*, Ed. by Y. Tokura (Gordon and Breach, Amsterdam, 2000), p. 22.
20. H. Y. Hwang, S.-W. Cheong, N. P. Ong, and B. Batlogg, Phys. Rev. Lett. **77** (10), 2041 (1996).
21. E. Dan Dahlberg, K. Riggs, and G. A. Prinz, J. Appl. Phys. **63** (8), 4270 (1988).
22. Y.-A. Soh, G. Aeppli, C.-Y. Kim, N. D. Mathur, and M. G. Blamire, J. Appl. Phys. **93** (10), 8322 (2003).
23. K. Steenbeck and R. Hiergeist, Appl. Phys. Lett. **75** (12), 1778 (1999).
24. H. S. Wang, E. Wertz, Y. F. Hu, and Q. Li, J. Appl. Phys. **87** (9), 6749 (2000).

Translated by G. Skrebtsov

Physics of the Solid State, Vol. 47, No. 12, 2005, pp. 2287–2291. Translated from Fizika Tverdogo Tela, Vol. 47, No. 12, 2005, pp. 2195–2199.

MAGNETISM AND FERROELECTRICITY

Colossal Room-Temperature Magnetoresistance in Thin $La_{1-x}Ag_yMnO_3$ Epitaxial Films

R. V. Demin*, O. Yu. Gorbenko*, A. R. Kaul'*, L. I. Koroleva*, O. V. Mel'nikov*, A. Z. Muminov*, R. Szymczak, and M. Baran****

**Moscow State University, Vorob'evy gory, Moscow, 119992 Russia*
e-mail: koroleva@phys.msu.ru
***Institute of Physics, Polish Academy of Sciences, Warsaw, 02668 Poland*
Received February 9, 2005

Abstract—The first thin $La_{1-x}Ag_yMnO_3$ epitaxial films ($y \le x$) were grown on $SrTiO_3$ (110) substrates with silver present in the ionized state (Ag^+) only. The Curie temperatures T_C of the compositions with $x = y = 0.05$, $x = y = 0.1$, and $x = 0.3$ and $y = 0.27$ crystallizing in the hexagonal structure $R\bar{3}c$ lie above or close to room temperature. The temperature dependences of electrical resistivity ρ and of magnetoresistance $|\Delta\rho/\rho| = |(\rho_H - \rho_H = 0)/\rho_{H=0}|$ pass through maxima near T_C, with the magnetoresistance being negative and reaching colossal values of ~7–20% in a magnetic field $H = 8.2$ kOe not only at T_C but also at room temperature. The magnetic moment per formula unit as derived from the saturation magnetization at $T = 5$ K is substantially smaller than expected for complete ferromagnetic ordering. The magnetization in fields of up to 6 kOe depends on the actual sample cooling conditions, and the hysteresis loop of a field-cooled sample is displaced along the H axis by ΔH. The above properties can be accounted for by the fact that the films are in a two-phase magnetic (ferromagnetic–antiferromagnetic) state induced by strong *s–d* exchange. The maximum value of ΔH was used to calculate the energy of exchange coupling between the ferromagnetic and antiferromagnetic parts of a sample. © *2005 Pleiades Publishing, Inc.*

1. INTRODUCTION

The interest in the manganites $Re_{1-x}A_xMnO_3$ (*Re* stands here for a rare-earth ion, and *A*, for a dopant ion) should be assigned to the colossal magnetoresistance (CMR) which some of them exhibit at room temperature. Unfortunately, the magnitude of the CMR observed in the vicinity of the Curie point T_C decreases rapidly with increasing T_C in manganites doped with divalent ions of Ca, Sr, and Pb. Doping $LaMnO_3$ with univalent ions of Na has revealed, however, that the magnetoresistance also remains colossal at room temperature in compositions whose T_C approaches 300 K [1–4]. The question naturally arises as to whether this effect would be observed in manganites doped by other univalent ions, in particular, by silver. The possibility of doping $La_{1-x}MnO_{3+\delta}$ ceramics with silver, where Ag^+ ions substitute for the lanthanum vacancies, was demonstrated in [5–7]. CMR has been found to exist in these ceramics at room temperature [8]. However, doping the crystal structure of perovskite manganites with silver was questioned in [9], where doping with silver was found to be similar to the introduction of lanthanum vacancies into $La_{1-x}MnO_{3+\delta}$. Indeed, the evidence presented thus far for doping manganites with silver has been only indirect, such as, for instance, the absence of metallic silver among the reaction products [8, 10]. However, it should be noted that silver is a highly mobile component.

We forward here compelling evidence for possible silver doping of $La_{1-x}MnO_{3+\delta}$. It is well known that thin films of such materials would have considerable application potential. We fabricated thin epitaxial $La_{1-x}Ag_yMnO_3$ films ($y \le x$) on $SrTiO_3$ (110) substrates, some of which exhibit room-temperature CMR.

2. SAMPLE PREPARATION AND EXPERIMENTAL TECHNIQUES

Because of the volatile compounds of silver having low thermal stability, the following two-stage technique of synthesis was proposed: (1) preparation of thin lanthanum-deficient $La_{1-x}MnO_3$ films (through MOCVD) at rates $v(O_2) = v(Ar) = 7$ l/h, a pressure $P_{tot} = 10$ mbar, and $T = 830$°C and (2) saturation of films with silver by annealing lanthanum-deficient compositions in silver vapor in an oxygen environment (at a total pressure of 1 or 20 atm). The changes in film structure were monitored by x-ray diffraction. The chemical composition of the films was established by x-ray microprobe analysis. $LaMnO_3$ films do not absorb silver at saturation. Silver can be absorbed at positive values of x only. X-ray photoelectron spectroscopy revealed that the silver in the films is only in the

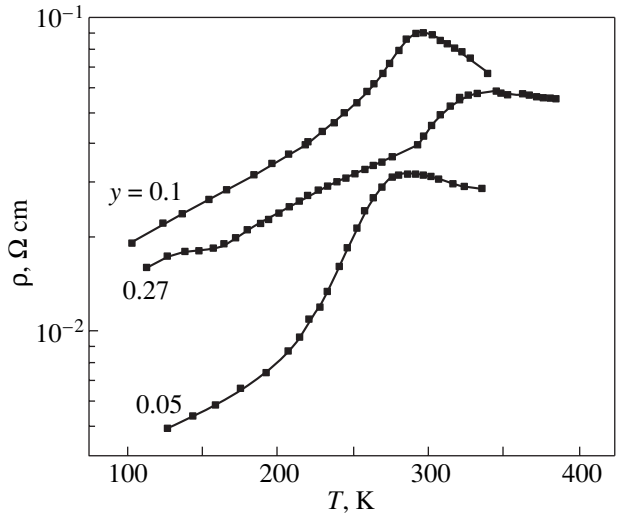

Fig. 1. Temperature dependence of the electrical resistivity ρ of thin $La_{1-x}Ag_yMnO_3$ films ($y \le x$).

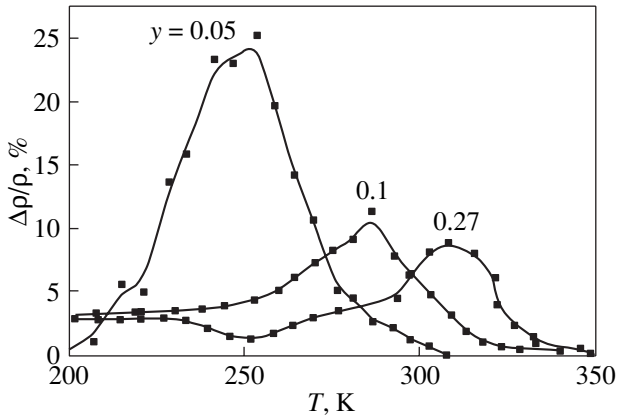

Fig. 2. Temperature dependence of the magnetoresistance Δρ/ρ of thin $La_{1-x}Ag_yMnO_3$ films ($y \le x$).

ionized state (metallic silver is not observed). $La_{0.95}Ag_{0.05}MnO_3$, $La_{0.9}Ag_{0.1}MnO_3$, and $La_{0.7}Ag_{0.27}MnO_3$ films were found to have the hexagonal structure $R\bar{3}c$.

We studied the magnetization σ, electrical resistivity ρ, and magnetoresistance $\Delta\rho/\rho = (\rho_H - \rho_{H=0})/\rho_{H=0}$ of the thin epitaxial films indicated above. The magnetization was studied with a SQUID magnetometer in the temperature range $5 \le T \le 350$ K in magnetic fields of up to 50 kOe. The values of ρ and Δρ/ρ were measured by the standard four-probe method. The electrical resistivity and magnetoresistance were investigated at temperatures ranging from 77 to 350 K. The magnetoresistance was measured in the film plane, with the current through the film being parallel to the applied magnetic field *H*, which did not exceed 8.2 kOe.

3. EXPERIMENTAL RESULTS AND DISCUSSION

Figure 1 displays in graphical form the temperature dependence of the electrical resistivity ρ(*T*) of the films studied by us. The ρ(*T*) curves are seen to exhibit maxima. The temperatures of these maxima, $T_{\rho max}$, and the values of ρ at the maxima are listed in the table. Figure 2 shows {Δρ/ρ}(*T*) curves for $La_{1-x}Ag_yMnO_3$ films ($x > y$). The magnetoresistance is negative, and its absolute value reaches a maximum at a temperature $T = T_{(\Delta\rho/\rho)max}$, which is slightly less than T_C (see table). Incidentally, $T_{\rho max}$ is slightly higher than $T_{(\Delta\rho/\rho)max}$, a feature typical of magnetic semiconductors [11]. At the maximum, |Δρ/ρ| reaches a colossal value of 25% for a composition with $y = x = 0.05$, 12% for $y = x = 0.1$, and 8% in $La_{0.7}Ag_{0.27}MnO_3$ at $H = 8.2$ kOe. Note that the room-temperature magnetoresistance of the last two films is high. As seen from Fig. 2, it is ~7% at $H = 8.2$ kOe. Obviously enough, in compositions intermediate between that with $y = x = 0.1$ and $La_{0.7}Ag_{0.27}MnO_3$, one should expect even higher room-temperature values of Δρ/ρ, approaching $|\Delta\rho/\rho|_{max}$ in the extreme compositions. In contrast to $La_{1-x}A_xMnO_3$ systems ($A = Sr^{2+}$, Ca^{2+}; $x \le 0.3$) and traditional magnetic semiconductors (doped europium monochalcogenides and chalcogenide spinels), in which $|\Delta\rho/\rho|_{max}$ decreases rapidly as the doping level increases, in $La_{1-x}Ag_yMnO_3$ films ($y \le x$) it varies very little with increasing *y*. For instance, in going from $y = 0.05$ to $y = 0.1$, $|\Delta\rho/\rho|_{max}$ decreases 2.1 times and then, as one goes from the compound

Magnetic, electrical, and galvanomagnetic characteristics of thin $La_{1-x}Ag_yMnO_3$ films ($y \le x$) grown on $SrTiO_3$ (110) substrates

Composition	T_C, K	$T_{\rho_{max}}$, K	$T_{(\Delta\rho/\rho)_{max}}$, K	ρ_{max}, 10^{-2} Ω cm	$(\Delta\rho/\rho)_{max}$, %	μ_{exp}, μ_B	μ_{th}, μ_B
$y = x = 0.05$	296 (100 Oe) 323 (6 kOe)	275	252	5.8	25	2.67	3.9
$y = x = 0.1$	308 (100 Oe) 316 (6 kOe)	297	289	8	12	2.2	3.8
$x = 0.3$, $y = 0.27$	325 (100 Oe) 333 (6 kOe)	350	315	5.5	8	1.34	3.46

with $y = 0.1$ to $La_{0.7}Ag_{0.27}MnO_3$, this quantity decreases 1.2 times; i.e., the decrease slows down. Significantly, the magnetoresistance isotherms do not saturate in the region of T_C up to the highest fields tried, $H = 8.2$ kOe, and are smooth; so one could expect even higher values of magnetoresistance in stronger fields.

The above properties may be due to the samples being in a two-phase magnetic (ferromagnetic–antiferromagnetic) state initiated by strong *s–d* exchange [12]. It is known that $La_{1-x}MnO_3$ may be considered an antiferromagnet $LaMnO_3$ with La vacancies acting as doubly charged defects. Adding Ag to $La_{1-x}MnO_3$ in an amount y compensates y vacancies and thereby creates y singly charged acceptors, the net result being that $La_{1-x}Ag_yMnO_3$ ($y \le x$) becomes a doped antiferromagnetic (AFM) semiconductor containing y singly charged Ag^+ acceptor ions and $x - y$ doubly charged acceptors, more specifically, La vacancies. Because ρ in the films studied is ~10^{-3}–10^{-1} Ω cm and the conduction has metallic character below T_C, it may be conjectured that these films are in a conducting two-phase magnetic state (TPMS), where insulating AFM microregions are embedded in a ferromagnetic (FM) matrix. The conducting TPMS is characterized by a sharp growth of ρ in the region of T_C. Here, one can conceive of two mechanisms by which impurity-induced magnetic interaction can affect the resistivity, namely, the scattering of carriers (which reduces their mobility) and the formation of a carrier band tail made up of localized states. In the vicinity of T_C, the mobility of carriers decreases sharply and they become partially localized in the band tail, which accounts for the maximum in the $\rho(T)$ curve near T_C. The applied magnetic field delocalizes carriers out of the band tail and increases their mobility, thereby giving rise to CMR.

The existence of a TPMS in the films under study is also argued for by the specific features of their magnetic properties. Figure 3 displays a hysteresis loop of a $La_{0.9}Ag_{0.1}MnO_3$ sample obtained at $T = 5$ K with the highest magnetic field of 50 kOe. Saturation of the magnetization is seen to be reached at 4 kOe, with the coercive force being 70 Oe. A similar pattern is also observed in the two other films studied. The magnetic moments per formula unit as calculated from the saturation magnetization at $T = 5$ K (μ_{exp}) are listed in the table for all films. As is evident from the table, the values of μ_{exp} are substantially smaller than those expected under complete FM ordering (μ_{th}). This may be attributed to the presence of an FM–AFM TPMS in the sample.

Inspection of Fig. 4 reveals that the magnetization measured at $T < T_C$ depends on the sample cooling conditions chosen; namely, the value of σ of a sample cooled in a magnetic field from 350 to 5 K (FC sample) is higher than the magnetization measured under heating of a sample preliminarily cooled to 5 K in a zero field (ZFC sample). The magnetizations of FC and ZFC samples remain different up to 6 kOe. FC samples

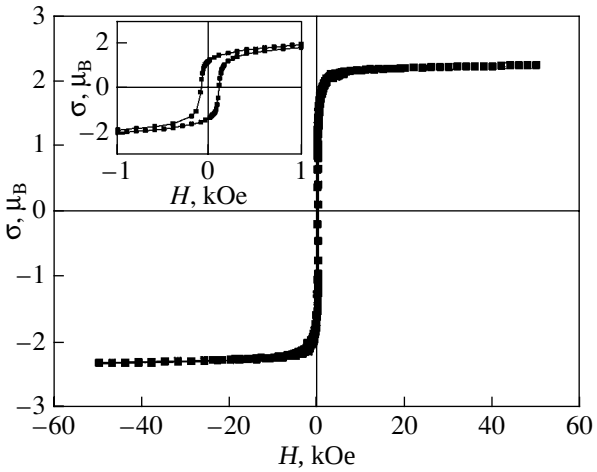

Fig. 3. Hysteresis loop of a thin $La_{0.9}Ag_{0.1}MnO_3$ film obtained at 5 K. The inset shows, in an expanded scale, a part of this loop measured in the field range from –1 to 1 kOe.

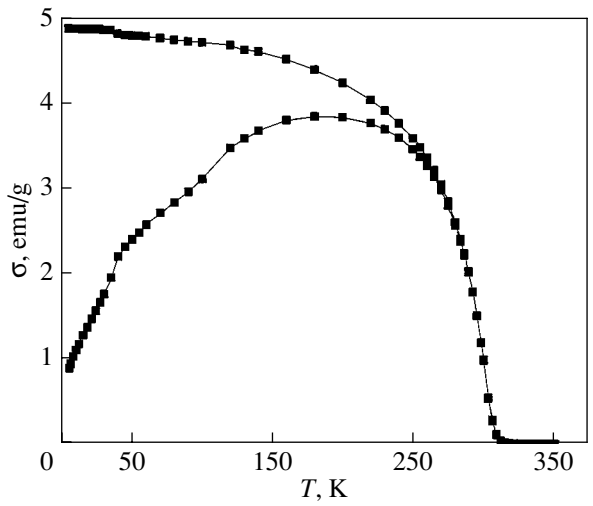

Fig. 4. Temperature dependence of the magnetization σ obtained in different conditions of cooling of a thin $La_{0.7}Ag_{0.27}MnO_3$ film. The top curve corresponds to the case where the magnetization was measured as the sample was cooled from 350 to 5 K in a magnetic field $H = 100$ Oe. The bottom curve corresponds to the case where the sample was zero-field-cooled from 350 to 5 K, after which its magnetization was measured under heating at $H = 100$ Oe.

reveal a shift of the hysteresis loops along the H axis at $H < 300$ Oe (Fig. 5), with the shift being largest, $\Delta H = 16$ Oe, for the $La_{0.7}Ag_{0.27}MnO_3$ composition at $H = 100$ Oe. The shift of hysteresis loops of the FC films along the H axis show unambiguously the presence of a TPMS. Although this property is likewise observed in spin glasses, it can be accounted for only by the existence in them of FM and AFM regions and exchange interaction between them, a point first made by Kouvel [13]. In [14], using the magnitude of this shift ΔH, we

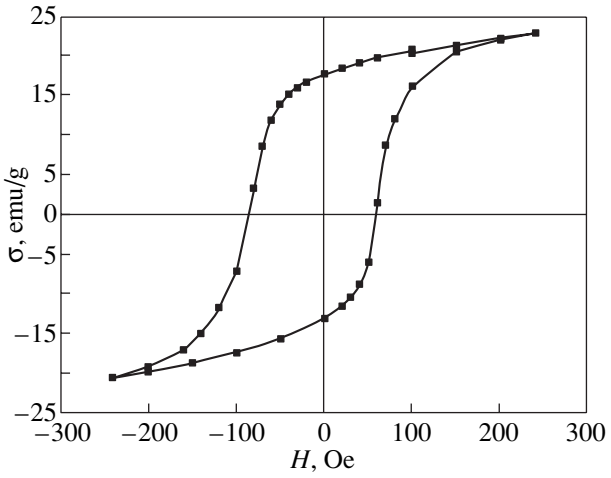

Fig. 5. Hysteresis loop of a thin field-cooled $La_{0.7}Ag_{0.27}MnO_3$ film measured at 5 K.

estimated the exchange integral J describing one Mn–O–Mn bond through the FM/AFM interface for a number of manganite compositions in an insulating FM–AFM TPMS. It was found that $|J| \sim 10^{-6}$ eV, which is two orders of magnitude smaller than the negative exchange integral between FM layers in $LaMnO_3$, $|J_1| = 5.8 \times 10^{-4}$ eV, a figure extracted from neutron scattering experiments [15]. This implies that the presence of a layer with canted spins at the abovementioned interface is very unlikely. In a sample residing in a TPMS, the carriers are concentrated in the FM phase and are absent in the AFM phase. Therefore, the TPMS topology is dictated by Coulomb forces and the surface interface energy. Judging from the magnitude of spontaneous magnetization at 5 K, the FM phase is comparable in volume to the AFM phase in the $La_{1-x}Ag_yMnO_3$ films ($y \le x$) grown on $SrTiO_3$ substrates. As already pointed out, it is conceivable that our films are in a conducting TPMS, with the FM phase being actually jumpers between AFM insulating spheres. It should be noted that, in the films in a conducting TPMS and in the manganite samples studied in [14] and residing in an insulating TPMS, the exchange anisotropy constants K_u between the FM and AFM phases are of the same order of magnitude. Therefore, it may be suggested that the FM/AFM interface surface areas are likewise of the same order of magnitude in these two cases; so the conclusions reached in [14] can be readily extended to $La_{1-x}Ag_yMnO_3$ films ($y \le x$) and the presence of a canted spin layer at the above interface is hardly likely. Using the magnetic field in which the hysteresis loop with the maximum shift of 100 Oe was measured, we estimated the exchange coupling energy between the FM and AFM parts of a sample to be ~10^4 erg/cm^3.

The existence of a TPMS in the films under study is also argued for by the diffuse pattern of the transition from the FM to a paramagnetic state. It may be appropriate to note here that the Curie temperature is a fairly conventional quantity for samples in a TPMS and is defined as the temperature at which the FM state in the FM part of a sample breaks down. At present, the exact scenario by which thermal breakdown of the TPMS occurs remains unclear; it is not clear whether the first to break down is the AFM phase at T_N and that only after this is the FM phase destroyed (at a higher temperature) or quite the reverse may be true. Nagaev [12] pointed out that T_N and T_C are close in magnitude for a sample in a TPMS. The films studied by us here did not reveal a maximum for $T > T_C$ in the $\sigma(T)$ curves up to the highest fields used (50 kOe), which indicates the absence of an AFM phase above T_C. The Curie temperatures of all the films studied, which were determined by extrapolating the steepest part of the $\sigma(T)$ curve to its intersection with the temperature axis, are listed in the table. They are seen to lie in the room-temperature region or higher. It is known that a correct method for measuring T_C should not involve the application of an external magnetic field to a sample, because the field broadens and suppresses the phase transition. The Curie temperature in the films treated in the present study depends strongly on the field at which it is measured. As seen from the table, the value of T_C increases strongly with H in all the films studied. For instance, T_C of the $La_{0.95}Ag_{0.05}MnO_3$ film as determined in a field of 100 Oe is 296 K, while in 6 kOe it is 323 K, i.e., higher by 27 K. In uniform impurity-free ferromagnets (for example, in Gd and $CdCr_2Se_4$), the increase in T_C in the same H interval is only a few kelvins [16]. By contrast, in $Eu_{0.7}Sr_{0.3}MnO_3$, a compound in which an insulating TPMS was observed to exist, it was altogether impossible to determine T_C by the above technique, because it grew from 30 K at $H = 0.5$ kOe to 150 K at $H = 45$ kOe [17]. This increase in T_C should be attributed to a magnetic-field-induced increase in the FM phase volume in a sample residing in a TPMS. The strong dependence of T_C on the magnetic field in which it was measured in $La_{1-x}Ag_yMnO_3$ films ($y \le x$) obviously argues for the existence of the TPMS in them.

ACKNOWLEDGMENTS

This study was supported by the Russian Foundation for Basic Research, project nos. 03-02-16100 and 02-03-33258.

REFERENCES

1. W. H. McCarroll, I. D. Fawcett, M. Greenblatt, and K. V. Ramanujachary, J. Solid State Chem. **146** (1), 88 (1999).
2. M. Sahana, R. N. Singh, C. Shivakumara, N. Y. Vasanthacharya, M. S. Hegde, S. Subramanian, V. Prasad, and S. V. Subramanyam, Appl. Phys. Lett. **70** (21), 2909 (1997).

3. G. H. Rao, J. R. Sun, K. Baerner, and N. Hamad, J. Phys.: Condens. Matter **11** (12), 1523 (1999).
4. S. L. Ye, W. H. Song, J. M. Dai, K. Y. Wang, S. G. Wang, J. J. Du, Y. P. Sun, J. Fang, J. L. Chen, and B. J. Gao, J. Appl. Phys. **90** (6), 2943 (2001).
5. T. Tao, Q. Q. Cao, K. M. Gu, H. Y. Xu, S. Y. Zhang, and Y. W. Du, Appl. Phys. Lett. **77** (1), 723 (2000).
6. S. L. Ye, W. H. Song, J. M. Dai, K. Y. Wang, S. G. Wang, C. L. Zhang, J. J. Du, Y. P. Sun, and J. Fang, J. Magn. Magn. Mater. **248** (1), 26 (2002).
7. N. T. Hien and N. P. Thuy, Physica B (Amsterdam) **319** (2), 168 (2002).
8. L. Pi, M. Hervieu, A. Maignan, C. Martin, and B. Raveau, Solid State Commun. **126** (2), 229 (2003).
9. V. L. Joseph Joly, P. A. Joy, and S. K. Date, Appl. Phys. Lett. **78** (23), 3747 (2001).
10. D. Zhu, A. Maignan, M. Hervieu, S. Hervieu, and B. Raveau, Solid State Commun. **127** (3), 551 (2003).
11. L. I. Koroleva, *Magnetic Semiconductors* (Moscow State University, Moscow, 2003) [in Russian].
12. E. L. Nagaev, *Colossal Magnetoresistance and Phase Separation in Magnetic Semiconductors* (Imperial College Press, London, 2002).
13. J. S. Kouvel, J. Phys. Chem. Solids **21** (1), 57 (1961).
14. R. V. Demin, L. I. Koroleva, R. Szymszak, and H. Szymszak, Pis'ma Zh. Éksp. Teor. Fiz. **75** (5), 402 (2002) [JETP Lett. **75**, 331 (2002)].
15. F. Moussa, M. Hennion, and J. Rodriguez-Carvajal, Phys. Rev. B: Condens. Matter **54** (21), 15 149 (1996).
16. K. P. Belov, L. I. Koroleva, M. A. Shalimova, V. T. Kalinnikov, and T. G. Aminov, Zh. Éksp. Teor. Fiz. **72** (6), 1994 (1977) [Sov. Phys. JETP **45**, 1047 (1977)].
17. A. I. Abramovich, R. V. Demin, L. I. Koroleva, A. V. Michurin, and A. I. Smirnitskaya, Pis'ma Zh. Éksp. Teor. Fiz. **69** (5), 404 (1999) [JETP Lett. **69**, 404 (1999)].

Translated by G. Skrebtsov

Physics of the Solid State, Vol. 47, No. 12, 2005, pp. 2292–2298. Translated from Fizika Tverdogo Tela, Vol. 47, No. 12, 2005, pp. 2200–2206.

MAGNETISM AND FERROELECTRICITY

Optical Properties of Thulium Orthoferrite $TmFeO_3$

P. A. Usachev*, R. V. Pisarev*, A. M. Balbashov, A. V. Kimel***, A. Kirilyuk***, and Th. Rasing*****

**Ioffe Physicotechnical Institute, Russian Academy of Sciences, Politekhnicheskaya ul. 26, St. Petersburg, 194021 Russia*

e-mail: usachev@mail.ioffe.ru

***Moscow Power Engineering Institute, ul. Krasnokazarmennaya 17, Moscow, 111250 Russia*

****Institute of Molecules and Materials, Radboud University Nijmegen, 6525 ED Nijmegen, The Netherlands*

Received February 11, 2005

Abstract—Optical properties of the orthorhombic thulium orthoferrite $TmFeO_3$ were studied in the spectral range from 0.64 to 5.4 eV. In the weak absorption region, below 2.2 eV, the energies of localized optical transitions in the Tm^{3+} and Fe^{3+} ions were determined. The dispersion relations of the real and imaginary parts of the principal refractive indices along three crystallographic axes were found. In the region of strong absorption, above 2.2 eV, the energies of six charge-transfer transitions were determined. The experimental data fit well to the concept of charge-transfer transitions in the FeO_6^{9-} octahedral complexes providing a dominant contribution to the optical properties of the orthoferrites. Optical birefringence and its temperature dependence were measured for the three principal directions of light propagation, and the anisotropic magnetic contribution to birefringence in the region of spin-orientational transitions was isolated. © *2005 Pleiades Publishing, Inc.*

1. INTRODUCTION

The strongly correlated compounds of 3*d* transition metals have been attracting intense interest for several decades, and the results of studies of them have been described in numerous monographs and reviews. The ions of transition metals in these compounds completely or partially govern their magnetic, optical, and other properties, which should primarily be assigned to strong electron correlations and tight coupling between the spin, charge, and orbital degrees of freedom in the compounds of the 3*d* metals. As a remarkable manifestation of these correlations one could recall here the high-temperature superconductivity in copper oxide compounds [1], the colossal magnetoresistance in rare-earth manganites [2], etc. The character of the electronic states and the nature of the fundamental absorption edge in dielectric compounds of transition metals are quite frequently described by contradictory theories, and experimental studies have produced in some cases ambiguous results. To cite an example, the feature seen as an unusually strong and narrow absorption band near 1.6 eV in the spectrum of $LuMnO_3$ was assigned in [3] to a symmetry-allowed local *d–d* transition in the Mn^{3+} ion, whereas in [4] this band in the spectra of an analogous hexagonal manganite ($YMnO_3$) and other compounds was attributed to a charge-transfer transition from oxygen O^{2-} to manganese Mn^{3+}. As another illustration, we may mention the optical properties of numerous oxides of the trivalent ion Fe^{3+}, which is octahedrally coordinated to oxygen with approximately equal iron–oxygen distances. In transparent $FeBO_3$ and $GdFe_3(BO_3)_4$ [5]; in moderately transparent ferrite garnets (like $Y_3Fe_5O_{12}$) [6], orthoferrites (like $YFeO_3$), and iron gallate $GaFeO_3$ [7, 8]; and in the hematite α-Fe_2O_3, which is completely opaque in the visible range [9], the position of the fundamental absorption edge depends substantially on the crystal structure, chemical composition, and, apparently, the number of iron ions per unit cell. This dependence gives rise to strong variations in the intensity of forbidden *d–d* transitions, allowed charge-transfer transitions, and hence, the optical properties of the materials.

Typical representatives of transition-metal oxide compounds are the rare-earth orthoferrites $RFeO_3$, where *R* stands for ions of rare-earth elements, from La to Lu [10–12]. These compounds have the widespread and well-known perovskite structure, which, due to its comparative simplicity, allows *ab initio* and other nonempirical calculations of the energy spectrum, electronic structure, and exchange interactions of the FeO_6^{9-} complexes [13, 14]. By contrast to ideal perovskites, the oxygen environment of the R^{3+} cation in rare-earth orthoferrites is strongly distorted. The octahedral environment of the Fe^{3+} ion is likewise distorted, which gives rise to splitting of the e_g and t_{2g} states of the transition ion [13]. Such phenomena as magnetic and optical anisotropy are accounted for by the noncubic distortions of the ideal perovskite structure or, on the microscopic scale, by local crystal-field distortions in the

FeO_6^{9-} complexes. Another aspect of particular significance is the extremely large magnetooptical Faraday effect in orthoferrites observed in the visible and near infrared spectral ranges, where these materials exhibit a comparatively high transparency [15].

To the best of our knowledge, the literature lacks comprehensive studies of the optical absorption, refractive indices, and optical anisotropy of orthoferrites. Such studies have acquired particular significance in connection with the recent experiments [16] on the effect of a short laser pulse on thulium orthoferrite, which brings about an ultrafast change in magnetization on a characteristic time scale of a few picoseconds. We report here on a study of the optical properties of $TmFeO_3$. We investigated the absorption spectra in the energy range 0.64–2.2 eV, determined the dispersion of the real and imaginary parts of the complex refractive index along three crystallographic axes in the range 0.64–5.4 eV (using spectroscopic ellipsometry), and studied optical birefringence and its temperature dependence at specific wavelengths. We believe that the results obtained provide a sound basis for future purposeful experiments on the spin dynamics of oxide magnets.

2. OPTICAL PROPERTIES

The symmetry of $RFeO_3$ orthoferrite crystals is described by the orthorhombic space group D_{2h}^{16}–*Pbmn* [10, 11], and their unit cell contains four formula units. The magnetic structure of the orthoferrites makes them noncollinear antiferromagnets [11, 17, 18]. The state in which they usually reside at high temperatures is characterized by the antiferromagnetism vector $\mathbf{G} = (\mathbf{M}_1 - \mathbf{M}_2 + \mathbf{M}_3 - \mathbf{M}_4)/4$ directed along the *x* axis and by the weak ferromagnetic moment $\mathbf{F} = (\mathbf{M}_1 + \mathbf{M}_2 + \mathbf{M}_3 + \mathbf{M}_4)/4$ aligned with the *z* axis, where $\mathbf{M}_1$, $\mathbf{M}_2$, $\mathbf{M}_3$, and $\mathbf{M}_4$ are the magnetic moments of the four iron-ion sublattices. As the temperature is lowered, certain orthoferrites, including the thulium orthoferrite, undergo spin reorientation in which the system transfers to a state with the vector **F** directed along the *x* axis.

The $TmFeO_3$ single crystals used in our experiments were grown by the floating-zone method under optical heating [19]. The crystals were oriented by x-ray diffractometry. Since orthoferrites are optically biaxial crystals, the samples were prepared in the form of platelets polished down to a thickness of 80–100 μm, with the surface normal oriented perpendicular to the *x*, *y*, or *z* crystallographic axes to within a few degrees, as well as of platelets with the normal approximately aligned with the optical axis lying in the *yz* plane.

Figure 1 shows the spectral response of absorbance of the thulium orthoferrite $TmFeO_3$ measured with a Cary 2300 spectrophotometer in the range extending from 0.62 to 2.2 eV. The spectral characteristic was

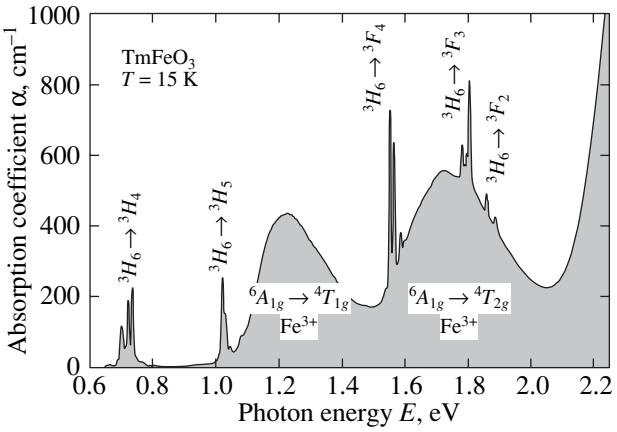

Fig. 1. Unpolarized absorption spectrum of $TmFeO_3$ obtained with light propagated along the *z* axis at 15 K.

obtained with light propagating along the *z* axis at a temperature of 15 K. Absorption in this spectral range derives from transitions in iron ions in the crystal field and transitions to the excited states of the thulium multiplet. An ion of trivalent iron contains five 3*d* electrons, which reside in a high-spin state and occupy the only spin sextet and orbital singlet ^6S lying below the other terms [20]. Optical crystal-field *d*–*d* transitions should occur from the $^6A_{1g}$ ground state to spin quartets and doublets and, hence, are spin and parity forbidden. These transitions produce only a relatively weak absorption due to a partial lifting of the forbiddenness by noncubic crystal-field distortions, lattice vibrations, spin–orbital coupling, and other perturbations. The first excited state of a free iron ion is the ^4G term, which is split by the octahedral crystal field into $^4T_{1g}$, $^4T_{2g}$, ^4E_g, and $^4A_{1g}$ levels. The transitions ending at the $^4T_{1g}$ and $^4T_{2g}$ levels lie below those involving charge transfer and are therefore observed as broad absorption bands centered at about 1.22 and 1.72 eV [7, 21]. These transitions do not, however, manifest themselves in any way in the dispersion of the refractive index (Fig. 2). The transition to the ^4E_g and $^4A_{1g}$ level is located near the charge-transfer transitions. It has a fairly high intensity and, therefore, is seen in the refractive-index spectra.

The narrow split absorption lines peaking at 0.73, 1.01, 1.55, 1.8, and 1.87 eV derive from transitions on the thulium sublattice from the $^3H_6$ ground state to the $^3H_4$, $^3H_5$, $^3F_4$, $^3F_3$, and $^3F_2$ excited states, respectively [22, 23]. Note the clearly pronounced transitions in thulium to the $^3F_4$ multiplet sublevels, which lie in the range covered by the titanium–sapphire laser and can be employed to pump the rare-earth ion magnetic system when studying the ultrafast magnetization dynamics. As the temperature increases, the absorption lines of thulium ions broaden considerably to finally merge into absorption bands in the temperature region of orientational phase transitions [23].

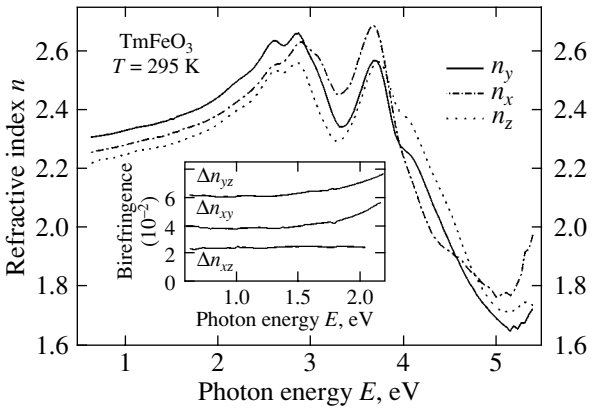

Fig. 2. Dispersion of the real part of the $TmFeO_3$ refractive index calculated for three crystallographic axes from ellipsometric measurements in reflection. The inset shows the dispersion relation of the birefringence derived from ellipsometric measurements in the transmission mode.

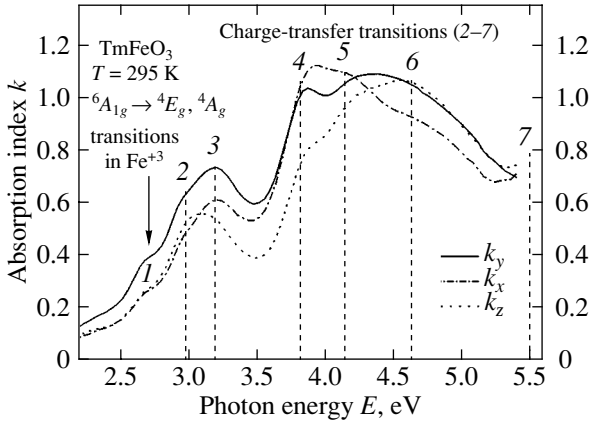

Fig. 3. Dispersion of the imaginary part of the $TmFeO_3$ refractive index calculated for three crystallographic axes. The numerals refer to the oscillator energies (see also Fig. 4 and table) obtained from Eq. (1).

The room-temperature complex refractive index of thulium orthoferrite was studied by reflection spectroscopic ellipsometry using a computerized ellipsometer equipped with a rotating analyzer. Since this material is strongly anisotropic, the general inverse problem is anything but trivial [24]. The real and imaginary parts of the complex refractive index $N = n - ik$ were determined by approximately solving the ellipsometric equation for optically biaxial crystals [25]. The error of this method (revealed as an overestimated value of k) is largest in the region of weak absorption, 0.62–2.2 eV. This error stems from the simplifications accepted in the model used, which, in particular, disregards the roughness of the surface layer and the presence in it of defects and surface strains generated by mechanical treatment. Nevertheless, this model provides a qualitatively correct picture of the behavior of the complex refractive index. Combined ellipsometric measurements in reflection and transmission offer the possibility of obtaining quantitative estimates with a reasonable accuracy. In particular, knowing the three principal values of the absolute refractive index, one can readily determine the directions of the optical axes in a crystal and their dispersion.

Figures 2 and 3 illustrate measurements of the real and imaginary parts of the principal refractive indices of $TmFeO_3$ along the three crystallographic axes. The main features of these spectra can be described in terms of crystal-field theory, according to which the ground-state electronic configuration of the FeO_6^{9-} complexes (the main optical centers in orthoferrites) contains several filled oxygen $2p$ valence orbitals and half-filled iron t_{2g} and e_g $3d$ orbitals. The part of the spectrum above 3.0 eV, as is evident from Fig. 3, exhibits stronger absorption and should be attributed to allowed electric-dipole transitions. The parity and spin selection rules allow six electric-dipole charge-transfer transitions ${}^6A_{1g} \longrightarrow {}^6T_{1u}$ related to one-electron transitions from the $t_{2u}(\pi)$, $t_{1u}(\pi)$, and $t_{1u}(\sigma)$ levels to the t_{2g} and e_g levels [13], whose energies lie above 3 eV.

Calculations were carried out in the cubic crystal-field approximation. However, the number of observed transitions, as will be seen further on, is in excess of the theoretical predictions, and this provides compelling experimental evidence for the important part played by noncubic distortions in the formation of the electronic structure of orthoferrites and, as a consequence, of the anisotropy of their magnetic, optical, and magnetooptical properties. The data summarized in Figs. 2 and 3 permit one to determine the transition parameters, calculate the spectrum of the complex dielectric function $\varepsilon = \varepsilon_1 - i\varepsilon_2 = (n - ik)^2$, and decompose it into single oscillators using the relation

$$\varepsilon = \varepsilon_0 + \varepsilon_b E + \sum_j \frac{f_j}{E_j^2 - E^2 - iE\gamma_j}, \qquad (1)$$

where ε_0 is a real addition independent of photon energy; ε_b is a complex coefficient accounting for the sum effect of oscillators located considerably higher energywise than the range of energies E covered here; E_j are the oscillator resonance energies; and f_j and γ_j are parameters describing the strength of the oscillators and their damping, respectively. Proper treatment of the experimental data revealed seven oscillators, one of which corresponds to a localized transition to the ${}^4E_g$ and ${}^4A_{1g}$ levels at an energy $E_1 = 2.67$ eV and the others to six charge-transfer transitions in the FeO_6^{9-} complexes having resonance energies in the range from 2.96 to 5.56 eV. The oscillator parameters found for all diagonal components of the permittivity tensor are listed in the table.

Oscillator parameters of the permittivity tensor components found from experimental data using Eq. (1)

j	ε^{xx}			ε^{yy}			ε^{zz}		
	E_j, eV	γ_j, eV	f_j	E_j, eV	γ_j, eV	f_j	E_j, eV	γ_j, eV	f_j
1	2.67(1)	0.18(3)	0.13(3)	2.665(5)	0.26(3)	0.33(6)	2.668(5)	0.18(3)	0.15(3)
2	2.97(1)	0.32(4)	0.8(2)	2.961(9)	0.37(4)	1.3(3)	2.993(9)	0.42(3)	1.9(2)
3	3.19(1)	0.41(2)	1.9(2)	3.19(1)	0.43(2)	2.2(3)	3.20(1)	0.33(3)	0.8(2)
4	3.828(5)	0.39(2)	3.6(6)	3.812(3)	0.35(1)	2.7(2)	3.827(3)	0.32(1)	1.8(2)
5	4.13(1)	0.69(9)	6(1)	4.17(1)	0.70(9)	5(1)	4.146(8)	0.61(7)	4(1)
6	4.70(3)	1.12(8)	8.3(9)	4.61(5)	1.34(7)	13(2)	4.61(2)	1.17(5)	14(1)
7	5.50(2)	0.29(5)	1.4(3)	5.47(3)	0.08(3)	0.26(9)	5.56(3)	0.51(8)	2.0(4)
	ε_0	$\varepsilon_{1,b}$	$\varepsilon_{2,b}$	ε_0	$\varepsilon_{1,b}$	$\varepsilon_{2,b}$	ε_0	$\varepsilon_{1,b}$	$\varepsilon_{2,b}$
	3.78(2)	0.047(5)	0.253(5)	3.81(4)	0.006(6)	0.262(7)	3.54(3)	0.052(5)	0.225(5)

Equation (1) for the imaginary part of the permittivity is actually a decomposition into Lorentzian functions. This decomposition of an experimental spectrum for the ε^{zz} component of the permittivity tensor is presented graphically in Fig. 4. We readily see that experimental data fit well to calculations based on the decomposition parameters found. In Fig. 5, the energies of transitions in the FeO_6^{9-} complexes obtained in this study are compared with the values quoted in [8] and a theoretical analysis reported in [13]. Note that, in contrast to [8], the ellipsometric method in combination with the data treatment approach described above yielded more accurate parameters of charge-transfer transitions split by a noncubic crystal field.

3. DISPERSION AND TEMPERATURE DEPENDENCE OF BIREFRINGENCE

Rare-earth orthoferrites are optically biaxial crystals possessing inherent birefringence. Therefore, the polarization state of light of wavelength λ propagating through these crystals changes. In the energy range 0.64–2.1 eV, these materials are relatively transparent, thus permitting one to derive the dispersion relation for birefringence from ellipsometric measurements during transmission. We measured the phase difference between the *s* and *p* polarizations of light transmitted through a sample for each wavelength in the case where light is incident normal to the sample and is linearly polarized at 45° to the crystallographic axes. Next, we determined the total number of full turns made by the measured phase difference with varying wavelength and, subsequently, the total phase angle σ through which the wave polarization vector was rotated in the wave transmitted through a plate of thickness *d*. The difference between the refractive indices Δn (birefringence) for each wavelength was found from the relation

$$\sigma = \frac{2\pi d\Delta n}{\lambda}. \quad (2)$$

The birefringence dispersion relations are shown graphically in the inset to Fig. 2. The optical anisotropy of orthoferrites is determined primarily by the contribution of electric dipole charge-transfer transitions in the FeO_6^{9-} octahedral complexes [13]. In the range 0.64–2.1 eV, the birefringence depends on the photon energy only weakly and grows as one approaches the region of strong absorption lying above 2.2 eV. Ellipsometric measurements performed using the transmission mode with an error of $\pm 5 \times 10^{-4}$ yielded the following values of birefringence at a wavelength of 800 nm (1.55 eV):

$$\Delta n_{xy} = 0.0405, \quad \Delta n_{xz} = 0.026, \quad \Delta n_{yz} = 0.067. \quad (3)$$

The birefringence measured at 1550 nm (0.8 eV) was found to be

$$\Delta n_{xy} = 0.0382, \quad \Delta n_{xz} = 0.0246, \quad \Delta n_{yz} = 0.0615. \quad (4)$$

These values are in good agreement with the theoretical estimate $\Delta n_{xy} = 0.0389$ quoted in [10] but differ from the experimental values $\Delta n_{xy} = 0.0312$ and $\Delta n_{xz} =$

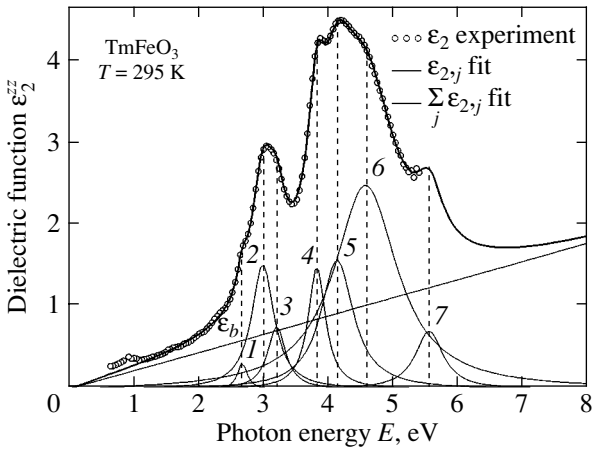

Fig. 4. Decomposition of an experimental spectrum of the imaginary part of the permittivity tensor *zz* component into Lorentzians (j = 1, 2, …, 7) according to Eq. (1).

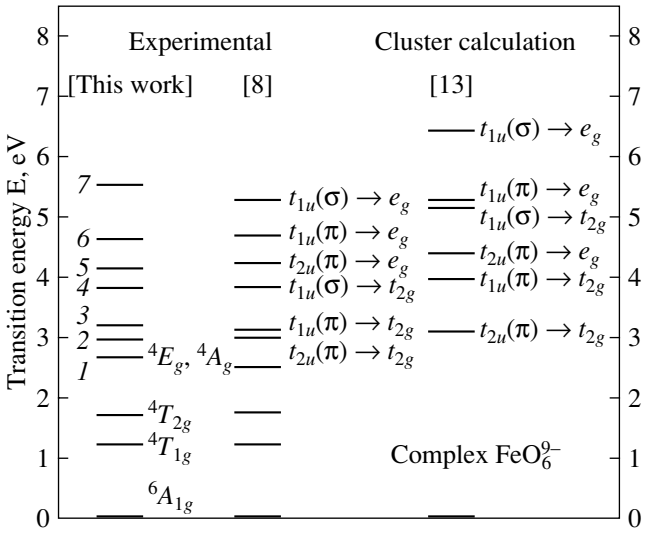

Fig. 5. Diagrams of localized and charge-transfer transitions in the FeO_6^{9-} complex as derived from this work, obtained in [18], and calculated in [13].

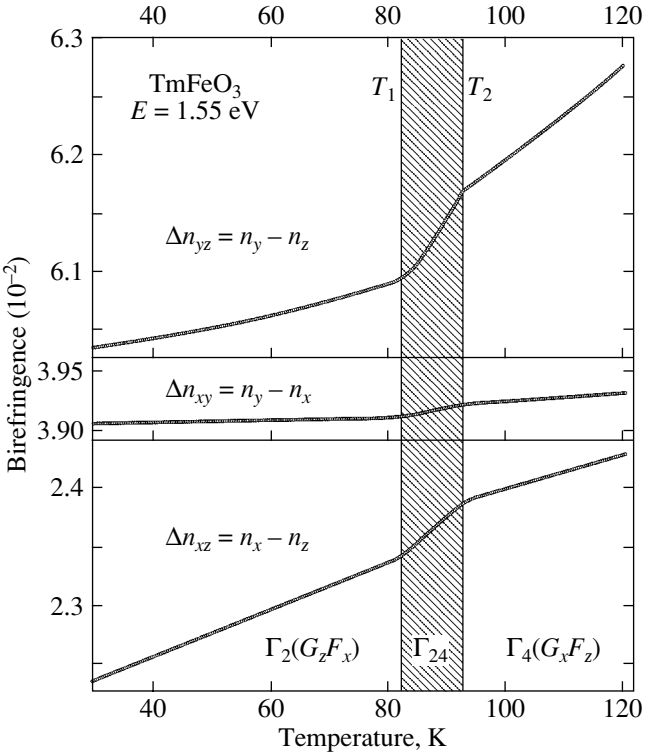

Fig. 6. Temperature dependence of birefringence along the three principal crystallographic directions. The birefringence anomalies occur at the orientational-transition temperatures T_1 and T_2. The room-temperature values of birefringence are presented in Eqs. (3).

0.0205 given in [26], which should possibly be attributed to imperfections in the birefringence measurement technique employed in [26].

As the temperature is lowered, spontaneous spin reorientation occurs in $TmFeO_3$ as a result of variation of the magnetic anisotropy. In this process, the ferromagnetic moment **F** turns continuously from its position along the *z* axis at a temperature T_2 to the position along the *x* axis at a temperature T_1. These points are the temperatures of second-order phase transitions ($\Gamma_4 \longrightarrow \Gamma_{24} \longrightarrow \Gamma_2$) [11] in which anomalies in the physical properties are observed.

The temperature dependence of birefringence was studied with a sample placed between crossed polarizers. The phase shift *R* of the incident radiation polarized linearly at 45° to the crystallographic axes was varied with the use of an acoustic modulator operating at a frequency *f*. The photodetector signal had harmonic components at frequencies *f* and 2*f* with amplitudes $J_1(R_0)\sin\theta$ and $J_2(R_0)\cos\theta$, respectively, where $J_i(R_0)$ is a Bessel function, R_0 is the phase shift modulation amplitude, and θ is the phase difference between *s*- and *p*- polarized light beams. The temperature dependence of birefringence was found using Eq. (2) from the total phase angle σ obtained for a given wavelength in room-temperature ellipsometric measurements and the temperature-dependent phase difference θ, which was derived from the relation

$$\tan\theta = \frac{V_{1f}}{V_{2f}}\frac{J_2(R_0)}{J_1(R_0)}, \qquad (5)$$

where V_{1f} and V_{2f} are signal amplitudes measured at frequencies *f* and 2*f*, respectively.

The temperature dependence of linear birefringence is plotted in Fig. 6 and is seen to exhibit two second-order orientational phase transitions at temperatures of 83 and 93 K. According to the Landau theory [11, 27], the possible spin configurations can be found by minimizing (with respect to the vectors **F** and **G**) the thermodynamic potential

$$\Phi = \Phi_0 + K_1(T)\sin^2\Theta + K_2\sin^4\Theta, \qquad (6)$$

where Φ_0 is the part of the energy that is independent of spin orientation; K_1 and K_2 are the first and second anisotropy constants, respectively; and Θ is the angle made by the antiferromagnetism vector **G** and the *x* axis of an orthorhombic crystal. A spin reorientation accompanies two second-order phase transitions of the type $\Gamma_4(G_xF_z) \longrightarrow \Gamma_{24} \longrightarrow \Gamma_2(G_zF_x)$, during which the magnetic moment is rotated in the *xz* plane of the crystal. Besides the equilibrium states with the vector **F** oriented along the *z* axis (at $T > T_2$) or the *x* axis (at $T < T_1$), the system passes (in the interval $T_1 < T < T_2$) through a state in which the vector **F** is canted at an angle Θ to the *z* axis

$$\sin^2\Theta = -K_1/2K_2. \qquad (7)$$

The change in birefringence due to spin-orientational transitions originates both from the temperature

dependence of the crystallographic contribution to birefringence, which also includes an isotropic magnetic contribution, and from a change in the anisotropic magnetic contribution [28]. The isotropic magnetic contribution can be derived from the temperature-induced variation of the absolute refractive indices. We studied here only the variation of birefringence with temperature, which permits one to determine only the anisotropic magnetic contribution. Using the change in the diagonal components of the permittivity tensor

$$\Delta\varepsilon_{ii} = \beta_{iijk} G_j G_k \quad (8)$$

we can find the magnitude of birefringence in the Γ_2 and Γ_4 phases:

$$\Delta n_{yz}(\Gamma_2) = \frac{\varepsilon_{yy} - \varepsilon_{zz}}{2n} + \frac{(\beta_{yyzz} - \beta_{zzzz}) G_z^2}{2n}, \quad (9)$$

$$\Delta n_{yz}(\Gamma_4) = \frac{\varepsilon_{yy} - \varepsilon_{zz}}{2n} + \frac{(\beta_{yyxx} - \beta_{zzxx}) G_x^2}{2n}. \quad (10)$$

Here, the first term describes the crystallographic contribution to birefringence and the second term is the anisotropic magnetic contribution. The latter contribution is nonzero if $\beta_{yyxx} - \beta_{zzxx} - \beta_{yyzz} + \beta_{zzzz} \neq 0$, which can only occur in noncubic crystals. As follows from Fig. 6, the anisotropic magnetic contribution to birefringence reaches a maximum for $\Delta n_{yz}^{\text{mag}} \approx 5 \times 10^{-4}$ and a minimum for $\Delta n_{xy}^{\text{mag}} \approx 1 \times 10^{-4}$. It is this contribution that was used to monitor the ultrafast spin dynamics in the region of orientational phase transitions induced by 100-fs laser pulses [16].

4. CONCLUSIONS

The main results obtained in our study of the optical properties of thulium orthoferrite can be summed up as follows.

(1) In the transparency window below 2.2 eV, optical *d–d* transitions in the Fe^{3+} iron ion from the $^6A_{1g}$ ground state to the $^4T_{1g}$ and $^4T_{2g}$ excited levels are observed as broad absorption bands peaking at about 1.22 and 1.72 eV, respectively. The transitions occurring in the thulium sublattice from the ground state $^3H_6$ to the $^3H_4$, $^3H_5$, $^3F_4$, $^3F_3$, and $^3F_2$ excited states manifest themselves as narrow split absorption lines with mean energies of 0.73, 1.01, 1.55, 1.8, and 1.87 eV, respectively.

(2) In the region of strong absorption, one observes a localized transition from the $^6A_{1g}$ state to the ^4E_g and $^4A_{1g}$ states with an energy of 2.67 eV and six charge-transfer transitions in the FeO_6^{9-} complexes having resonance energies in the interval from 2.96 to 5.56 eV. The number of observed transitions is larger than that predicted from calculations, which is compelling experimental evidence for the importance of noncubic distortions in the formation of the electronic structure of orthoferrites and, as a consequence, of the anisotropy in the magnetic, optical, and magnetooptical properties.

(3) In the spectral range 0.64–2.1 eV, optical birefringence depends on photon energy only weakly and grows as one approaches the strong absorption region above 2.2 eV. As the temperature is lowered, birefringence passes through two anomalies at the orientational-transition temperatures T_1 and T_2. The change in birefringence due to the spin-orientational transitions should be assigned to the temperature dependence of the crystallographic contribution to birefringence (which also includes the isotropic magnetic contribution) and to that of the anisotropic magnetic contribution. The temperature dependence of birefringence reveals that the anisotropic magnetic contribution to birefringence is maximum for $\Delta n_{yz}^{\text{mag}} \approx 5 \times 10^{-4}$ and is minimum for $\Delta n_{xy}^{\text{mag}} \approx 1 \times 10^{-4}$. The variation of this contribution can be used to monitor the ultrafast spin dynamics in the region of orientational phase transitions induced by 100-fs laser pulses.

ACKNOWLEDGMENTS

The authors are indebted to V.V. Pavlov for providing a code for determination of the oscillator parameters and H.-J. Weber for assistance in measurements of the absorption spectra.

The support of the Russian Foundation for Basic Research (project nos. 03-02-17575, 04-02-16599), the program under the Presidium of the Russian Academy of Sciences "Low-Dimensional Quantum Structures," the EU program "RTN Dynamics," de Nederlandse Organisatie voor Wetenschappelijk Onderzoek (NWO), and de Stichting voor Fundamenteel Onderzoek der Materie (FOM) is gratefully acknowledged.

REFERENCES

1. *Model and Methods of High-Temperature Superconductivity: Some Frontal Aspects*, Ed. by J. K. Srivastava and S. M. Rao (Nova Science Publishers, New York, 2003), Vol. 1; *Studies of High-Temperature Superconductivity (Advances in Research and Applications)*, Ed. by A. Narlikar (Nova Science Publishers, New York, 2002), Vol. 41; *Studies of High-Temperature Superconductivity (Advances in Research and Applications)*, Ed. by A. Narlikar (Nova Science Publishers, New York, 2003), Vol. 45.
2. *Colossal Magnetoresistance, Charge Ordering, and Related Properties of Manganese Oxides*, Ed. by C. N. R. Rao and B. Raveau (World Sci., Singapore, 1998).
3. A. B. Souchkov, J. R. Simpson, M. Quijada, H. Ishibashi, N. Nur, J. S. Ahn, S. W. Cheong, A. J. Millis, and H. D. Drew, Phys. Rev. Lett. **91**, 027 203 (2003).
4. A. M. Kalashnikova and R. V. Pisarev, Pis'ma Zh. Éksp. Teor. Fiz. **78** (3), 175 (2003) [JETP Lett. **78**, 143 (2003)].

5. A. M. Kalashnikova, V. V. Pavlov, R. V. Pisarev, L. N. Bezmaternykh, M. Bayer, and Th. Rasing, Pis'ma Zh. Éksp. Teor. Fiz. **80** (5), 339 (2004) [JETP Lett. **80**, 293 (2004)].
6. *Landolt–Börnstein Numerical Data and Functional Relationships in Science and Technology: New Series* (Springer, Berlin, 1991), Group III, Vol. 27E.
7. R. V. Pisarev, Fiz. Tverd. Tela (Leningrad) **6**, 2545 (1964) [Sov. Phys. Solid State **6**, 2026 (1964)]; Fiz. Tverd. Tela (Leningrad) **7**, 207 (1965) [Sov. Phys. Solid State **7**, 158 (1965)].
8. F. J. Kahn, P. S. Pershan, and J. P. Remeika, Phys. Rev. **186** (3), 891 (1969).
9. R. G. Burns, *Mineralogical Applications of Crystal Field Theory* (Cambridge University Press, Cambridge, 1993).
10. *Landolt–Börnstein Numerical Data and Functional Relationships in Science and Technology: New Series* (Springer, Berlin, 1994), Group III, Vol. 27F3.
11. K. P. Belov, A. K. Zvezdin, A. M. Kadomtseva, and R. Z. Levitin, *Orientational Transitions in Rare-Earth Magnets* (Nauka, Moscow, 1979) [in Russian].
12. V. D. Buchel'nikov, N. K. Dan'shin, L. T. Tsymbal, and V. G. Shavrov, Usp. Fiz. Nauk **166** (6), 585 (1996) [Phys. Usp. **39**, 547 (1996)].
13. A. I. Likhtenshteĭn, A. S. Moskvin, and V. A. Gubanov, Fiz. Tverd. Tela (Leningrad) **24** (12), 3596 (1982) [Sov. Phys. Solid State **24** (12), 2049 (1982)].
14. A. S. Moskvin, A. V. Zenkov, E. A. Ganshina, G. S. Krinchik, and M. M. Nishanova, J. Phys. Chem. Solids **54**, 101 (1993).
15. A. K. Zvezdin and V. A. Kotov, *Modern Magneto-Optics and Magneto-Optical Materials* (Bristol Institute of Physics, Bristol, 1997).
16. A. V. Kimel, A. Kirilyuk, A. Tsvetkov, R. V. Pisarev, and Th. Rasing, Nature (London) **429** (6994), 850 (2004).
17. R. M. White, R. J. Nemanich, and C. Herring, Phys. Rev. B: Condens. Matter **25**, 1822 (1982).
18. E. A. Turov, A. V. Kolchanov, V. V. Men'shenin, I. F. Mirsaev, and V. V. Nikolaev, *The Symmetry and the Physical Properties of Antiferromagnets* (Fizmatlit, Moscow, 2001) [in Russian].
19. A. M. Balbashov and S. K. Egorov, J. Cryst. Growth, Part 2 **52**, 498 (1981).
20. A. B. P. Lever, *Inorganic Electronic Spectroscopy* (Elsevier, Amsterdam, 1984; Mir, Moscow, 1987).
21. D. L. Wood and J. P. Remeika, J. Appl. Phys. **38**, 1038 (1967).
22. G. H. Dieke, *Spectra and Energy Levels of Rare-Earth Ions in Crystals* (Interscience, New York, 1968).
23. A. P. Malozemoff, J. Phys. Chem. Solids **32**, 1669 (1971).
24. R. V. A. Azzam and N. M. Bashara, *Ellipsometry and Polarized Light* (North-Holland, Amsterdam, 1977; Mir, Moscow, 1981).
25. D. E. Aspnes, J. Opt. Soc. Am. **70** (10), 1275 (1980).
26. M. V. Chetkin, Yu. I. Shcherbakov, A. P. Volenko, and L. D. Shevchuk, Zh. Éksp. Teor. Fiz. **67** (3), 1027 (1975) [Sov. Phys. JETP **40**, 509 (1975)].
27. L. D. Landau and E. M. Lifshitz, *Statistical Physics* (Nauka, Moscow, 1976; Pergamon, Oxford, 1980).
28. J. Ferré and G. A. Gehring, Rep. Prog. Phys. **47** (5), 513 (1984).

Translated by G. Skrebtsov

Physics of the Solid State, Vol. 47, No. 12, 2005, pp. 2299–2303. Translated from Fizika Tverdogo Tela, Vol. 47, No. 12, 2005, pp. 2207–2211.

MAGNETISM AND FERROELECTRICITY

Long-Time Relaxation Phenomena in $Pb_{0.94}Ba_{0.06}Sc_{0.5}Nb_{0.5}O_3$ (PBSN-6) Single Crystals

A. I. Burkhanov*, S. V. Kravchenko*, A. V. Shil'nikov†, *, I. P. Raevskiĭ, and V. P. Sakhnenko****

**Volgograd State Architecture and Civil Engineering University, Volgograd, 400074 Russia*
e-mail: postmaster@vgasa.ru
***Institute of Physics, Rostov State University, pr. Stachki 194, Rostov-on Don, 344090 Russia*
Received January 28, 2005

Abstract—Long-time polarization relaxation in the temperature range where PBSN-6 single crystals reside in the relaxor state was studied. An analysis of the time dependence of the permittivity $\varepsilon'(t)$ performed at measuring frequencies from 1 Hz to 1 kHz in weak electric fields E_0 showed that the relaxation (or freezing) times derived by extrapolating relations of the type $\varepsilon'(t) \sim \log(t/t_0)$ and $\varepsilon'(t) \sim \exp\{-[\ln(t/t_0)]^\beta\}$ range from 10^8 to 10^{11} min and depend substantially on the bias voltage applied to the sample. A study of the pattern of the dielectric response in moderate and strong infralow-frequency fields revealed that, after a sample was maintained under a bias lower than the coercive force, it no longer exhibited the additional anomalies in the amplitude dependences of the effective loss tangent $\tan_{\text{eff}}(E_0)$ that were observed in a thermally recuperated sample.

1. INTRODUCTION

It is known that barium-doped lead scandium niobate (PBSN) single crystals exhibit relaxor properties [1]. A characteristic property of relaxors is a variation with time at a constant temperature of some electrophysical parameters, for instance, of the permittivity ε' and dielectric losses ε'' [2–5]. A study of temporal variations $\varepsilon'(t)$ and $\varepsilon''(t)$ in a PMN single crystal performed in the low-temperature region has revealed breakdown of a monotonic (log) decay of $\varepsilon'(t)$ and $\varepsilon''(t)$ after a certain time t_d [5]. The time t_d has been found to depend on the bias electric field $E_=$ applied to the sample; namely, the larger $E_=$, the shorter the time of observation of a sharp drop (step) in the $\varepsilon'(t)$ and $\varepsilon''(t)$ curves. This phenomenon was ascribed in [5] to a kinetic phase transition from the relaxor to ferroelectric phase, which becomes possible in a sample biased by an electric field $E_=$.

A similar pattern of dielectric response in the low- and high-frequency ranges has likewise been observed in lead scandium niobate doped with 6 at % Ba (PBSN-6) [6]. However, the studies of the $\varepsilon'(t)$ variation on biased samples, both of PMN and of PBSN-6, included the so-called initial time interval; in other words, the variation in the dielectric response was recorded immediately after the application of a bias field $E_=$ to a sample which had been preliminarily cooled from $T > T_m$ (T_m is the temperature of the maximum in permittivity $\varepsilon'(t)$) to the temperature of interest $T_i < T_m$. It has been demonstrated [7], however, in the particular example of the SBN-75 relaxor, that the effect of the time of preliminary aging (before application of a field) of a given relaxor at a chosen temperature on the pattern of $\varepsilon'(t)$ and $\varepsilon''(t)$ decay can be substantial and that the shorter the aging time, the more sensitive the sample to a field $E_=$ (and vice versa). In this case, the situation resembles that observed with a spin glass (glass has been reported to become progressively "harder" to a magnetic field with aging [8]). Thus, the processes occurring in a relaxor at the moment of field application (immediately after sample cooling) are difficult to use in interpreting various physical phenomena that take place in such objects.

These considerations motivated the present study of relaxation in PBSN-6 over times substantially in excess of the time of sample cooling to the temperature of interest and subsequent application of a bias or strong ac fields, an approach which assumed the possibility of identifying the dominant polarization relaxation mechanisms throughout the temperature range where the diffuse phase transition occurs in the given system.

2. SAMPLES AND EXPERIMENTAL TECHNIQUES

PBSN single crystals were grown by mass crystallization. The growth technique used and the x-ray diffraction data for these crystals can be found in [9, 10]. We report here on a study of the dielectric properties in the range 0.1–1000 Hz performed both by the bridge method in ultraweak measuring fields (E_0 = 0.8 V/cm) at various dc voltages ($E_=$ = 0–1000 V/cm) and oscillo-

† Deceased.

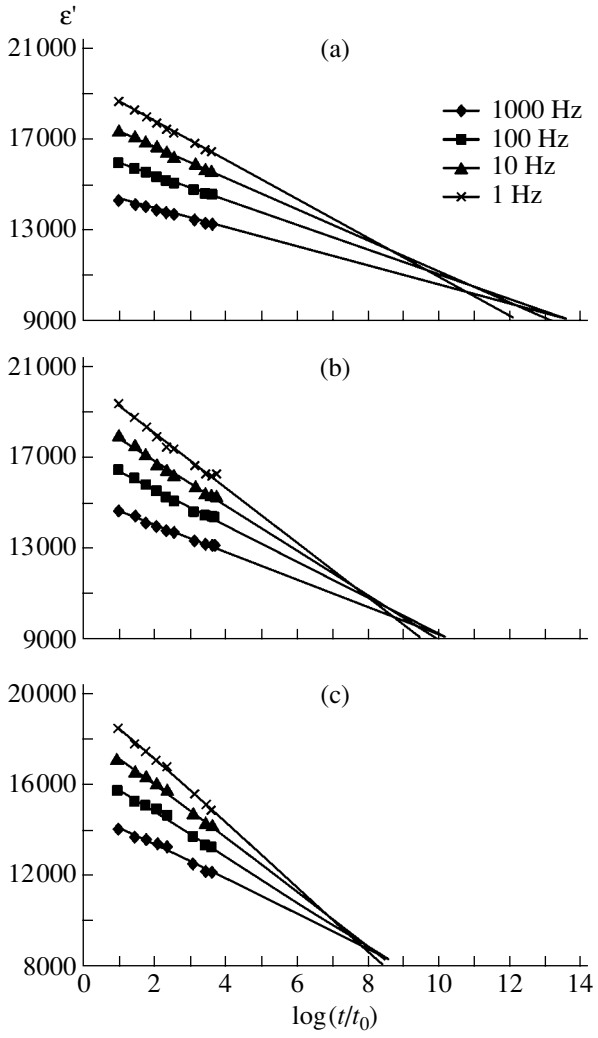

Fig. 1. Variation of the permittivity $\varepsilon'(t/t_0)$ of a PBSN-6 single crystal with time measured at various field frequencies in a bias field $E_=$ equal to (a) 0, (b) 500, and (c) 1000 V/cm. Sample aging temperature T_i = 30°C.

graphically on a modified Sawyer–Tower circuit within a broad range of ac field amplitudes E_0 (from weak to strong, i.e., above the coercive field, $E_0 > E_c$). Before each experiment, a sample was annealed at a temperature $T > T_m$ for 30 min. After this, the sample was cooled down to the given temperature T_i. The rate of temperature variation did not exceed 1°C/min.

3. EXPERIMENTAL RESULTS AND DISCUSSION

Figure 1 shows the variation of permittivity $\varepsilon'[\log(t/t_0)]$ (t_0 = 1 min) with time measured at field frequencies of 1, 10, 100, and 1000 Hz for a period of 5000 min over which the sample was aged at T_i = 30°C. Figure 1a presents graphs obtained before the bias $E_=$ was applied, and Figs. 1b and 1c, graphs obtained after the application of two different biases $E_=$. The straight lines were drawn by approximating experimental data with a log relation,

$$\varepsilon'(t) = A - B\log(t/t_0), \quad (1)$$

where A and B are fitting parameters.

Inspection of the $\varepsilon'[\log(t/t_0)]$ curves does not reveal any qualitative change in the pattern of the relation throughout the measurement time covered, either before or after the application of a bias; there is no sharp decrease in the values of ε' (a step) over this time interval. However, estimation of the relaxation time (polarization freezing time) τ from the crossing of the extrapolated $\varepsilon'[\log(t/t_0)]$ relations suggests that the application of a bias and its increase bring about a gradual decrease in τ (Table 1). Even at $E_=$ = 1000 V/cm, the relaxation time τ is very long, which is consistent with the idea that the physical reason for the relaxor state in materials with diffuse phase transitions is the coexistence of the ferroelectric and glass states [11, 12].

Another point to note is that, if we separate the infralow- and high-frequency relaxation time intervals, where the 1- to 10-Hz (infralow) and 100- to 1000-Hz (high frequency) straight lines intersect, respectively, then the difference between the relaxation times $\tau_{1\text{–}10\ \mathrm{Hz}}$ and $\tau_{100\text{–}1000\ \mathrm{Hz}}$ turns out to be noticeable. Table 2 lists the difference between the exponents in $\tau_{1\text{–}10\ \mathrm{Hz}} = 1 \times 10^{n1}$ and $\tau_{100\text{–}1000\ \mathrm{Hz}} = 1 \times 10^{n2}$ for different values of the bias field across a PBSN-6 sample.

As is evident from Table 2, the difference $\Delta n = n1 - n2$ decreases with increasing $E_=$ by several units. It is conceivable that, under certain conditions, the difference Δn characterizes the relaxation time distribution for relaxing objects of different types. In this case, the application of a bias to a sample (in our case, $E_= < E_c$) "switches off" part of the relaxing objects that contribute to ε*. We may further assume that, in PBSN-6,

Table 1. Polarization relaxation (freezing) times in a PBSN-6 single crystal measured at different bias field values at a constant temperature T_i = 30°C

$E_=$, V/cm	τ, min
0	1×10^{11}
500	1×10^{9}
1000	1×10^{8}

Table 2. Exponent difference Δn obtained at different values of the bias field applied to a PBSN-6 sample at a temperature T_i = 30°C

$E_=$, V/cm	Δn
0	4.4
500	2.67
1000	0.95

where the relaxor state can change spontaneously to the ferroelectric state, relaxing objects are switched off at $E_{=} < E_c$ not only due to the orienting action of the bias on individual polar nanoregions but also due to the bias-induced partial merging of polar nanoregions (clusters), with the subsequent formation of a domain structure in the material. This assumption is in good agreement with the data in Fig. 2 corresponding to the case where the aging temperature T_i is chosen close to the temperature of the so-called spontaneous phase transition (T_{sph}) from the relaxor to ferroelectric state in PBSN-6.

In contrast to the cases demonstrated in Fig. 1, where the time dependence of $\varepsilon'(t)$ is approximated by a logarithmic function, the permittivity decay at T_i = 7°C in Fig. 2 is fitted better with a function

$$\varepsilon'(t) \sim \exp\{-[\ln(t/t_0)]^{\beta}\}, \qquad (2)$$

where $\beta < 1$ and $t \gg t_0$ (t_0 = 1 min).

The application of a bias to a sample at T_i = 7°C brings about a substantial decrease in the frequency dispersion of ε^* (as compared to the action of a biasing field of the same magnitude at T_i = 30°C; see Fig. 1).

The most probable explanation for the change in the pattern of the time asymptotic of the permittivity observed to occur as the aging temperature approaches T_{sph} is that, as a sample is cooled from $T > T_m$ to $T \approx T_{sph}$, the system changes its phase state from relaxor to glasslike; i.e., close to T_{sph}, we witness the manifestation of an interaction among polar nanoregions. This may give rise, on the one hand, to glasslike freezing, and on the other, to the formation of structures of the fractal-cluster type (microelectrets) [13, 14] or tweeds [15], as is the case with martensitic phase transformations [16].

Similar variations in the type of time dependences have been observed [17] in PLZT-8/35/65 relaxor ceramics as the sample aging temperature approached a characteristic relaxor temperature T_d (the temperature of macroscopic sample depolarization). In the case of PBSN-6, the application of relatively weak external fields at $T \approx T_{sph}$ accelerates apparently to a considerable extent the formation of such a mesoscopic structure, which subsequently transforms to a domain structure of the ferroelectric phase of the material.

The effect of preliminary aging of a relaxor under a bias at a temperature close to T_{sph} on polarization and repolarization in a PBSN-6 single crystal can be seen in Fig. 3. Figure 3 presents the amplitude dependences of the effective loss tangent $\tan_{eff}\delta(E_0)$ as derived from polarization switching loops for a thermally recuperated PBSN-6 sample and a PBSN-6 sample aged at T_i = 7°C ($T_i \approx T_{sph}$) in a field $E_{=}$ = 500 V/cm. We readily see that, as the measuring frequency decreases in the range of moderate field amplitudes ($E_0 \sim$ 1500–1600 V/cm), the recuperated sample exhibits an anomaly in the form of a break in the $\tan_{eff}\delta(E_0)$ relation. No such anomaly is seen in the aged sample.

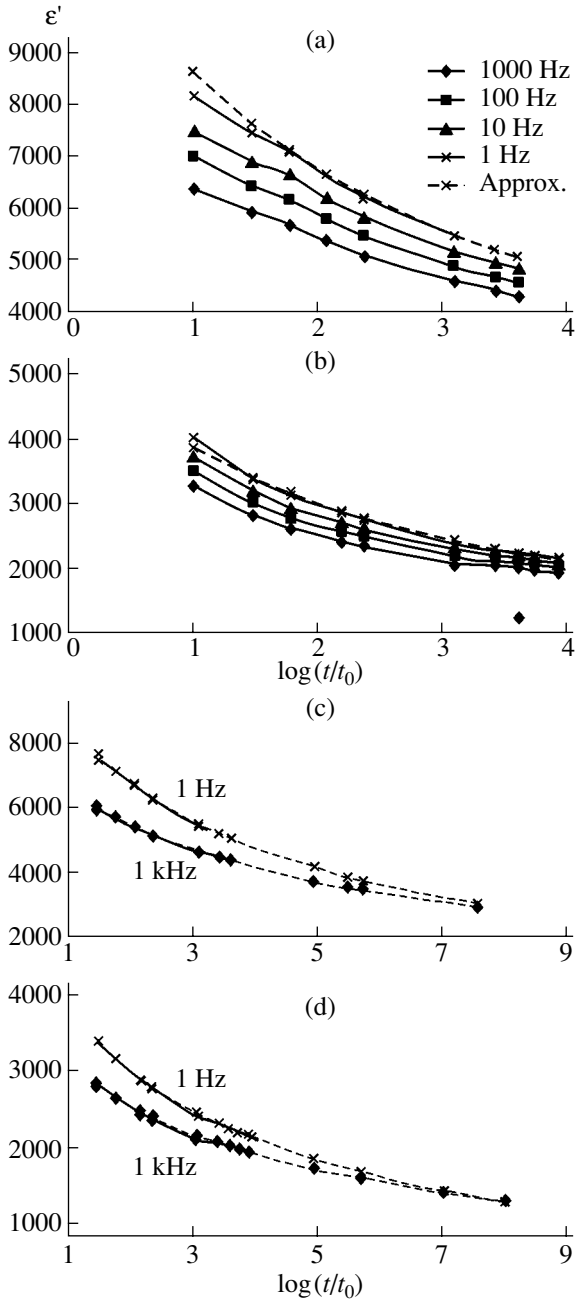

Fig. 2. Time dependences of $\varepsilon'(t/t_0)$ for a PBSN-6 single crystal measured for different field frequencies in a bias field $E_{=}$ equal to (a, c) 0 and (b, d) 500 V/cm. Sample aging temperature T_i = 7°C.

Note that, in our earlier study of this material [18], the temperature dependences of $\tan_{eff}\delta(T)$ as measured at various field amplitudes E_0 revealed an anomaly in this parameter in the form of an additional maximum in $\tan_{eff}\delta(T)$ near $T \approx$ 10°C, but only for fields $E_0 \geq$ 1650 V/cm. This behavior suggests that this value of the ac field amplitude is critical for PBSN-6; above this value, a ferroelectric state could be induced at temperatures corresponding to the relaxor state of the material.

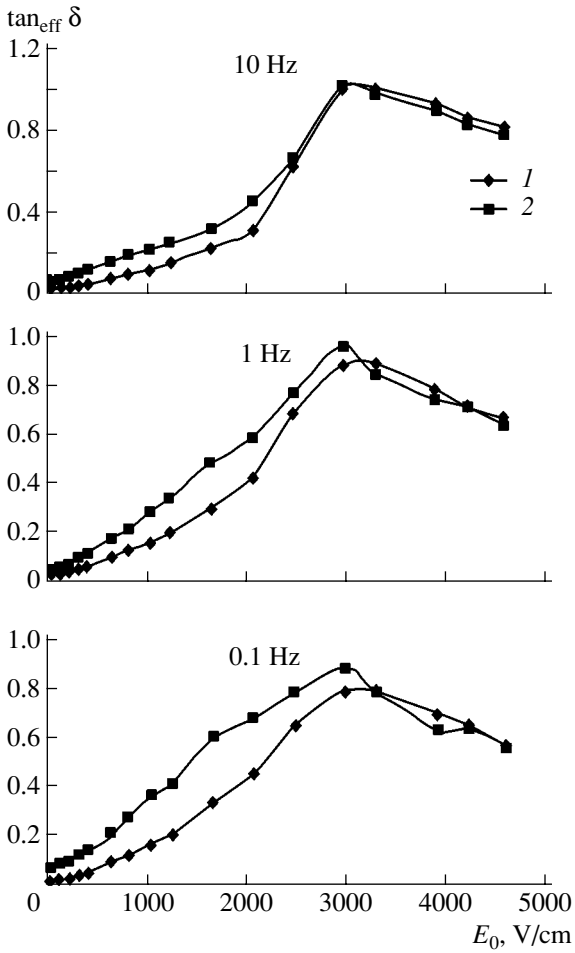

Fig. 3. Amplitude dependences of the effective loss tangent $\tan_{eff}\delta(E_0)$ as derived from polarization switching loops for (*1*) a PBSN-6 sample preliminarily aged at T_i = 7°C ($T \approx T_{sph}$) in a bias field $E_=$ = 500 V/cm and (*2*) a thermally recuperated PBSN-6 sample.

The fact that the aged sample did not exhibit any effects in the amplitude dependences of $\tan_{eff}\delta(E_0)$ at such fields suggests that the prolonged action of a bias field on a sample stimulated a phase transition from the relaxor to ferroelectric state in a sizable part of the sample volume, after which the polarization switching processes occurred primarily via domain wall motion mechanisms.

One should, however, also bear in mind that the properties of ferroelectric and related materials that have been subjected to prolonged aging are strongly influenced by defects (due to pinning and depinning of domain walls and phase boundaries) [19, 20]. The pinning of domain or phase boundaries is indicated by a decrease in $\tan_{eff}\delta(E_0)$ in a well-aged sample as compared to a recuperated sample for field amplitudes not in excess of 3000 V/cm (Fig. 3). For E > 3000 V/cm, the values of $\tan_{eff}\delta(E_0)$ for an aged and a recuperated sample practically coincide, which may indicate the complete breakaway of domain walls and phase boundaries from defects in these fields and involvement of the entire volume of the sample in the polarization and repolarization processes under the given experimental conditions.

4. CONCLUSIONS

(1) An analysis of the time dependences of ε'(*t*) performed over a broad interval of measuring frequencies suggests that the relaxation (freezing) times in the region of the diffuse phase transition in a PBSN-6 single crystal lie in the range from 10^8 to 10^{11} min and depend substantially on the magnitude of the bias field applied to the crystal.

(2) The changes in the pattern of long-time relaxation in PBSN-6 observed to occur as the aging temperature T_i approaches the temperature T_{sph} of the so-called spontaneous (with no external field applied) phase transition to the ferroelectric state are most probably due to the material passing through the following phase states: superparaelectric for $T_i > T_m$, relaxor for $T_i \approx T_m$, and glasslike for $T_{sph} < T_i < T_m$.

(3) The existence of an additional anomaly (in addition to that occurring at T_m) in the temperature dependences of the polarization characteristics at temperatures below T_m observed before the application of a bias to the sample and the absence of this anomaly after application of the bias suggest that aging a sample under a bias even below the coercive field brings about a gradual disappearance of the relaxor phase and the formation of the ferroelectric phase in the temperature range from T_{sph} to T_m.

REFERENCES

1. I. P. Raevskiĭ, V. V. Eremkin, V. G. Smotrakov, E. S. Gagarina, and M. A. Malitskaya, Fiz. Tverd. Tela (St. Petersburg) **42** (1), 154 (2000) [Phys. Solid State **42** (1), 161 (2000)].
2. A. V. Shil'nikov, A. I. Burkhanov, and E. Kh. Birks, Fiz. Tverd. Tela (Leningrad) **29** (3), 899 (1987) [Sov. Phys. Solid State **29** (3), 520 (1987)].
3. W. Y. Pan, T. R. Shrout, and L. E. Cross, J. Mater. Sci. Lett. **8**, 771 (1989).
4. A. I. Burkhanov, A. V. Shilnikov, and A. Sternberg, Ferroelectrics **90**, 39 (1989).
5. E. V. Colla, E. Yu. Koroleva, N. M. Okuneva, and S. B. Vakhrushev, Phys. Rev. Lett. **74** (9), 1681 (1995).
6. I. P. Raevski, M. A. Malitskaya, E. S. Gagarina, V. G. Smotrakov, E. V. Sahkar, S. I. Raevskaya, and V. V. Eremkin, Ferroelectrics **299**, 115 (2004).
7. A. I. Burkhanov, A. V. Shil'nikov, and R. E. Uzakov, Proc. SPIE-Int. Soc. Opt. Eng. **2967**, 199 (1997).
8. V. S. Dotsenko, Usp. Fiz. Nauk **163** (6), 1 (1993) [Phys. Usp. **36**, 455 (1993)].
9. I. P. Raevski, V. G. Smotrakov, V. V. Eremkin, E. S. Gagarina, and M. A. Malitskaya, Ferroelectrics **247**, 27 (2000).

10. I. P. Raevskiĭ, V. V. Eremkin, V. G. Smotrakov, E. S. Gagarina, and M. A. Malitskaya, Kristallografiya **46** (1), 144 (2001) [Crystallogr. Rep. **46**, 133 (2001)].
11. M. D. Glinchuk and V. A. Stephanovich, J. Phys.: Condens. Matter **10**, 11 081 (1998).
12. S. A. Gridnev, Ferroelectrics **266**, 171 (2002).
13. A. I. Burkhanov, in *Proceedings of the International Conference on Relaxation Phenomena in Solids, Voronezh, Russia, 1995* (Voronezh Technical Univ., Voronezh, 1996), Part 1, p. 89 [in Russian].
14. A. I. Burkhanov, A. V. Shil'nikov, and R. E. Uzakov, Kristallografiya **42** (6), 1069 (1997) [Crystallogr. Rep. **42**, 993 (1997)].
15. Dwight Viehland, M. Y. Kim, Z. Xu, and Jie-Fang Li, in *Proceedings of the 5th International Conference on Electroceramics, Averio, Portugal, 1996*, Ed. by J. L. Baptista, J. A. Labrincha, and P. M. Vilarino (University of Averio, Averio, Portugal, 1996), Book 1, p. 97.
16. A. Bratkovsky, E. K. H. Salje, and V. Heine, Phase Transform. **52**, 77 (1994).
17. A. I. Burkhanov and A. V. Shil'nikov, Ferroelectrics **299**, 153 (2004).
18. A. V. Shil'nikov, S. V. Kravchenko, A. I. Burkhanov, I. P. Raevskiĭ, V. P. Sakhnenko, and L. I. Ievleva, in *Proceedings of the 4th International Conference "Crystals: Growth, Properties, Real Structure, and Application," Aleksandrov, Russia, 2003* (VNIISIMS, Aleksandrov, 2003), p. 236.
19. B. A. Strukov and A. P. Levanyuk, *Ferroelectric Phenomena in Crystals* (Nauka, Moscow, 1995; Springer, Geidelberg, 1998).
20. A. V. Shil'nikov, Doctoral Dissertation (1998).

Translated by G. Skrebtsov

Physics of the Solid State, Vol. 47, No. 12, 2005, pp. 2304–2308. Translated from Fizika Tverdogo Tela, Vol. 47, No. 12, 2005, pp. 2212–2216.

MAGNETISM AND FERROELECTRICITY

Heat Capacity Study of Double Perovskite-Like Compounds $BaTi_{1-x}Zr_xO_3$

M. V. Gorev*, V. S. Bondarev*, I. N. Flerov*, Ph. Sciau, and J.-M. Savariault****

**Kirensky Institute of Physics, Siberian Division, Russian Academy of Sciences, Akademgorodok, Krasnoyarsk, 660036 Russia*

e-mail: gorev@iph.krasn.ru

***CEMES–CNRS, 29 rue Jeanne Marvig, Toulouse, 31055 France*

Received February 21, 2005

Abstract—The temperature dependence of the heat capacity of two compositions in the solid solution system $BaTi_{1-x}Zr_xO_3$ ($x = 0.25, 0.35$) was measured using adiabatic calorimetry. In the T–x phase diagram, these compounds occupy positions near the crossover from conventional ferroelectric behavior to the relaxor state. Both compounds reveal diffuse heat capacity anomalies: two anomalies in the temperature ranges 250–350 and 150–200 K at $x = 0.35$ and one anomaly within the range ~150–320 K at $x = 0.25$. The results obtained are discussed together with structural and dielectric measurements. © *2005 Pleiades Publishing, Inc.*

1. INTRODUCTION

Relaxor ferroelectrics have been attracting research interest for a long time due to their remarkable dielectric and piezoelectric properties and the application potential they demonstrate in various areas of technology.

Dielectric, structural, spectroscopic, and other studies have established that the main relaxor features originate from the compositional and structural inhomogeneities of these materials and the presence of interacting polar nanodomains in a nonpolar matrix. The possible mechanisms responsible for these nonuniformities and for the formation of polar nanodomains have been debated intensely in the literature and are apparently different in different relaxor ferroelectric groups [1–3].

Most of the relaxors are mixed lead-containing perovskites. However, reports have recently appeared on the discovery of several groups of compounds which feature relaxor properties and are derivatives of $BaTiO_3$ with substituted isovalent or heterovalent cations [4–6]. The intense research interest in barium compounds stems to a considerable extent from their being more environmentally friendly.

Conventional relaxor ferroelectrics, which are similar to classical relaxors such as $PbMg_{1/3}Nb_{2/3}O_3$ (PMN) or $Na_{1/2}Bi_{1/2}TiO_3$ (NBT), possess three distinctive features: the presence in their composition of positionally disordered Pb^{2+} or Bi^{3+} ions, which occupy position A of the perovskite lattice because of their electronic structure; heterovalent disorder (at any rate, in one position, A or B); and, unlike solid solutions, the tendency to form a chemical compound with a fixed composition.

The solid solution system $BaTi_{1-x}Zr_xO_3$ with $Ti^{4+} \longrightarrow Zr^{4+}$ ion substitution in position B exhibits none of these features, which makes its relaxor behavior all the more remarkable [7–9]. Moreover, a continuous variation from typically ferroelectric to relaxor behavior is a unique characteristic of lead-free solid solutions.

Mixed compounds with Zr concentrations $x < 0.1$–0.12 exhibit permittivity anomalies corresponding to three phase transitions, as is the case with the original $BaTiO_3$. As the zirconium concentration increases, the temperature of the transition from the cubic to tetragonal phase decreases, while the temperatures of the other two transitions between distorted phases increase. In the range $0.12 < x < 0.25$, there occurs only one fairly strong permittivity anomaly, which corresponds to a direct transition from the cubic to rhombohedral phase and exhibits a weakly pronounced frequency dispersion. For $x > 0.25$, these compounds reveal only one broad peak in $\varepsilon(T)$ with a maximum at T_m. Note that the values of the maximum permittivity and T_m depend markedly on the measuring field frequency, as should be expected in relaxors. The phase diagram of compounds with slight additions of Ca^{2+} has a narrow region of concentrations x within which, in addition to the maximum in $\varepsilon(T)$ at T_m, a classical transition to the ferroelectric state is observed at $T_3 < T_m$ [7, 10]. The $T_m(x)$ and $T_{VF}(x)$ (the Vogel–Fulcher temperature) lines in the relaxor region join smoothly with the $T_c(x)$ line for compositions that exhibit conventional ferroelectric behavior. The reasons for this relation and the mechanisms governing the relaxor behavior in barium-containing relaxors are discussed in [6].

1063-7834/05/4712-2304$26.00

Studies of barium-containing relaxors have placed major emphasis on the behavior of the dielectric properties of these materials near T_m. The interval about the Burns temperature T_d where polar nanodomains form and the mechanisms governing the formation of these domains have not been considered up to now.

The present study was aimed at establishing the main features in the behavior of the heat capacity of $BaTi_{1-x}Zr_xO_3$ solid solutions with zirconium concentrations close to the crossover from the ferroelectric to relaxor state. The calorimetric method makes it possible to reveal anomalies in the heat capacity of any origin associated with changes in both the electrical and elastic subsystems and determine the energy characteristics of these changes. The temperature range covered by our studies extends over all characteristic temperatures of relaxors, namely, T_d, T_m, and T_c (the temperature of transition to the ferroelectric state), thus opening up the possibility of refining the $T(x)$ diagram.

2. SAMPLE PREPARATION AND EXPERIMENTAL TECHNIQUE

The $BaTi_{1-x}Zr_xO_3$ samples with $x = 0.25$ and 0.35 chosen for the study belong to different regions of the phase diagram and undergo transitions to the conventional ferroelectric and the relaxor state, respectively.

$BaTi_{1-x}Zr_xO_3$ solid solutions were obtained in powder form by solid-phase synthesis in an oxygen environment from oxides in the reaction $BaCO_3 + (1 - x)TiO_2 + xZrO_2 \longrightarrow Ba(Ti_{1-x}Zr_x)O_3 + CO_2$ at temperatures of 1100–1200°C.

Ceramic samples ~10 mm in diameter and 4- to 7-mm thick were likewise synthesized in a dry oxygen atmosphere at 1250–1400°C from oxides without any sintering additives in 4 h. The grain size was about 1–2 μm, and the density reached 90–95% of the calculated value. X-ray diffraction analysis confirmed that the samples were single-phase and that the compounds had cubic structure $Pm3m$ [11, 12].

The heat capacity studies in the range 100–370 K were carried out by adiabatic calorimetry, a method providing high accuracy in absolute measurements. The sample mass was 2.7 g for $x = 0.35$ and 4.9 g for $x = 0.25$. Measurements were made using the traditional method of discrete heating ($\Delta T = 1.5$–2.5 K) and in automated regime of continuous heating at a temperature variation rate $dT/dt \approx (0.2–0.3)$ K/min [13]. The accuracy of total heat capacity measurements depends on the heating regime chosen and is 0.1–0.5%.

3. EXPERIMENTAL RESULTS

Figure 1a presents the results of the heat capacity measurements of $BaTi_{0.65}Zr_{0.35}O_3$. It has been reported that the permittivity of this compound exhibits one frequency-dependent anomaly near 200 K [6]. The $C_p(T)$ curve did not reveal any clearly pronounced anomalies characteristic of traditional phase transitions. In the temperature ranges 250–350 and 150–200 K, however, one observes broad diffuse features in the heat capacity, which stand out distinctly in the temperature dependence of the excess heat capacity (Fig. 1b).

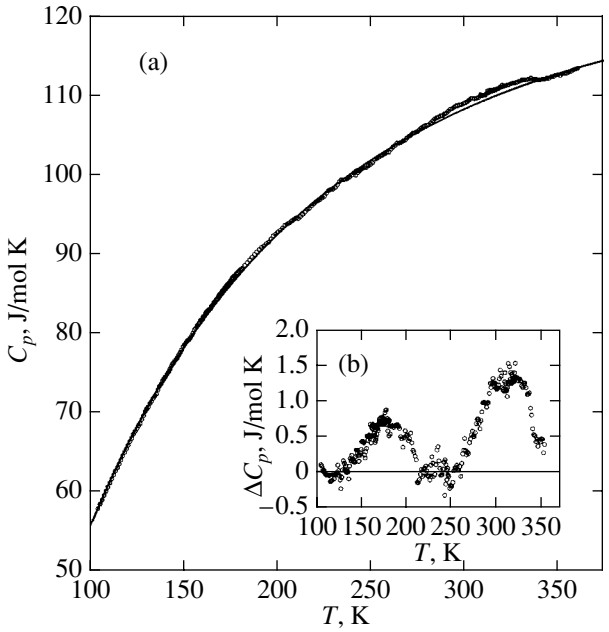

Fig. 1. (a) Temperature dependence of the specific heat of $BaTi_{0.65}Zr_{0.35}O_3$; the solid line is the lattice specific heat. (b) Anomalous specific-heat component.

The lattice (C_L) and anomalous (ΔC_p) contributions to the specific heat of our compounds were separated using a simple model in which the lattice heat capacity is described by a combination of the Debye and Einstein functions. In the temperature region of interest, the heat capacity is only weakly sensitive to fine features in the lattice vibration spectrum, which justifies, in our opinion, the approximation of the lattice contribution in the above way. The anharmonic contributions and the difference between C_p and C_V were neglected because this difference, as a rule, is small as a result of the smallness of the thermal expansion coefficients of the compounds under study [14].

Reverting now to Fig. 1b, we note that the high-temperature anomaly is located near the temperature where the permittivity curve starts to deviate from the Curie–Weiss law [6], i.e., near the Burns temperature T_d. The temperature of the low-temperature anomaly is close to that of the maximum in permittivity T_m.

$BaTi_{0.75}Zr_{0.25}O_3$ undergoes a conventional phase transition to the ferroelectric phase [6, 11]. The small dispersion in permittivity was assigned to inhomogeneities of the samples. Compositionally, the compound is close to the point of crossover from the conventional to relaxor behavior. The temperature dependence of the

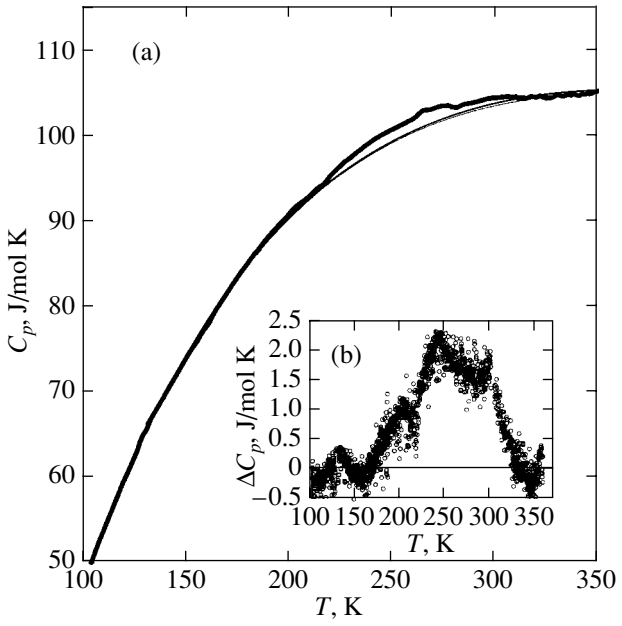

Fig. 2. (a) Temperature dependence of the specific heat of $BaTi_{0.75}Zr_{0.25}O_3$; the solid line is the lattice specific heat. (b) Anomalous component of the specific heat.

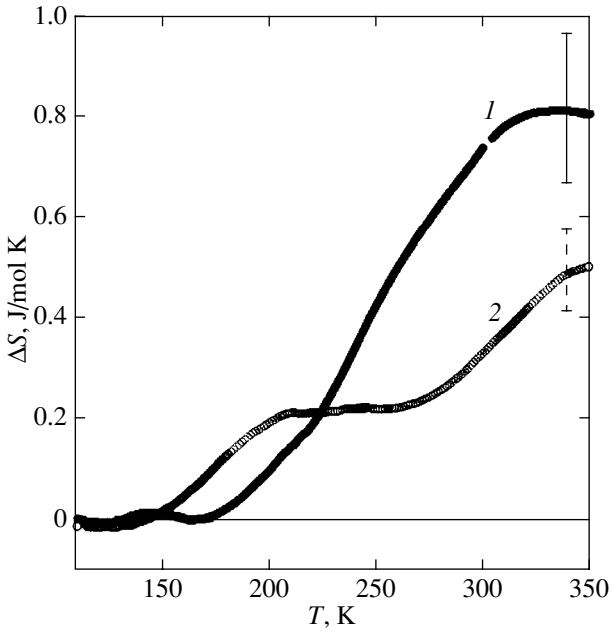

Fig. 3. Temperature dependence of the change in entropy of the $BaTi_{1-x}Zr_xO_3$ compounds with x equal to (*1*) 0.25 and (*2*) 0.35.

specific heat plotted in Fig. 2a reveals a broad region of anomalous behavior of $C_p(T)$ extending from ~150 to ~320 K.

We believe that the fairly large scatter of experimental points observed for $BaTi_{0.75}Zr_{0.25}O_3$ (Fig. 2b) is intimately connected with the specific features of this compound, namely, its being close to the practically vertical boundary separating the relaxor phase from the ferroelectric phase in the T–x diagram [6]. The $C_p(T)$ curves in the anomalous region were obtained in several series of measurements. In each series, the sample was cooled to nitrogen temperature and then heated at a high rate (~1–2 K/min) to the starting temperature in the series. This could bring about a lack of reproducibility in the results because of the attainment of equilibrium in the sample being a slow process. The main difficulty experienced in separating the lattice and anomalous contributions is associated with the fact that the regions of the normal behavior of $C_p(T)$ below 150 K and above 320 K are very narrow, and it is this factor that accounts for the lower reliability of $\Delta C_p(T)$ determination.

The anomalous component of the specific heat $\Delta C_p = C_p - C_L$, shown in Figs. 1b and 2b, is only 2 J/mol K, or ~2% of the lattice specific heat C_L.

The entropy changes related to the anomalous behavior of the specific heat and defined as $\Delta S = \int(\Delta C_p/T)dT$ are shown graphically in Fig. 3. The small values $\Delta S_{0.25} \approx 0.8$ J/mol K and $\Delta S_{0.35} \approx 0.5$ J/mol K imply that the processes involved are not of the order–disorder type, regardless of what reasonable fraction of the polar phase they are identified with. This is no surprise, because in barium compounds, unlike in compounds containing lead, the Ba^{2+} cation does not contribute noticeably either to the polarization or to the transition entropy.

4. DISCUSSION AND CONCLUSIONS

In order to gain insight into the origin of the broad anomalies in the temperature dependence of the specific heat, we consider the specific features in the structure of these materials and the corresponding models of the phenomena involved.

In a solid-solution system, according to the Vegard law, the unit cell parameter of the mixed compound varies linearly with increasing concentration of the second component. This involves a change in the interaction parameters in the lattice and, accordingly, changes in the temperatures and sequences of the phase transitions.

This is exactly what occurs in the $BaTiO_3$–$BaZrO_3$ system at low zirconium concentrations. The unit cell parameter varies in a linear manner [15], the intermediate tetragonal and orthorhombic phases gradually vanish, and the temperature of transition from the cubic phase decreases.

Starting, however, with zirconium concentrations $x > 0.2$–0.3, the temperature and frequency dependences of the permittivity change. The anomaly becomes strongly diffuse, and its temperature T_m is heavily dependent on the measuring frequency. Note that the macroscopic spontaneous polarization does not

appear below T_m in this case. This behavior is typical of relaxors.

This transition coincides in concentration with the appearance of additional reflections in the x-ray diffraction patterns and a change in the pattern of the concentration dependence of the cell parameter [15], which apparently indicates a multiphase state of the samples and a breakup of the solid solutions. In this concentration range, the samples may be assumed to consist of nanoregions with different zirconium concentrations. The long-range order characteristic of the low-temperature phase of pure barium titanate and solid solutions with $x < 0.2$ breaks down. Regions rich in Ti^{4+} become polar below the Burns temperature T_d, whereas regions with a high Zr^{4+} content remain paraelectric, like pure $BaZrO_3$, so that finally only polar nanodomains are left in the samples.

Thus, for $x \geq 0.25$, the situation in $BaTi_{1-x}Zr_xO_3$ becomes similar in a certain sense to that observed earlier in $PbMg_{1/3}Nb_{2/3}O_3$, where compositional inhomogeneities were reliably detected on the nanoscopic level and where regions with local Mg/Nb = 1 stoichiometry were observed [16].

The measured temperature dependence of the specific heat of $BaTi_{0.65}Zr_{0.35}O_3$ is likewise similar to $C_p(T)$ of lead magnesium niobate, where anomalies in the specific heat have been observed near the maximum in permittivity at T_m [17, 18] and at the temperature T_d of formation of polar nanodomains [18].

A model of relaxors for the temperature range $T < T_d$, namely, the spherical random bond–random field model (SRBRF), was proposed in [2]. This model considers a system of randomly interacting reorienting nanoclusters in the presence of random electric fields. Both random interactions (bonds) and random electric fields are assumed to have a Gaussian distribution. With no external field applied ($E = 0$), the system allows two sets of solutions. One of them, where the mean cluster polarization $\langle P \rangle = 0$ and the rms polarization $\langle P^2 \rangle \neq 0$, corresponds to a phase with no long-range order (spherical glass, SG). The other solution, with $\langle P \rangle \neq 0$ and $\langle P^2 \rangle \neq 0$, can be identified with a long-range-order phase, i.e., the ferroelectric (FE) phase.

If the mean interaction strength J_0 is less than a critical value, no long-range order sets in and the system remains in the SG state down to 0 K but the permittivity and the heat capacity pass through a maximum at a temperature T_m. If J_0 is larger than the critical value, long-range order may appear as a result of a phase transition into an inhomogeneous ferroelectric phase at $T_c < T_m$.

In $BaTi_{0.65}Zr_{0.35}O_3$, the interaction parameter J_0 is apparently less than the critical value and the ferroelectric transition with the formation of a macroscopic order parameter (polarization) does not occur. Accordingly, no classical heat capacity anomalies appear. However, the existence of the parameter $\langle P^2 \rangle \neq 0$ and its variation with temperature give rise to an additional contribution to the free energy and heat capacity. The temperature dependence of the heat capacity was calculated numerically in [17] for various parameter values of the model proposed in [2]. It was found that, even in the absence of the ferroelectric transition, the heat capacity passes through a broad anomaly peaking at T_m.

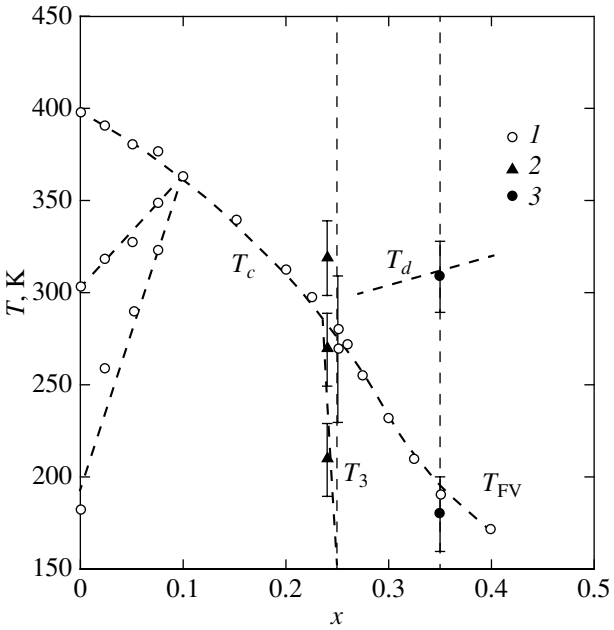

Fig. 4. Phase diagram of the $BaTi_{1-x}Zr_xO_3$ system. (*1*) Dielectric measurements [6, 12], (*2*) calorimetric studies of $Ba_{0.92}Ca_{0.08}Ti_{0.76}Zr_{0.24}O_3$ [14], and (*3*) present study.

In $Ba_{0.92}Ca_{0.08}Ti_{0.76}Zr_{0.24}O_3$, J_0 exceeds the critical value and this compound reveals, besides anomalies in the permittivity and heat capacity at $T_m \approx 270$ K, the long-range order and the phase transition to a nonuniform ferroelectric phase at $T_3 = 210$ K [7, 14].

Unfortunately, the anomalous heat capacity components, as already mentioned, are fairly small, with the associated uncertainties reaching as high as 20–30%, which precluded any attempt at quantitative treatment.

Thus, the temperatures of the heat capacity anomalies observed in our study may be identified, in our opinion, with T_d, T_m, or T_{VF}.

The data obtained suggest that the temperature versus composition phase diagram [6] should be complemented by one more line, namely, $T_d(x)$. Figure 4 sums up the results reported in [6], the results obtained in this study for $BaTi_{1-x}Zr_xO_3$ with $x = 0.25$ and 0.35, and the characteristic temperatures for $Ba_{0.92}Ca_{0.08}Ti_{0.76}Zr_{0.24}O_3$ [14].

An increase in zirconium concentration above a certain critical level $x_{f-r} \approx 0.25$–0.27 [6] initiates, in our opinion, the formation of compositionally nonuniform nanoregions, part of which, that with a lower Zr content, transfers to the polar state at the Burns temperature

T_d. The value of T_d depends both on the actual composition of a nanoregion and on its size; so we have here a range of Burns temperatures. This suggestion is corroborated by the results obtained in a study of $BaTiO_3$ thin films and nanopowders [19]. Interaction among polar nanoregions gives rise to the appearance of maxima in the permittivity and heat capacity at T_m, followed by a ferroelectric transition at T_3. As the zirconium concentration is increased further, the interaction among the polar nanoregions decreases and the transition to a phase with macroscopic polarization does not occur.

ACKNOWLEDGMENTS

This study was supported by the Russian Foundation for Basic Research and the Krasnoyarsk Kraĭ Science Foundation (project no. 05-02-97707-p_enisei_a), a grant from the President of the Russian Federation for support of leading scientific schools (project no. NSh-939.2003.2), and a program under the Presidium of the Russian Academy of Sciences (project no. 9.1).

REFERENCES

1. G. A. Samara, J. Phys.: Condens. Matter **15** (9), R367 (2003).
2. R. Pirc and R. Blinc, Phys. Rev. B: Condens. Matter **60** (19), 13 470 (1999).
3. W. Kleemann, J. Non-Cryst. Solids **307–310**, 66 (2002).
4. J. Ravez and A. Simon, Phys. Status Solidi A **178** (2), 793 (2000).
5. J. Ravez and A. Simon, J. Solid State Chem. **162**, 260 (2001).
6. A. Simon, J. Ravez, and M. Maglione, J. Phys.: Condens. Matter **16** (6), 963 (2004).
7. J. Ravez, R. von der Muhll, A. Simon, and P. Sciau, J. Mater. Chem. **9** (11), 2829 (1999).
8. Ph. Sciau and A. M. Castagnos, Ferroelectrics **270** (1), 259 (2002).
9. J. Kreisel, P. Bouvier, M. Maglione, B. Dkhil, and A. Simon, Phys. Rev. B: Condens. Matter **69** (9), 092104 (2004).
10. P. Sciau, G. Calvarin, and J. Ravez, Solid State Commun. **113** (2), 77 (1999).
11. J. Ravez and A. Simon, Eur. J. Solid State Inorg. Chem. **34**, 1199 (1997).
12. R. Farhi, M. El. Marssi, A. Simon, and J. Ravez, Eur. Phys. J. B **9** (4), 599 (1999).
13. V. S. Bondarev, A. V. Kartashev, A. G. Kozlov, I. Ya. Makievskiĭ, I. N. Flerov, and M. V. Gorev, Preprint No. 829, F (Kirensky Institute of Physics, Siberian Division, Russian Academy of Sciences, Krasnoyarsk, 2005).
14. M. V. Gorev, I. N. Flerov, V. S. Bondarev, Ph. Sciau, and J.-M. Savariault, J. Phys.: Condens. Matter **16** (39), 7143 (2004).
15. R. Pantou, C. Dubourdieu, F. Weiss, J. Kreisel, G. Kobernik, and W. Haessler, Mater. Sci. Semicond. Process. **5** (2–3), 237 (2002).
16. S. Miao, J. Zhu, X. Zhang, and Z.-Y. Cheng, Phys. Rev. B: Condens. Matter **65** (5), 052101 (2002).
17. M. V. Gorev, I. N. Flerov, V. S. Bondarev, and Ph. Sciau, Zh. Éksp. Teor. Fiz. **123** (3), 599 (2003) [JETP **96**, 531 (2003)].
18. Y. Moriya, H. Kawaji, T. Tojo, and T. Atake, Phys. Rev. Lett. **90** (20), 205 901 (2003).
19. B. A. Strukov, S. T. Davitadze, S. N. Kravchun, S. A. Taraskin, B. M. Goltzman, V. V. Lemanov, and S. G. Shulman, J. Phys.: Condens. Matter. **15** (25), 4331 (2003).

Translated by G. Skrebtsov

Physics of the Solid State, Vol. 47, No. 12, 2005, pp. 2309–2314. Translated from Fizika Tverdogo Tela, Vol. 47, No. 12, 2005, pp. 2217–2222.

MAGNETISM AND FERROELECTRICITY

Statistical Mechanics of Cation Ordering in $PbSc_{1/2}Ta_{1/2}O_3$ and $PbSc_{1/2}Nb_{1/2}O_3$ Solid Solutions

V. I. Zinenko and S. N. Sofronova

Kirensky Institute of Physics, Siberian Division, Russian Academy of Sciences, Krasnoyarsk, 660036 Russia

e-mail: zvi@iph.krasn.ru

Received March 15, 2005

Abstract—A model Hamiltonian for *B* cation ordering (Sc–Nb(Ta)) in $PbSc_{1/2}Nb_{1/2}O_3$ and $PbSc_{1/2}Ta_{1/2}O_3$ solid solutions is constructed. The parameters of the model Hamiltonian are determined from the *ab initio* calculation within the ionic crystal model with allowance made for the deformability and the dipole and quadrupole polarizabilities of the ions. The temperatures of the phase transition due to the ordering of the *B* cations are calculated by the Monte Carlo method in the mean-field and cluster approximations. The phase transition temperatures calculated by the Monte Carlo method (1920 K for $PbSc_{1/2}Ta_{1/2}O_3$ and 1810 K for $PbSc_{1/2}Nb_{1/2}O_3$) are consistent with the experimental data (1770 and 1450 K, respectively). The thermodynamic properties of the cation ordering are investigated using the Monte Carlo method. © *2005 Pleiades Publishing, Inc.*

1. Solid solutions of $AB'_xB''_{1-x}O_3$ oxides with a perovskite structure have been continuing to attract the attention of researchers for several decades. The physical properties of these compounds have been investigated experimentally and theoretically. The $AB'_xB''_{1-x}O_3$ solid solutions are of great interest from both the applied and scientific standpoints owing to their unusual electrical and mechanical properties [1–3], as well as to the interesting phenomena revealed in these compounds that have not been observed earlier in oxides with a perovskite structure [4, 5]. Among the large number of $AB'_xB''_{1-x}O_3$ solid solutions, it is possible to distinguish an important class of so-called heterovalent alloys, i.e., solid solutions with *B*' and *B*'' elements belonging to different groups of the periodic table.

The solid solutions $PbSc_{1/2}Ta_{1/2}O_3$ (*PST*) and $PbSc_{1/2}Nb_{1/2}O_3$ (*PSN*), which belong to this class of compounds, have been intensively studied both experimentally and theoretically [6–10]. In particular, these compounds undergo phase transitions due to the ordering of *B*' and *B*'' cations; in this case, the degree of ordering depends on the cooling rate [6]. In turn, the physical properties of these solid solutions (for example, the ferroelectric phase transition and its attendant anomalies observed in the electrical and mechanical properties) substantially depend on the degree of ordering of the *B* cations [1, 5].

The phase transitions associated with the Sc^{3+}–$Nb^{5+}(Ta^{5+})$ ordering have been investigated theoretically by a number of researchers [7–10]. Bellaiche and Vanderbilt [7] studied an electrostatic model of atomic ordering with allowance made only for the Coulomb interactions of excess (as compared to the average charge $q = +4$) charges $\Delta q = \pm 1$ localized at sites of a simple cubic lattice. The authors of [7] established that, within the model under consideration, the structure with Sc^{3+}–$Nb^{5+}(Ta^{5+})$ ordering along the [111] spatial diagonal of the perovskite cell is energetically most favorable, which corresponds to the experimentally observed type of ordering. A somewhat changed electrostatic model that accounts for the probability of *B* cations jumping over the sites of the crystal lattice was investigated by Gao *et al.* [8] using the Monte Carlo method with the interaction constant serving as an adjustable parameter.

Burton and Cohen [9] considered *B* cation ordering in the $PbSc_{1/2}Ta_{1/2}O_3$ compound within the cluster approximation. In this case, the interaction constants involved in the model Hamiltonian describing the cation ordering were obtained from the *ab initio* calculation of the energy of the crystal within the so-called potential-induced breathing (PIB) model, i.e., within the model of an ionic crystal with a spherical deformability of the ions. However, it is known that, in oxide compounds, the dipole and quadrupole distortions of the electron density have a substantial effect on the static and dynamic properties.

In this work, we investigated the phase transitions occurring in the $PbSc_{1/2}Nb_{1/2}O_3$ and $PbSc_{1/2}Ta_{1/2}O_3$ solid solutions due to the ordering of scandium and niobium (tantalum) ions. For this purpose, we performed *ab initio* calculations within the ionic crystal model taking into account the dipole and quadrupole polarizabilities and the deformability of the ions. Then, we introduced a model Hamiltonian describing a phase transition of the order–disorder type in the system of a binary

alloy (B'/B''). The parameters of the model Hamiltonian accounting for the interactions within three coordination shells were determined by calculating the total energy of the crystal in different ordered phases. The temperatures of the phase transitions were calculated using the Monte Carlo method in the mean-field and cluster approximations with the obtained parameters of the model Hamiltonian.

2. The phase transitions occurring in $AB'B''O_3$ solid solutions due to the ordering of B cations will be described using a model Hamiltonian accounting for only those degrees of freedom that are associated with the positional disorder of scandium and niobium (tantalum) atoms located at sites of the crystal lattice (the position b in the space group O_h^1). In this case, the problem of B cation ordering in the $AB'B''O_3$ solid solution is equivalent to the problem of ordering in a binary alloy. Hence, we can use a model based on the assumption that the atoms involved in the solid solution are located at sites of a rigid crystal lattice [11]. Therefore, the configuration energy of the solid solution can be represented as the sum of all pair atomic interaction potentials. Within this model, the Hamiltonian of the system can be written in the form

$$H = \frac{1}{2}\sum_{k,j}[v_{B'B'}(\mathbf{r}_k, \mathbf{r}_j)n_k^{B'}n_j^{B'} + v_{B''B''}(\mathbf{r}_k, \mathbf{r}_j)n_k^{B''}n_j^{B''} + 2v_{B'B''}(\mathbf{r}_k, \mathbf{r}_j)n_k^{B'}n_j^{B''}] - \sum_j [n_j^{B'}\mu_{B'}(\mathbf{r}_j) + n_j^{B''}\mu_{B''}(\mathbf{r}_j)], \quad (1)$$

where $v_{B'B'}$, $v_{B''B''}$, and $v_{B'B''}$ are the pair interaction potentials of the B' atoms, the B'' atoms, and the B' and B'' atoms, respectively, which are located at lattice sites described by the vectors $\mathbf{r}_k$ and $\mathbf{r}_j$; and $\mu_{B'}$ and $\mu_{B''}$ are the chemical potentials of the B' and B'' cations, respectively. The quantities $n_j^{B'}$ and $n_j^{B''}$ are random functions determined as follows: if the jth site is occupied by the B' atom, we have $n_j^{B'} = 1$ and $n_j^{B''} = 0$; and, if the jth site is occupied by the B'' atom, we have $n_j^{B'} = 0$ and $n_j^{B''} = 1$. The quantities $n_j^{B'}$ and $n_j^{B''}$ are related by the expression $n_j^{B'} + n_j^{B''} = 1$.

Taking into account this relationship, expression (1) can be rewritten in the following form [11]:

$$H = \frac{1}{2}\sum_{k,j} v(\mathbf{r}_k, \mathbf{r}_j)n_k^{B'}n_j^{B''} - \mu\sum_j n_j^{B'} + H_0, \quad (2)$$

where

$$v(\mathbf{r}_k, \mathbf{r}_j) = v_{B'B'}(\mathbf{r}_k, \mathbf{r}_j) + v_{B''B''}(\mathbf{r}_k, \mathbf{r}_j) - 2v_{B'B''}(\mathbf{r}_k, \mathbf{r}_j)$$

is the effective interaction constant,

$$\mu = \mu_{B'}(\mathbf{r}_j) - \mu_{B''}(\mathbf{r}_j) + \sum_{i,k}(v_{B'B'}(\mathbf{r}_k, \mathbf{r}_j) - v_{B''B''}(\mathbf{r}_k, \mathbf{r}_j))$$

is the chemical potential of the system, and H_0 is the energy independent of the arrangement of the B' and B'' ions (this energy can be taken as the origin).

For the binary alloy considered in our case, in which the concentration of both components is equal to 1/2, relationship (2) can be written in the equivalent form through the Pauli matrices $\sigma_i^z = \pm 1$:

$$H = \sum_{i \neq j} J_{ij}\sigma_i^z\sigma_j^z. \quad (3)$$

The effective interaction constants can be obtained from the *ab initio* calculation of the total energy of the crystal within the Gordon–Kim model taking into account the dipole and quadrupole polarizabilities of the ions [12, 13]. The expression for the total energy has the form

$$E_{\text{total}} = E_s + E_p + E_q + E_{pq} + E_{\text{self}}, \quad (4)$$

where

$$E_s = -\frac{1}{2}\sum_{i,j=1}^{N_a} Z_i C_{ij}^{(0)} Z_j + \sum_{i,j=1}^{N_a} \Phi_{ij}^{(00)}(V_i, V_j, |\mathbf{R}_i - \mathbf{R}_j|), \quad (5)$$

$$E_p = \frac{1}{2}\sum_{i,j=1}^{N_a}\sum_{\alpha,\beta=1}^{3} P_i^\alpha\left(\frac{\delta_{ij}}{\alpha_i^p(V_i)} + \Phi_{ij,\alpha\beta}^{(11)}(V_i, V_j, |\mathbf{R}_i - \mathbf{R}_j|) - C_{ij,\alpha\beta}^{(2)}\right)P_j^\beta \quad (6)$$

$$+ \sum_{i,j=1}^{N_a}\sum_{\alpha=1}^{3} P_i^\alpha(\Phi_{ij,\alpha}^{(10)}(V_i, V_j, |\mathbf{R}_i - \mathbf{R}_j|) - C_{ij,\alpha}^{(1)}Z_j),$$

$$E_{pq} = \frac{1}{2}\sum_{i,j=1}^{N_a}\sum_{\alpha,\beta,\gamma,\delta=1}^{3} q_i^{\alpha\beta}\left[\frac{\delta_{ij}}{\alpha_i^q(V_i)} - \frac{1}{36}(\Phi_{ij,\alpha\beta\gamma\delta}^{(22)}(V_i, V_j, |\mathbf{R}_i - \mathbf{R}_j|) - C_{ij,\alpha\beta\gamma\delta}^{(4)})\right]q^{\gamma\delta} \quad (7)$$

$$- \frac{1}{6}\sum_{i,j=1}^{N_a}\sum_{\alpha,\beta=1}^{3} q_i^{\alpha\beta}(\Phi_{ij,\alpha\beta}^{(20)}(V_i, V_j, |\mathbf{R}_i - \mathbf{R}_j|) - C_{ij,\alpha\beta}^{(2)}Z_j),$$

$$E_q = -\frac{1}{6}\sum_{i,j=1}^{N_a}\sum_{\alpha,\beta,\gamma=1}^{3} q_i^{\alpha\beta}(\Phi_{ij,\alpha\beta\gamma}^{(21)}(V_i, V_j, |\mathbf{R}_i - \mathbf{R}_j|) - C_{ij,\alpha\beta\gamma}^{(3)})P_j^{\gamma}. \quad (8)$$

Here, E_s is the energy of interaction of the spherically symmetric ions; E_p, E_q, and E_{pq} are the energies of interaction of the dipole and quadrupole moments; $E_{\text{self}} = \sum_{i=1}^{N_a} E_i^{\text{ion}}$ is the self-energy energy of the ions; $C_{ij}^{(n)} = \nabla^n \frac{1}{|\mathbf{R}_i - \mathbf{R}_j|}$ is the long-range part of the interactions, which is calculated by the Ewald method; $\Phi_{ij,\alpha\beta\gamma}^{(mn)}(V_i, V_j, |\mathbf{R}_i - \mathbf{R}_j|)$ is the short-range part of the interactions; and $P_i^{\alpha}(q_i^{\alpha\beta})$ are the dipole (quadrupole) moments of the ions, which are calculated from the minimum condition of the total energy of the crystal [13].

In order to determine the energy of the crystal in the disordered phase, we use the virtual crystal approximation. In this approximation, the short-range part of the pair interactions of the virtual ion $\langle B\rangle$ with other ions (i) has the form

$$\Phi_{iB}^{ll'} = \frac{1}{2}\Phi_{iB'}^{ll'} + \frac{1}{2}\Phi_{iB''}^{ll'}. \quad (9)$$

The contribution of the virtual ion to the self-energy energy is given by the formula

$$E_B^{\text{ion}} = \frac{1}{2}E_{B'}^{\text{ion}} + \frac{1}{2}E_{B''}^{\text{ion}}. \quad (10)$$

The dipole and quadrupole polarizabilities of the virtual ion B are defined as

$$\alpha_B^{d,q} = \frac{1}{2}\alpha_{B'}^{d,q} + \frac{1}{2}\alpha_{B''}^{d,q}. \quad (11)$$

In the calculation of the long-range Coulomb contributions, the charge of the virtual ion B is determined as follows:

$$Z_B = \frac{1}{2}Z_{B'} + \frac{1}{2}Z_{B''}. \quad (12)$$

3. Using the model Hamiltonian, we restrict our consideration to the special case of interactions within three coordination shells. In order to obtain the effective interaction constants, we calculate the energies of several structures with different degrees of ordering of the B' and B'' ions. We consider only ordered structures with a perovskite cell volume enlarged by a factor of 8 (Fig. 1). The first column in Table 1 presents the configuration motif of the ordered structures with the notation taken from the paper by Burton and Cohen [9], who carried out a similar calculation for the $PbSc_{1/2}Ta_{1/2}O_3$ solid solution. The second column in this table lists the lattice parameters of the ordered structures. The calculated energies E_i per formula unit ABO_3 are given in columns 3 and 4 for the *PSN* and *PST* solid solutions, respectively:

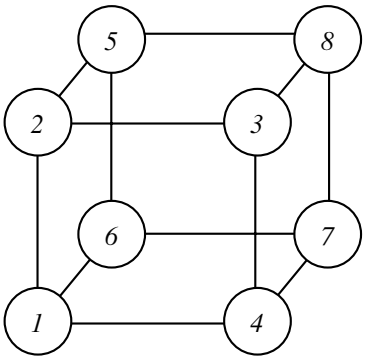

Fig. 1. Perovskite cell enlarged by a factor of 8 (only the B cations are shown).

$$E_i = E_{\text{total}} - E_{\text{self}} - E_0. \quad (13)$$

Here, E_{total} is the total energy of the crystal, E_{self} is the self-energy energy of the ions [see relationship (4)], and E_0 is the energy independent of the arrangement of the B' and B'' ions, which is equal to –161.455721 eV for the *PSN* solid solution and –157.692153 eV for the *PST* solid solution.

In column 5 in Table 1, the energies of the ordered structures are expressed through the effective interaction constants involved in expression (3). It should be noted that, since the model Hamiltonian accounts only for the degrees of freedom associated with the positional disorder of the B' and B'' ions, the effective interaction constants are calculated in terms of the energies of the unrelaxed structures.

The calculated effective interaction constants are presented in Table 2. It can be seen from this table that the effective interaction constants J_1, J_2, and J_3 have the same sign and correspond to the attraction of the scandium and niobium (tantalum) ions in the first, second, and third coordination shells. Therefore, we are dealing here with competition between antiferromagnetic interactions. It is known that, in this case, the mean-field approximation leads to substantially incorrect numerical values of the phase transition temperature. Actually, in the mean-field approximation, the phase transition temperature is given by the expression

$$T_c^{\text{mf}} = \frac{6J_1 - 12J_2 + 8J_3}{k_B}. \quad (14)$$

The calculated values of the phase transition temperature T_c^{mf} are listed in Table 3. As can be seen from this table, the calculated temperatures T_c^{mf} exceed the experimental values by a factor of more than 3. Such a large difference between the calculated and experimentally obtained temperatures of the phase transition is associated with the fact that, in the system with compet-

Table 1. Energies of ordered structures of the $PbSc_{1/2}Ta_{1/2}O_3$ and $PbSc_{1/2}Nb_{1/2}O_3$ solid solutions

Configuration {*I J K L*} {*M N O P*} (*B*' = +1, *B*" = –1)	Lattice parameters	Calculated energies, E_i, eV		Energies expressed through the effective interaction constants J_i
		PSN (a_0 = 3.95 Å)	*PST* (a_0 = 4.01 Å)	
1	2	3	4	5
{–1 1 –1 1} {1 –1 1 –1} (*B*'*B*" along the [111] direction)	$a = b = c = 2a_0$	–0.399357	–0.448150	$-6J_1 + 12J_2 - 8J_3$
{–1 1 –1 –1} {1 1 1 –1}	$a = b = c = 2a_0$	–0.193832	–0.292024	$-8J_3$
{1 1 1 1} {–1 –1 –1 –1} (*B*'*B*" along the [100] direction)	$a = b = a_0$, $c = 2a_0$	–0.125324	–0.239982	$2J_1 - 4J_2 - 8J_3$
{1 –1 1 –1} {1 –1 1 –1} (*B*'*B*" along the [110] direction)	$a = b = \sqrt{2}a_0$, $c = a_0$	–0.349156	–0.378210	$-2J_1 4J_2 + 8J_3$
{–1 –1 –1 1} {1 1 1 –1}	$a = b = c = 2a_0$	–0.305748	–0.361138	$-2J_1$
{1 –1 –1 –1} {1 1 1 –1}	$a = b = c = 2a_0$	–0.237239	–0.309096	$-4J_2$
{1 1 1 1} {1 1 1 1}+ {–1 –1 –1 –1} {–1 –1 –1 –1}	$a = b = a_0$, $c = 4a_0$	0.848736	1.031372	$4J_1 + 4J_2$

ing interactions, an important role is played by the short-range correlations, which are ignored in the mean-field approximation. It is known that these correlations can be taken into account in another version of the self-consistent field approximation, the so-called cluster approximation [14, 15].

4. The algorithm employed in the cluster field method was described in detail by Vaks *et al.* [14, 15]. We will use this method for calculating the temperatures of the phase transition in the *PSN* and *PST* solid solutions. In the cluster field method, the crystal lattice whose sites are occupied by ordering atoms is separated into clusters containing some number of "spins" and the relationships between the cluster fields are established.

In our case, we deal with antiferromagnetic interactions. Therefore, we can separate the crystal lattice into two sublattices, namely, the *A* and *B* sublattices, in such a way that, in the ordered state with the lowest energy, the scandium ions will occupy sites of the *A* sublattice ($\sigma_A^z = +1$, spins *1*, *3*, *5*, *7* in Fig. 1), whereas the niobium ions will be located at sites of the *B* sublattice ($\sigma_B^z = -1$, spins *2*, *4*, *6*, *8* in Fig. 1). For the interactions occurring within three coordination shells, there exist six cluster fields, namely, ϕ_1, ϕ_2, ϕ_3, ψ_1, ψ_2, and ψ_3 (where ϕ and ψ are the cluster fields acting on the spins of the *A* and *B* sublattices, respectively).

Table 2. Calculated effective interaction constants

Crystal	Effective interaction constants, eV		
	J_1	J_2	J_3
PSN	0.152874	0.0593099	0.024229
PST	0.180569	0.077274	0.036503

In order to obtain relationships between the cluster fields, we separate the crystal lattice into six clusters (see Fig. 1): an eight-particle cluster containing spins *1–8*; two seven-particle clusters, namely, the 7_a cluster containing spins *1–7* and the 7_b cluster containing spins *1–6*, *8*; a six-particle cluster containing spins *1–6*; and two five-particle clusters, namely, the 5_a cluster containing spins *1–5* and the 5_b cluster containing spins *1–4*, *6*. As a result, the free energy can be written in the form

$$\beta D = \frac{11}{4}\ln Z_8 - \frac{5}{2}\ln Z_{7a} - \frac{5}{2}\ln Z_{7b} - 3\ln Z_6 + 3\ln Z_{5a} + 3\ln Z_{5b}, \quad (15)$$

where $\beta = \frac{1}{kT}$, $Z_i = \mathrm{Sp}\{\exp(-\beta H_i)\}$ are the corresponding cluster partition functions, and H_i is the cluster

Hamiltonian. For brevity, we present explicit expressions only for the cluster Hamiltonian H_i; that is,

$$\begin{aligned}H_8 &= J_1(\sigma_1(\sigma_2+\sigma_4+\sigma_6)+\sigma_3(\sigma_2+\sigma_4+\sigma_8)\\ &+\sigma_5(\sigma_2+\sigma_6+\sigma_8)+\sigma_7(\sigma_4+\sigma_6+\sigma_8))\\ &+J_2(\sigma_1\sigma_3+\sigma_1\sigma_5+\sigma_1\sigma_7+\sigma_2\sigma_8+\sigma_2\sigma_4+\sigma_2\sigma_6\\ &+\sigma_3\sigma_5+\sigma_3\sigma_7+\sigma_4\sigma_6+\sigma_4\sigma_8+\sigma_5\sigma_7+\sigma_6\sigma_8)\\ &+J_3(\sigma_1\sigma_8+\sigma_2\sigma_7+\sigma_4\sigma_5+\sigma_3\sigma_6)\\ &+(3\phi_1+9\phi_2+7\phi_3)(\sigma_1+\sigma_3+\sigma_5+\sigma_7)\\ &+(3\psi_1+9\psi_2+7\psi_3)(\sigma_2+\sigma_4+\sigma_6+\sigma_8),\end{aligned} \quad (16)$$

$$\begin{aligned}H_{7a} &= J_1(\sigma_1(\sigma_2+\sigma_4+\sigma_6)+\sigma_3(\sigma_2+\sigma_4)\\ &+\sigma_5(\sigma_2+\sigma_6)+\sigma_7(\sigma_4+\sigma_6))\\ &+J_2(\sigma_1\sigma_3+\sigma_1\sigma_5+\sigma_1\sigma_7+\sigma_2\sigma_4+\sigma_2\sigma_6\\ &+\sigma_3\sigma_5+\sigma_3\sigma_7+\sigma_4\sigma_6+\sigma_5\sigma_7)\\ &+J_3(\sigma_2\sigma_7+\sigma_4\sigma_5+\sigma_3\sigma_6)+\sigma_1(3\phi_1+9\phi_2+8\phi_3)\\ &+(\sigma_3+\sigma_5+\sigma_7)(4\phi_1+9\phi_2+7\phi_3)\\ &+(\sigma_2+\sigma_4+\sigma_6)(3\psi_1+10\psi_2+7\psi_3),\end{aligned} \quad (17)$$

$$\begin{aligned}H_6 &= J_1(\sigma_1(\sigma_2+\sigma_4+\sigma_6)+\sigma_3(\sigma_2+\sigma_4)\\ &+\sigma_5(\sigma_2+\sigma_6))\\ &+J_2(\sigma_1(\sigma_3+\sigma_5)+\sigma_2\sigma_4+\sigma_2\sigma_6+\sigma_3\sigma_5+\sigma_4\sigma_6)\\ &+J_3(\sigma_4\sigma_5+\sigma_3\sigma_6)+\sigma_1(3\phi_1+10\phi_2+8\phi_3)\\ &+(\sigma_3+\sigma_5)(4\phi_1+10\phi_2+7\phi_3)\\ &+\sigma_2(3\psi_1+10\psi_2+8\psi_3)\\ &+(\sigma_4+\sigma_6)(4\psi_1+10\psi_2+7\psi_3),\end{aligned} \quad (18)$$

$$\begin{aligned}H_{5a} &= J_1(\sigma_1(\sigma_2+\sigma_4)+\sigma_3(\sigma_2+\sigma_4)+\sigma_5\sigma_2)\\ &+J_2(\sigma_1(\sigma_3+\sigma_5)+\sigma_2\sigma_4+\sigma_3\sigma_5)\\ &+J_3\sigma_4\sigma_5+(\sigma_1+\sigma_3)(4\phi_1+10\phi_2+8\phi_3)\\ &+\sigma_5(5\phi_1+10\phi_2+7\phi_3)+\sigma_2(3\psi_1+11\psi_2+8\psi_3)\\ &+\sigma_4(4\psi_1+11\psi_2+7\psi_3).\end{aligned} \quad (19)$$

The expressions for H_{7b} and H_{5b} can be obtained from relationships (17) and (19) with the changes $\phi_i \longleftrightarrow \psi_i$, $\sigma_1 \longleftrightarrow \sigma_2$, $\sigma_3 \longleftrightarrow \sigma_4$, $\sigma_5 \longleftrightarrow \sigma_6$, and $\sigma_7 \longleftrightarrow \sigma_8$.

The cluster fields ϕ_i and ψ_i can be found from the variational condition

$$\partial F/\partial\phi_1 = \partial F/\partial\psi_i = 0, \quad (20)$$

which, in this case, leads to a system of six equations.

The temperature of the phase transition due to the *B* cation ordering can be calculated from expression (20).

Table 3. Calculated and experimental temperatures of the phase transition due to the *B* cation ordering (in degrees Kelvin)

Crystal	T_c^{mf}	T_c^{cl}	T_c^{mc}	T_c^{exp}
PSN	4630	2250	1810	1480
PST	5200	2400	1920	1770

Note: mf is the mean-field approximation, cl is the cluster approximation, mc is the Monte Carlo method, and exp is the experimental data [6].

For this purpose, expression (20) is expanded in powers of ϕ_i and ψ_i up to linear terms and the determinant composed of the coefficients of the cluster fields ϕ_i and ψ_i is taken equal to zero.

Using the effective interaction constants J_1, J_2, and J_3 presented in Table 2, we can determine the temperature of the phase transition (Table 3). As can be seen from Table 3, the obtained temperatures of the phase transition are substantially less than the phase transition temperature T_c^{mf} calculated in the mean-field approximation. It should be noted that, within a simple Ising model, in which competing interactions are disregarded, the phase transition temperatures calculated using the cluster field method do not differ greatly from those obtained in the mean-field approximation [15].

Thus, the partial inclusion of the short-range correlations associated with the competition of the interactions leads to a considerable decrease in the critical temperatures (as compared to those obtained in the mean-field approximation) of the phase transitions due to the cation ordering in the *PSN* and *PST* solid solutions. However, the phase transition temperatures T_c^{cl} obtained in the framework of the cluster field method are appreciably higher than the experimental values.

5. For a more complete inclusion of the correlation effects in the description of the phase transition caused by the *B* cation ordering, we used the numerical Monte Carlo method, which has been successfully applied in the investigation of the phase transitions in different systems, including those observed in ordering alloys [16, 17].

We examined crystal lattices $12\times12\times12$, $18\times18\times18$, and $30\times30\times30$ in size with periodic boundary conditions. The first 10 000 steps for each temperature were rejected and disregarded in the averaging. The average values of the energies, order parameters, and heat capacities were calculated in two stages. After 50 steps, we determined the group averages and, then, carried out the averaging over 500 groups.

The temperature dependences of the heat capacity and those of the short-range order parameter and long-range order parameter for the $PbSc_{1/2}Nb_{1/2}O_3$ and $PbSc_{1/2}Ta_{1/2}O_3$ solid solutions with a $30\times30\times30$ lat-

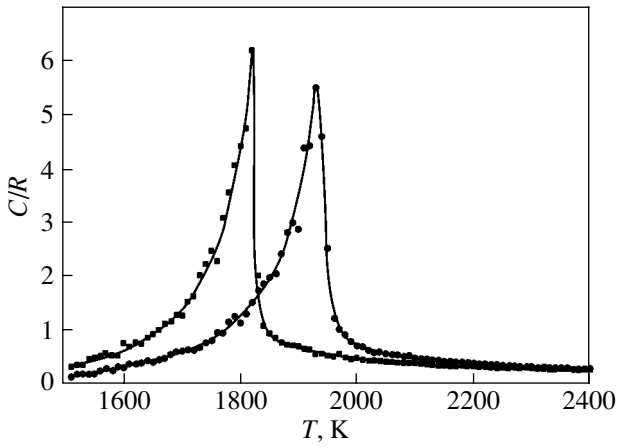

Fig. 2. Temperature dependences of the excess heat capacity due to the ordering of the *B* cations in the *PSN* (squares) and *PST* (circles) solid solutions.

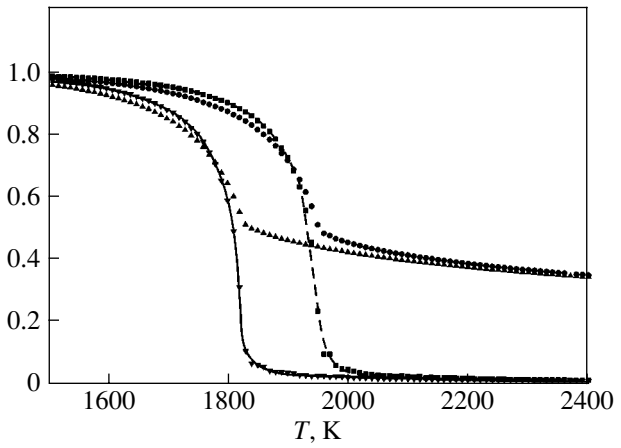

Fig. 3. Temperature dependences of the long-range order parameter for the *PSN* (solid line) and *PST* (dashed line) solid solutions and the short-range order parameter for the *PSN* (triangles) and *PST* (circles) solid solutions.

tice are shown in Figs. 2 and 3, respectively. It should be noted that the size of the lattice does not affect the temperature of the phase transition or the temperature dependences of the order parameters. As the size of the lattice increases, the peak of the heat capacity becomes sharper. The calculated temperatures of the phase transitions are listed in Table 3. These temperatures are in agreement with the experimental data.

6. Thus, the temperatures of the phase transitions associated with the cation ordering in the $PbSc_{1/2}Nb_{1/2}O_3$ and $PbSc_{1/2}Ta_{1/2}O_3$ solid solutions were calculated using the model Hamiltonian within the ionic crystal model accounting for the dipole and quadrupole distortions of the electron density and the deformability of the ions. It was established that the effective interactions between ordering cations exhibit a competitive nature. The temperatures of the phase transition due to the cation ordering, which were calculated in the framework of the cluster approximation and the Monte Carlo method, are in reasonable agreement with the experimental values.

ACKNOWLEDGMENTS

This work was supported by the Russian Foundation for Basic Research (project no. 03-02-16076) and the Council on Grants from the President of the Russian Federation (grant no. NSh-939-2003.2).

REFERENCES

1. L. E. Cross, Ferroelectrics **76**, 241 (1987).
2. R. F. Service, Science (Washington) **275**, 1878 (1997).
3. S.-E. Park and T. R. Shrout, J. Appl. Phys. **82**, 1804 (1997).
4. B. Noheda, J. A. Gonzalo, L. E. Cross, R. Guo, S.-E. Park, D. E. Cox, and G. Shirane, Phys. Rev. B: Condens. Matter **61** (13), 8687 (2000).
5. N. Setter and L. E. Cross, J. Appl. Phys. **51**, 4356 (1980).
6. C. G. F. Stenger and A. J. Burggraaf, Phys. Status Solidi A **61**, 275 (1980).
7. L. Bellaiche and David Vanderbilt, Phys. Rev. Lett. **81** (6), 1318 (1998).
8. X. S. Gao, J. Lim, J. M. Xue, J.-S. Wang, J.-M. Liu, and J. Wang, J. Phys.: Condens. Matter **14**, 8639 (2002).
9. B. P. Burton and R. E. Cohen, Ferroelectrics **151** (1–4), 331 (1994).
10. B. P. Burton and R. E. Cohen, Ferroelectrics **164** (1–3), 201 (1995).
11. A. G. Khachaturyan, *Theory of Structural Transformations in Solids* (Nauka, Moscow, 1974; Wiley, New York, 1983).
12. O. V. Ivanov, D. A. Shport, and E. G. Maksimov, Zh. Éksp. Teor. Fiz. **114**, 33 (1998) [JETP **87**, 186 (1998)].
13. V. I. Zinenko, N. G. Zamkova, and S. N. Sofronova, Zh. Éksp. Teor. Fiz. **123** (4), 846 (2003) [JETP **96**, 747 (2003)].
14. V. G. Vaks and V. G. Orlov, J. Phys. F: Met. Phys. **18**, 883 (1988).
15. V. G. Vaks and V. I. Zinenko, J. Phys. C: Solid State Phys. **19**, 3083 (1986).
16. *Monte Carlo Methods in Statistical Physics*, Ed. by K. Binder (Springer, Berlin, 1979).
17. L. Guttman, J. Chem. Phys. **34** (3), 1024 (1961).

Translated by O. Moskalev

Physics of the Solid State, Vol. 47, No. 12, 2005, pp. 2315–2320. Translated from Fizika Tverdogo Tela, Vol. 47, No. 12, 2005, pp. 2223–2227.

LATTICE DYNAMICS AND PHASE TRANSITIONS

Thermodynamics of the γ–α Transformation of Cerium

L. N. Dzhavadov

Vereshchagin Institute of High-Pressure Physics, Russian Academy of Sciences, Troitsk, Moscow oblast, 142190 Russia

e-mail: dzhavadov@hppi.troitsk.ru

Received February 4, 2005

Abstract—The thermodynamic functions for cerium in the vicinity of the isomorphous γ–α phase transformation are calculated from the results of adiabatic experiments. The experimental data are approximated within a modified model of a binary solution. This model is fitted to the experimental results. The behavior of the thermodynamic functions in the ranges of temperatures and pressures covering the γ–α phase transformation is actually characteristic of a critical point of the liquid–vapor type. The critical exponent for the density is found to be $\beta = 0.46$. The other exponents are virtually identical to those obtained in the framework of the classical models describing the thermodynamic functions in the vicinity of the critical point. © *2005 Pleiades Publishing, Inc.*

1. INTRODUCTION

The abnormal behavior of a cerium volume under compression was noted earlier by Bridgmam [1]. Subsequently, Lawson and Ting Yuang Tang [2] established using x-ray diffraction analysis that the crystal structure of the high-pressure cerium phase has a face-centered cubic lattice; i.e., this phase is structurally identical to the low-temperature modification α-Ce under normal atmospheric pressure. A few years later, Likhter *et al.* [3] found that the volume effect of the phase transformation decreases with increasing temperature. Ponyatovskiĭ [4] revealed that an increase in the temperature leads to a decrease in the thermal effect of the phase transformation to the point of disappearance at $T > 550$ K. The author of [4] analyzed the above data in combination with the behavior of the volume effect and assumed that a critical point of the liquid–vapor type should lie in the phase diagram on a line corresponding to the γ–α phase transformation. It is believed that the first-order transformation of the γ phase into the α phase of cerium is the electronic transition between the valence 4*f* states and the conduction band. The specific features of the isomorphous γ–α phase transformation, including a minimum in the melting line, have long attracted considerable research attention (see, for example, [5]).

The results of measuring the change in the temperature of cerium due to the adiabatic variation in the pressure in the ranges of temperatures and pressures covering the γ–α phase transformation of cerium were reported earlier in [6]. Under the condition $S = \text{const}$ at a small value of ΔP, these results allow one to determine the derivative $(\partial T/\partial P)_S$ from the following expression:

$$J_S \equiv \left(\frac{\partial T}{\partial P}\right)_S = \lim\left(\frac{\Delta T}{\Delta P}\right)_{S,\,\Delta P \to 0}.$$

With knowledge of the quantity $J_S(T, P)$ as a function of the temperature and pressure, we can directly calculate not only the family of isentropes but also, under known boundary conditions [for example, $S(T, 0)$], the function $S(T, P)$ and, consequently, the temperature and pressure dependences of the heat capacity C_P and the thermal expansion $(\partial V/\partial T)_P$ [7]. In the case of cerium, the occurrence of a first-order phase transition requires that the boundary conditions be also specified along the transformation line because the entropy undergoes a jump. Similar estimates were made in [6]. It was found that the obtained family of isentropes is actually characteristic of the critical point. However, the assumptions used to specify the boundary conditions along the transformation line, as well as the necessity of knowing the derivative $(\partial T/\partial P)_S$ at each point in the pressure and temperature ranges under consideration (which implies interpolation), made calculations of the thermodynamic functions impossible.

In this work, prior to calculating the thermodynamic function for cerium from the results of the adiabatic experiments, we determined the Gibbs potential $G(T, P)$ for the system under consideration. The criterion for choosing the potential, specifically, the function $J_S(T, P)$, which follows from this potential, must be in satisfactory agreement with the experimental data. Within this approach, the studied system can be completely described using the function $J_S(T_i, P_i)$ obtained from the adiabatic experiments and the following five parameters: the entropy, the volume, and the bulk modulus under normal pressure, i.e., $S(298, 0)$, $V(298, 0)$, and $K_T(298, 0)$, respectively; the volume jump at room temperature $\Delta V_{tr}(298)$; and the bulk modulus $K_T(298, P)$ at a pressure P away from the $\gamma \longleftrightarrow \alpha$ phase transformation.

1063-7834/05/4712-2315$26.00

According to Aptekar' and Ponyatovskiĭ [8], who used the mean-field model [9], cerium can be considered a binary regular pseudosolution (Ce^{3+}–Ce^{4+}). In this case, the thermodynamic potential can be written in the form

$$G(T, P, x) = (1-x)G_1(T, P) + xG_2(T, P) + RT[x\ln x + (1-x)\ln(1-x)] + x(1-x)U. \quad (1)$$

Here, $G_1(T, P)$ and $G_2(T, P)$ are the Gibbs potentials for the pure components, x is the phase concentration, and U is a quantity determining the energy of mixing.

Under the assumption that the differences between the internal energies ($E_1 - E_2$), entropies ($S_1 - S_2$), and volumes ($V_1 - V_2$) of the pure components are constant and independent of the temperature and pressure and that the quantity U is also constant and independent of the concentration, Aptekar' and Ponyatovskiĭ [8] offered a satisfactory description for the specific features of the thermodynamic functions. Based on the obtained P–T dependence of the concentration and, hence, the P–T dependences of the heat capacity C_p, thermal expansion β, and compressibility χ, those authors demonstrated that the behavior of these quantities is actually characteristic of the critical point. However, this model is quantitatively inconsistent with a number of experimental data, including the later results of adiabatic experiments [6], which, in my opinion, most thoroughly describe the thermodynamic functions (obtained by one method) in the vicinity of the phase transformation under investigation. This is not surprising even if the Strässler–Kittel model were to be used, because the ranges of temperatures and pressures studied in [6] are sufficiently wide. Therefore, one of the reasons for this discrepancy can be associated with the fact that the above differences between the thermodynamic functions for the pure phases cannot, under any circumstances, be considered to be constant.

Table 1. Data available in the literature on the properties of cerium

$S(298, 0) = 57.78$ J/(mol K)	[10]
$V(298, 0) = 20.68$ cm^3/mol	[10]
$K_T(298, 0) = 19.1$ GPa	[11]
$K_T(298, 3.0) = 35.5$ GPa	[11]
$\Delta V_{tr}(298) = 2.688$ cm^3/mol	[12]
K' (γ phase) = K' (α phase) = 4*	[13]

* According to Frantsevich *et al*. [13], the derivative of the bulk modulus with respect to the pressure for simple substances lies in the range 3–5.

Table 2. Parameters obtained for pure phases of cerium in the standard state

Phase	V, cm^3/mol	Θ, K	$\gamma(1)$	K_0, GPa	G_0, J/mol
γ phase	20.75	120	0.751	21.34	0
α phase	17.36	201	1.155	24.17	2216

2. CALCULATION OF THE THERMODYNAMIC FUNCTIONS

Let us assume that expression (1) with some modifications is an appropriate trial function for describing the thermodynamic potential of the system under investigation. In our calculations, we also use a potential of form (1) for an analytical description of the function $J_S(T_i, P_i)$ obtained from the adiabatic experiments. However, in our case, unlike the approach employed in [8], the P–T dependences of the properties are taken into account for each phase and the quantity U is a function of the temperature and concentration, i.e., $U = U(T, x)$. (Note that the dependences of the properties on the pressure P, which are quite natural in the model of a solution, are not related to the case under consideration, because these dependences would lead to a curve $T_c(P)$ of critical points, which has no physical meaning; hence, these dependences are omitted.) Therefore, the above problem is reduced to the problem of determining both the parameters of the equations of state for pure phases and the form of the function $U(T, x)$. The criterion is the minimization of the root-mean-square deviation of the experimental and calculated values $J_S(T_i, P_i)$. In this statement of the problem, the model of a binary solution is fitted to the results of the experiment. However, since the function $U(T, x)$ can be chosen arbitrarily, the statement that the calculation is carried out within the model of regular solutions is incorrect.

The equations of state for each of the phases are determined under the following conditions:

(i) the pressure dependence of the isothermal bulk modulus at room temperature (T_0) is represented by the linear expansion (the Murnaghan equation)

$$K_T = -V\left(\frac{\partial P}{\partial V}\right)_T = K_0 + K'P;$$

(ii) the temperature dependence of the heat capacity C_V is described by the Debye function; and

(iii) the Grüneisen parameter is proportional to the volume

$$\gamma(v) = \gamma(1)v, \quad v = \frac{V(T, P)}{V(T_0, 0)}.$$

This means that each of the pure phases can be described by the following six parameters: the volume

$V(298, 0)$, the Debye temperature $\theta(1)$, the Grüneisen parameter $\gamma(1)$, the isothermal bulk modulus K_0, the constant K', and the standard Gibbs potential $G(298, 0)$.

As a function $U(T, x)$, we used the four-parameter relationship

$$U(T, x) = a_0\left[1 + \frac{a_1}{t} + \frac{a_2}{t^2} + \frac{a_3}{t}(x - 0.5)^2\right], \qquad (2)$$

where $t = T/298$.

The above form of the function $U(T, x)$ was obtained as follows. A set of experimental values $J_S(T_i, P_i)$ was divided into several groups belonging to different temperature ranges. For each temperature range, the quantity U was represented as a function of the concentration only: $U = b_0 + b_1(x - 0.5)^2$. The quantity U given in the form of an asymmetric second-degree polynomial did not allow us to achieve satisfactory agreement with experiment. The minimization performed at these intermediate stages made it possible to determine the temperature dependence of the coefficients b_0 and b_1.

In this representation, the Gibbs potential includes 15 parameters (the Gibbs potential of one of the phases in the standard state is taken to be equal to zero). The use of the experimental data presented in Table 1 and the values obtained for the direct and reverse phase transitions at room temperature, which were estimated from the results of the adiabatic experiments ($P_{\gamma\to\alpha}$ = 0.77 GPa, $P_{\alpha\to\gamma}$ = 0.57 GPa), made it possible to decrease the number of parameters from 15 to 6. In the case of the minimization, the calculated value $J_S(T_i, P_i)$ was determined according to the expression

$$\left(\frac{\partial T}{\partial P}\right)_S = \left(\frac{\partial^2 G}{\partial P \partial T}\right)_T \left(\frac{\partial^2 G}{\partial T^2}\right)_P^{-1}. \qquad (3)$$

The equilibrium concentration (two solutions in the hysteresis region) was determined from the equation

$$\left(\frac{\partial G(T, P, x)}{\partial x}\right)_{T, P} = 0.$$

3. RESULTS

The parameters obtained for the equation of state for pure components are presented in Table 2. The parameters of the function $U(T, x)$ are as follows: a_0 = 13.5 kJ/mol, $a_1 = -0.632$, $a_2 = 0.117$, and $a_3 = 0.39$. Figure 1 shows the function $J_S(T, P)$ describing the functions $J_S(T_i, P_i)$ obtained from experimental data in [6]. The root-mean-square deviation of the calculated and experimental values $J_S(T_i, P_i)$ was less than 8%. The number of points was ~400; the ranges of pressures and temperatures were 0–2.8 GPa and 280–650 K, respectively; and the error in the measurement of the quantity $(\partial T/\partial P)_S$ was approximately equal to 3%.

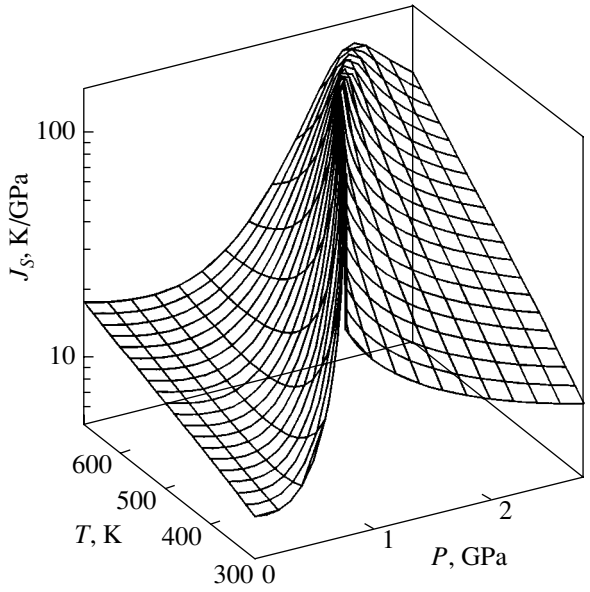

Fig. 1. P–T dependences of the derivative $J_S = (\partial T/\partial P)_S$ for the case of the α ⟶ γ phase transformation of cerium. The dependences are calculated from relationship (3) with the use of the Gibbs potential defined by relationships (1) and (2).

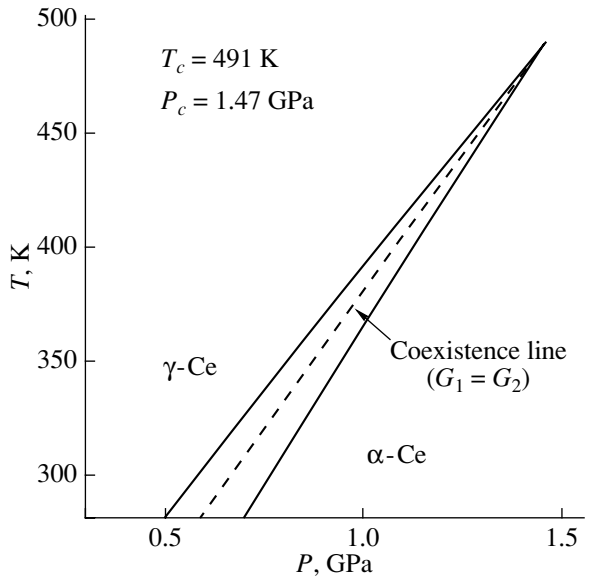

Fig. 2. Phase diagram of the γ–α phase transformation of cerium.

The phase diagram of cerium in the region of the γ ⟷ α phase transformation is depicted in Fig. 2. This phase diagram was calculated using the Gibbs potential (1) with the energy of mixing determined by function (2). Figures 3–9 present the results of the cal-

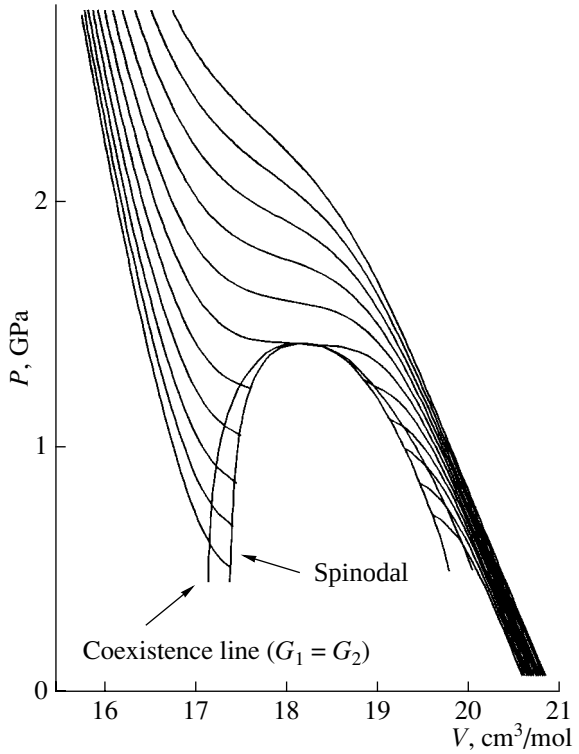

Fig. 3. Family of volume isotherms. The temperature range is 40 K.

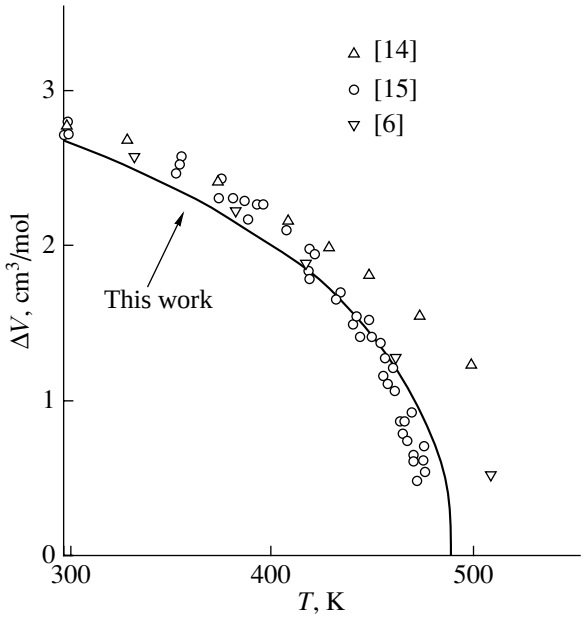

Fig. 4. Volume jump as a function of the temperature along the transformation line. The solid line represents the values of ΔV calculated for the equality between the Gibbs potentials of two phases ($G_1 = G_2$). Beecroft and Swenson [14] measured the displacement of a piston upon heating of a high-pressure cell filled with the sample. Kutsar [15] measured the linear size of the sample by varying the temperature and pressure (hydrostatics). In my earlier work [6], the corresponding data were obtained using thermobaric analysis (hydrostatics).

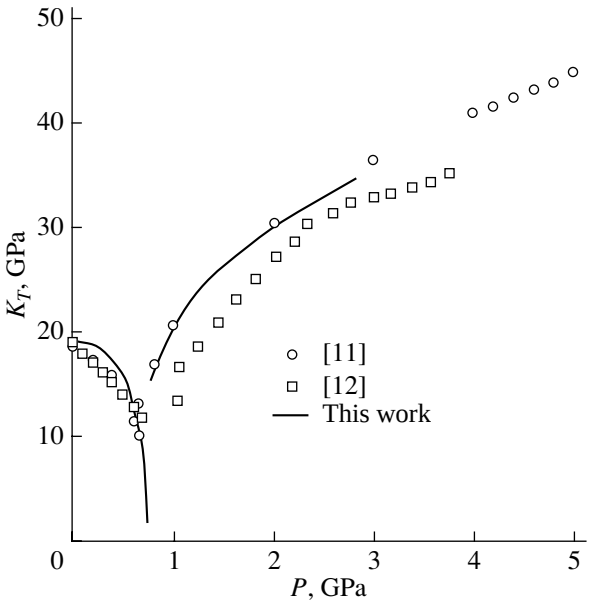

Fig. 5. Bulk modulus at room temperature. The experimental data are obtained using the ultrasonic method [11] and the piston displacement method [12].

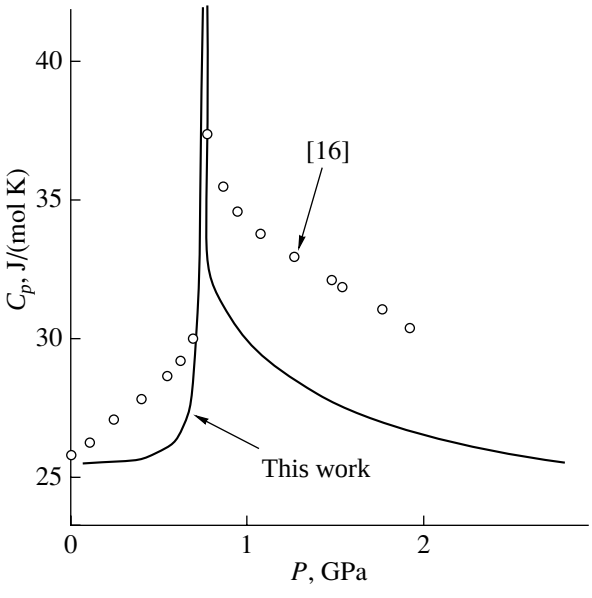

Fig. 6. Heat capacity C_p at room temperature. The experimental data on the heat capacity are obtained using the pulse method [16], i.e., Joule heating of a wire sample, and the measurement of the temperature from the electrical resistance as a function of the temperature.

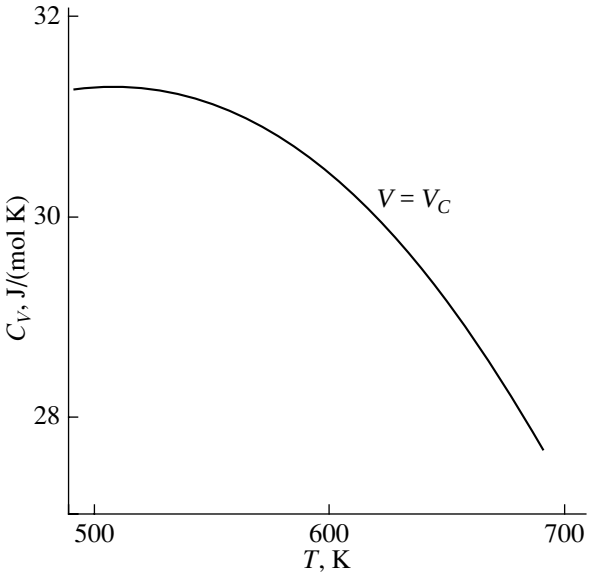

Fig. 7. Heat capacity C_V along the critical isochore ($T > T_c$).

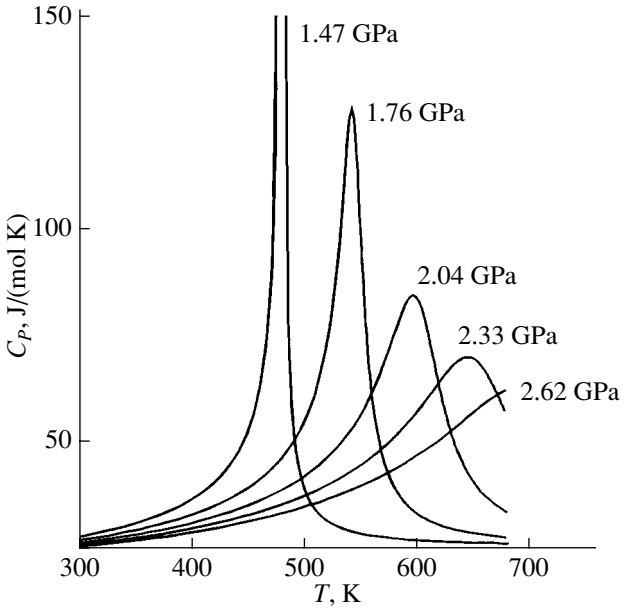

Fig. 8. Isobaric lines of the heat capacity C_p at $T \geq T_c$.

culation of thermodynamic functions, namely, the volume, the bulk modulus, the heat capacity, and the compressibility. The calculated bulk modulus and compressibility (Figs. 4, 5) are in satisfactory agreement with the experimental data [11, 12, 15].

Figure 4 shows the calculated dependence of the volume jump along the phase coexistence line in comparison with the data available in the literature. Correct estimation of the volume jump from the experimental data is complicated by the fact that the compressibility of cerium substantially increases as the line of stability loss is approached. Moreover, the phase transformation itself is "smeared" under variations in the temperature or pressure due to the fact that the coefficient of filling of the high-pressure cell, of course, differs from zero. As a consequence, the pressure in the high-pressure cell is a function of the density of the sample. This circumstance can apparently explain the spread of the experimental data in these ranges of temperatures and pressures. Buras and Niimura [17] estimated the critical jump in the density from neutron diffraction data and determined the critical exponent for the density to be equal to $\beta = 0.36$ at the following coordinates of the critical point: $T_c = 519$ K and $P_c \approx 1.5$ GPa. According to Kutsar [15], these coordinates are as follows: $T_c = 480$ K and $P_c = 1.45$ GPa.

In our case, the critical exponent for the density jump was found to be $\beta = 0.36$ at the coordinates of the critical point $T_c = 491$ K and $P_c = 1.47$ GPa. The critical volume was determined to be $V_c = 18.13$ cm^3/mol. The exponent for the heat capacity C_V along the critical isochore was $\delta = 0$ (Fig. 7). The overestimated values of the heat capacity C_V as compared to the Dulong–Petit value were obtained as a result of variations in the phase concentration along the isochore. The critical exponent α for the heat capacity C_p and the critical exponent γ for the compressibility χ along the critical isobar (P_c) were found to be equal: $\alpha = \gamma = -(0.95–1.0)$.

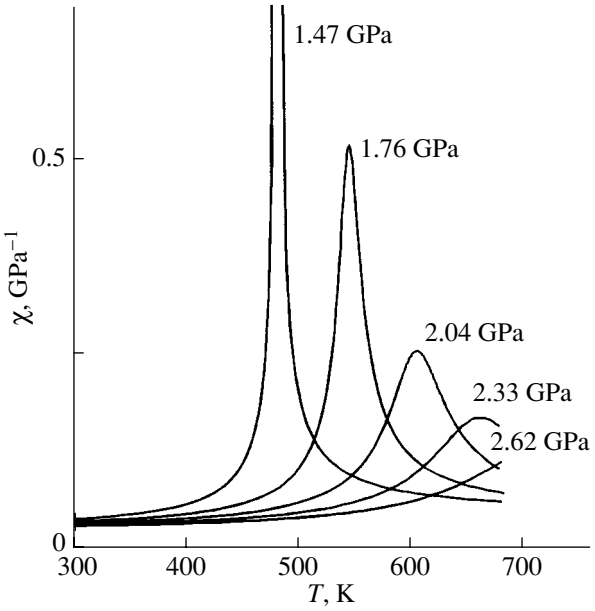

Fig. 9. Isobaric lines of the compressibility χ at $T \geq T_c$.

4. CONCLUSIONS

It can be seen from the figures presented in this paper that the thermodynamic quantities obtained from the modified trial function of form (1) or (2) are in satisfactory agreement with the experimental values in the ranges of temperatures and pressures under consideration. As should be expected, the critical exponents thus calculated do not differ significantly from those obtained within the classical models describing the thermodynamic functions in the vicinity of the critical point, because, as was mentioned previously, the trial function is defined in the mean-field model. It can also be seen from relationship (2) and Table 2 that the function $U(T, x)$, which determines the energy of mixing in the model used for a solution, increases with increasing temperature in the range from 280 to 650 K for all concentrations ($0 < x < 1$). Substantiation of the form of the function obtained and the physical meaning of the parameters involved is beyond the scope of the present paper.

ACKNOWLEDGMENTS

The author would like to thank S.M. Stishov, A.P. Kochkin, and V.N. Ryzhov for their participation in discussions of the results obtained in this study and helpful remarks.

REFERENCES

1. P. W. Bridgman, Proc. Am. Acad. Arts Sci. **62**, 207 (1927).
2. A. F. Lawson and Ting Yuang Tang, Phys. Rev. **76**, 301 (1949).
3. A. I. Likhter, Yu. N. Ryabinin, and L. F. Vereshchagin, Zh. Éksp. Teor. Fiz. **33**, 610 (1957) [Sov. Phys. JETP **6**, 469 (1957)].
4. E. G. Ponyatovskiĭ, Dokl. Akad. Nauk SSSR **120**, 1021 (1958).
5. E. Yu. Tonkov, *Phase Diagrams of the Elements at High Pressures* (Nauka, Moscow, 1979) [in Russian].
6. L. N. Dzhavadov, High Temp.–High Pressures **21**, 401 (1989).
7. L. N. Dzhavadov, Zh. Fiz. Khim. **4**, 1106 (1987).
8. I. L. Aptekar' and E. G. Ponyatovskiĭ, Fiz. Met. Metalloved. **25** (5), 777 (1968); Fiz. Met. Metalloved. **25** (6), 1049 (1968).
9. S. Strässler and C. Kittel, Phys. Rev. **139**, A758 (1965).
10. *Thermodynamic Properties of Individual Substances: A Handbook*, Ed. by V. P. Glushko (Akad. Nauk SSSR, Moscow, 1962) [in Russian].
11. F. F. Voronov, V. A. Goncharova, and O. V. Stal'gorova, Zh. Éksp. Teor. Fiz. **76**, 1351 (1979) [Sov. Phys. JETP **49**, 687 (1979)].
12. A. K. Singh, High Temp.–High Pressures **12**, 47 (1980).
13. I. N. Frantsevich, F. F. Voronov, and S. A. Bakuta, *Elastic Constants and Elastic Moduli of Metals and Nonmetals: A Handbook* (Naukova Dumka, Kiev, 1982) [in Russian].
14. R. I. Beecroft and C. A. Swenson, J. Phys. Chem. Solids **15**, 234 (1960).
15. A. R. Kutsar, Dokl. Akad. Nauk SSSR **245** (6), 1360 (1979).
16. J.-P. Bastide, C. Loriers, H. Massat, and B. Coqblin, High Temp.–High Pressures **10**, 427 (1978).
17. B. Buras and N. Niimura, Riso Rep., No. 352 (1976).

Translated by N. Korovin

Physics of the Solid State, Vol. 47, No. 12, 2005, pp. 2321–2324. Translated from Fizika Tverdogo Tela, Vol. 47, No. 12, 2005, pp. 2228–2231.

LOW-DIMENSIONAL SYSTEMS AND SURFACE PHYSICS

Acoustoelectronic Interaction in InGaAsP/InP Laser Heterostructures

L. A. Kulakova

Ioffe Physicotechnical Institute, Russian Academy of Sciences, Politekhnicheskaya ul. 26, St. Petersburg, 194021 Russia

e-mail: L.Kulakova@mail.ioffe.ru

Received February 21, 2005

Abstract—The dynamics of change in the spectral characteristics of the emission from a laser heterostructure due to an alternating strain induced by a surface acoustic wave is investigated. The spectral distributions of the laser radiation intensities are analyzed with the aim of elucidating the mechanisms responsible for the interactions occurring in the laser heterostructure. A model is proposed for describing the experimental data, and their theoretical analysis is performed. It is demonstrated that the acoustoelectronic interaction is dominant under the action of surface waves. The deviation of the observed frequency modulation of radiation is determined from a comparison of the theoretical calculations with experimental data. © *2005 Pleiades Publishing, Inc.*

1. INTRODUCTION

It is known that, in semiconductors, the elastic strain (owing to the deformation potential) can lead to a change both in the properties of the electronic subsystem, specifically in the band gap [1, 2], and in the permittivity [3, 4]. It can be expected that the change in the band gap under deformation will manifest itself in laser heterostructures, which should result in a change in the lasing conditions and spectral characteristics of radiation, in particular, in the lasing frequency. The change in the refractive index of the laser cavity under deformation should also affect the spectral characteristics of radiation. In our earlier work [5], we experimentally revealed the frequency modulation of heterolaser radiation due to an alternating strain induced by a bulk ultrasonic wave. This paper reports on the first results of investigations into the mechanism of the strain effect exerted by surface ultrasonic waves on the radiation characteristics of InGaAsP/InP laser heterostructures.

2. SAMPLE PREPARATION AND EXPERIMENTAL TECHNIQUE

In order to investigate the acoustoelectronic and acousto-optic interactions in heterolasers under the action of surface waves, we developed a technique for fabricating heterostructures on $LiNbO_3$ (*YZ* cut) dielectric piezoelectric substrates serving as an acoustic line for Rayleigh surface acoustic waves. The geometry of the interaction with the surface wave differs from that with the bulk wave [5]. The case in point is the ratio between the acoustic wavelength and the thickness of the active region that provides the appropriate time parameters for the action of the alternating strain on the active region of the structure. For the bulk acoustic wave, the wave propagation across the active region of the heterostructure satisfies the required relationship $a \ll \Lambda$, where a is the thickness of the active region in the heterostructure ($a \simeq 200$ Å) and Λ is the acoustic wavelength ($\Lambda \approx 400$ μm). As a result, the electronic and optical parameters of the structure can be treated as parameters varying in time with the period of the alternating strain, which, in our case, is induced by the bulk ultrasonic wave. For the surface acoustic wave, the wave propagation occurs in the plane of the active layer; i.e., the role of the parameter a is played by the active layer width, which is equal to the width d of the contact strip (the electrical contact used for supplying the operating current). In order for the above condition to be satisfied, we prepared a structure with a strip width $d = 6$ μm. This structure was fabricated on the substrate (Fig. 1). The surface wave (frequency, 10 MHz) excited by interdigital transducers (Fig. 1)

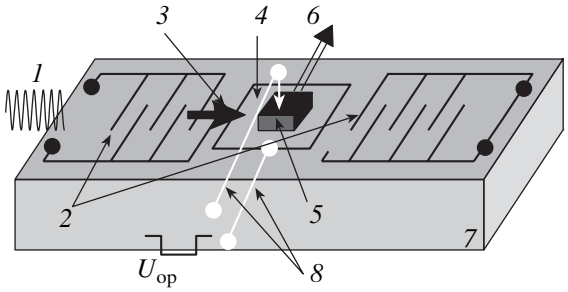

Fig. 1. Scheme for excitation of surface acoustic waves: (*1*) high-frequency pulse, (*2*) interdigital transducers, (*3*) surface acoustic wave, (*4*) thin metal film, (*5*) laser diode, (*6*) laser beam, (*7*) piezoelectric substrate, and (*8*) electric contacts.

1063-7834/05/4712-2321$26.00 © 2005 Pleiades Publishing, Inc.

propagated in the $LiMnO_3$ piezoelectric substrate in the Z direction. The duration and delay of the acoustic pulse could be varied in order to provide different conditions for a complete or partial overlap with a pulse of the operating heterolaser current. We examined InGaAsP/InP laser heterostructures (optical cavity length, 750 μm) operating at room temperature in a pulsed mode with a pulse duration of up to 3 μs at a wavelength of 1.48 μm. The threshold current I_{th} was equal to 30–35 mA, and the operating current I_{op} was varied from the threshold current to triple the threshold current [$I_{op} = (1–3)I_{th}$]. The half-width of the emission line was 0.1–0.2 nm. The radiation was measured according to the following three schemes: (1) direct measurements; (2) measurements after passing radiation through a Fabry–Perot etalon, whose dynamic dispersion range was equal to 18.25 Å; and (3) measurements of the emission spectrum on an MDR23 spectrometer modified for recording pulsed radiation.

3. RESULTS AND DISCUSSION

The experimental data obtained with the Fabry–Perot etalon demonstrated that the dynamics of change in the spectral characteristics of radiation (in real time) under the action of surface acoustic waves is qualitatively similar to that observed for bulk acoustic waves [5]. The excitation of the acoustic wave (when the acoustic pulse coincides in time with the operating current pulse) leads to an almost 100% modulation of the radiation pulse with a frequency equal to the frequency of the ultrasonic wave. An increase in the ultrasonic frequency results in a corresponding decrease in the modulation period of the laser pulse. A decrease in the delay of the current pulse leads to a partial overlap of these pulses and is accompanied by a partial modulation of the laser pulse. It is quite evident that the observed modulation results from a change in the transmission of the Fabry–Perot etalon due to the frequency modulation of laser radiation passing through this etalon. The maximum range of frequency tuning per half-period of the acoustic wave can be estimated using the technique proposed in [5]. The modulation amplitude thus estimated is as large as 4–4.5 Å (at an acoustic power of 1–2 W), which is close to the estimates obtained for bulk waves.

Unlike the experiments with bulk waves, the experiments with the surface acoustic waves allowed us to observe the change in the modulation phase (by 180°) of the transmission of the etalon with an increase in the operating current up to values providing transmission over the entire dispersion range of the etalon and, hence, the changeover from a direct dependence of the transmission of the etalon on the wavelength to an inverse dependence (and vice versa). This confirms once again that our interpretation of the frequency modulation of radiation under the action of acoustic waves is correct and counts in favor of a more stable emission from the laser heterostructures. Therefore, these samples were used for investigating the mechanism responsible for the action of elastic waves on laser heterostructures with the observed changes in the spectral characteristics of generated radiation. Recall that this action can predominantly occur through two mechanisms.

(1) The acousto-optic interaction leads to a change in the permittivity $\delta\varepsilon$ and, hence, in the refractive index Δn. This change is determined by the ultrasonic strain S_j [3] and the corresponding component p_{ij} of the photoelastic coefficient; that is,

$$\Delta n_i = 1/2(\varepsilon_i)^{3/2} p_{ij} S_j^0 \sin\Omega t, \quad (1)$$

where $\varepsilon_i = (\varepsilon_m\varepsilon_n)^{1/2}$, $i = mn$, and $j = lk$ (m, n, l, $k = 1, 2, 3$). The modulation of the refractive index results in a change in the resonance frequencies $\Delta\lambda_k$ of the optical cavity of the heterostructure,

$$\frac{\Delta\lambda_k}{\lambda_k} = \frac{\Delta n}{n}, \quad (2)$$

where k is the number of the resonant mode.

(2) The acoustoelectronic interaction is attended by a change in the band gap of the active region of the heterostructure ($E_g = E_g^0 + \Delta E_g$). This change is determined by the ultrasonic strain and the deformation potential constant Λ_j [1]; that is,

$$\Delta E_g = \Lambda_j S_j^0 \sin\Omega t. \quad (3)$$

The change in the band gap should lead to a change in both the quantum efficiency of the laser heterostructure and the frequency of the maximum amplification,

$$\omega_m = \omega_m^0 + 2\pi F \sin\Omega t, \quad (4)$$

where F is the frequency modulation amplitude (deviation), which can be calculated using relationship (3) from the formula $F = \Lambda_j S_j^0/h$ (this requires knowledge of the deformation potential constant and the strain amplitude of the elastic wave) or from the experimental data on the change in the spectrum under deformation.

Knowledge of the role and relative contributions of these mechanisms is of fundamental and practical significance. The latter circumstance has stimulated the search for structures in which the effective contributions are made by both interaction mechanisms, so that the combined effect on the electronic and optical properties should be represented by their sum. This can ensure the most efficient control over the spectral characteristics of heterostructures.

Let us now analyze one of the possible mechanisms of the observed frequency modulation. When this modulation is associated with the band gap modulation E_g induced by the strain $S(t) \sim \sin\Omega t$, i.e., $E_g \sim \sin\Omega t$, the appearance of the frequency-modulated component should be accompanied by modulation of the quantum efficiency and, hence, the gain due to the modulation of

the concentration of excited electrons. Since the modulation depth ΔE_g is small (of the order of ~10^{-3}), this effect should be observed in the immediate vicinity of the lasing threshold; i.e., the relationship $(I_{op} - I_{th})/I_{th} \ll 1$ must be satisfied. It is necessary that the heterostructure be highly homogeneous over the entire length of the laser cavity. Our measurements of the radiation intensity near the threshold by using direct recording of fast processes with a fast-response ($\tau_d \le 5$ ns) receiving photodiode, a relatively broadband amplifier (bandwidth, up to 400 MHz), and an oscilloscope (bandwidth, 100 MHz) revealed amplitude modulation of the generated radiation with a period equal to the period of the acoustic wave. The intensity of the amplitude-modulated component amounts to approximately 10% of the radiation intensity near the threshold. As the operating current increases, the intensity of this component remains virtually unchanged and its percentage decreases to 10^{-1}–10^{-2}%, as could be expected. As a consequence, with an increase in the operating current (away from the lasing threshold), this component becomes insignificant as compared to the lasing intensity. Therefore, the revealed component of the amplitude modulation proves conclusively the effect of the alternating strain on the electronic subsystem of the active region in the heterolaser, on the one hand, and indicates a high quality of the fabricated structures, on the other hand. These findings suggest that the acoustoelectronic interaction makes a considerable contribution. However, all these observations are necessary but insufficient to make the inference that the contribution of the acoustoelectronic interaction dominates over the contribution of the acousto-optic interaction. In our opinion, these contributions can be separated only using spectrometric data.

In order to elucidate the above mechanisms, we performed a spectral analysis of radiation with the use of the MDR23 spectrometer modified for recording fast processes. Unlike the dynamic spectral analysis carried out in real time with the Fabry–Perot etalon, the investigation into the spectral distribution of the laser radiation is a static variant of the spectral analysis. This variant provides a means for determining a fine structure of the emission spectrum and is a convenient method for solving the posed problem associated with revealing different interaction mechanisms. Let us briefly consider how the ultrasonic waves can affect the spectrum in the case of different interaction mechanisms.

As is known, the time-averaged spectrum, i.e., one or several lines depending on the lasing regime (single-mode, multimode), is recorded at the exit of the spectrometer. The linewidth is determined by the Q factor, the line separation depends on the length of the optical cavity of the structure, and the intensity and the number of lines are governed by the frequency and width of the amplification line of the active layer.

In the case where the acousto-optic interaction is dominant, the excitation of the acoustic wave should lead to oscillations of the emission line with respect to the equilibrium position at the rate of change in the ultrasonic strain. Upon time averaging of the spectrum, this should result in a decrease in the intensity of the line at the center and in line broadening. For the acoustoelectronic interaction, a similar effect should be observed for the amplification line. In this case, the intensities of the emission lines should be redistributed: the intensity of the principal central line should decrease, and the intensities of the side lines should increase.

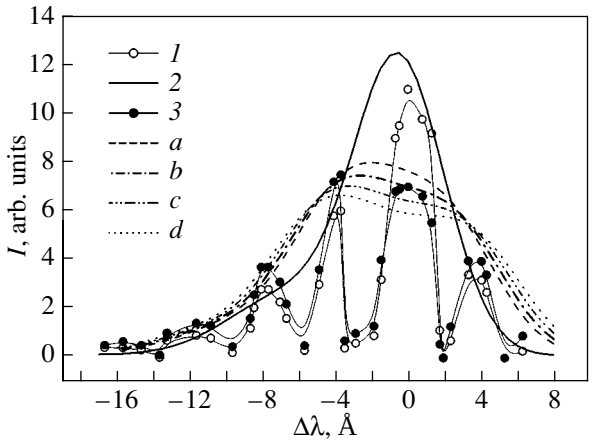

Fig. 2. Spectral distributions of the intensities of the heterolaser emission in the (*1*) presence and (*3*) absence of elastic waves. (*2*) Spectral distribution obtained by theoretical fitting with expression (5). (*a*–*d*) Theoretical spectral distributions constructed with due regard for the influence of the surface acoustic wave according to expression (7) at amplitudes of radiation wavelength tuning $\Delta\lambda_s$ = (*a*) 4.0, (*b*) 4.5, (*c*) 5.0, and (*d*) 5.5 Å.

Figure 2 (curve *1*) depicts the experimental spectral distributions of the radiation intensities for the heterostructure under investigation, in which the variable is the deviation $\Delta\lambda$ of the radiation wavelength from the wavelength λ_0 corresponding to the maximum intensity: $\Delta\lambda = \lambda - \lambda_0$ ($\lambda_0 = 1.48$ μm). The excitation of the acoustic wave leads to the aforementioned redistribution of the intensities of the emission lines without noticeable line broadening (Fig. 2, curve *3*).

Now, we analyze the results obtained. Since the amplification line of the laser heterostructure is asymmetric owing to its origin, this line can be described by a Gaussian distribution with two maxima,

$$I(\Delta\lambda) = I_0 + A_1 \exp\left(-\frac{2(\Delta\lambda - \Delta\lambda_{m1})^2}{w_1^2}\right) + A_2 \exp\left(-\frac{2(\Delta\lambda - \Delta\lambda_{m2})^2}{w_2^2}\right), \quad (5)$$

where I_0 is the constant background intensity, $\Delta\lambda_{m1,\,m2} = \lambda_{m1,\,m2} - \lambda_0$, $\lambda_{m1,\,m2}$ are the wavelengths of the maxima,

and w_1 and w_2 are the widths of the corresponding distributions. For the spectral distribution obtained in the absence of the acoustic action, the results of fitting according to relationship (5) are represented by curve *2* for Fig. 2 with the following parameters: $I_0 = 0.1$, $A_1 = 12$, $w_1 = 5$ Å, $\Delta\lambda_{m1} = -0.5$ Å, $A_2 = 2.4$, $w_2 = 6.5$ Å, and $\Delta\lambda_{m2} = -6.7$ Å.

Since $2\pi F/\omega_m^0 = |\Delta\lambda_s/\lambda_0|$, the influence of sound can be taken into account through the change in the position of the emission maximum along the wavelength axis with the period equal to the period of the acoustic wave. This means that, in the presence of the acoustic wave, the change in the spectral distribution function with time can be represented in the form

$$I(\Delta\lambda, t) = I_0 + A_1\exp\left(-\frac{2(\Delta\lambda - \Delta\lambda_{m1} + \Delta\lambda_s\sin\Omega t)^2}{w_1^2}\right) + A_2\exp\left(-\frac{2(\Delta\lambda - \Delta\lambda_{m2} + \Delta\lambda_s\sin\Omega t)^2}{w_2^2}\right). \quad (6)$$

The relationship describing the averaged spectrum with due regard for the influence of the elastic wave can be obtained by averaging expression (6) over the period of the ultrasonic wave; that is,

$$I(\Delta\lambda) = \frac{1}{2\pi}\int_{-\pi}^{\pi} I(\Delta\lambda, \Omega t)d(\Omega, t). \quad (7)$$

The results of numerical integration according to relationship (7) with the integrand determined by expression (6) for different values of $\Delta\lambda_s$ are represented by curves *a*–*d* in Fig. 2. It can be seen from this figure that the best agreement between the experimental and calculated data is observed at $\Delta\lambda_s = 4.5$ Å. Then, from the formula $F = (c\Delta\lambda_s)/\lambda_0^2$ (where c is the velocity of light), we calculate the frequency deviation $F = 60$ GHz, which agrees well with the above result obtained from the dynamic spectral analysis. Therefore, the analysis of the experimental spectral data demonstrates that the excitation of the acoustic wave in the heterostructures under investigation leads predominantly to modulation of their band gap. In turn, this results in modulation of the lasing frequency due to the temporal oscillations of the amplification line. All these facts indicate that the acoustoelectronic interaction is dominant under the given conditions.

4. CONCLUSIONS

The results obtained in this study can be summarized as follows.

A technique providing efficient excitation of surface acoustic waves in laser heterostructures was developed and implemented. Ultrasonic waves at a frequency of 10 MHz were excited in InGaAsP/InP heterostructures.

Dynamic and static spectral analyses of the emission from the heterostructures under investigation were performed in the presence of Rayleigh surface acoustic waves.

The results obtained from the dynamic analysis are qualitatively and quantitatively similar to those for bulk acoustic waves.

The static spectral analysis demonstrated that the excitation of the surface acoustic wave in the studied heterostructures leads predominantly to their band gap modulation, which, in turn, results in modulation of the lasing frequency due to the temporal oscillations of the amplification line. A theoretical model was proposed for describing the effect of the alternating strain on the spectral distribution of the radiation intensity. A comparison of the experimental data with the results of the theoretical calculations made it possible to determine the frequency deviation $F = 60$ GHz, which is in good agreement with the estimates obtained from the dynamic spectral analysis. From analyzing all the results obtained in this study, the conclusion was drawn that the acoustoelectronic interaction is dominant under the given conditions.

ACKNOWLEDGMENTS

This work was performed within the framework of the program “Basic Research in the Field of Physical Sciences” of the Ministry of Science and Education of the Russian Federation (project no. 37.029.1.1.0029/1) and supported by the Russian Foundation for Basic Research (project no. 04-02-16205).

REFERENCES

1. G. L. Bir and G. E. Pikus, *Symmetry and Strain-Induced Effects in Semiconductors* (Nauka, Moscow, 1972; Wiley, New York, 1974).
2. Yu. V. Ilisavskiĭ and L. A. Kulakova, Fiz. Tverd. Tela (Leningrad) **23** (11), 3299 (1981) [Sov. Phys. Solid State **23**, 1916 (1981)].
3. F. Pockels, Ann. Phys. Chem. (Leipzig) **37**, 269 (1889).
4. N. S. Averkiev, Yu. V. Ilisavskiĭ, and L. A. Kulakova, Fiz. Tverd. Tela (St. Petersburg) **38** (12), 3556 (1996) [Phys. Solid State **38**, 1945 (1996)].
5. L. A. Kulakova and I. S. Tarasov, Pis’ma Zh. Éksp. Teor. Fiz. **78** (2), 77 (2003) [JETP Lett. **78**, 67 (2003)].

Translated by O. Borovik-Romanova

Physics of the Solid State, Vol. 47, No. 12, 2005, pp. 2325–2332. Translated from Fizika Tverdogo Tela, Vol. 47, No. 12, 2005, pp. 2232–2238.

LOW-DIMENSIONAL SYSTEMS AND SURFACE PHYSICS

Stochastic Resonance in Single-Domain Nanoparticles with Cubic Anisotropy

Yu. P. Kalmykov*, Yu. L. Raikher, W. T. Coffey***, and S. V. Titov******

**Lab. Mathématiques et Physique des Systémes, Université de Perpignan, Perpignan Cedex, 66860 France*
e-mail: kalmykov@univ-perp.fr
***Institute of Continuum Mechanics, Ural Division, Russian Academy of Sciences, ul. Akademika Koroleva 1, Perm, 614013 Russia*
e-mail: raikher@icmm.ru
****Department of Electronic and Electrical Engineering, Trinity College, Dublin 2, Ireland*
e-mail: wcoffey@mee.tcd.ie
*****Institute of Radio Engineering and Electronics, Russian Academy of Sciences, pl. Vvedenskogo 1, Fryazino, Moscow oblast, 141190 Russia*
e-mail: svt245@ire216.msk.su

Received November 10, 2004; in final form, March 17, 2005

Abstract—The signal-to-noise ratio for magnetic stochastic resonance in a superparamagnetic particle with cubic anisotropy is shown to be strongly dependent on the Larmor precession damping α. This phenomenon is due to the coupling of the relaxation and precession modes and can be used for measuring α. The dependence of the signal-to-noise ratio on α is characteristic of particles with nonaxial anisotropy; so the effect is absent in uniaxial particles. © *2005 Pleiades Publishing, Inc.*

1. INTRODUCTION

Investigation of the superparamagnetism of single-domain nanoparticles is increasingly important for magnetic recording applications, since this phenomenon has become the main factor laying the physical limit to reducing the dimensions of a carrier of a bit of information [1]. Indeed, thermal fluctuations at room temperature are negligible only for macroscopic magnetic particles. In microscopic particles, thermal fluctuations cause the magnetization to become unstable [2]. One manifestation of such instability in single-domain nanoparticles is stochastic resonance. This phenomenon is due to the coupling of fluctuations and deterministic processes in a noisy system and is widely known in different branches of physics (such as optics, the mechanics of solids, the physics of superconductors, superparamagnetism, and surface physics), radio engineering (optimal rectification and signal detection), chemistry, and biology. Comprehensive reviews of stochastic resonance can be found in [3–5].

Usually, stochastic resonance is modeled by a strongly damped oscillator with a bistable potential in contact with a heat bath. The oscillator is driven by an oscillating external force whose frequency Ω is usually quite low and whose amplitude is insufficient, in itself, to force the system from one stable state into another. However, if the oscillator is in contact with a heat bath, such a transition becomes possible as a result of the combined influence of the driving force and noise. It has been found that the dependence of the signal-to-noise ratio on the noise intensity for such a system is bell-shaped, which is characteristic of stochastic resonance. Thus, noise can facilitate transitions between the stable and/or metastable states of an oscillator. Stochastic resonance can be defined as a noise-induced increase in the signal-to-noise ratio or in the spectral power gain [6].

A single-domain nanoparticle ($\lesssim$10 nm in size) is a physical system in which the conditions of stochastic resonance in magnetization (magnetic stochastic resonance) are satisfied. In the micromagnetics approximation, the particle magnetization **M** precesses under the influence of an external field and the anisotropy field. The combined action of thermal fluctuations (superparamagnetism) and a weak oscillating magnetic field **H** with a frequency Ω can cause transitions of the magnetization **M** between local equilibrium positions. At present, magnetic stochastic resonance is well-studied for bistable systems (particles with uniaxial anisotropy). The free energy V of a uniaxial particle in a spherical coordinate frame (with polar angle ϑ and azimuthal angle φ) is given by

$$\beta V(\vartheta) = \Xi \sin^2 \vartheta, \qquad (1)$$

where $\beta = v/kT$, k is the Boltzmann constant, T is the temperature, v is the particle volume, $\Xi = \beta K_u$ is the dimensionless barrier height, and K_u is the anisotropy constant. The magnetization of a uniaxial particle has two equivalent metastable states, at $\vartheta = 0$ and $\vartheta = \pi$.

1063-7834/05/4712-2325$26.00 © 2005 Pleiades Publishing, Inc.

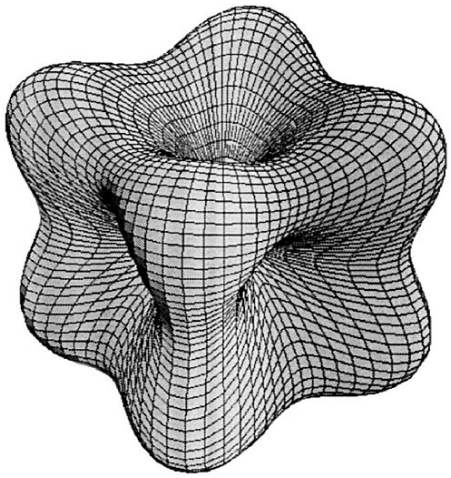

Fig. 1. Cubic-anisotropy potential with $K_c > 0$.

Magnetic stochastic resonance in uniaxial particles was studied, for example, in [7–13].

Stochastic resonance in single-domain particles in the absence of axial symmetry of the magnetic anisotropy potential has not been studied previously. In the present paper, we consider the stochastic resonance of superparamagnetic particles with cubic anisotropy. The free energy of a crystal with a cubic-anisotropy potential in the spherical coordinate frame is given by [14]

$$\beta V(\vartheta, \varphi) = \sigma(\sin^4\vartheta \sin^2 2\varphi + \sin^2 2\vartheta), \quad (2)$$

where $\sigma = \beta K_c/4$ is a dimensionless parameter characterizing the barrier height and K_c is the anisotropy constant.

If $K_c > 0$ (which is the case, for example, for iron), the potential V has six minima (potential wells), eight maxima, and twelve saddle points (Fig. 1). If $K_c < 0$ (which is the case, for example, for nickel), the saddle points retain their positions but the maxima and minima exchange places.

We assume that the magnitude of magnetization **M** is of the single-domain particle is constant. Therefore, we limit our consideration to the rotation of the unit vector $\mathbf{e} = \mathbf{M}/M_S$, which identifies the direction of **M** (here, M_S is the saturation magnetization).

In macroscopic magnetodynamics, the precession of the magnetization **M** of a particle in the absence of fluctuations (at zero temperature) is described by the Landau–Lifshitz–Gilbert equation [2]

$$\dot{\mathbf{e}} = [\mathbf{e} \times (\gamma \mathbf{H}_{\text{eff}} - \alpha \dot{\mathbf{e}})], \quad (3)$$

where $\mathbf{H}_{\text{eff}} = -\frac{1}{M_S}\frac{\partial V}{\partial \mathbf{e}}$, γ is the gyromagnetic ratio, and the dimensionless coefficient α characterizes damping of the Larmor precession. As follows from Eq. (3), in the case of the cubic anisotropy described by Eq. (2), the projection of the moment of the friction force $-\alpha\dot{\mathbf{e}}$ on the precessing vector **e** oscillates and, therefore, strongly modulates the angular velocity of **e**. As a result, the damping parameter α strongly affects the magnetodynamic properties of the particle. Obviously, the additional relaxation mode related to the precession is intrinsic to all systems in which the potentials have no axial symmetry.

In particular, a similar effect [15] arises when a uniaxial particle with an anisotropic potential described by Eq. (1) is subjected to a magnetic field directed at an angle to the symmetry axis.

2. BASIC EQUATIONS

Magnetic stochastic resonance in a weak field can be described based on the linear response approximation as follows. The Fourier transforms of the particle magnetization M_ω and of an external ac field H_ω are related by the complex magnetic susceptibility $\chi(\omega) = \chi'(\omega) - i\chi''(\omega)$:

$$M_\omega = \chi(\omega) H_\omega. \quad (4)$$

The spectral density $\Phi_M^{(s)}(\Omega)$ of forced magnetic oscillations in an oscillating magnetic field $H(t) = H\cos\Omega t$ (the signal) is given by

$$\Phi_M^{(s)}(\Omega) = \frac{1}{2}\lim_{\Delta\Omega\to 0}\int_{\Omega-\Delta\Omega}^{\Omega+\Delta\Omega} (H|\chi(\omega)|)^2[\delta(\omega+\Omega) + \delta(\omega-\Omega)]d\omega,$$

where we made use of the fact that $\chi^*(\omega) = \chi(-\omega)$. Thus, the signal spectral density at the excitation frequency is

$$\Phi_M^{(s)} = \frac{1}{2}H^2|\chi(\Omega)|^2. \quad (5)$$

The spectral density of thermal fluctuations of the magnetic moment $\Phi_M^{(n)}(\Omega)$ (noise) can be calculated using the fluctuation dissipation theorem [16]:

$$\Phi_M^{(n)}(\Omega) = \frac{\chi''(\Omega)}{\pi\beta\Omega}. \quad (6)$$

The sum of the signal and noise components $\Phi_M^{(s)}(\Omega) + \Phi_M^{(n)}(\Omega)$ is equal to the total spectral density $\Phi_M(\Omega)$. From Eqs. (5) and (6), we obtain the signal-to-noise ratio (SNR) [17]:

$$\text{SNR} = \frac{\Phi_M^{(s)}}{\Phi_M^{(n)}} = \frac{\pi\Omega H^2 v|\chi(\Omega)|^2}{2kT\chi''(\Omega)}, \quad (7)$$

This ratio involves only the linear ac susceptibility of the particle. For cubic crystals, Eq. (7) can be written as

$$\mathrm{SNR} = \frac{2\pi\omega_K}{3}\left(\frac{M_S H}{K_c}\right)^2 R_\Omega, \tag{8}$$

where the dimensionless factor R_Ω is given by

$$R_\Omega = \frac{\Omega\tau_0|\sigma|}{\chi_0}\frac{|\chi(\Omega)|^2}{\chi''(\Omega)}. \tag{9}$$

Here, $\omega_K = 2\gamma K_c/M_S$ is a characteristic Larmor precession frequency in the anisotropy field and $\tau_0 = \beta M_S/2\gamma$. In Eq. (9), $\chi_0 = \beta M_S^2/3$ is the static susceptibility per particle volume; we took into account that $\langle\cos^2\vartheta\rangle_0 = 1/3$, which is valid for a cubic magnetic anisotropy potential (the subscript 0 indicates that the statistical average is taken at the equilibrium state).

In the linear response approximation, the ac susceptibility can be expressed as [18]

$$\frac{\chi(\Omega)}{\chi_0} = 1 - i\Omega\int_0^\infty C(t)e^{-i\Omega t}dt, \tag{10}$$

where $C(t)$ is the equilibrium correlation function of the projection of the magnetization **M** (or **e**) onto the direction of the external field, which is defined by

$$C(t) = \frac{\langle\cos\vartheta(t)\cos\vartheta(0)\rangle_0}{\langle\cos^2\vartheta(0)\rangle_0}. \tag{11}$$

In the adiabatic limit ($\Omega \longrightarrow 0$), we have

$$\frac{\chi(\Omega)}{\chi_0} \approx 1 - i\Omega\int_0^\infty C(t)dt = 1 - i\Omega\tau_c, \tag{12}$$

where τ_c is a correlation time defined as the area under the $C(t)$ curve,

$$\tau_c = \int_0^\infty C(t)dt. \tag{13}$$

In the high-temperature limit ($\sigma \longrightarrow 0$), we have

$$\tau_c \longrightarrow \tau_N = \tau_0(\alpha + \alpha^{-1}), \tag{14}$$

where τ_N is the diffusion time of the magnetization vector in the absence of an external field [18]. Substituting Eq. (12) into Eq. (9), we get

$$R_0 = \frac{|\sigma|\tau_0}{\tau_c(\sigma,\alpha)}. \tag{15}$$

Note that Eq. (15) can be derived using a simple exponential law $M_\parallel(t) = M_\parallel(0)e^{-t/\tau_c}$ to approximate the magnetization relaxation. In this case, the susceptibility is given by $\chi(\Omega)/\chi_0 = (1 + i\Omega\tau_c)^{-1}$. Accordingly, the signal-to-noise ratio is given by Eq. (8) in combination with Eq. (15) and becomes independent of Ω.

As shown in [9, 10], in the case where the potential V is axially symmetric, the damping α is simply related to the magnetic signal-to-noise ratio. Namely, in the uniaxial case, the damping α is merely a scale for the relaxation time: $\tau \propto 1/\alpha$. It is tempting to extend this conclusion to particles with cubic anisotropy. However, this extension would be incorrect. Our results clearly show that, in the case of cubic anisotropy, the scaling $\tau \propto 1/\alpha$ occurs only for $\alpha \gtrsim 1$ (intermediate or high damping). However, the most interesting magnetic materials from both the experimental and theoretical points of view have damping in the range 0.01–0.1, where the dependence of the signal-to-noise ratio on α is highly nonmonotonic.

3. CALCULATIONAL METHOD

The complex susceptibility $\chi(\Omega)$ and the correlation time τ_c (and, consequently, the signal-to-noise ratio) of a superparamagnetic particle can be exactly calculated using the matrix continued fraction method [18]. In order to do this, Eq. (3) is first transformed into the Langevin equation (describing the effect of thermal fluctuations) by adding a random white-noise Gaussian field [2, 18, 19]. Next, the Fokker–Planck equation is written for the orientation distribution function of the particle magnetization $W(\mathbf{e}, t)$. This equation has the form [2, 18]

$$\frac{\partial}{\partial t}W = L_{\mathrm{FP}}W = \frac{1}{2\tau_N}\{\beta[\alpha^{-1}\mathbf{e}\cdot(\nabla V\times\nabla W) + \nabla\cdot(W\nabla V)] + \Delta W\}, \tag{16}$$

where ∇ and Δ are the angular parts of the gradient and Laplace operators, respectively. A solution to the Fokker–Planck equation (16) is sought in the form of an expansion in spherical harmonics $Y_{l,m}(\vartheta, \varphi)$ [20, 21]. As a result, the problem reduces to solving an infinite set of recurring differential equations for the correlation functions $c_{lm}(t)\langle\cos\vartheta(0)Y_{l,m}[\vartheta(t), \varphi(t)]\rangle_0$. The solution we look for is the function $c_{10}(t)$, which is related to $C(t)$ from Eqs. (11)–(13) by the simple relation $C(t) = c_{10}(t)/c_{10}(0)$. The original set of equations can be written in a matrix form as [20, 21]

$$\frac{d}{dt}c_{lm}(t) = \sum_{l'm'} d_{lml'm'}c_{l'm'}(t). \tag{17}$$

Here, $d_{lml'm'}$ are the matrix elements of the Fokker-Planck operator L_{FP} involved in Eq. (16). Equations (17) for an arbitrary free-energy function $V(\vartheta, \varphi)$ were

derived in [22]. Equations (17) can be transformed into a recurring trinomial matrix equation,

$$\tau_N \frac{d}{dt}\mathbf{C}_n(t) = \hat{Q}_{n-1}^{-}\mathbf{C}_{n-1}(t) + \hat{Q}_n\mathbf{C}_n(t) + \hat{Q}_{n+1}^{+}\mathbf{C}_{n+1}(t) \quad (n \geq 1), \tag{18}$$

where $\mathbf{C}_n(t)$ is a column vector composed of the correlation functions $c_{lm}(t)$, with $\mathbf{C}_0 = 0$, and $\hat{Q}_{n-1}^{-}$, $\hat{Q}_n$, and $\hat{Q}_{n+1}^{+}$ are matrices whose elements are determined by $d_{lml'm'}$. The exact solution to Eqs. (18) for the Laplace transform of the vector $\mathbf{C}_1(t)$ is given by [20]

$$\tilde{\mathbf{C}}_1(s) = \tau_N \Delta_1 \left\{ \mathbf{C}_1(0) + \sum_{n=2}^{\infty} \left[\prod_{k=2}^{n} \hat{Q}_{k-1}^{+}\hat{\Delta}_k \right] \mathbf{C}_n(0) \right\}, \tag{19}$$

where the matrix continued fraction $\hat{\Delta}_n(s)$ is defined by

$$\hat{\Delta}_n(s) = \cfrac{\hat{I}}{\tau_N s\hat{I} - \hat{Q}_n - Q_n^{+}\cfrac{\hat{I}}{\tau_N s\hat{I} - Q_{n+1} - Q_{n+1}^{+}\cfrac{\hat{I}}{\tau_N s\hat{I} - \hat{Q}_{n+2} - \ldots}\hat{Q}_{n+2}^{-}}\hat{Q}_{n+1}^{-}}.$$

Here, $\hat{I}$ is the unity matrix and the fraction bar denotes multiplication by the inverse matrix. A detailed derivation of solution (19) for cubic crystals can be found in [20, 21]. With $\tilde{\mathbf{C}}_1(s)$ obtained from Eq. (19), we can calculate the correlation time $\tau_c = \tilde{C}(0) = \tilde{c}_{10}(0)/c_{10}(0)$ and the ac susceptibility $\chi(\Omega)/\chi_0 = 1 - i\Omega\tilde{c}_{10}(i\Omega)/c_{10}(0)$ [20, 21]. These results, combined with Eqs. (9) and (15), permit us to estimate the signal-to-noise ratio in the adiabatic approximation and to study its frequency dependence.

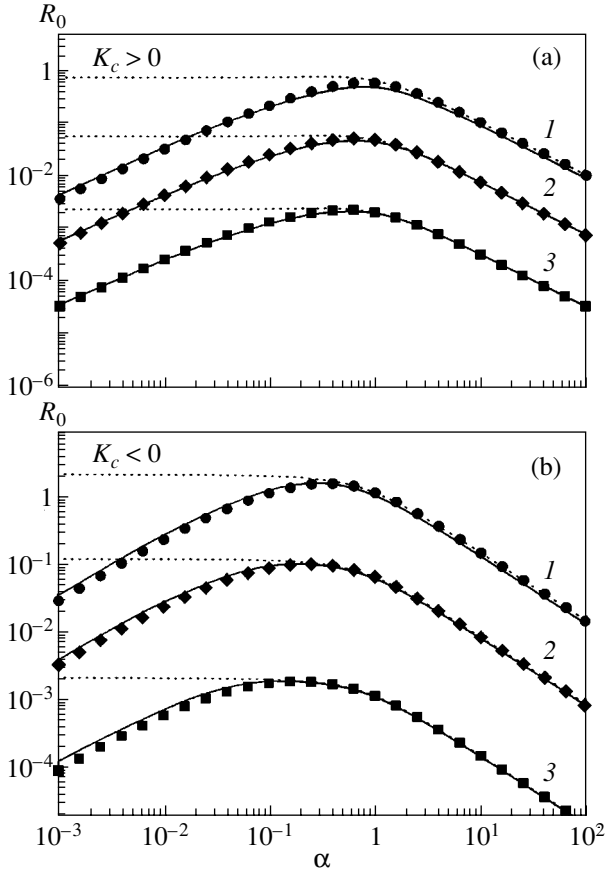

Fig. 2. Signal-to-noise ratio calculated as a function of damping α for various values of 1/σ. The solid lines are calculated using the matrix continued fraction method [Eqs. (15), (19)], symbols correspond to approximate expression (20), and the dashed lines correspond to approximate expression (21) for IHD. The values of 1/σ are (a) (*1*) 0.250, (*2*) 0.125, and (*3*) 0.083 and (b) the values of 1/|σ| are (*1*) 0.083, (*2*) 0.040, and (*3*) 0.025.

4. CALCULATIONAL RESULTS

The signal-to-noise ratio calculated as a function of α and $|\sigma|^{-1}$ in the adiabatic approximation ($\Omega \longrightarrow 0$) is presented in Figs. 2 and 3. Note that, for fixed values of the volume and anisotropy constant of a particle, the quantity $|\sigma|^{-1}$ can be considered a dimensionless temperature. The frequency dependences of the SNR are presented in Figs. 4 and 5. As follows from these figures, the main feature of magnetic stochastic resonance in particles with cubic anisotropy is the dependence of the SNR on the damping α even at $\Omega \longrightarrow 0$, contrary to the seemingly obvious conclusion that the magnetization precession should manifest itself only in the high-frequency spectral range, $\Omega\tau_N \gg 1$. As already mentioned, it is the SNR(α) dependence that makes stochastic resonance in particles with cubic anisotropy fundamentally different from that in particles with an axially symmetric magnetic-anisotropy potential. The reason behind this dependence is a more complicated energy landscape. Indeed, in the case of axially symmetric potential (1), there is a uniform equatorial potential barrier separating two minima situated at the poles of the energy surface; saddle points are absent at this surface. In the case of cubic anisotropy, the shape of the energy surface is more complicated: there are several maxima and minima and multiple saddle points (Fig.1). Therefore, the trajectories of the particle magnetization

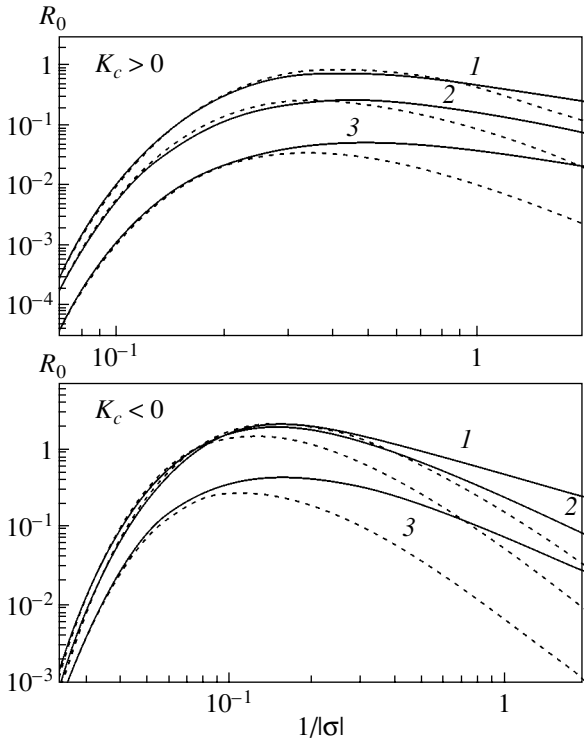

Fig. 3. Signal-to-noise ratio calculated as a function of $1/\sigma$ for various values of damping α. The solid lines are calculated using the matrix continued fraction method, and the dashed lines correspond to approximate expression (20). The values of damping α are (*1*) 1.0, (*2*) 0.1, and (*3*) 0.01.

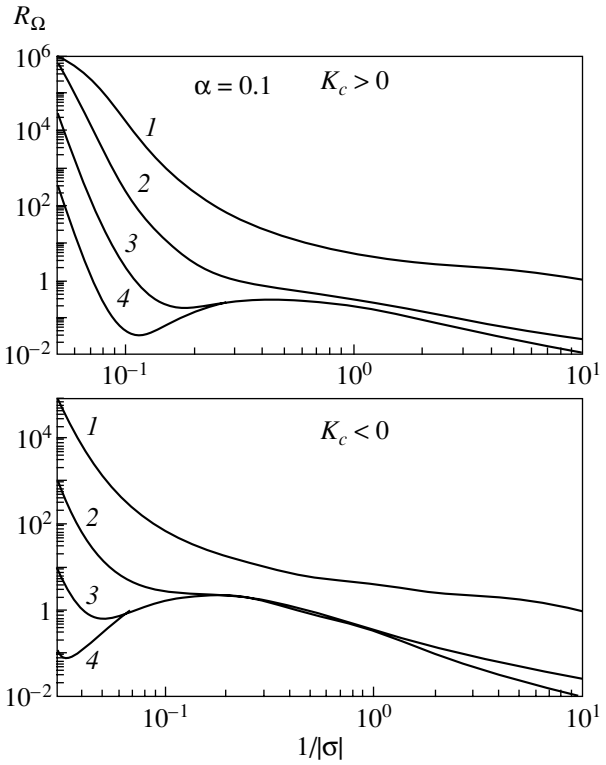

Fig. 4. Signal-to-noise ratio calculated as a function of $1/\sigma$ using the matrix continued fraction method for $\alpha = 0.1$ and various values of the normalized frequency $\Omega\tau_N$: (*1*) 10, (*2*) 1, (*3*) 0.1, and (*4*) 0.01.

on the surface are tortuous and the longitudinal relaxation and precession of the magnetization are closely coupled. As a result, a new phenomenon arises: the signal-to-noise ratio becomes strongly dependent on the rate of spin–lattice relaxation, i.e., on the Larmor precession damping rate. In particular, it turns out that there is a temperature-dependent value of α at which the SNR reaches a maximum.

As shown above, it is possible to calculate the SNR exactly by using the matrix continued fraction method. However, in order to make a qualitative analysis, it is convenient to have approximate but simple analytical expressions. These can be obtained in the low-temperature limit ($\sigma \gg 1$), where the correlation time τ_c can be estimated using the Kramers theory [23]. This theory calculates the escape rate of a Brownian particle from a potential well. It was generalized for superparamagnetic particles in [19, 24–26]. For cubic crystals, approximate asymptotic expressions for τ_c, which are valid for very low damping (VLD, $\alpha \ll 1$) and for intermediate-to-high damping (IHD, $\alpha > 0.1$), were obtained in [24] and [2, 19, 25], respectively. In addition, a universal expression for τ_c, which is applicable in the entire range of damping parameter values, was obtained in [27] using the escape rate calculation technique developed by Melnikov and Meshkov [28]. Using the results from [27], the following asymptotic expression can be written for R_0 for the case of $\sigma \gg 1$:

$$R_0 \sim R_{\mathrm{IHD}} \exp\left\{\frac{1}{\pi}\int_0^\infty \ln[1 - e^{-8\sqrt{2}\alpha|\sigma|(\lambda^2 + 1/4)/9}] \times \frac{d\lambda}{\lambda^2 + 1/4}\right\}, \tag{20}$$

where R_{IHD} is the value of R_0 in the IHD region

$$R_{\mathrm{IHD}} \sim \begin{cases} \dfrac{2\sqrt{2}\sigma^2 e^{-\sigma}}{\pi(1+\alpha^2)}(\sqrt{9\alpha^2 + 8} + \alpha), & K_c > 0 \\ \dfrac{2\sqrt{2}\sigma^2 e^{-|\sigma|/3}}{3\pi(1+\alpha^2)}(\sqrt{9\alpha^2 + 8} - \alpha), & K_c < 0, \end{cases} \tag{21}$$

and the exponential factor matches the VLD and IHD regions. Equation (20) provides a simple and sufficiently precise description of stochastic resonance in single-domain particles with cubic anisotropy in the case of a high potential barrier (the low-temperature limit). The corresponding curves are shown in Figs. 2 and 3. It can be seen that, at any temperature, there is a certain value $\alpha_{\max}$ at which the SNR reaches a maxi-

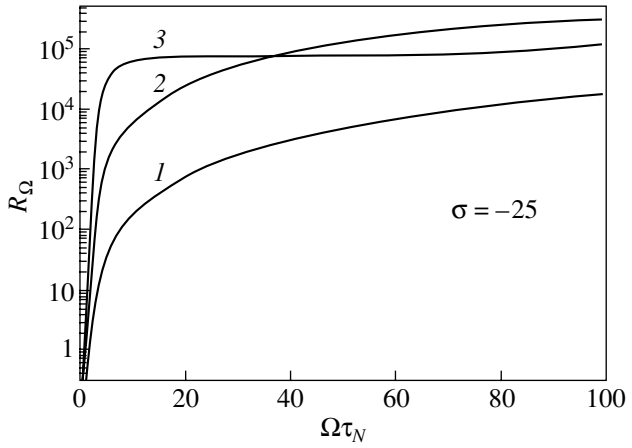

Fig. 5. Signal-to-noise ratio calculated as a function of the normalized frequency $\Omega\tau_N$ using the matrix continued fraction method for $1/\sigma = -0.04$ and various values of α: (*1*) 0.01, (*2*) 0.1, and (*3*) 1.

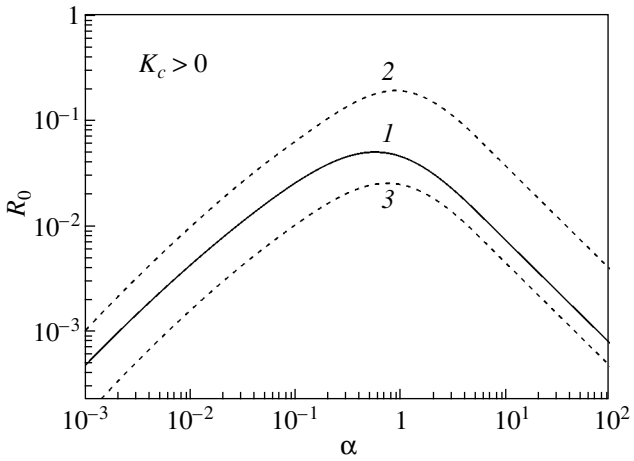

Fig. 6. Signal-to-noise ratio calculated for (*1*) identical particles [from Eq. (20)] and (*2*, *3*) for a gamma distribution in particle volume ($v_0K_c/4kT = 8$). The distribution parameter *b* is (*2*) 0.5 and (*3*) 2.0.

mum $R_{max} \approx R_{IHD}|_{\alpha \to 0}$. Analytical expressions (20) and (21) give simple estimates for R_{max}. It follows from Eq. (21) that $R_{max} \sim 8\sigma^2 e^{-\sigma}/\pi$ for $K_c > 0$ and $R_{max} \sim 8\sigma^2 e^{-\sigma/3}/3\pi$ for $K_c < 0$.

Stochastic resonance can be employed to find the damping factor in nanoparticles with cubic anisotropy in the low-frequency range $\Omega\tau_N \ll 1$ (it should be remembered that we considered stochastic resonance in the adiabatic limit). As is known [29], the values of the damping factor α for real crystals are derived from experimental studies of low-frequency spectra of linear and nonlinear susceptibilities [30, 31], ferromagnetic resonance [32], etc., since virtually insurmountable difficulties are encountered in microscopic calculations of this parameter. The values of α obtained in this way are affected by a number of factors, including the measurement frequency and the sample dimensions. Indeed, the spin-wave spectrum in nanoparticles is substantially discrete, with the interlevel spacing $\Delta\omega$ being on the order of $\sim 8n\pi^2 A/v^{2/3}$, where $A \sim 10^{-6}$ erg/Oe is the inhomogeneous-exchange constant and *n* is the number of a level [29]. For a typical particle volume $v \sim 10^{-18}$ cm^3, we get $\Delta\omega/2\pi \gtrsim n \times 10$ MHz (instead of a continuous spectrum for macroscopic samples). The stochastic-resonance technique enables one to estimate damping from energy data (the spectral density) rather than from phase–amplitude measurements. When comparing calculated and measured values of the SNR, the only free parameter is α; thus, its value can be determined.

In addition, this technique makes it possible to find the temperature dependence of α. The $\alpha(T)$ dependence can be used to distinguish different magnetization relaxation mechanisms. Therefore, it can be useful, for example, when dealing with macroscopic quantum tunneling [33]. From the point of view of application, knowledge of the $\alpha(T)$ dependence is important for developing so-called thermal magnetic recording. Thus, the problem in question is not only interesting for basic research but also has important practical applications.

In all previous calculations, it was assumed that the particles in an ensemble are identical. However, this assumption rarely holds in experiments. In order to take into account the dependence of the SNR on the particle-volume distribution, the SNR should be averaged over the corresponding distribution function $f(v)$. As an

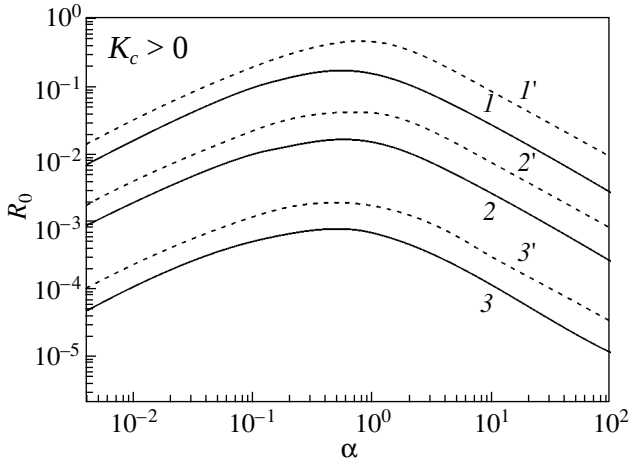

Fig. 7. Signal-to-noise ratio calculated as a function of damping α for the sum of cubic anisotropy with $K_c > 0$ and uniaxial anisotropy with (*1*–*3*) $\Xi = 4$ and (*1*'–*3*') $\Xi = 0$ for various values of $1/\sigma$: (*1*, *1*') 0.250, (*2*, *2*') 0.125, and (*3*, *3*') 0.083.

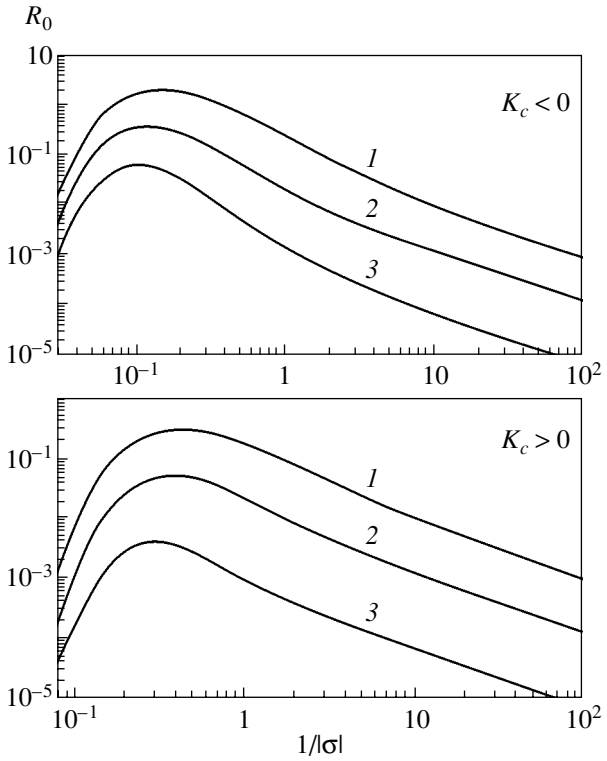

Fig. 8. Signal-to-noise ratio calculated as a function of $1/\sigma$ for $\alpha = 0.1$, $\Omega\tau_N = 0$, and various values of Ξ: (*1*) 0, (*2*) 4, and (*3*) 8.

example, Fig. 6 shows the calculated SNR for the frequently employed gamma distribution [30]

$$f(v)dv = \frac{(v/v_0)^b}{v_0\Gamma(b+1)}\exp(-v/v_0)dv,$$

where v_0 is a typical volume and b is a parameter that defines the shape of the distribution and can be determined by fitting to an experimental histogram $f(v)$. As seen in Fig. 6, the distribution of the particle volumes significantly affects the SNR and can cause it both to decrease (for example, for $b = 0.5$, which corresponds to a distribution with a maximum at $v/v_0 < 1$) and to increase (for $b = 2$, which corresponds to a distribution with a maximum at $v/v_0 > 1$).

The technique developed here for calculating the SNR can be generalized to other types of anisotropy. As an example, Figs. 7 and 8 present calculations of the SNR for a potential that is the sum of a cubic potential ($K_c > 0$) and axial potential (1) for various values of Ξ (in this case, the denominator in the right-hand side of Eq. (15) contains an extra factor $3\langle\cos^2\vartheta\rangle_0$). The height of the potential barrier is characterized in this case by the parameter $\sigma + \Xi$. This parameter is responsible, for the most part, for the decrease in the SNR with an increase in Ξ. This important case will be considered in detail in a later paper. Note that all the results obtained in this study are valid for systems without memory (i.e., with white noise). However, as demonstrated in [24], these results will also be applicable to systems with long-term memory if an effective damping parameter is used.

ACKNOWLEDGMENTS

This work was supported in part by INTAS (grant no. 01-2341) and CRDF (grant no. PE-009).

REFERENCES

1. A. Moser, K. Takano, D. T. Margulies, M. Albrecht, Y. Sonobe, Y. Ikeda, S. Sun, and E. E. Fullerton, J. Phys. D: Appl. Phys. **35** (19), R157 (2002).
2. W. F. Brown, Jr., IEEE Trans. Magn. **15** (5), 1196 (1979).
3. R. K. Adair, Proc. Natl. Acad. Sci. USA **100** (21), 12099 (2003).
4. B. Lindner, J. García-Ojalvo, A. Neiman, and L. Schimansky-Geier, Phys. Rep. **392** (6), 321 (2004).
5. L. Gammaitoni, P. Hänggi, P. Jung, and F. Marchesoni, Rev. Mod. Phys. **70** (1), 223 (1998).
6. R. Fox, Phys. Rev. A: At. Mol., Opt. Phys. **39** (8), 4148 (1989).
7. A. N. Grigorenko, V. I. Konov, and P. I. Nikitin, Pis'ma Zh. Éksp. Teor. Fiz. **52** (11), 1182 (1990) [JETP Lett. **52**, 593 (1990)].
8. L. B. Kiss, Z. Gingl, Z. Márton, J. Kertész, F. Moss, G. Schmera, and A. Bulsara, J. Stat. Phys. **70** (1–2), 451 (1993).
9. Yu. L. Raikher and V. I. Stepanov, J. Phys.: Condens. Matter **6** (22), 4137 (1994).
10. Yu. L. Raikher and V. I. Stepanov, Phys. Rev. B: Condens. Matter **52** (5), 3493 (1995).
11. Yu. L. Raikher, V. I. Stepanov, and P. C. Fannin, J. Magn. Magn. Mater. **258**–**259** (1), 369 (2003).
12. Yu. L. Raikher, V. I. Stepanov, A. N. Grigorenko, and P. I. Nikitin, Phys. Rev. E: Stat. Phys., Plasmas, Fluids, Relat. Interdiscip. Top. **56** (6), 6400 (1997).
13. Yu. L. Raikher and V. I. Stepanov, Phys. Rev. Lett. **86** (10), 1923 (2001).
14. S. Chikatzumi, *Physics of Magnetism* (Wiley, New York, 1964).
15. W. T. Coffey, D. S. F. Crothers, J. L. Dormann, Yu. P. Kalmykov, E. C. Kennedy, and W. Wernsdorfer, Phys. Rev. Lett. **80** (25), 5655 (1998).
16. L. D. Landau and E. M. Lifshitz, *Statistical Physics*, 3rd ed. (Pergamon, New York, 1980), Part 1.
17. M. I. Dykman, R. Mannella, P. V. E. McClintock, and N. G. Stocks, Phys. Rev. Lett. **68** (20), 2985 (1992).
18. W. T. Coffey, Yu. P. Kalmykov, and J. T. Waldron, *The Langevin Equation*, 2nd ed. (World Sci., Singapore, 2004).
19. W. F. Brown, Jr., Phys. Rev. **130** (5), 1677 (1963).
20. Yu. P. Kalmykov, S. V. Titov, and W. T. Coffey, Phys. Rev. B: Condens. Matter **58** (6), 3267 (1998).
21. Yu. P. Kalmykov and S. V. Titov, Zh. Éksp. Teor. Fiz. **115** (1), 101 (1999) [JETP **88**, 58 (1999)].

22. Yu. P. Kalmykov and S. V. Titov, Phys. Rev. Lett. **82** (14), 2967 (1999).
23. P. Hänggi, P. Talkner, and M. Borkovec, Rev. Mod. Phys. **62** (2), 251 (1990).
24. I. Klik and L. Gunther, J. Appl. Phys. **67** (9), 4505 (1990).
25. D. A. Smith and F. A. de Rozario, J. Magn. Magn. Mater. **3** (3), 219 (1976).
26. W. T. Coffey, D. A. Garanin, and D. J. McCarthy, Adv. Chem. Phys. **117**, 528 (2001).
27. Yu. P. Kalmykov, W. T. Coffey, and S. V. Titov, Fiz. Tverd. Tela (St. Petersburg) **47** (2), 260 (2005) [Phys. Solid State **47** (2), 272 (2005)].
28. V. I. Melnikov and S. V. Meshkov, J. Chem. Phys. **85** (2), 1018 (1986); V. I. Melnikov, Phys. Rep. **209** (1), 1 (1991).
29. A. G. Gurevich and G. A. Melkov, *Magnetization Oscillations and Waves* (Nauka, Moscow, 1994; CRC, Boca Raton, FL, 1996).
30. Yu. L. Raikher and V. I. Stepanov, Phys. Rev. B: Condens. Matter **55** (22), 15 005 (1997).
31. L. Spinu, D. Fiorani, H. Srikanth, F. Lucari, F. D'Orazio, E. Tronc, and M. Noguès, J. Magn. Magn. Mater. **226–230** (2), 1927 (2001).
32. D. G. Rancourt, Rev. Mineral. Geochem. (Nanopart. Environ.) **44**, 217 (2001).
33. L. Gunther, Phys. World **3** (12), 28 (1990).

Translated by G. Tsydynzhapov

Physics of the Solid State, Vol. 47, No. 12, 2005, pp. 2333–2340. Translated from Fizika Tverdogo Tela, Vol. 47, No. 12, 2005, pp. 2239–2245.

FULLERENES AND ATOMIC CLUSTERS

Thermal Desorption States of C_{60} Fullerene Molecules in Polymer Matrices

A. O. Pozdnyakov*, B. M. Ginzburg*, T. A. Maricheva, V. V. Kudryavtsev**, M. A. Yagovkina***, and O. F. Pozdnyakov*****

** Institute for Problems in Mechanical Engineering, Russian Academy of Sciences, Bol'shoĭ pr. 61, Vasil'evskiĭ Ostrov, St. Petersburg, 199178 Russia*

e-mail: ao.pozd@mail.ioffe.ru

*** Institute of Macromolecular Compounds, Russian Academy of Sciences, Bol'shoĭ pr. 31, St. Petersburg, 199004 Russia*

**** Ioffe Physicotechnical Institute, Russian Academy of Sciences, Politekhnicheskaya ul. 26, St. Petersburg, 194021 Russia*

Received March 23, 2005

Abstract—Polymer–C_{60} fullerene composite coatings are studied using thermal desorption mass spectrometry. It is found that thermal desorption spectra of C_{60} fullerene molecules can exhibit several resolved peaks (at a specified heating rate) corresponding to thermal desorption states. The relative intensity of the thermal desorption peaks depends on the procedure used for preparing the composite coatings, in particular, on the time of sedimentation of the polymer–fullerene suspension. The occurrence of different stages in thermally stimulated desorption of C_{60} fullerene molecules is explained by the fact that the fullerene molecules can exist in several phase states characterized by different densities and degrees of ordering in the polymer matrix. © *2005 Pleiades Publishing, Inc.*

1. INTRODUCTION

Experimental verification of the natural assumption that the macroscopic properties of polymer–fullerene composite systems should depend on the structural state of the fullerene molecules has necessitated investigation into the mechanisms of formation of the fullerene structure and the temperature behavior of fullerenes in polymer matrices [1–6]. From general considerations, it follows that fullerene molecules being in different structural states in the polymer matrix should exhibit different thermal behaviors.

Experimental investigations have revealed that, in fullerite samples, C_{60} molecules can exist in dispersed, amorphous, and crystalline states [7–10]. Moreover, it has been found that fullerene molecules in polymer matrices can also occur in similar structural states [11–16]. However, the distribution of fullerene molecules over structural states and the thermal properties of the fullerene molecules in these states are still not clearly understood [17]. In the present work, these problems were investigated using thermal desorption mass spectrometry. In our earlier papers [11–16], we demonstrated that thermal desorption mass spectrometry is an efficient tool for measuring a discrete spectrum of thermal desorption states of fullerene molecules even at an extremely low fullerene concentration in a polymer matrix. Two polymers with radically different thermal properties were chosen as the matrices. One of these polymers, namely, polyimide, belongs to rigid-chain polymers with a high glass transition temperature $T_g \sim 320$°C [3]. The other polymer, namely, poly(dimethylsiloxane) (PDMS), belongs to flexible-chain polymers with a low glass transition temperature $T_g \sim -127$°C [18].

2. SAMPLE PREPARATION AND EXPERIMENTAL TECHNIQUE

Polymer–fullerene composites were prepared from a C_{60} fullerite with a purity of higher than 98% (Fullerene Technologies Co., St. Petersburg, Russia). A polyimide–fullerene composite was prepared using a polyimide prepolymer, i.e., polyamic acid (PAA), which was synthesized from 3,3',4,4'-oxydiphthalic anhydride (ODPA), *p*-phenylenediamine (PPD), and 2,5-bis(4-aminophenyl)pyrimidine (APP). The components of the ODPA–PPD–APP copolyimide were taken in the molar ratio 100 : 50 : 50. Suspensions of the C_{60} fullerene in PAA were prepared by introducing a C_{60} fullerene solution in *o*-dichlorobenzene into a PAA solution in dimethylacetamide (the polymer content was approximately equal to 12 wt %), followed by careful stirring of the prepared mixture for a few hours. The synthesis of PAA was described in detail in our previous paper [16]. The calculated weight of the C_{60} fullerene in the initial PAA solution amounted to 2% of the weight of the PAA synthesized. After prolonged sedimentation of the suspension, the formation of a sediment at the bottom of the vessel was observed visu-

ally. After sedimentation of the PAA–C_{60} fullerene suspension for a specified time, the PAA–fullerene solution was poured onto a tantalum substrate (heater) with the aim of forming a composite coating. Moreover, composite coatings were prepared from a sediment formed upon separation of the suspension.

The PAA–C_{60} fullerene composite coatings were dried at room temperature in air for 1 h. Then, the coatings were subjected to curing through thermal imidization of PAA. For this purpose, the coatings were heated in a vacuum chamber of the mass spectrometer to a temperature of ~280°C at a rate of ~ 3 K min^{-1}. The thickness of the coatings formed on the substrate was approximately 2 μm.

Suspensions of the C_{60} fullerene in PDMS were prepared by introducing the C_{60} fullerene into a solution of PDMS (DC-200; Fluka Chemika; viscosity, 67 Pa s) in toluene (the polymer content was approximately equal to 10 wt %), followed by careful stirring of the prepared mixture. The calculated weight of the C_{60} fullerene in the samples amounted to 10 wt % of the weight of PDMS. The suspension was violet in color, which is characteristic of toluene solutions of the C_{60} fullerene. Coatings were applied to the substrate after sedimentation of the suspension within different time intervals. After prolonged sedimentation of the suspension, the formation of a sediment at the bottom of the vessel was observed visually. The thickness of the coatings formed on the substrate was approximately 2 μm.

The processes of thermally stimulated desorption were investigated on an MX-1320 magnetic mass spectrometer (energy of ionizing electrons, 70 eV) equipped with a device for controlled heating of the samples. An oxidized tantalum ribbon (thickness, 200 μm) used as a heater was heated under an electric current at a constant rate of 7 K s^{-1}. The temperature was measured by a chromel–alumel thermocouple welded to the opposite side of the substrate. The pressure in the chamber of the mass spectrometer prior to the experiment was maintained at 10^{-5} Pa.

The absolute sensitivity of the instrument to C_{60} fullerene flow was determined from experiments with a known amount of the fullerene deposited from the toluene solution on the surface of a preliminarily prepared polyimide coating on a metal substrate. The number of fullerene molecules desorbed from the polymer coating was determined using the measured absolute sensitivity of the instrument. The actual volume concentration $n_{C_{60}}$ of fullerene molecules in the coating was calculated as the ratio between the number of fullerene molecules desorbed from the coating (which was determined by integrating the dependence $dN_{C_{60}}/dt$) and the calculated volume of the coating. The volume of the coating was determined from the known area of the coating surface and the calculated coating thickness.

In our experiments on thermally stimulated desorption, we measured the intensity of the principal line of the mass spectrum of the C_{60} fullerene (m/z = 720) simultaneously with the total ion current. The intensity of the total ion current is directly proportional to the rate of release of all volatile products from the studied sample and, consequently, to the rate of mass loss for this sample over the entire temperature range under investigation.

The wide-angle x-ray diffraction experiments with polyimide-based samples were carried out using synchrotron radiation at a wavelength λ = 0.15 nm for a sample–detector distance of 180 cm (A2 Polymer Beamline, Hasylab, Hamburg, Germany) [19]. The x-ray diffraction patterns of PDMS-based samples were recorded on a Rigaku Geigerflex-D/max-RC powder diffractometer using Cu$K\alpha$ radiation (λ = 0.15 nm). In these experiments, the electric current in the x-ray tube was equal to 8 mA and the voltage across the x-ray tube was 40 kV. Taking into account that PDMS is a liquid, the PDMS and PDMS–C_{60} fullerene samples were placed between the substrate and a thin cover glass. This provided a uniform thickness of the studied sample.

3. RESULTS AND DISCUSSION

The temperature dependences of the rate of thermally stimulated desorption of C_{60} fullerene molecules from polyimide–C_{60} composite coatings upon heating are depicted in Fig. 1. In the case of composite coatings prepared from the PAA–C_{60} fullerene suspension after prolonged sedimentation, the thermally stimulated desorption of C_{60} fullerene molecules (Fig. 1a, curve *1*), according to the results obtained in our earlier study [15], occurs in two stages at characteristic temperatures in the range 300–550°C, with the highest rate at a temperature T_1^{max} ~ 450°C (the full width at half-maximum δ of the peak is approximately equal to 150°C), and in the range 500–600°C, with the highest rate at a temperature T_2^{max} ~ 580°C (δ ~ 40°C). The high-temperature portion (550–700°C) in the temperature dependence of the total ion current (Fig. 1a, curve *2*) corresponds to thermal destruction of the polyimide. Therefore, the polymer is retained on the substrate at temperatures higher than T_2^{max}. It should be noted that the low-temperature portion in the temperature dependence of the total ion current corresponds to desorption of the residual solvent and the product of the possible additional imidization (water) from the composite coating.

The specific features of the desorption of C_{60} fullerene molecules are determined by the fullerene concentration in the coating. For coatings prepared from the sediment of the suspension after sedimentation within different time intervals (Fig. 1b, curves *3*, *4*), the thermally stimulated desorption of C_{60} fullerene molecules occurs in two stages in the temperature

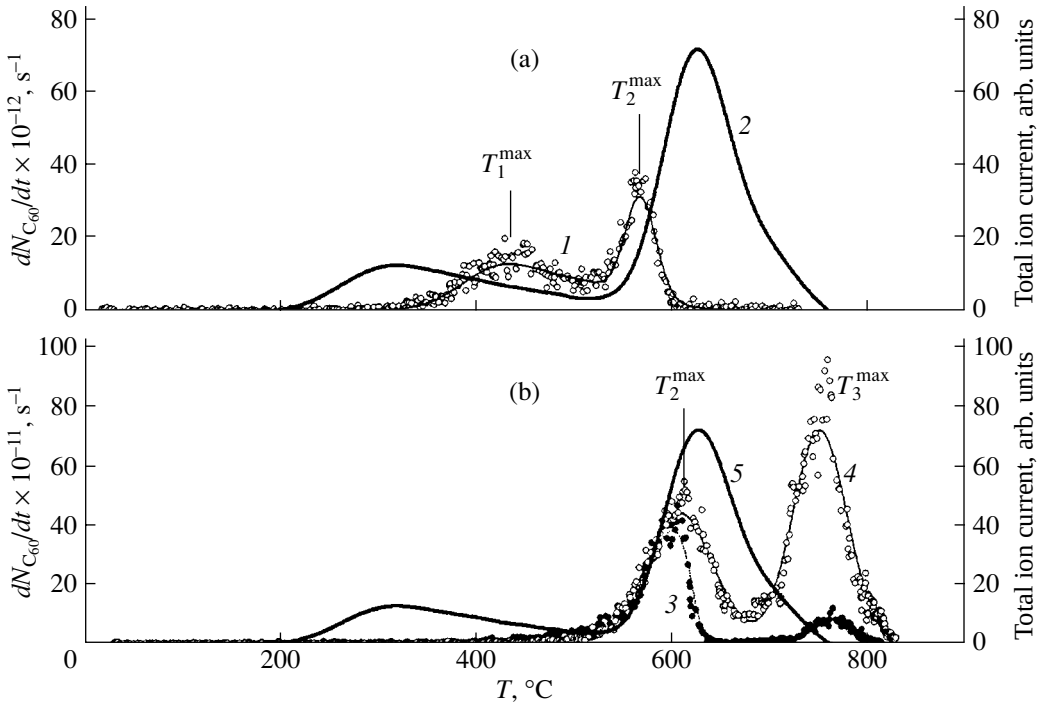

Fig. 1. Temperature dependences of the rate of C_{60} fullerene desorption from polyimide–C_{60} composite coatings prepared from (a) (*1*) the PAA–C_{60} suspension (the weight ratio of the components in the suspension is approximately equal to 100 : 2) after sedimentation for more than 30 days ($n_{C_{60}} \sim 10^{19}$ cm^{-3}) and (b) sediments of the PAA–C_{60} suspension after sedimentation for (*3*) several hours ($n_{C_{60}} \sim 5 \times 10^{19}$ cm^{-3}) and (*4*) more than 30 days ($n_{C_{60}} \sim 10^{20}$ cm^{-3}). Curves *2* (panel a) and *5* (panel b) represent the temperature dependences of the total ion current.

ranges 500–700°C ($T_2^{max} \sim 600$°C, $\delta \sim 100$°C) and 650–830°C ($T_3^{max} \sim 760$°C, $\delta \sim 90$°C). It is worth noting that, in this case, the desorption rate is one order of magnitude higher than the desorption rate obtained for the coating whose behavior is described by curve *1* in Fig. 1a. Taking into account that the weights of the coatings in all experiments are comparable to each other in magnitude, this finding indicates that the actual concentration of fullerene molecules in the coating prepared from the solution over the sediment is less than the calculated concentration. This difference is explained by the process of sedimentation. It should also be noted that the thermal desorption peak observed at the temperature T_1^{max} is absent in curves *3* and *4* (Fig. 1b). The disappearance of the resolved peak at the temperature T_1^{max} with an increase in the fullerene concentration in the polymer matrix is a subject for further experimental investigation. It seems likely that an increase in the concentration of C_{60} fullerene molecules in the polyimide matrix should predominantly lead to an increase in the density of the structural states responsible for the high-temperature peaks of thermally stimulated desorption. A comparison of curves *3* and *4* in Fig. 1b shows that an increase in the time of sedimentation of the suspension brings about an increase in the intensity of the thermal desorption peak at the temperature T_3^{max} for the sample prepared from the sediment of the suspension. Consequently, the concentration of C_{60} fullerene molecules in the course of sedimentation considerably increases in the sediment and decreases in the solution over the sediment. The wide-angle x-ray diffraction patterns of the samples prepared from the sediment formed after prolonged sedimentation of the polyimide–C_{60} fullerene suspension exhibit reflections of crystalline C_{60} fullerene in the polymer matrix (Fig. 2, curve *3*). This suggests that an increase in the actual concentration of the C_{60} fullerene in the coating leads to an increase in the number of C_{60} fullerene molecules occurring in the crystalline state in the polymer matrix at the temperature of the experiment (at room temperature in our case). More detailed analysis of the evolution of the x-ray diffraction patterns measured for polymer–fullerene samples during heating calls for further experimental investigation.

The x-ray diffraction pattern of the sample prepared from the PAA–C_{60} fullerene suspension after prolonged sedimentation is shown by curve *2* in Fig. 2. It can be seen that this pattern does not contain lines corresponding to pure fullerite (Fig. 2, curve *1*). This gives grounds to believe that fullerene regions from which C_{60} mole-

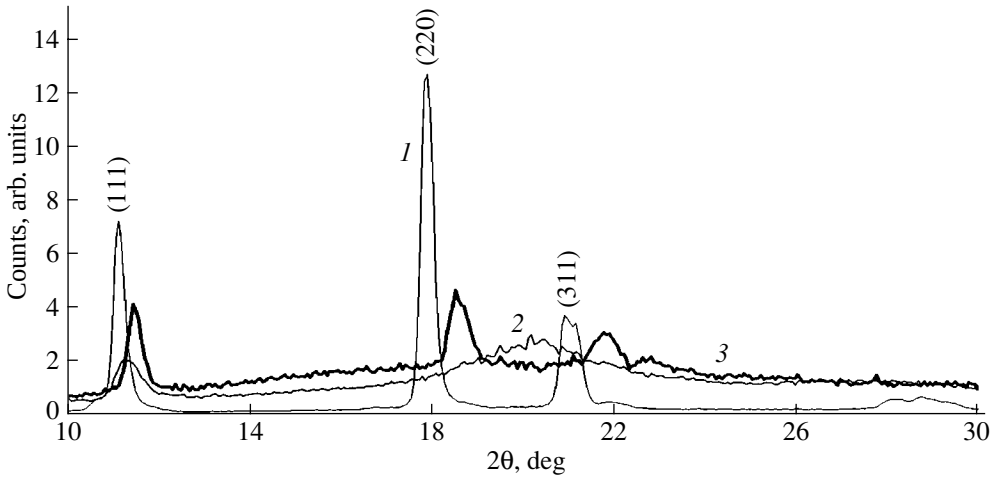

Fig. 2. Wide-angle x-ray diffraction patterns recorded at room temperature: (*1*) the C_{60} fullerite, (*2*) composite films prepared from the PAA–C_{60} suspension, and (*3*) composite films prepared from the sediment of the PAA–C_{60} suspension after prolonged sedimentation.

cules are desorbed at temperatures T_1^{max} and T_2^{max} (the thermal desorption spectrum of this sample is depicted by curve *1* in Fig. 1a) are in a more dispersed state in the polymer matrix as compared to the regions from which C_{60} fullerene molecules are desorbed at the temperature T_3^{max}.

Figure 3 shows the thermal desorption spectra of the samples obtained from the PDMS–C_{60} fullerene suspension immediately after preparation (curve *1*) and after prolonged sedimentation (curve *2*). It can be seen from Fig. 3 that, like the thermal desorption spectra of the polyimide–C_{60} fullerene composite samples, the thermal desorption spectra of the PDMS–C_{60} fullerene composite coatings contain a low-temperature peak at ~ 450°C and a high-temperature peak at ~ 660°C. Note that the low-temperature peak ($\delta \sim 250$°C) is considerably broader than the high-temperature peak ($\delta \sim 150$°C). The high-temperature peak disappears in the course of sedimentation (compare curves *1* and *2* in Fig. 3). The large width δ of the low-temperature peak for the PDMS–C_{60} fullerene composite coatings suggests that this peak can be associated with several stages of the thermally stimulated desorption of C_{60} fullerene molecules characterized by desorption peaks with a smaller value of δ. The approximation of the envelope of the low-temperature peak by two narrower peaks with $\delta \sim 100$°C at temperatures T_1^{max} and T_2^{max} is shown by dotted lines in Fig. 3. It should be noted that, at higher fullerene concentrations in the PDMS matrix (i.e., at short times of sedimentation of the suspension), these peaks are less resolved. As a consequence, the low-temperature peak appears to be sharper, but its width δ remains large (Fig. 3, curve *1*). It is worth noting that the low-temperature desorption states are predominantly formed in the PDMS matrix, even though the actual concentration of C_{60} fullerene molecules in the PDMS matrix ($n_{C_{60}} \sim 5 \times 10^{19}$ cm^{-3}; curve *2* in Fig. 3) is higher than the concentration of fullerene molecules in the polyimide matrix ($n_{C_{60}} \sim 10^{19}$ cm^{-3}; curve *1* in Fig. 1a). Therefore, the results obtained indicate that an increase in the concentration of C_{60} fullerene molecules leads to an increase in the density of the structural states responsible for the high-temperature peaks of thermally stimulated desorption and that this effect is more pronounced in the polyimide matrix as compared to the PDMS matrix.

The x-ray diffraction pattern of the sample prepared from the PDMS–C_{60} fullerene suspension at a fullerene content of 1 wt % is shown by curve *2* in Fig. 4. The x-ray diffraction pattern of the coating prepared from pure PDMS is depicted by curve *1* in Fig. 4. These diffraction patterns have specific features, namely, a characteristic slope of the peak associated with the primary beam and an amorphous halo. It can be seen from Fig. 4 that the x-ray diffraction pattern of the PDMS–C_{60} fullerene sample exhibits a shoulder (indicated by the arrow in Fig. 4) in the slope of the peak of the primary beam at angles close to $2\theta = 10.81°$ for the most intense (111) reflection from the face-centered cubic lattice of the C_{60} fullerene crystals. This suggests that fullerene clusters are formed in the PDMS matrix being in the liquid state at the temperatures used in the x-ray diffraction experiment. Note that the formation of C_{60} fullerene clusters was also revealed by x-ray diffraction in the polymer matrices being in the glassy state at the temperature of the measurement [12, 19, 22].

The position of the asymmetric amorphous halo observed in the x-ray diffraction patterns of the PDMS samples remains almost unchanged upon introduction of the C_{60} fullerene. This suggests that the C_{60} fullerene does not substantially affect the intermolecular dis-

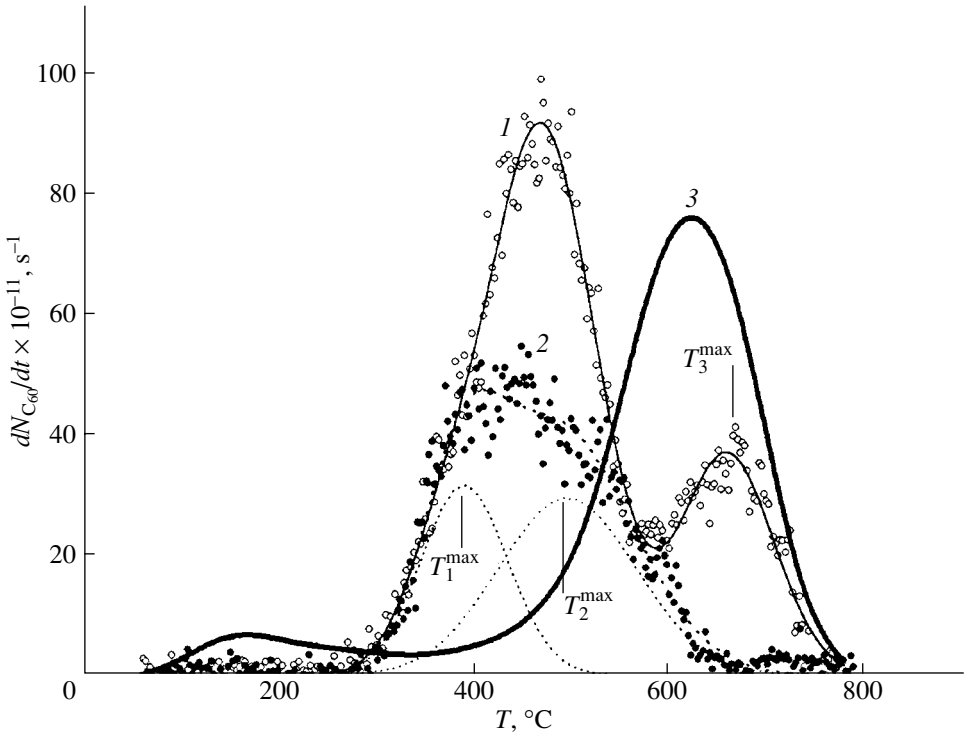

Fig. 3. Temperature dependences of the rate of C_{60} fullerene desorption from the PDMS–C_{60} composite coatings obtained from (*1*) the as-prepared suspension (the weight ratio of the components in the suspension is approximately equal to 100 : 10; $n_{C_{60}} \sim 10^{20}$ cm^{-3}) and (*2*) the suspension after sedimentation for more than 24 h ($n_{C_{60}} \sim 5 \times 10^{19}$ cm^{-3}). Dotted lines indicate the results of the approximation of the low-temperature peak by two narrower desorption peaks. Curve *3* represents the temperature dependence of the total ion current.

tances in the polymer matrix. The mean intermolecular distances X_m determined from the formula $2X_m \sin\theta = K\lambda$ (K = 1.2–1.3) [20] are equal to 0.44–0.48 nm; i.e., they fall in the range characteristic of polymers. A slight decrease in the halo width for the fullerene-containing sample can be caused by two factors: (i) an increase in the size of coherent scattering regions and (ii) a decrease in the spread of intermolecular distances [21]. Both factors indicate a higher degree of ordering of macromolecules in the polymer matrix. This can manifest itself in an increase in the matrix density. Note that similar changes in the shape of the amorphous halo have been observed for other polymer matrices [12, 19] and low-molecular aromatic solvents [23].

The x-ray diffraction data confirm that, in a polymer matrix, C_{60} fullerene molecules occur in a dispersed state even at room temperature, i.e., prior to the thermal desorption experiment. It should be emphasized once again that the evolution of the x-ray diffraction patterns of polymer–fullerene samples during heating, as well as with a change in the initial fullerene concentration and in the procedure used for preparing the sample, calls for detailed experimental investigation.

Analysis of the mass spectrum of the gaseous phase formed upon heating of the coatings revealed that, at the temperature T_3^{max}, the intensity ratio $I_{720} : I_{721} : I_{722}$ of the lines attributed to the C_{60}^+ molecular ion (m/z = 720, 721, 722) is almost identical to the intensity ratio

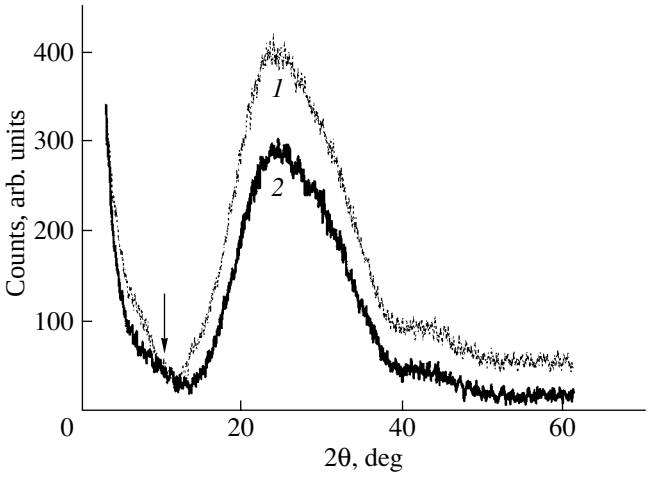

Fig. 4. Wide-angle x-ray diffraction patterns recorded at room temperature: (*1*) the PDMS coating and (*2*) the composite film prepared from the PDMS–C_{60} suspension at a C_{60} fullerene content of approximately 1 wt %.

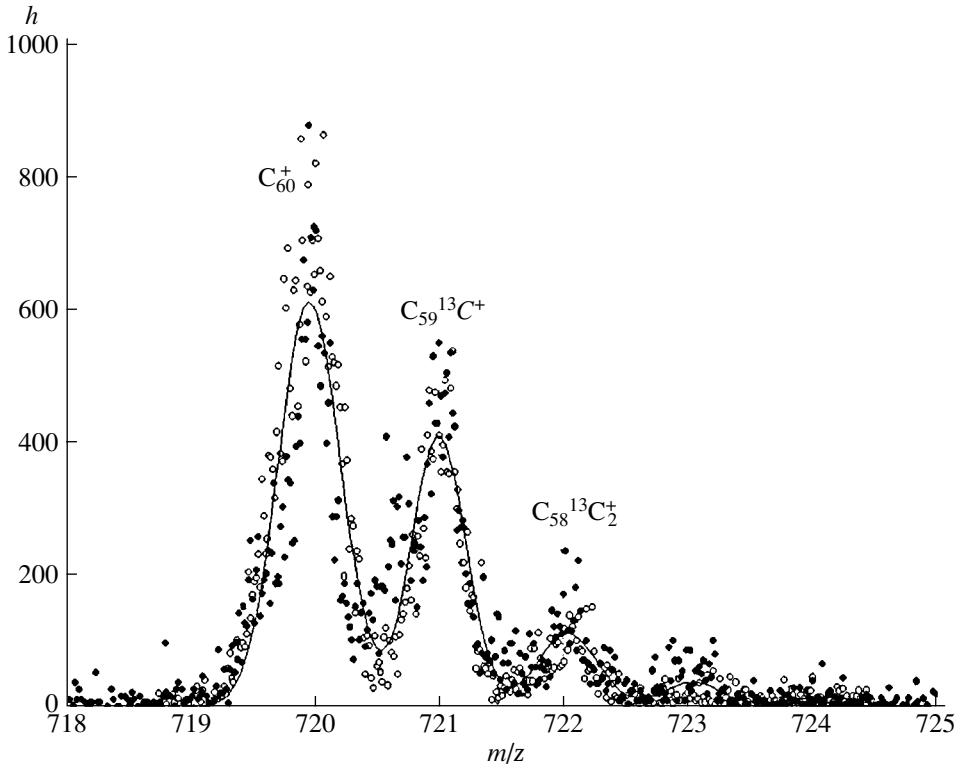

Fig. 5. Mass spectrum measured upon sublimation of the pure C_{60} fullerite at a temperature of ~400°C (solid line), the mass spectrum measured upon heating of the polyimide–C_{60} composite coating (curve *4* in Fig. 1b) at a temperature T_3^{max} (open circles), and the mass spectrum measured upon heating of the PDMS–C_{60} composite coating (curve *1* in Fig. 3) at a temperature T_3^{max} (closed circles).

(100 : 64 : 24) of the corresponding lines in the mass spectrum measured upon sublimation of the fullerite (Fig. 5). This gives grounds to argue that chemically unbound fullerene molecules contained in the sediment hypothetically are in the crystalline state.

The occurrence of diferent stages in thermally stimulated desorption of C_{60} fullerene molecules can be explained by the fact that fullerene molecules can exist in different phase states in the polymer matrix. These states are characterized by different energy barriers to desorption u_i. The structural organization of C_{60} fullerene molecules in the polymer matrix can be represented as an instantaneous "image" of the coexisting gaseous, liquid, and ordered solid phases (Fig. 6). The relative intensity and shape of thermal desorption peaks can depend on the fullerene concentration in the matrix, the matrix properties (thermal stability, reactivity), the procedure used for preparing the composite (conditions of annealing and quenching), and other factors. The phase state with a higher energy barrier to desorption u_i corresponds to a lower desorption probability, which is proportional to the quantity $\exp(-u_i/RT)$, and, consequently, to a higher temperature T_i^{max} of the *i*th desorption stage.

According to the wide-angle x-ray diffraction experiments (Fig. 2), the initial polyimide–C_{60} fullerene samples characterized by the most intense thermal desorption peak at the temperature T_3^{max} contain the crystalline phase of the fullerene. Hence, there are grounds to believe that the thermal desorption stage at the temperature T_3^{max} is associated with the desorption of C_{60} fullerene molecules from crystalline regions. It is significant that, in the experiments under consideration, the temperature range corresponding to the desorption stage at the temperature T_3^{max} coincides with the temperature range of thermal decomposition of the initial polymer (i.e., with the high-temperature portion in the temperature dependence of the total ion current). Consequently, in the experiments on thermally stimulated desorption, C_{60} fullerene molecules contained in crystalline regions of the polymer matrix are desorbed from the coating upon thermal decomposition of the polymer. This circumstance should be taken into account in analyzing the thermally stimulated desorption of fullerene molecules from matrices formed by polymers with a lower thermal stability (see, for example, [11–13]).

Fullerene molecules in a less ordered state (C_{60} fullerene molecules in clusters, individual C_{60} fullerene molecules) are most likely desorbed from the sample at lower temperatures (i.e., at temperatures T_2^{max} and T_1^{max}). We note once again that these temperatures are lower than the temperatures of thermal decomposition of the polymer matrices under investigation. The fraction of C_{60} fullerene molecules involved in the C_{60}–C_{60} interaction in the amorphous and molecularly dispersed states of the fullerene in the polymer matrix is smaller than that in the crystalline state of the fullerene in the matrix. This can result in a decrease in the energy barrier to desorption of C_{60} fullerene molecules from the polymer matrix, because the C_{60}–macromolecule interaction is relatively weak. In the case of the polyimide matrix, C_{60} fullerene molecules are incorporated into the reactive material with respect to the C_{60} fullerene. Actually, PAA macromolecules contain terminal amine groups that exhibit electron–donor properties and can interact with fullerene molecules to form strong chemical bonds of the C_{60}–N type. Therefore, the possibility of dissociating C_{60}–macromolecule chemical bonds (for example, at the temperature T_2^{max}) in the course of thermally stimulated desorption must not be ruled out. The formation of these bonds is indirectly confirmed by the fact that the IR spectra of the PAA–C_{60} fullerene sediment and the polyimide–C_{60} fullerene composite coatings [3] contain absorption bands at frequencies of 617 and 668 cm^{-1}. Although these bands are forbidden for C_{60} fullerene molecules, they indicate that the aforementioned bonds are formed in the matrix.

The stage of thermally stimulated desorption at the temperature T_1^{max} can be attributed to the desorption of fullerene molecules that are in the most dispersed state in the polymer matrix. This state corresponds to the lowest volume concentration of fullerene molecules. Therefore, in this state, the fraction of C_{60} fullerene molecules involved in the C_{60}–C_{60} interaction is considerably smaller than the fraction of C_{60} fullerene molecules participating in the C_{60}–macromolecule interaction. Let us assume that individual C_{60} fullerene molecules diffuse toward the surface of the polyimide–C_{60} fullerene composite coating [15]. Under this assumption, the experimental data obtained at the desorption stage corresponding to the temperature T_1^{max} can be parameterized using the solution to the equation of the second diffusion law. As a result, we obtain a reasonable value of the activation energy for diffusion of individual C_{60} fullerene molecules (~90 kJ/mol). This suggests that fullerene molecules in a dispersed state are desorbed at the temperature T_1^{max}. The activation energies for desorption of fullerene molecules at temperatures T_2^{max} and T_3^{max} are roughly estimated at ~180 and ~270 kJ/mol, respectively.

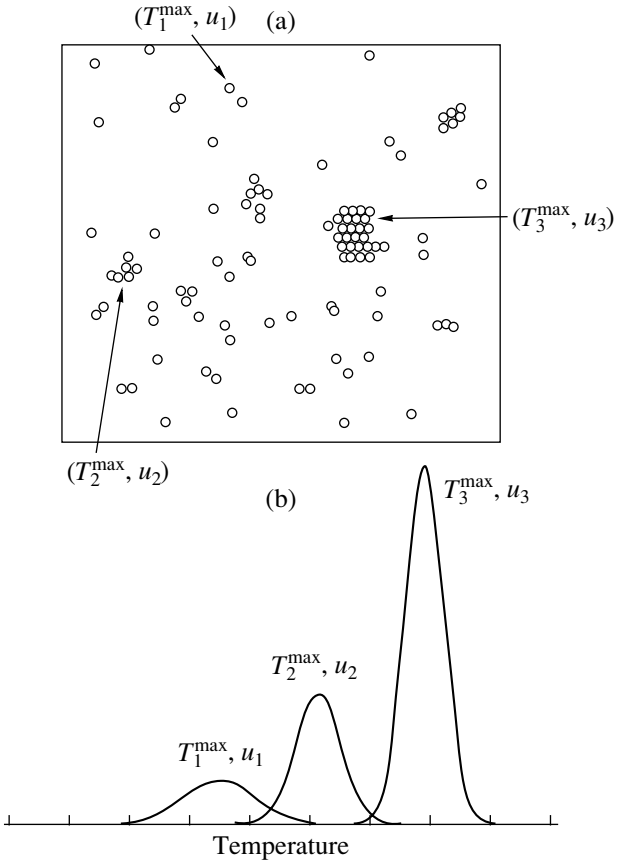

Fig. 6. (a) Schematic diagram illustrating three structural states of C_{60} fullerene molecules: (*1*) C_{60} molecules in a dispersed state, (*2*) C_{60} molecules in clusters, and (*3*) C_{60} molecules in crystallites. (b) Schematic thermal desorption spectrum corresponding to these three structural states characterized by the thermal peaks T_1^{max}, T_2^{max}, and T_3^{max} and the energy barriers to desorption u_1, u_2, and u_3. The relative intensity of the desorption peaks is determined by the concentration of fullerene molecules in the relevant structural state.

A comparison of the thermal desorption spectra shown in Figs. 1 and 3 (the sample volumes and fullerene concentrations in the samples are comparable to each other) demonstrates that, in the PDMS–C_{60} composite coatings, unlike the polyimide–C_{60} coatings, the number of C_{60} fullerene molecules desorbed from the sample at temperatures T_1^{max} and T_2^{max} is considerably larger than the number of C_{60} fullerene molecules desorbed from the sample at the temperature T_3^{max}. Therefore, the content of dispersed fullerene molecules in the PDMS matrix is considerably higher than that in the polyimide matrix. This is explained by the higher flexibility of PDMS chains and by the larger free volume in the PDMS polymer as compared to those of the polyimide at the temperatures of desorption of

fullerene molecules from the PDMS matrix, because the polyimide at these temperatures is in the glassy state.

4. CONCLUSIONS

Thus, polyimide–C_{60} and PDMS–C_{60} composite coatings were investigated using thermal desorption mass spectrometry. It was revealed that thermally stimulated desorption of C_{60} fullerene molecules from a rigid-chain polyimide matrix is similar to thermally stimulated desorption of fullerene molecules from a flexible-chain PDMS polymer matrix. This indicates that fullerene molecules can exist in dispersed, amorphous, and crystalline states in polymer matrices with radically different thermal properties. The distribution of fullerene molecules over the structural states can be governed by the nature of the matrix and the procedure used for preparing the composite coatings.

ACKNOWLEDGMENTS

This work was supported by the Division of Physical Sciences of the Russian Academy of Sciences within the framework of the "New Materials and Structures" program (project "Mechanisms of Formation and Properties of Membranes Prepared from Polymer–Fullerene Composites"). A.O. Pozdnyakov acknowledges the support of the Alexander von Humboldt Stiftung for providing an opportunity to perform x-ray diffraction experiments at the Desy Laboratory (Hamburg, Germany) and would also like to thank M.E. Cagiao and M. Krumova for their assistance in performing the measurements.

REFERENCES

1. V. N. Zgonnik, L. V. Vinogradova, E. Yu. Melenevskaya, K. Yu. Amsharov, O. V. Ratnikova, Yu. F. Biryulin, A. V. Novoselova, and P. N. Lavrenko, Fiz. Tverd. Tela (St. Petersburg) **44** (4), 592 (2002) [Phys. Solid State **44**, 615 (2002)].
2. Yu. F. Biryulin, V. N. Zgonnik, E. Yu. Melenevskaya, S. N. Mikov, S. S. Moliver, S. E. Orlov, A. V. Novoselova, V. D. Petrikov, V. V. Rozanov, D. A. Sykmanov, and M. A. Yagovkina, Fiz. Tekh. Poluprovodn. (St. Petersburg) **37** (3), 365 (2003) [Semiconductors **37**, 347 (2003)].
3. A. O. Pozdnyakov, V. V. Kudryavtsev, and K. Friedrich, Wear **254**, 501 (2003).
4. N. Kamanina, L. Kaporskii, A. O. Pozdnyakov, and B. Kotov, Proc. SPIE-Int. Soc. Opt. Eng. **3939**, 228 (2000).
5. M. Ya. Goikhman, I. V. Gofman, I. V. Podeshvo, E. L. Aleksandrova, A. O. Pozdnyakov, and V. V. Kudryavtsev, Vysokomol. Soedin., Ser. A **45** (7), 1 (2003).
6. Yu. N. Sazanov, M. V. Mokeev, A. V. Novoselova, V. L. Ugolkov, G. N. Fedorova, A. V. Gribanov, and V. N. Zgonnik, Zh. Prikl. Khim. (St. Petersburg) **76** (3), 467 (2003).
7. V. V. Kozlov, Yu. M. Korolev, and G. P. Karpacheva, Vysokomol. Soedin., Ser. A **41** (5), 836 (1999).
8. Yu. M. Korolev, V. V. Kozlov, V. M. Polikarpov, and E. M. Antipov, Vysokomol. Soedin., Ser. A **43** (1), 1933 (2001).
9. G. V. Andrievsky, V. K. Klochkov, A. B. Bordyuh, and G. I. Dovbeshko, Chem. Phys. Lett. **364**, 8 (2002).
10. G. V. Andrievsky, V. K. Klochkov, E. L. Karyakina, and N. O. Mchedlov-Petrossyan, Chem. Phys. Lett. **300**, 392 (1999).
11. A. O. Pozdnyakov, B. M. Ginzburg, O. F. Pozdnyakov, and B. P. Redkov, Zh. Prikl. Khim. (St. Petersburg) **73** (1), 134 (2000).
12. B. M. Ginzburg, E. Yu. Melenevskaya, A. V. Novoselova, A. O. Pozdnyakov, O. F. Pozdnyakov, B. P. Redkov, A. S. Smirnov, A. A. Shepelevskiĭ, L. A. Shibaev, and O. A. Shiryaeva, Vysokomol. Soedin., Ser. A **46** (2), 295 (2004).
13. A. O. Pozdnyakov, E. Yu. Melenevskaya, O. V. Ratnikova, and B. M. Ginzburg, Zh. Prikl. Khim. (St. Petersburg) **76** (12), 2015 (2003).
14. A. O. Pozdnyakov, B. L. Baskin, and O. F. Pozdnyakov, Pis'ma Zh. Tekh. Fiz. **30** (19), 87 (2004) [Tech. Phys. Lett. **30**, 839 (2004)].
15. A. O. Pozdnyakov, B. M. Ginzburg, T. A. Maricheva, V. V. Kudryavtsev, and O. F. Pozdnyakov, Fiz. Tverd. Tela (St. Petersburg) **46** (7), 1328 (2004) [Phys. Solid State **46** (7), 1371 (2004)].
16. A. O. Pozdnyakov, B. M. Ginzburg, O. F. Pozdnyakov, B. P. Redkov, T. A. Maricheva, V. N. Artem'eva, and V. V. Kudryavtsev, Pis'ma Zh. Tekh. Fiz. **26** (17), 46 (2000) [Tech. Phys. Lett. **26**, 775 (2000)].
17. N. W. Ashcroft, Nature (London) **365** (6445), 387 (1993).
18. *Polymer Handbook*, Ed. by J. Brandrup and E. H. Immergut, 3rd ed. (Wiley, New York, 1989).
19. A. O. Pozdnyakov, M. Krumova, M. E. Cagiao, S. S. Funari, V. V. Kudryavtsev, K. Friedrich, and F. J. Balta-Calleja, in *HASYLAB Annual Report*, Ed. by R. Gehrke, U. Krell, and J. R. Schneider (HASYLAB, Hamburg, 2001).
20. A. Guinier, *Théorie et technique de la radiocrystallographie*, 2nd ed. (Dunod, Paris, 1956).
21. B. K. Vainshtein, *Diffraction of X-rays by Chain Molecules* (Akad. Nauk SSSR, Moscow, 1963; Elsevier, New York, 1966).
22. B. M. Ginzburg, L. A. Shibaev, E. Yu. Melenevskaja, A. O. Pozdnyakov, O. F. Pozdnyakov, V. L. Ugolkov, A. V. Sidorovich, A. S. Smirnov, and A. M. Leksovskii, J. Macromol. Sci., Phys. **43** (6), 1193 (2004).
23. B. M. Ginzburg, Sh. Tuĭchiev, S. Kh. Tabarov, V. K. Lavrent'ev, E. Yu. Melenevskaya, A. O. Pozdnyakov, O. F. Pozdnyakov, A. A. Shepelevskiĭ, and L. A. Shibaev, Zh. Prikl. Khim. (St. Petersburg) **78** (6), 1047 (2005).

Translated by O. Borovik-Romanova